Catalyst Development for the Ring-Opening Copolymerisation of Epoxides and Anhydrides

Wilfred Thomas Diment



University of Oxford

Department of Chemistry

Exeter College

September 2021

A thesis submitted in partial fulfilment of the requirements for the degree of Doctor of Philosophy in Chemistry

For my family

Declaration

All work presented in this thesis was carried out at the University of Oxford, by the author, unless otherwise stated.

The copyright of this thesis rests with the author and is made available under a Creative Commons Attribution Non-Commercial No Derivatives licence. Researchers are free to copy, distribute or transmit the thesis on the condition that they attribute it, that they do not use it for commercial purposes and that they do not alter, transform or build-upon it. For any reuse or distribution, researchers must make clear to others the licence terms of this work.

Abstract

This thesis describes the development of a range of catalysts for polyester synthesis *via* the ring-opening copolymerisation (ROCOP) of epoxides and anhydrides.

Chapter 1 provides an introduction to the ROCOP of epoxides and anhydrides, with a particular focus on catalyst development and mechanism. It also introduces the concept of switchable catalysis and describes its application to the synthesis of block polyesters.

Chapter 2 details the synthesis and characterisation of a series of monometallic M(III) complexes (M = Al, Cr, Mn, Fe, Co). Their application as catalysts for the ROCOP of cyclohexene oxide (CHO) and phthalic anhydride (PA), and the ROP of ε-decalactone (ε-DL), is explored. The complexes featuring Al(III) and Co(III) are found to be the most active catalysts for these polymerisations.

Chapter 3 details the application of the Al(III) and Co(III) complexes synthesised in Chapter 2 to the one-pot switchable catalysis reaction of CHO, PA and ε-DL. Triblock copolymers with molar masses up to 57 kg mol^{-1} are synthesised. The catalytic activity of these complexes is shown to be significantly higher than previously used commercial salen catalyst systems.

Chapter 4 details the synthesis and characterisation of a series of heterodinuclear Al(III)/M(I) (M(I) = Group 1 metal) complexes. All are shown to be excellent catalysts for the ROCOP of CHO and PA, with the Al(III)/K(I) and Al(III)/Rb(I) congeners being the most active. Subsequent kinetic investigations, combined with DFT calculations, result in the proposal of a mechanism where the epoxide is bound and activated by the Al(III) centre and the M(I) ion binds the carboxylate chain end. The scope of the catalysis is established for a wide range of epoxides with anhydrides and CO_2.

Chapter 5 details the development of an Al(III)/K(I) complex bearing organometallic coligands. It is demonstrated that use of this complex, in conjunction with bifunctional protic chain transfer agents, can yield monodisperse high molar mass polyesters *via* the ROCOP of vinyl-cyclohexene oxide (vCHO) and PA. The mechanical and thermal properties of the polyesters are investigated to establish the impact of increasing polymer molar mass.

Chapter 6 outlines the key developments of this thesis and suggests future avenues for research that build on the work described.

Chapter 7 provides experimental details for Chapters 2 – 5.

An Appendix is provided that contains supplementary figures and data that support the discussion throughout Chapter 2 – 5.

Acknowledgments

Firstly, I would like to thank Prof. Charlotte Williams for giving me the opportunity to work in her research group, and for her supervision over the course of my DPhil. Your guidance, support, and encouragement over the past three years were greatly appreciated.

I would also like to thank the Williams group as a whole for creating a great working environment. In particular, thanks must go to Dr. Ryan Kerr and Dr. Andreas Phanopoulos for their capable, and essential, crystallography skills and to Dr. Georgina (George) Gregory and Dr. Fernando Vidal for the many useful (and patient) discussions on polymers - this catalysis chemist is very grateful. A further thank you, in some cases repeated, goes to those who proof-read sections of this thesis: Dr. Fernando Vidal, Dr. Bradley Cowie and Dr. Andreas Phanopoulos all provided many useful comments. Thank you also to Gloria for spending a cloudy weekend with me reading from cover to cover. Commiserations to George, Ryan, Arron, and Greg for having to putting up with a substantial amount of my excellent chat.

Hi Mum and Dad and Milly I know this will be the only comprehensible bit but rest assured that your enthusiastic support throughout this whole process was vital. A special, final, word goes to Gloria, who made this last year more fun than it had any right being; long may it last.

Abbreviations

Å	Angstrom
AGE	Allyl Glycidyl Ether
alt	alternating
Ar	Aryl
ATR-IR	Attenuated Total Reflectance Infrared
A. U.	Arbitrary Units
b	block
β-BL	β-butyrolactone
BDM	Benzenedimethanol
BDI	β-Diimine
BO	Butylene Oxide
Bz	Benzoate
DMTA	Dynamic Mechanical Thermal Analysis
C	Celsius
Cat.	Catalyst
cf.	compare
CHD	Cyclohexene-1,2-diol
CHO	Cyclohexene Oxide
COSY	Correlated Spectroscopy
Conv.	Conversion
Cp	Cyclopentadienyl
CRM	Chemical Recycling to Monomer
CTA	Chain Transfer Agent

D	Diffusion Coefficient
Đ	Dispersity
DBU	1,8-Diazabicyclo[5.4.0]undec-7-ene
ΔG	Change of Gibbs Free Energy
DGA	Diglycolic Anhydride
DFT	Density Functional Theory
DMAP	4-Dimethylaminopyridine
DOSY	Diffusion Ordered NMR Spectroscopy
DSC	Differential Scanning Calorimetry
equiv.	Equivalents
ε-CL	ε-caprolactone
ε-DL	ε-decalactone
Et	Ethyl
FT	Fourier Transform
g	gram
GPC	Gel Permeation Chromotography
h	hour
HMBC	Heteronuclear Multiple Bond Correlation
HSQC	Heteronuclear Single Quantum Coherence
IR	Infrared
k	Rate Constant
kcal	kilocalories
kg	kilogram
k_{obs}	Observed Rate Constant

L	Ligand
LA	Lactide
LO	Limonene Oxide
m	minute
μ	Magnetic Moment
M	Metal
MALDI	Matrix Assisted Laser Desorption Ionisation
MBA	Methyl Benzyl Alcohol
Me	Methyl
mg	milligram
mol	mole
M_n	Number Average Molecular Mass
NBA	Norbornene Anhydride
NMR	Nuclear Magnetic Resonance
OAc	Acetate
P	Polymer chain
PA	Phthalic Anhydride
PBL	Poly(butyrolactone)
PCHC	Poly(cyclohexene carbonate)
PCL	Poly(caprolactone)
PET	Poly(ethylene terephthalate)
Ph	Phenyl
PCHPE	Poly(cyclohexene phthalate)
PLA	Poly(lactide)

PMMA	Poly(methyl methacrylate)
PO	Propylene Oxide
ppm	Parts Per Million
PPN	Bis(triphenylphosphine)imine
PSC	Poly(styrene carbonate)
PvCHPE	Poly(vinyl cyclohexene phthalate)
R	Generic Substituent
RAFT	Reversible Addition Fragmentation Chain Transfer
RDS	Rate Determining Step
RHS	Right Hand Side
ROCOP	Ring-Opening Copolymerisation
ROP	Ring-Opening Polymerisation
s	second
SEC	Size Exclusion Chromatography
SO	Styrene Oxide
SQUID	Superconducting Quantum Interference Device
t	Time
T	Temperature
T_d	Decomposition Temperature
τ	Structural Parameter
tBGE	*tert*-butyl glycidyl ether
tBu	*tert*-butyl
TCA	Tricyclic Anhydride
T_g	Glass Transition Temperature

TGA	Thermogravimetric Analysis
THF	Tetrahydrofuran
ToF	Time of Flight
TOF	Turnover Frequency
TON	Turnover Number
vCHO	4-Vinyl-1-cyclohexene oxide
vs.	versus
X	Generic coligand
XRD	X-ray Diffraction

List of Figures, Schemes and Tables

Chapter 1: Introduction

Scheme 1.1	Synthesis of PET from dimethyl terephthalate and ethylene glycol, *via* step growth polymerisation.	23
Scheme 1.2	Synthesis of poly(cyclohexene phthalate) (PCHPE) from phthalic anhydride (PA) and cyclohexene oxide (CHO), *via* chain growth polymerisation.	24
Scheme 1.3	General mechanism for the ROCOP of epoxides and anhydrides.	26
Figure 1.1	A typical bimodal polymer molar mass distribution for a polyester produced by epoxide/anhydride ROCOP	28
Scheme 1.4	Cross-linking of epoxy resins with phthalic anhydride.	30
Scheme 1.5	ROCOP of PO and PA using a **1.1**/Et_4NX.	31
Scheme 1.6	A plausible catalytic mechanism for the ROCOP of CHO and DGA utilising **1.2**.	33
Figure 1.2	Selected metal salen catalyst systems reported for the ROCOP of epoxides and anhydrides.	34
Scheme 1.7	Mechanism proposed by Coates and Tolman for the ROCOP of butylene oxide (BO) and norbornene anhydride (NBA) using **1.5**/PPNCl.	36
Figure 1.3	Tethered multi-metallic salen catalyst systems reported for the ROCOP of CHO and PA.	38
Figure 1.4	A tethered bimetallic salen catalyst system reported for the ROP of PO.	39
Figure 1.5	Dinuclear complexes applied to the ROCOP of epoxides and anhydrides.	40
Scheme 1.8	Chain-shuttling mechanism exhibited by dinuclear catalysts	41

Figure 1.6	Organo- and metal salt catalysts reported for the ROCOP of epoxides and anhydrides.	42
Scheme 1.9	Mechanism proposed for the ROCOP of CHO and PA with complex **1.14**.	43
Scheme 1.10	Switchable catalysis between the ROCOP of epoxides and anhydrides and ROP of lactones.	46
Figure 1.7	Selection of catalysts reported for switchable catalysis.	47

Chapter 2: Monometallic complexes for the ROCOP of epoxides and anhydrides and ROP of lactones

Scheme 2.1	Synthesis of complexes **1** – **5**.	59
Figure 2.1	Molecular structures of complexes **1** – **6**.	61
Table 2.1	Selected bond lengths, obtained from the solid-state molecular structures, and angles of complexes **3** – **6**.	62
Figure 2.2	^{1}H NMR spectrum of complex **6**.	63
Figure 2.3	^{1}H NMR spectrum of complex **3**.	65
Figure 2.4	Overlaid IR spectra of complex **6** and the pro-ligand, $L_{van}H_2$.	66
Figure 2.5	Plot of χ_{mol}^{-1} *vs*. Temperature for complexes **2 - 4**.	67
Table 2.2	Magnetometry data for complexes **2** – **4**.	68
Scheme 2.2	ROCOP of PA and CHO to form poly(cyclohexene phthalate) (PCHPE) with complexes **1** – **5**.	68
Table 2.3	Data for the ROCOP of CHO and PA using complexes **1 - 5** and [SalcyCrCl].	69
Figure 2.6	GPC trace of PCHPE obtained with complex **5**	71
Scheme 2.3	ROP of ε-DL to form poly(decalactone) (PDL) with complexes **1**, **2** and **5**.	72
Table 2.4	Data for the ROP of ε-DL with complexes **1**, **2**, **5** and [SalcyCrCl].	72

Scheme 2.4	ROCOP of CHO and CO2 to form poly(cyclohexene carbonate) PCHC with complex **5**.	74
Table 2.5	Data for the ROCOP of CHO and CO_2 with complex **5**.	74
Figure 2.7	A heterodinuclear complex, [LCoK(OAc)2] reported for CO2/epoxide ROCOP and the proposed dinuclear active species for the **5**/NaOAc catalyst system.	75
Table 2.6	Data for the ROCOP of CHO and CO_2 with **5**/MOAc catalyst systems.	76
Table 2.7	Data for the ROCOP of CHO and CO_2 with **5**/KOAC at varied temperatures.	77

Chapter 3: Monometallic complexes for the switchable catalysis of epoxides, anhydrides and lactones

Scheme 3.1	Monofunctional *vs*. bifunctional initiators	84
Figure 3.1	GPC traces of of PCHPE obtained with complex **1**.	85
Figure 3.2	MALDI-ToF spectrum of PCHPE obtained with complex **1**.	86
Scheme 3.2	One pot reaction of CHO, PA and ε-DL to yield triblock copolymers.	87
Figure 3.3	Data collected using ATR-IR spectroscopy illustrating switchable catalysis.	88
Figure 3.4	GPC traces of triblock copolymers obtained from aliquots taken during switchable catalysis.	89
Figure 3.5	$^{31}P\{^{1}H\}$ NMR spectra of PDL-*b*-PCHPE-*b*-PDL, PDL and PCHPE.	90
Table 3.1	Data for switchable polymerisations of CHO, PA and ε-DL utilising complexes **1** and **5**.	91
Figure 3.6	GPC traces of of PDL-*b*-PCHPE-*b*-PDL prepared with complex **1.**	92
Figure 3.7	DSC plots of triblock copolymers corresponding to Table 3.1, Entries 1, 4 and 5.	93

Table 3.2	Data for the ROCOP of CHO and PA, and ROP of ε-DL, using complex **1** with PPN_2PA.	95
Figure 3.8	GPC trace of PCHPE corresponding to Table 3.2, Entry 1.	96
Table 3.3	Data for switchable polymerisations of CHO, PA and ε-DL utilising complex **1** with PPNCl and PPN_2PA.	97
Figure 3.9	Catalysts reported for switchable catalysis of epoxides, anhydrides and lactones.	98
Table 3.4	Data for catalysts applied to the switchable catalysis of epoxides, anhydrides and lactones.	99

Chapter 4: Heterodinuclear Al(III)/M(I) complexes for ROCOP of epoxides and anhydrides

Scheme 4.1	Synthesis of heterodinuclear complexes **7** - **10**.	108
Figure 4.1	Molecular structure of complex **8**.	109
Table 4.1	Selected bond lengths and angles, obtained from the solid-state molecular structures, of complexes **7** – **10**.	110
Figure 4.2	^{1}H NMR spectrum of complex **8**.	111
Figure 4.3	^{1}H NMR spectrum of complex **8** at 25 °C and -80 °C.	112
Scheme 4.2	ROCOP of CHO and PA to form PCHPE with complexes **7** – **10**.	113
Figure 4.4	Plot showing $[PA]_t$ *vs*. Time for complexes **7** - **10**.	114
Figure 4.5	A) Plot of PCHPE molar mass and dispersity against PA conversion. B) GPC trace of PCHPE obtained with complex **8** at full PA conversion.	115
Figure 4.6	Complexes utilised to investigate the effects of metallic synergy in ROCOP catalysis	116
Table 4.2	Data for the ROCOP of CHO and PA using complexes **6**, **8**, and **11**.	116
Figure 4.7	Plot of $\ln\left(\frac{[CHO]_t}{[CHO]_0}\right)$ *vs*. time (m) obtained with complex **8**.	120

Figure 4.8	Plot of ln(k_{obs}) *vs*. ln([**8**]) at various concentrations of complex **8**.	121
Figure 4.9	Density Functional Theorem calculations for two possible propagation pathways for complex **8**.	123
Figure 4.10	Molecular structure of complex **12**.	124
Figure 4.11	Epoxide and anhydride (or CO_2) comonomers tested with complex **8**.	126
Table 4.3	Data for the ROCOP of a range of epoxides and comonomers with complex **8**.	126
Table 4.4	Comparisons between complex **8** and a selection of literature complexes.	127
Figure 4.12	Future catalyst design directions.	135

Chapter 5: Synthesis of high molar mass polyesters using non-initiating heterodinuclear complexes

Scheme 5.1	Synthesis of complex **13**.	141
Figure 5.1	^{1}H NMR spectrum of complex **13**.	142
Scheme 5.2	ROCOP of PA and vCHO to form poly(vinyl cyclohexene phthalate) (PvCHPE) with complex **13**.	143
Figure 5.2	A) GPC trace of PvCHPE obtained with complex **13**. B) MALDI-ToF spectrum of PvCHPE obtained using complex **13**.	144
Table 5.1	Data for the ROCOP of vCHO and PA with complex **13**.	144
Figure 5.3	GPC traces for PvCHPE synthesised at different catalyst loadings, corresponding to Table 5.1, Entries 1 – 4.	145
Figure 5.4	DSC traces of the PvCHPE weight series.	147
Figure 5.5	Polymer films of PvCHPE-91 obtained via hot press.	148
Figure 5.6	GPC Trace of PvCHPE-91 before and after processing *via* hot press.	149

Figure 5.7	Results from DMTA of PvCHPE-91 between 30 – 200 °C.	150
Table 5.2	Data for PvCHPE weight series from DMTA	150
Table 5.3	Controlled bimodality using various ratios of mono- and bifunctional CTAs.	152
Figure 5.8	GPC traces of bimodal PvCHPE corresponding to Table 5.3, Entries 1, 2 and 3.	152

Chapter 6: Thesis Conclusions and Outlook

Figure 6.1	Thesis summary.	158
Figure 6.2	Proposed future catalyst designs.	159
Figure 6.3	Proposed future research on polyesters.	161

Table of Contents

Declaration 2

Abstract 3

Abbreviations 6

List of Figures, Schemes and Tables 11

Chapter 1: Introduction 21

1.1 Plastics and Polyesters 22

1.2 Industrial Production of Polyesters 23

1.3 Ring-Opening Copolymerisation of Epoxides and Anhydrides 23

1.3.1 Mechanism for the ROCOP of Epoxides and Anhydrides 25

1.4 Catalysts for the ROCOP of Epoxides and Anhydrides 29

1.4.1 Heterogenous Catalysts 29

1.4.2 Early Catalyst Develop 30

1.4.3 Improved Homogenous Catalysts 31

1.4.4 Salen Metal(III) Catalysts 32

1.4.5 Tethered Multi-metallic Salen Catalysts 37

1.4.6 Dinuclear Catalysts 39

1.4.7 Organo- and Metal Salt Catalysts 42

1.5 Switchable Catalysis 44

1.6 Aims and Objectives 48

1.7 References for Chapter 1 51

Chapter 2: Monometallic complexes for the ROCOP of epoxides and anhydrides and ROP of lactones 56

2.1 Introduction 57

2.2 Aims 57

2.3 Synthesis and Characterisation of Monometallic Complexes supported by *ortho*-Vanillin Derived Ligands 59

2.3.1 X-ray Crystallography 60

2.3.2 NMR Spectroscopy 63

2.3.3 Infrared Spectroscopy 66

2.3.4 Superconducting Quantum Interference Device (SQUID) Magnetometry 67

2.4 ROCOP of CHO and PA, and ε-DL ROP, with Complexes **1** - **5** 68

2.5 ROCOP of CHO and CO_2 with Complex **5** 73

2.6 Conclusion and Outlook 79

2.7 References for Chapter 2 80

Chapter 3: Monometallic complexes for the switchable catalysis of epoxides, anhydrides and lactones 82

3.1 Introduction 83

3.2 Aims 83

3.3 Chain Transfer Agent Optimisation 84

3.4 Switchable Catalysis from a One-Pot Mixture of CHO, PA, and ε-DL 87

3.5 Synthesis of High Molar Mass Triblock Polyesters 91

3.6 A Bifunctional PPN-based Cocatalyst 94

3.7 Discussion 98

3.8 Conclusion and Outlook 102

3.9 References for Chapter 3 104

Chapter 4: Heterodinuclear Al(III)/M(I) complexes for ROCOP of epoxides and anhydrides 105

4.1 Introduction 106

4.2 Aims 107

4.3 Synthesis and Characterisation of Heterodinuclear Al(III)/M(I) Complexes 108

4.3.1 X-ray Crystallography 108

4.3.2 NMR Spectroscopy 110

4.4 ROCOP of CHO and PA with Complexes **7** - **10** 113

4.5 Kinetic Investigation of ROCOP of CHO and PA with Complex **8** 118

4.6 DFT Studies of Mechanism for ROCOP Catalysis 122

4.7 Scope of Catalysis 126

4.8 Discussion 129

4.9 Conclusion and Outlook 134

4.10 References for Chapter 4 136

Chapter 5: Synthesis of high molar mass polyesters using non-initiating heterodinuclear complexes 138

5.1 Introduction 139

5.2 Aims 140

5.3 Synthesis and Characterisation of an Organometallic Heterodinuclear Complex 141

5.4 ROCOP of vCHO and PA with Complex **13** 143

5.5 Thermal Properties and Processing of PvCHPE 146

5.6 Mechanical Properties of PvCHPE 149

5.7 Controlling Bimodality in Epoxide/Anhydride ROCOP 151

5.8 Conclusion and Outlook 153

5.9 References for Chapter 5 155

Chapter 6: Thesis conclusions and outlook 156

6.1 Thesis Summary 157

6.2 Outlook 159

6.2.1 Future Catalyst Design 159

6.2.2 Advanced Polyester Synthesis and Further Application 160

6.3 References for Chapter 6 163

Chapter 7: Experimental Details 164

7.1 General Considerations 165

7.2 General Polymerisation Procedure 166

7.3 End Group Analysis by $^{31}P\{^{1}H\}$ NMR Spectroscopy 166

7.4 Monomer Purification Procedures 166

7.5 Methods 168

7.6 Characterising Data for Chapter 2 171

7.7 Characterising Data for Chapter 3 177

7.8 Characterising Data for Chapter 4 178

7.9 Characterising Data for Chapter 5 184

7.10 References for Chapter 7 185

Appendix 186

Chapter 1

Introduction

1.1 Plastics and Polyesters

Plastics are a ubiquitous facet of modern life. In 2019 alone, an estimated 368 million tonnes of new plastic materials were produced, a 2.5% growth on the year preceding.[1] Despite their high utility and low cost, concerns around their end of life processing and management are substantial.[2] There is an urgent need for materials that can replace contemporary plastics, especially with regards to both their bio-renewability and recyclability.

Polyesters, a type of polymer in which monomer units are joined through ester linkages, make up a key segment of the plastic market. Polyethylene terephthalate (PET), an industrial thermoplastic polyester, makes up 7.9% of the plastic resin demand within Europe, representing the joint-5th most utilised plastic, alongside polyurethane.[1] PET is the most widely mechanically recycled plastic, which is currently the leading method for recycling such materials.[3] Issues persist with mechanical recycling, however. In particular, many plastics are in fact '*down*cycled': upon mechanical recycling the quality of the material is significantly reduced, and hence it cannot be used for the same application repeatedly.[4-6]

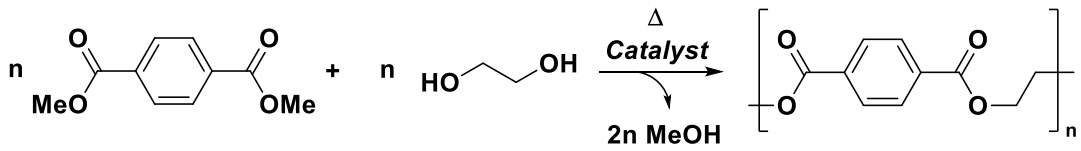
A growing area of interest with regards to the recycling of plastics lies in chemical recycling to monomers (CRM).[5] Through this method, polymers with hydrolysable linkages, such as polyesters (including PET) and polycarbonates, can be recycled back to their chemical feedstocks, which can subsequently be reused in polymer synthesis. Recent breakthroughs have demonstrated the applicability of this approach.[7-9] Whilst this form of recycling requires additional, energy intensive steps in comparison to mechanical recycling, it does allow for re-synthesis of polymers with identical properties to virgin polymers and hence may be attractive to overcome downcycling problems.

A further desirable property of polyesters is the potential to use bio-renewable monomers, which would allow for the decoupling of the synthesis of plastics from the petrochemical

industry.[10, 11] The pressing need for sustainable materials in the 21st century means that research into novel methods to synthesise polyesters is warranted.

1.2 Industrial Production of Polyesters

The most frequent industrial synthesis route to commercial polyesters is *via* step-growth polymerisations of diols with dicarboxylic acids or esters, or the self-condensation of a hydroxy-carboxylic acid (Scheme 1.1).[12] Catalysts are often used to aid reaction speed and supress side reactions. For example, in the synthesis of PET from dimethyl terephthalate and ethylene glycol, a dual catalyst system is used: in the initial phases of the reaction metal acetate (M = Mn, Zn, Ca, Co, Mg) catalysts are used whilst an Sb_2O_3 catalyst is utilised in the latter stages.[12]



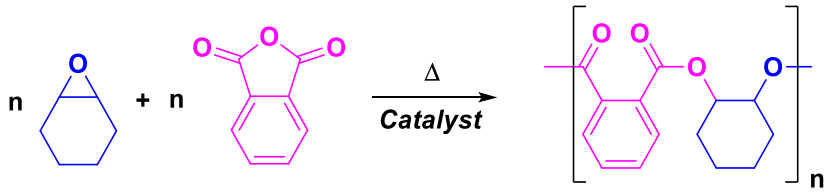
Scheme 1.1. Synthesis of PET from dimethyl terephthalate and ethylene glycol, *via* step growth polymerisation.

The downsides of such a process are the high temperatures and low pressures needed to remove the small molecule by-products produced from the condensation reaction, which is required to drive the polymerisations to high monomer conversions. Further, step polymerisations exhibit poor control of polymer dispersities ($Đ \geq 2$) and very high conversions of monomers (>98%) are required to yield polymers of high molar mass.[12]

1.3 Ring-Opening Copolymerisation of Epoxides and Anhydrides

An alternate route to the synthesis of polyesters is *via* chain-growth polymerisation (Scheme 1.2). In comparison to step growth methods, chain growth polymerisations do not produce small molecule byproducts which need to be driven off. As a result, lower operating temperatures and ambient pressures can be used. A further advantage is that, with suitable

catalyst selection, polymerisations are typically living, resulting in low polymer dispersities (Đ < 1.2) and high molar mass polymers that can be reached at lower monomer conversions.



Scheme 1.2. Synthesis of poly(cyclohexene phthalate) (PCHPE) from phthalic anhydride (PA) and cyclohexene oxide (CHO), *via* chain growth polymerisation.

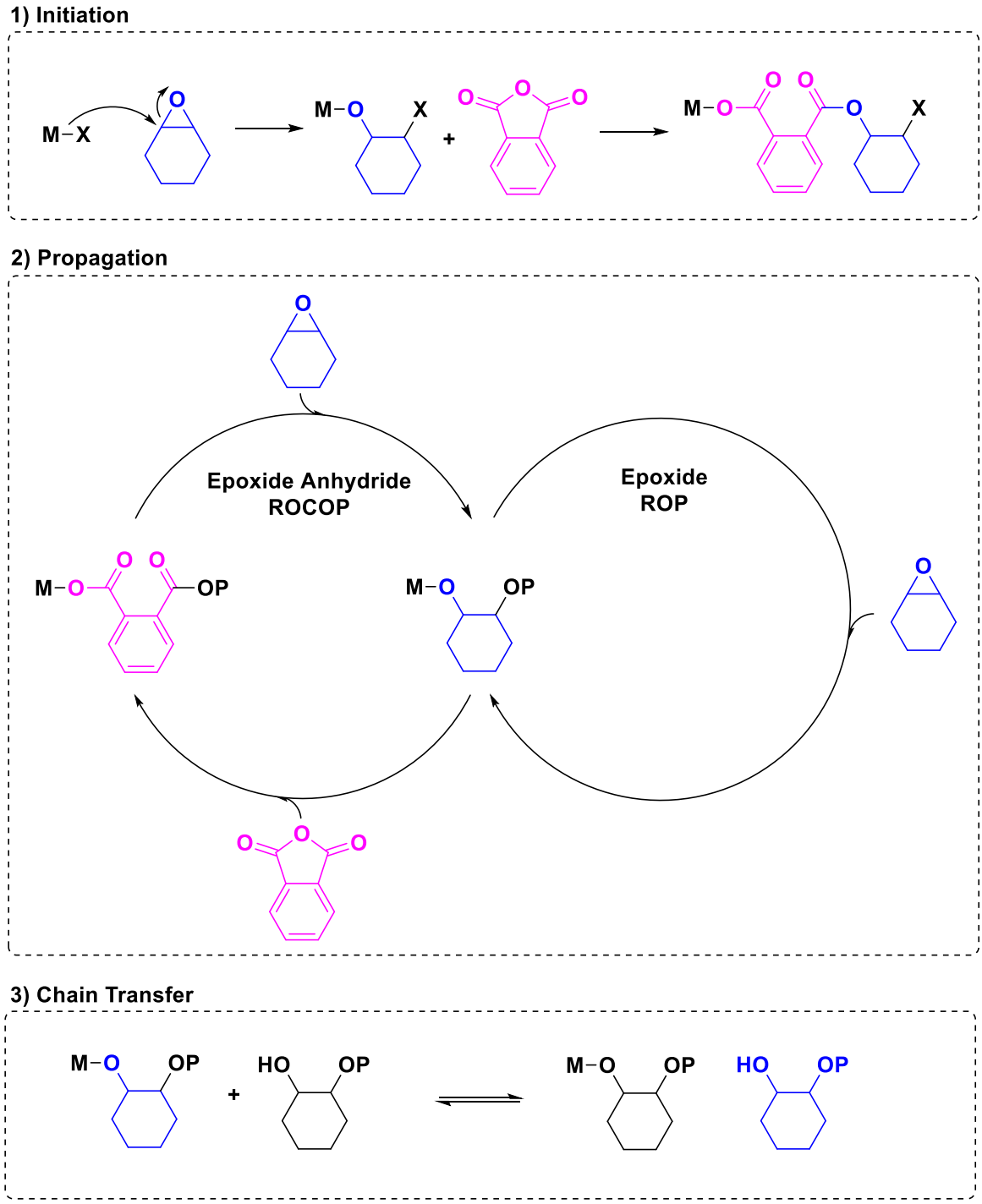
There are two main categories for the chain-growth synthesis of polyesters: ring-opening polymerisation (ROP) of cyclic ester monomers such as lactide or lactones, and the ring-opening copolymerisation (ROCOP) of epoxides and anhydrides. Whilst the former methodology is extensively developed, and a wide range of highly active catalysts for this process have been reported, there are some significant drawbacks that include polymerisations that are inhibited by intrinsic thermodynamic equilibria that prevent complete monomer conversion and a limited commercially available monomer library.[12, 13] This latter issue results in a restricted range of polymeric materials that can be accessed, hence narrowing the scope of application of polyesters derived from this methodology.

In the main, cyclic ester ROP is best suited to prepare aliphatic polyesters from unfunctionalised rings of sizes 4, 6 and 7. It is not well suited to make polyesters with side-chain substituents as the Thorpe-Ingold effect reduces the ring strain with each additional ring-substituent.[12, 14] It is also unsuited for the preparation of semi-aromatic polyesters such as PET. Although simple aliphatic polyesters do have some applications, they tend to suffer from low thermal stability and there are inherent narrow processing temperature windows.[15] In addition, they cannot access the entire material property profile and so tend to be better suited to applications requiring low glass transition temperature elastomers or, in the case of semi-crystalline PLA, brittle plastics.[16]

In comparison, the ROCOP of epoxides and anhydrides can utilise a wide range of commercial monomers and is not thermodynamically constrained, hence operates efficiently using substituted and aromatic monomers.[13] This allows for much greater scope, and tuning, of polymeric material properties and for the design of polymers which may challenge the incumbent petrochemicals well beyond where polyesters are conventionally applied. Because the polymerisations are thermodynamically highly favoured, they can usually proceed to full conversion which is desirable both from process efficiency and polymer purification stand-point.[13, 17] In spite of these clear benefits, the development of catalysts for these processes are significantly less advanced than for cyclic ester ROP; there remains scope for significant expansions in catalyst activity, tolerance and selectivity.

1.3.1 Mechanism for the ROCOP of Epoxides and Anhydrides

A general mechanism for the catalysed ROCOP of epoxides and anhydrides has been developed, although the specific role of the catalyst varies significantly (Scheme 1.3).[13] Typically, the polymerisation is living, and hence has initiation and propagation phases, without significant chain termination occurring. Chain transfer without concomitant chain termination can occur, however.



Scheme 1.3. General mechanism for the ROCOP of epoxides and anhydrides.

The principle phases of ROCOP polymerisation are as follows:

1. Initiation. This occurs through the ring opening of an epoxide molecule with a nucleophilic group, which is often a chloride or acetate. From the resultant metal-

alkoxide, rapid anhydride insertion generates a metal-carboxylate, which is typically the catalyst resting state.

2. Propagation. From the catalyst resting state, alternating insertion of epoxide followed by anhydride results in the generation of polyester. It is generally found that the epoxide insertion is the rate determining step, and hence reactions show no rate dependence on anhydride concentration. A consequence of this result is that reactions are often run in neat epoxide, which can simultaneously act as both a reagent and solvent. A common undesirable side reaction is the generation of ether linkages or even polyether blocks, which occurs through repeated epoxide insertions from a metal-alkoxide chain end.
3. Chain Transfer. As epoxide/anhydride ROCOP is a living polymerisation chain termination side-reactions do not occur. However, by adding alcohols or acids, rapid chain transfer can occur between the active polymer chain and the added protic reagents. This chain transfer usually occurs faster than chain propagation allowing for production of narrow dispersity molar mass distributions. The resultant metal bound species can subsequently initiate polymerisation following steps 1 and 2, leading to further polymer chains. Polymerisations following this mechanism are often termed ‘immortal’.

A corollary of points 1 and 3 is that all polymer chain ends present in the polymerisation grow at the same rate. Hence, polymers initiated from bifunctional species such as diols (which are either added to polymerisations or are formed due to the presence of residual water) increase in molar mass at a rate of twice that of those initiated from monofunctional species, such as chloride or acetate coligands. The overall effect of this is that bimodal polymer molar mass distributions are often obtained when catalyst systems with monofunctional initiators are used (Figure 1.1). When this is the case, the higher molar mass

peak features telechelic α,ω-hydroxy end capped polymers, and the lower weight peak features α-X-ω-hydroxy end capped polymers (where X is an initiating monofunctional species).

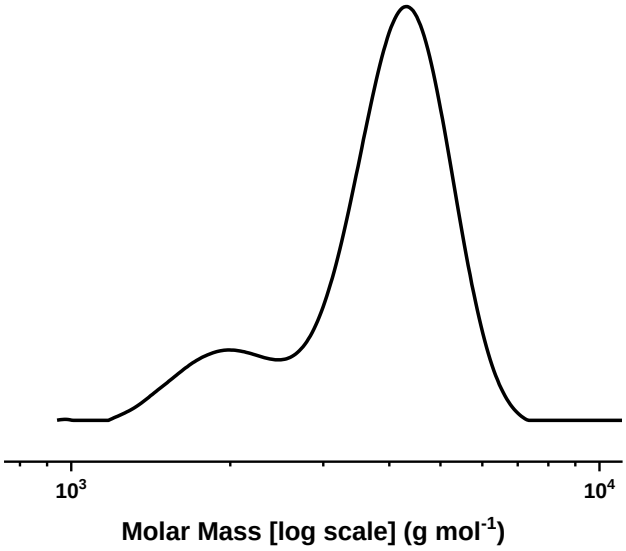


Figure 1.1. A typical bimodal polymer molar mass distribution (measured by GPC) for a polyester produced by epoxide/anhydride ROCOP.

Whilst the production of bimodal molar mass distributions is not necessarily problematic, there are several cases where monodisperse polyesters with only one type of end group are essential, such as the selective formation of more complex structures, e.g. triblock copolymers (*vide infra*). In these cases, the only solution is to add multiple (~10-20) equivalents of CTA in an attempt to supress the bimodality, resulting in a major form of polymer end-group being present but never totally suppressing other structures.

An alternative approach to this strategy is to use catalysts that feature non-initiating coligands, which are typically organometallic aryl or alkyl groups.[18-20] In this case, addition of alcohol CTAs results in the formation of alkoxide species *in situ* that can initiate the polymerisation directly *via* insertion in to an anhydride. Importantly, if the added CTAs are

bifunctional, monodisperse polymer distributions can be obtained, as the dominant impurity in most polymerisations is an epoxide-derived diol resulting from the presence of trace water.

1.4 Catalysts for the ROCOP of Epoxides and Anhydrides

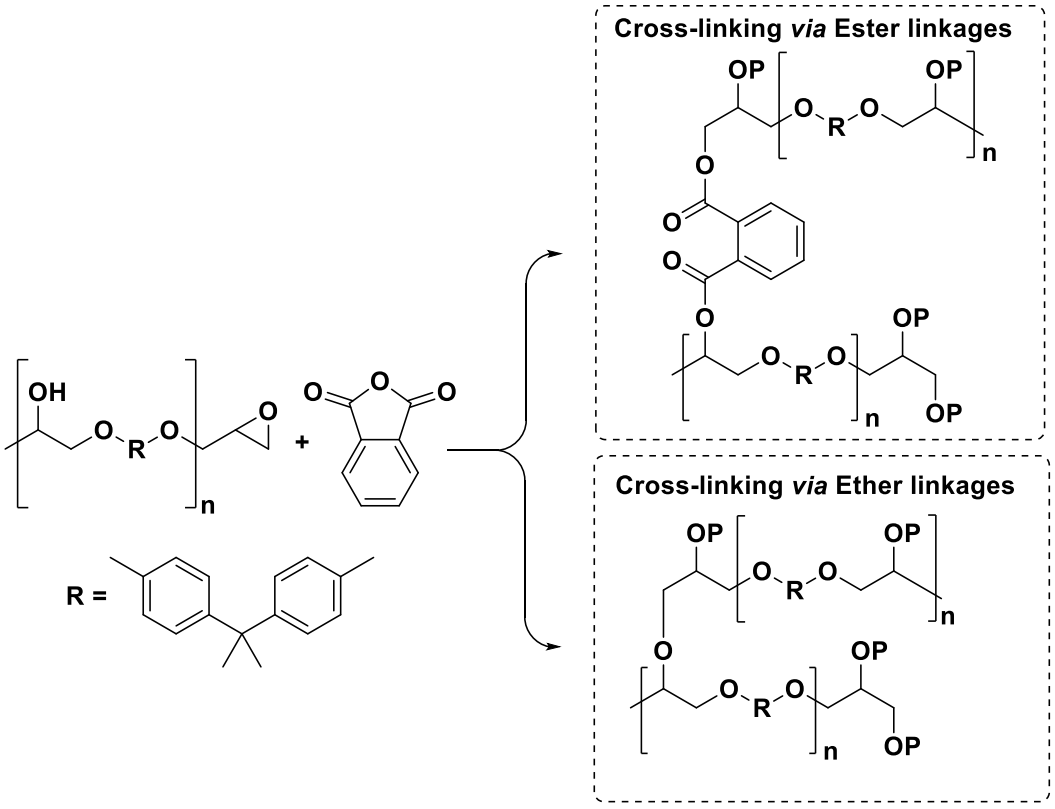
Since the first reports in the 1960s, a range of homogenous catalysts have been reported for the ROCOP of epoxides and anhydrides. The key milestones in catalyst development are discussed here, with a particular focus on catalytic mechanism and how further catalyst development was inspired from each discovery. The reader is directed to several excellent reviews that provide further details on the full range of complexes reported for ROCOP catalysis.[13, 17, 21] It should be noted that many of the complexes that display activity for the ROCOP of epoxides and anhydrides also show activity for the ROCOP of epoxides and CO_2, a related copolymerisation, although the relative activities often differ (*i.e.* not all good epoxide/anhydride ROCOP catalysts make for good epoxide/CO_2 ROCOP catalysts, and *vice versa*).

1.4.1 Heterogenous Catalysts

Alongside the homogenous systems discussed here, a range of heterogenous catalysts are also known for the ROCOP of epoxides and anhydrides. These include zinc-cobalt double metal cyanides, zinc glutarate and magnesium ethoxide.[22-26] Issues persist, however, with both the relatively low activity of the catalysts as well as low weights and high dispersities of the polymers obtained. Further, as with all heterogenous catalysts, the lack of a single, well-defined active site of catalysis makes detailed study into the catalytic mechanism, and hence further rational catalyst design, challenging.

1.4.2 Early Catalyst Development

Early investigations into the ROCOP of epoxides and anhydrides using homogenous catalysts came from attempts to cure (cross-link) epoxy resins using anhydrides (Scheme 1.4).[27, 28]



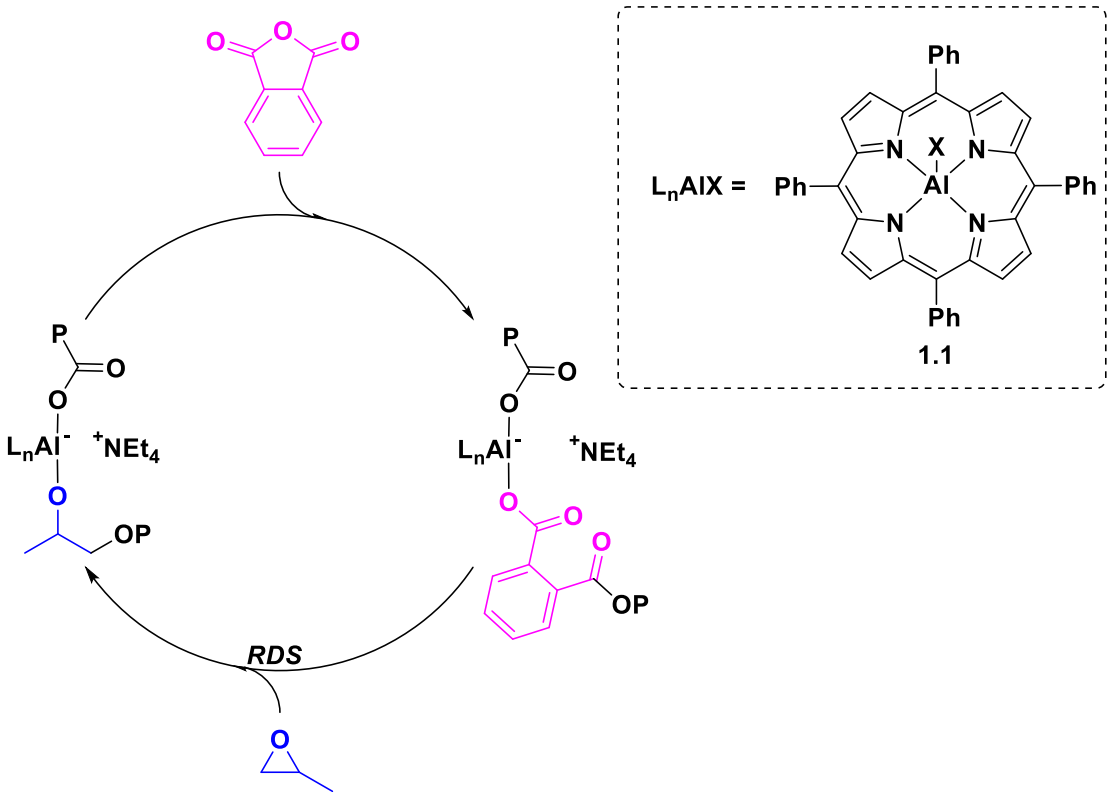
Scheme 1.4. Cross-linking of epoxy resins with phthalic anhydride.

With no catalyst present, the expected ester cross-links were accompanied by unexpected ether linkages. Subsequently, it was established that the use of tertiary amines suppressed this side reaction, allowing for selective diester crosslinks.[29-31] It naturally followed that application of these amine catalysts to mixtures of epoxides and anhydrides should generate linear polyesters.[31] In reactions between terminal epoxides and PA it was found that 99% selectivity for polyester linkages was obtained. However, for internal epoxides (including cyclohexene oxide (CHO)) with PA, the reaction was less selective, yielding around 75% polyester linkages, with the remaining linkages being polyether.

From these initial findings, further investigations saw application of a range compounds as catalysts for this reaction, including metal salts, organometallic compounds and main group Lewis acids.[32-36] In general, however, polymerisations were slow, the polyester molar masses obtained were low, and there remained a lack of clarity about the catalytic structure and mechanism, making further catalyst design challenging.

1.4.3 Improved Homogenous Catalysts

In 1985, a ground-breaking report by Inoue and coworkers, which marked the first application of a well-defined metal complex to the ROCOP of epoxides and anhydrides, described the polymerisation of propylene oxide (PO) with PA utilising a bicomponent catalyst system consisting of an aluminium porphyrin catalyst (**1.1**) and a quaternary ammonium salt cocatalyst (Scheme 1.5).[37]



Scheme 1.5. ROCOP of PO and PA using a **1.1**/Et_4NX (X = Cl, Br, AcO) bicomponent catalysts system. Adapted from reference 37.

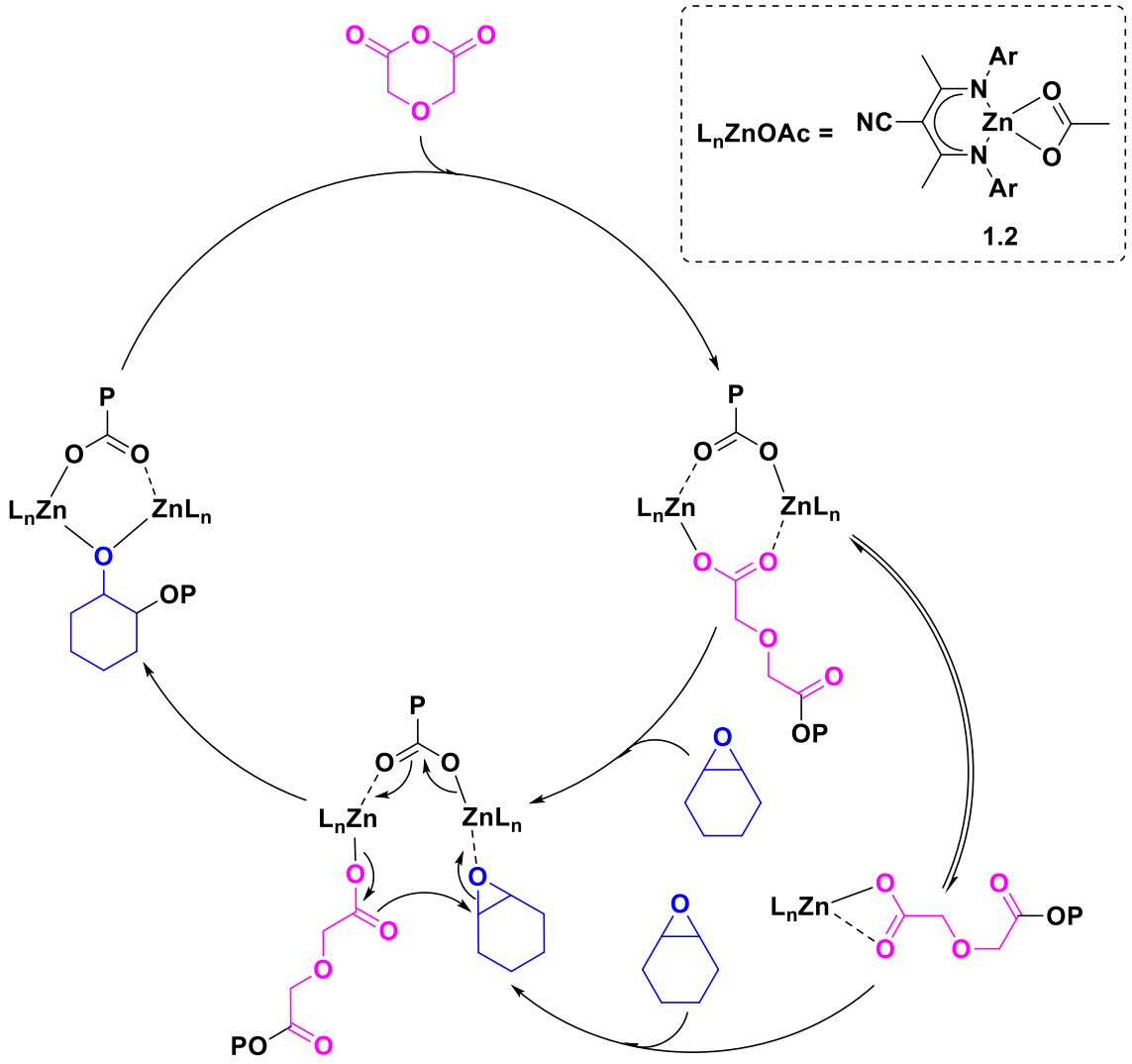
Although the activities were low (Turnover Frequency (TOF) = 4-6 day^{-1}, 4% *vs*. anhydride, T = 25 °C), the polymerisations produced no polyether, and exhibited good control of polymer dispersity (Đ = 1.1). The polymers obtained had low molar masses (up to 3.0 kg mol^{-1}), however.

Several important mechanistic insights, pertinent to much subsequent catalyst development, were revealed as part of this work. Through comparison of ^{13}C NMR spectra of poly(propylene oxide-*alt*-phthalate) with small molecule references, it was demonstrated that both the coligand of **1.1** and the anion of the quaternary salt functioned as initiators. Further, owing to the lack of signals attributable to an aluminium-alkoxide bound species, it was proposed that the aluminium-carboxylate species was the resting state and hence that epoxide insertion was the rate determining step. By using ^{1}H NMR spectroscopy it was also determined that a bis(carboxylate) aluminium species was present, *i.e.*, the resting state was an aluminate, with the quaternary salt cation remaining close as an bound ion (see RHS of catalytic cycle, Scheme 1.5).

Subsequent catalyst development improved the performance of monometallic porphyrin catalyst systems, with alterations to the ligand backbone, metal and cocatalyst all reported.[13, 17] Using a Cr(III) analogue of **1.1**, in conjunction with a bis(triphenylphosphine)iminium chloride (PPNCl) cocatalyst, TOFs of up to 52 h^{-1} (0.5% *vs.* anhydride, T = 30 °C) for the ROCOP of PO and methyl succinic anhydride were achieved.[38]

A further significant breakthrough came in 2007, when Coates and co-workers reported the use of a zinc β-diketiminate (BDI) (**1.2**) complex for the ROCOP of epoxides and anhydrides.[39] This catalyst displayed high activity for the ROCOP of CHO and diglycolic anhydride (DGA) (TOF = 79 h^{-1}, 0.5% *vs.* anhydride, T = 50 °C), displayed perfect selectivity for polyester over polyether, and demonstrated good substrate scope. Zinc BDI

complexes had previously been reported for the related ROCOP of epoxides and CO_2, and so much of the relevant mechanistic study was carried out for this closely related polymerisation.[40] The findings are discussed here as the overall catalytic mechanism could be expected to be similar for the two copolymerisations (Scheme 1.6).



Scheme 1.6. A plausible catalytic mechanism for the ROCOP of CHO and DGA utilising **1.2**, based on the findings of application of [(BDI)ZnOAc] complexes to the ROCOP of epoxides and CO_2. Adapted from reference 40.

It was demonstrated that the complex functions principally through a bimetallic mechanism, requiring the dimerisation of two molecules of **1.2** in order to yield an active species. The resting state of the catalyst was determined to be dependent on the steric bulk of the aryl groups of the ancillary ligand – those with significant steric bulk exist in equilibrium

between a monomeric and dimeric species whilst those with less exist exclusively as dimers. As a result, the rate law showed a non-linear dependence on the [**1.2**], which increased towards 2nd order at higher temperatures (as this favoured a monomeric resting state). A downside of these findings is that the catalyst would be expected to perform poorly at lower catalyst loadings and higher temperatures, both of which would inhibit formation of the catalytically active dimer.

1.4.4 Salen Metal(III) Catalysts

Another important class of catalysts for the ROCOP of epoxides and anhydrides are monometallic salen catalyst systems . In the mid-2000s, chromium(III) and cobalt(III) salen complexes, in combination with nucleophilic cocatalysts (*e.g.* DMAP or bis(triphenylphosphine)iminium chloride (PPNCl)) were reported for the ROCOP of epoxides and CO_2.[41] Application of such systems to the ROCOP of epoxides and anhydrides followed thereafter (Figure 1.2).

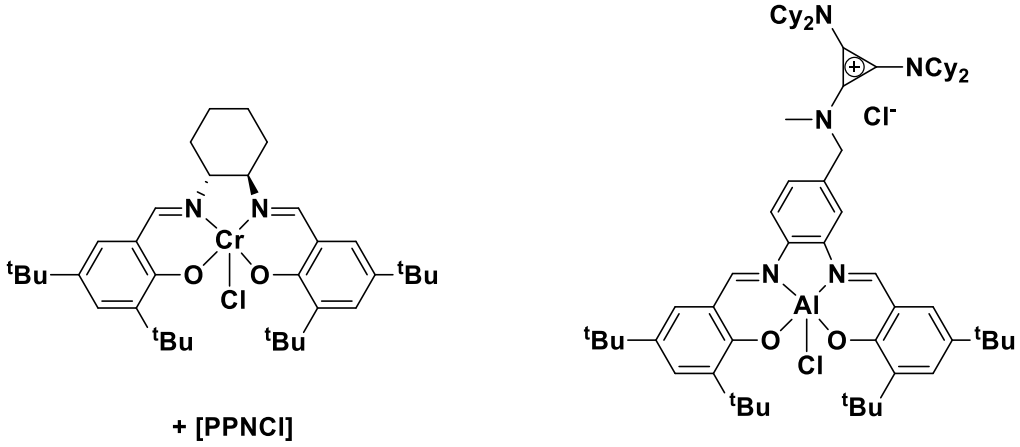
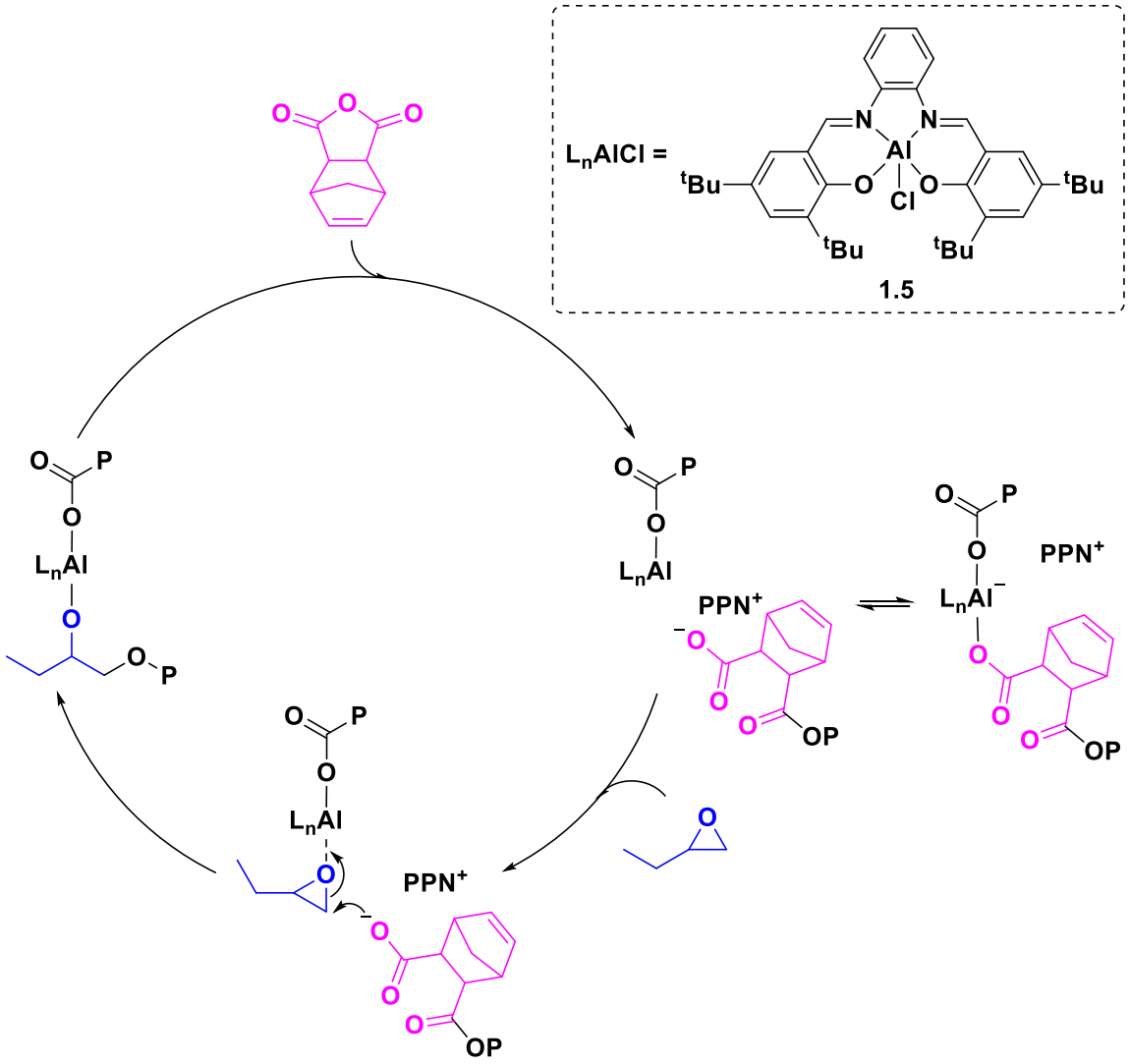


Figure 1.2. Selected metal salen catalyst systems reported for the ROCOP of epoxides and anhydrides. Bicomponent catalyst systems often use a cocatalyst of PPNCl.

Individual reports from the groups of Coates, Duchateau, and Darensbourg described the application of these catalyst systems in the early 2010s.[42-45] In a comprehensive study, Duchateau and co-workers investigated the role of metal, ligand backbone, and cocatalyst

selection in the activities of salen-type complexes.[44] From this it was established that, for a given salen-type ancillary ligand, the typical order of metal reactivity followed Cr(III) > Co(III) > Al(III). It also established the use of PPNCl as the most effective cocatalyst. A TOF of up to 245 h^{-1} (0.4% *vs*. anhydride, T = 110 °C) for the ROCOP of PA and CHO was obtained using this optimised catalyst system (**1.3**, Figure 1.2).

Although the general mechanism for epoxide/anhydride ROCOP was broadly understood (*vide supra*), key details including the specific role of the cocatalyst, remained ambiguous. In 2017, seminal work by Coates and Tolman aided in the elucidation of several key mechanistic details for metal salen catalyst systems (Scheme 1.7).[46]



Scheme 1.7. Mechanism proposed by Coates and Tolman for the ROCOP of butylene oxide (BO) and norbornene anhydride (NBA) using **1.5**/PPNCl. Adapted from reference 46.

Utilising an aluminium salen complex (**1.5**) in conjunction with PPNCl, it was established that, under the conditions investigated, the collective order of catalyst and PPNCl was 1, suggesting formation of an ion pair. Although these findings seem straightforward, many researchers had conflated the reactivity issues of these systems and there was much confusion on the role and rate influences of both different types of and different quantities of co-catalyst. According to the Coates and Tolman work, the overall rate law was finally rationalised as:

$$\nu = k[\mathbf{1.5}{+}\mathrm{PPNCl}]^{1}[\mathrm{Epoxide}]^{1}[\mathrm{Anhydride}]^{0}$$

The initiation of the reaction was also investigated and it was demonstrated that both the coligand of the metal complex and the chloride anion of the cocatalyst were capable of initiation, consistent with previous findings by Inoue and co-workers with bicomponent porphyrin catalyst systems.

Much of the work in these initial kinetic investigations were performed at relatively high catalyst loadings (~1-2% *vs*. anhydride). In subsequent work, Coates and co-workers demonstrated that at lower catalyst loadings (<0.25% *vs*. anhydride), bicomponent systems such as **1.5**/PPNCl showed significant decreases in activity (*i.e.* no longer operating under first order conditions).[47] This was attributed to the dissolution of the ion pair which is formed at high catalyst concentrations. These findings led to the development of highly effective catalysts featuring the cocatalytic moiety tethered to the ligand backbone (Figure 1.2, **1.4**).[47, 48] Complex **1.4** showed exceptional activities for the ROCOP of PO and NBA (TOF = 93 h^{-1}, 0.025% *vs*. anhydride, T = 60 °C). Further, as the cocatalytic moiety was covalently tethered to the ligand backbone, no decrease in reactivity at low catalyst loadings (up to 0.025% *vs.* anhydride) was observed as the catalytically active ion pair was not disrupted.

1.4.5 Tethered Multi-metallic Salen Catalysts

Alongside the development of catalysts featuring tethered cocatalytic moieties, an alternative approach to generating active catalysts epoxide/anhydride ROCOP with salen-type ancillary ligands has been to tether multiple such ligands together, thus creating multi-metallic catalysts (Figure 1.3). These catalysts almost all still require cocatalytic PPNCl, but often display hints of intermetallic synergy that provides enhanced rates over traditional metal salen catalyst systems. Without any co-catalyst the production of polyether is typically observed.

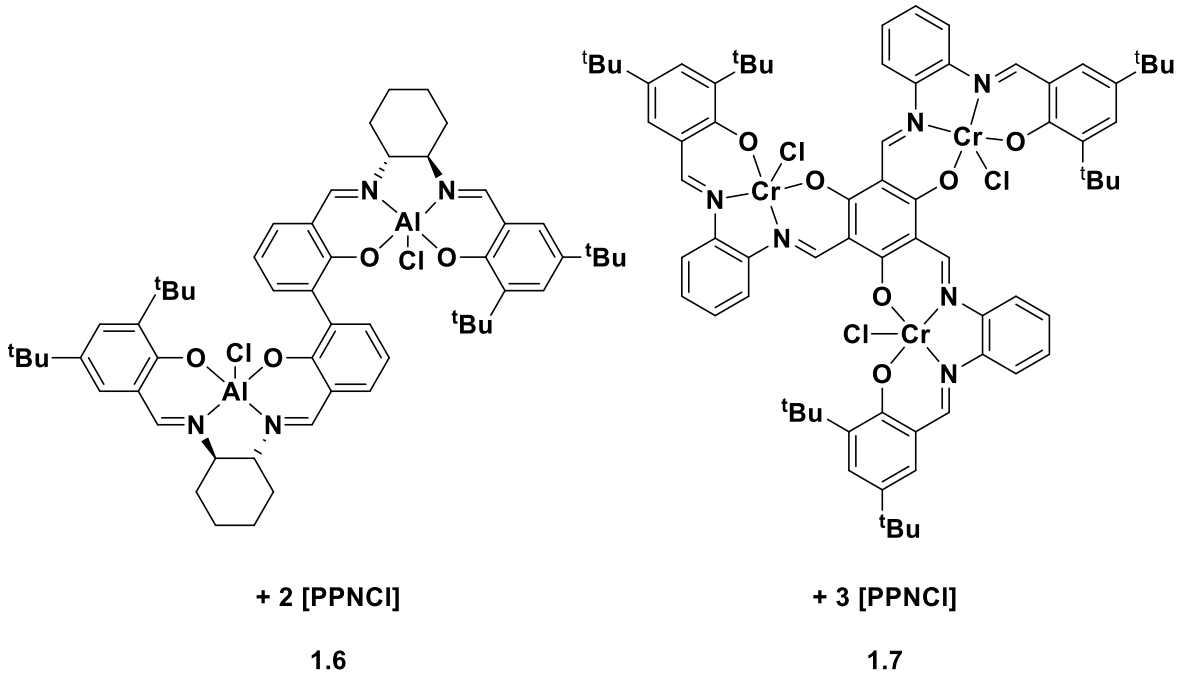


Figure 1.3. Tethered multi-metallic salen catalyst systems reported for the ROCOP of CHO and PA.

In 2016, Lu and co-workers reported a bimetallic aluminium complex (**1.6**) that displays very high activities (TOF = 750 h^{-1}, 0.4% *vs*. anhydride, T = 50 °C) for the ROCOP of CHO and PA.[49] Very recently, a tri-chromium salen catalyst system (**1.7**) was reported that displays an exceptionally high activity (TOF = 10,620 h^{-1}, 0.017% *vs.* anhydride, T = 100 °C) for the same polymerisation.[50] In such cases, comparison of activities to monometallic analogues allows for some quantification of the degree of intermetallic synergy: complex **1.7** provides a 50-fold increase in activity compared to its monometallic analogue, at equivalent [Cr].

It is likely that mechanistic similarities exist with the monometallic salen complexes, although no complete mechanistic picture has yet been developed which explains the significant enhancements in rate that are obtained through use of multi-metallic systems. Recently, Coates and co-workers reported a mechanistic study on a related bimetallic chromium salen, which was applied to the controlled ROP of PO.[51, 52] In this work it is

proposed that the two metal centres work in concert with PPNCl to generate a catalytically active site (Figure 1.4).

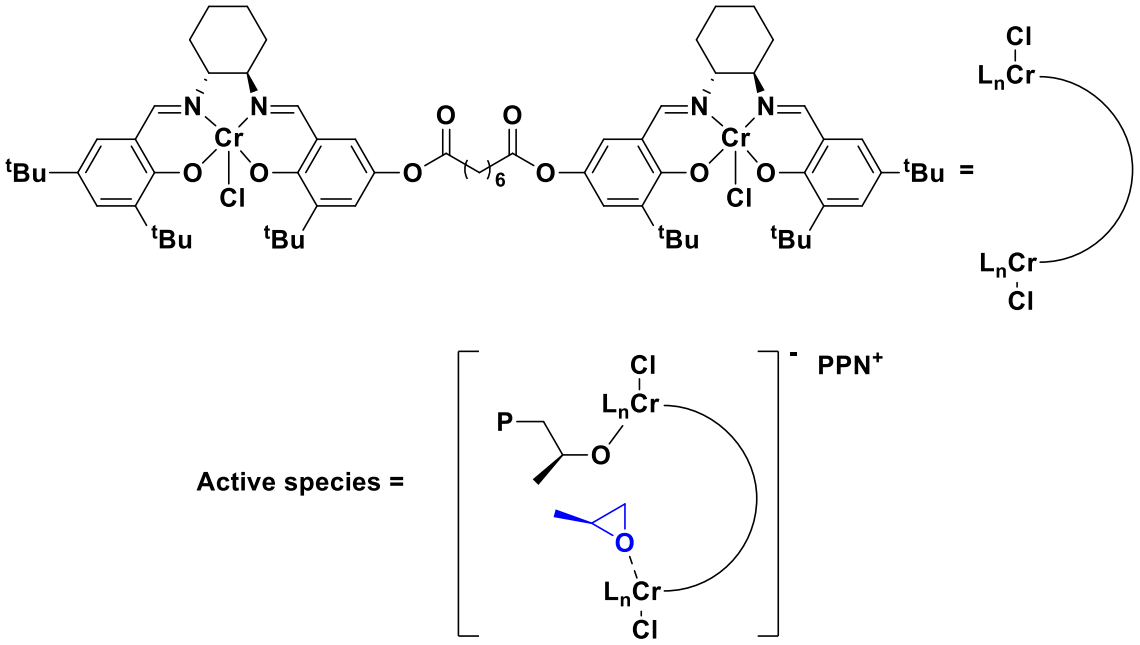
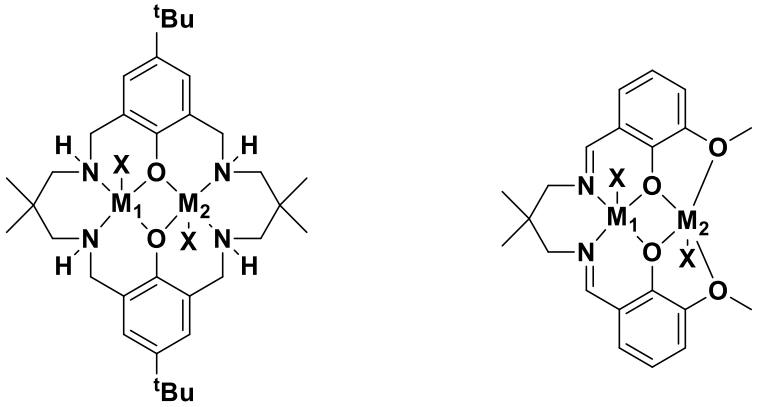


Figure 1.4. A tethered bimetallic salen catalyst system reported for the ROP of PO.

For this catalyst however, the linking backbone is a long aliphatic chain, which provides flexibility allowing for close approach of the metals (a separation of ~6 Å is considered optimal). Evidently, in complex **1.7** there is significantly less flexibility in the aromatic backbone, meaning the close approach of the metals is relatively prohibited. Computational calculations on complex **1.7** revealed a metallic separation of ~7.5 Å despite this lack of flexibility, which the authors hypothesised was enabling the high rates observed.

1.4.6 Dinuclear Catalysts

A further principle of catalyst design that has emerged recently is the application of dinuclear catalysis to the ROCOP of epoxides with both anhydrides and CO_2 (Figure 1.5).



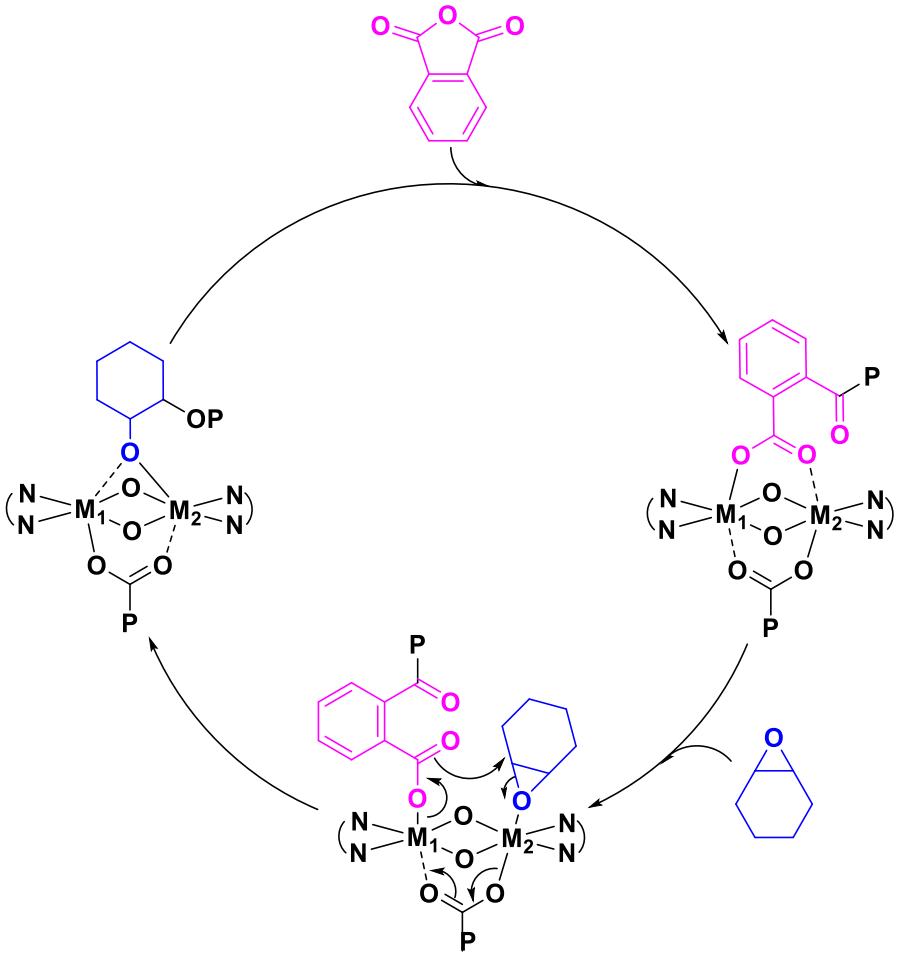
$M_1 = M_2 = Mg$, X = OAc (1.8)
$M_1 = M_2 = Zn$, X = OAc (1.9)
$M_1 = Mg$, $M_2 = Zn$, X = Br (1.10)

$M_1 = M_2 = Zn$, X = OAc (1.11)
$M_1 = Zn$, $M_2 = Cd$, X= I (1.12)

Figure 1.5. Dinuclear complexes applied to the ROCOP of epoxides and anhydrides.

In 2014, Williams and co-workers reported the application of homodinuclear magnesium (**1.8**) and zinc (**1.9**) complexes with a macrocyclic ancillary ligand to the ROCOP of CHO and PA.[53] Both complexes were fully selective for polyester formation, and gave moderate TOFs of 97 h^{-1} (**1.8**, 1% *vs.* anhydride, T = 100 °C) and 24 h^{-1} (**1.9**, 1% *vs.* anhydride, T = 100 °C). Subsequently, a heterodinuclear magnesium-zinc complex supported by the same ancillary ligand (**1.10**) was reported.[54] It displayed elevated activities (TOF = 188 h^{-1}, 1% *vs.* anhydride, T = 100 °C) compared to the homodinuclear analogues, demonstrating an important principle: the two metals within the framework perform different roles within the catalysis, with one likely binding and activating the epoxide, and the second binding the propagating polymeric chain.

This idea was subsequently expanded on with the development of a heterodinuclear magnesium-cobalt complex, which displayed exceptional activities for the ROCOP of epoxides and CO_2.[55] Detailed kinetic studies on dinuclear complexes resulted in the mechanistic proposal of a 'chain-shuttling' mechanism, which functions for both epoxide/anhydride and epoxide/CO_2 ROCOP (Scheme 1.8).[54-56]



Scheme 1.8. Chain-shuttling mechanism exhibited by dinuclear catalysts such as **1.10** for the ROCOP of PA and CHO. Adapted from references 54 and 55.

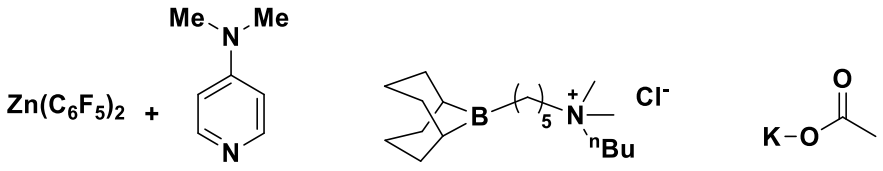
In common with previous catalyst systems, the rate determining step was found to be epoxide binding and insertion. However, in contrast with the mechanism proposed for previous monometallic catalysts, which require the dissociation of a polymer chain to yield a vacant metal coordination site, in the dinuclear complexes the polymer remains bound to M_1, whilst M_2 binds and activates an epoxide molecule. Insertion of the epoxide subsequently occurs, with the polymer chain 'shuttling' to M_2. Since the two metals play distinct roles within the catalysis, optimisation of each towards their respective roles results in improved activities.[54]

An advantage of dinuclear catalysis is that it obviates the need for cocatalysts. In turn, a first order dependence on catalyst concentration is observed, meaning the catalysts show exceptional performance at much lower catalyst loadings than typical bicomponent systems.

Heterodinuclear catalysts do not always outperform homodinuclear analogues, however, meaning that appropriate metal selection is essential.[56-59] A homodinuclear zinc complex with an *ortho*-vanillin derived ancillary ligand, [$L_{van}Zn_2(OAc)_2$] (**1.11**), displays the current highest reported activities for dinuclear complexes in epoxide/anhydride ROCOP (TOF = 198 h^{-1}, 1% *vs.* anhydride, T = 100 °C).[59] An investigation of different heterodinuclear combination focusing on [$L_{van}ZnM(I)_2$] (M = M^{I}, M^{II}) complexes found that all complexes investigated were outperformed by the homodinuclear **1.11**.[56] The best performing heterodinuclear complex was [$L_{van}ZnCd(I)_2$] (**1.12**), with a TOF of 67 h^{-1} (1% *vs*. anhydride, T = 100 °C).

1.4.7 Organo- and Metal Salt Catalysts

There have also been several reports of organocatalyst systems applied to the ROCOP of epoxides and anhydrides (Figure 1.6). In general, these complexes display lower activities than the best single site metal catalysts systems, but their appeal can be in terms of cost and commercial availability.[60-66]



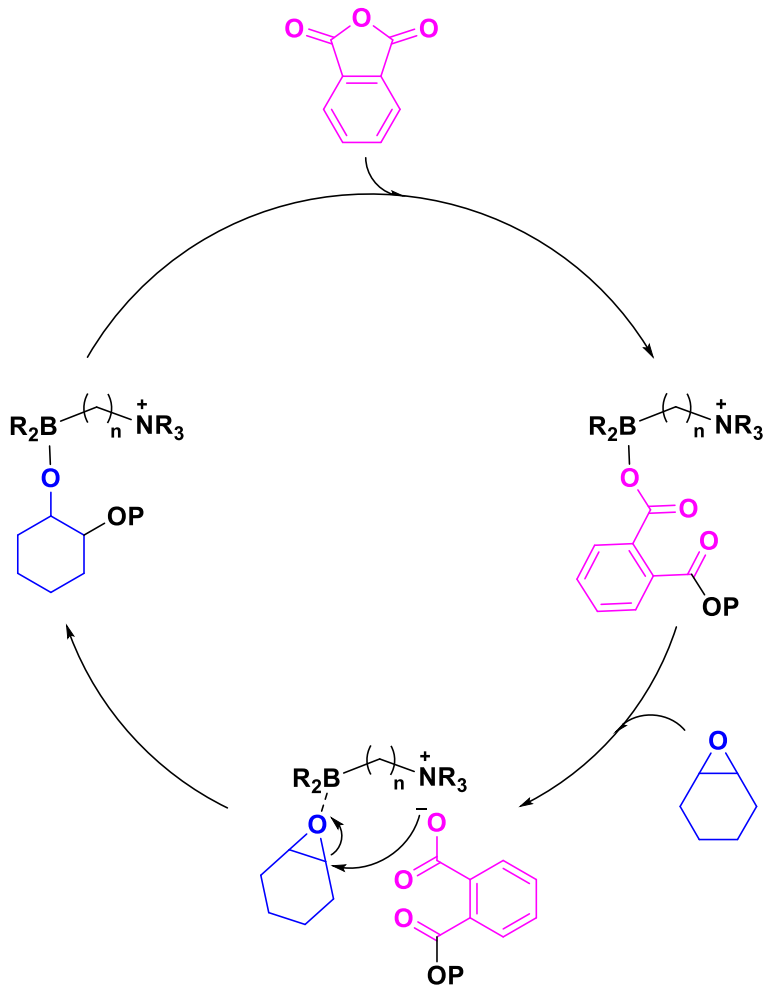
1.13 **1.14** **1.15**

Figure 1.6. Organo- and metal salt catalysts reported for the ROCOP of epoxides and anhydrides.

The most active of these are bicomponent metal/amine systems such as $Zn(C_6F_5)_2$/ 2 equiv. DMAP (**1.13**) which display moderate activities (TOF = 116 h^{-1}, 1% *vs.* anhydride, T = 110

°C) for the ROCOP of CHO and PA.[61] Simple metal acetate salts, such as KOAc (**1.15**) have also been applied to the same reaction, although activities are low (TOF = 22 h^{-1}, 1% *vs.* anhydride, T = 110 °C).[60]

Applying the same principle of catalytic design employed by Coates and co-workers in the development of **1.4**, a recently reported tethered organoboron/quaternary amine salt catalyst (**1.14**) displayed enhanced rates over many previous bicomponent organocatalyst systems (TOF = 258 h^{-1}, 0.5% *vs.* anhydride, T = 120 °C) for the ROCOP of CHO and PA.[65] A mechanistic study was carried out to determine the role of the two functional groups within the catalyst (Scheme 1.9).



Scheme 1.9. Mechanism proposed for the ROCOP of CHO and PA with complex **1.14**. Adapted from reference 65.

It was proposed that the boron Lewis acid binds and activates the epoxide, whilst the quaternary ammonium salt keeps the reactive carboxylate chain end bound in close proximity, in a manner similar to the mechanism proposed for **1.4**. A range of analogous organocatalysts with linking alkyl chain lengths between $n = 3 – 6$ were all reported, with complexes where $n = 5$ proving the most active, suggesting a compromise between the separation of the active sites of the catalyst and degrees of conformational freedom within the alkyl chain were important in delivering high activities.

1.5 Switchable Catalysis

An important class of polymeric materials is block copolymers: molecules where chemically distinct polymer segments are covalently linked together in sequence. The chemical tethering of distinct polymeric blocks, which would otherwise macro-separate, results in microphase separation of the constituent units into highly reproducible and predictable nanostructures. In turn this leads to novel materials properties distinctive to those of the constituent homopolymers.[67]

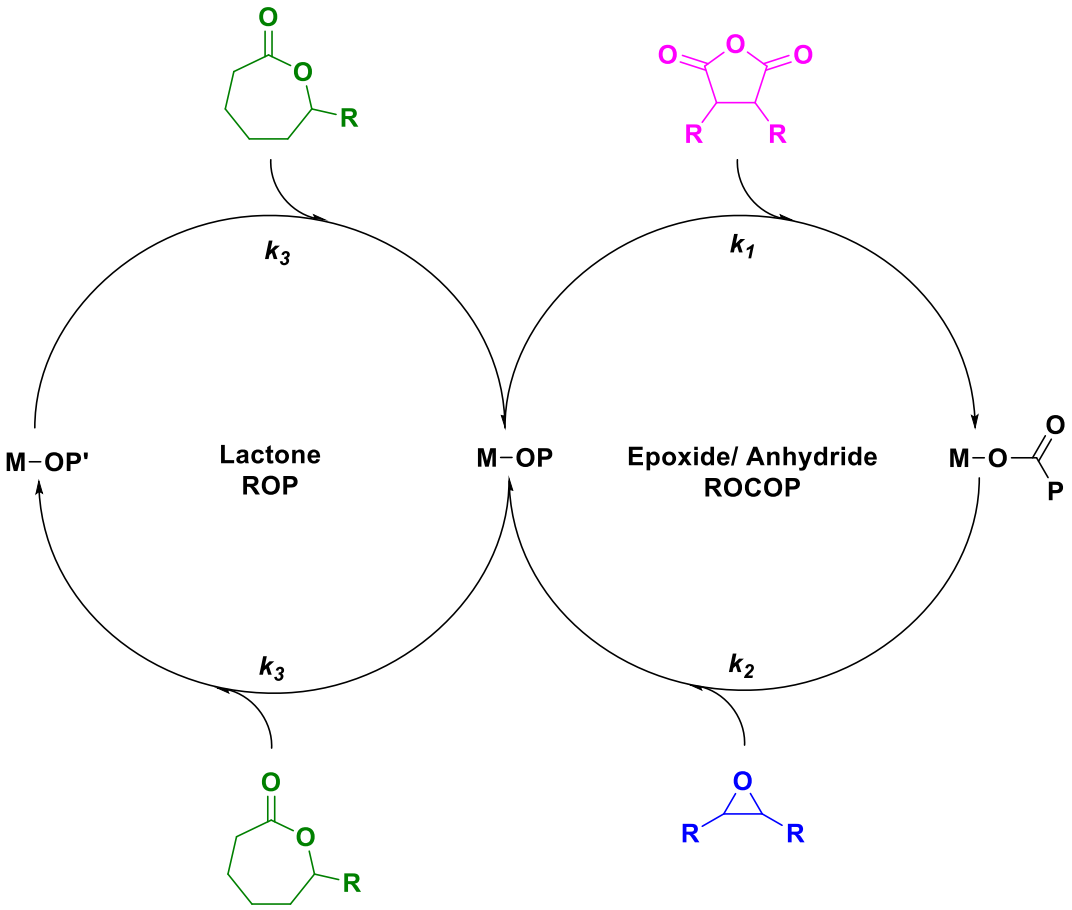
In general, block copolymers are typically prepared *via* sequential monomer addition to living polymerisations or coupling of homopolymers through reactive chain ends.[68] Block copolyesters where both blocks are derived from cyclic ester ROP have been prepared through sequential addition of monomers or *via* use of (ROP-derived) polyester macroinitiators.[67, 69, 70] There are, however, very few reports of processes that combine cyclic ester ROP and epoxide/heteroallene or epoxide/anhydride ROCOP to yield block copolymers. In 2012, Darensbourg and co-workers reported the synthesis poly(styrene carbonate) (PSC)-*b*-poly(lactide) (PLA) in one pot, using two separate catalysts. The reaction was triggered to switch catalyst *in situ* through the addition of water, yielding PSC-

b-PLA.[71] In the same year, Williams and co-workers reported the use of poly(cyclohexene carbonate) (PCHC) as a macroinitiator for lactide ROP, yielding diblock PCHC-*b*-PLA.[72]

In 2014, Williams and co-workers reported a novel route to the synthesis of block poly(carbonate-*b*-ester). Utilising one catalyst (**1.9**), it was demonstrated that from a 'one-pot' mixture of ε-caprolactone (ε-CL), CHO and CO_2, block copolymers could be synthesised.[73] Complex **1.9** was able to chemoselectively propagate CHO/CO_2 ROCOP to generate poly(cyclohexene carbonate) (PCHC), even in the presence of the lactone monomer. Once CO_2 was removed from the atmosphere, the catalyst began the ROP of ε-CL, using the PCHC as a macroinitiator. This novel methodology was subsequently termed 'switchable catalysis'.[74]

Reactivity of this type had been previously reported by Inoue and co-workers in 1985, but further work was not carried out and the significance of the mechanistic switch was not emphasised.[75] In this work, a bicomponent **1.1**/ quaternary phosphonium salt catalyst system was shown to sequentially polymerise the ROCOP of PO and PA and the ROP of β-butyrolactone (β-BL), leading to the formation of poly((PO-*alt*-PA)-*b*-PBL). The reaction was not performed in 'one-pot', however. Instead, β-BL was added to the reaction after the ROCOP of PO and PA had completed, with initiation of the lactone ROP occurring from the polyester chain-end – *i.e.* a macro-initiator concept rather than a mechanistic switch.

Following from the discovery of switchable carbon dioxide/epoxide/lactone block polymer formation, in 2015 Williams and co-workers reported switchable catalysis using the ROCOP of epoxides and anhydrides and lactone ROP, allowing for the synthesis of block polyesters.[76] As part of a detailed kinetic/DFT investigation, it was demonstrated that the selectivity arose from pre-rate determining selectivity dependent upon both the transition state barrier and the linkage stability (Scheme 1.10).[76, 77]



Scheme 1.10. Switchable catalysis between the ROCOP of epoxides and anhydrides and ROP of lactones.

Despite the catalysts utilised having higher activities for the ROP of lactones (either ε-decalactone (ε-DL) or ε-CL) over the ROCOP of epoxides with anhydrides or CO_2, it was found that the latter proceeded first. For the ROCOP of epoxides with anhydrides or CO_2, the rate determining step is usually the ring opening of the epoxide from a metal-bound carboxylate (k_2). The insertion of anhydride into a metal-bound alkoxide is significantly faster (k_1), yet it is from this latter metal-alkoxide species that lactone ROP also propagates. Provided that k_1 is significantly faster that k_3, the ROCOP process occurs before the ROP process, leading to selective formation of block polymers.

These findings were initially established with the homodinuclear zinc macrocyclic complexes **1.9**, **1.15** and **1.16** (Figure 1.7).[73, 76, 78] Since the initial report of this phenomenon in 2014, many catalysts and other monomer combinations have been shown to operate

successfully through the switch mechanism, including organocatalysts (**1.19**), metal acetate salts (**1.20**), and monometallic β-diketiminate- (BDI) and salen catalyst systems (**1.3** and **1.18**).[79-84] For a comprehensive overview of complexes reported for switchable catalysis the reader is directed to recent review by Williams and co-workers.[67]

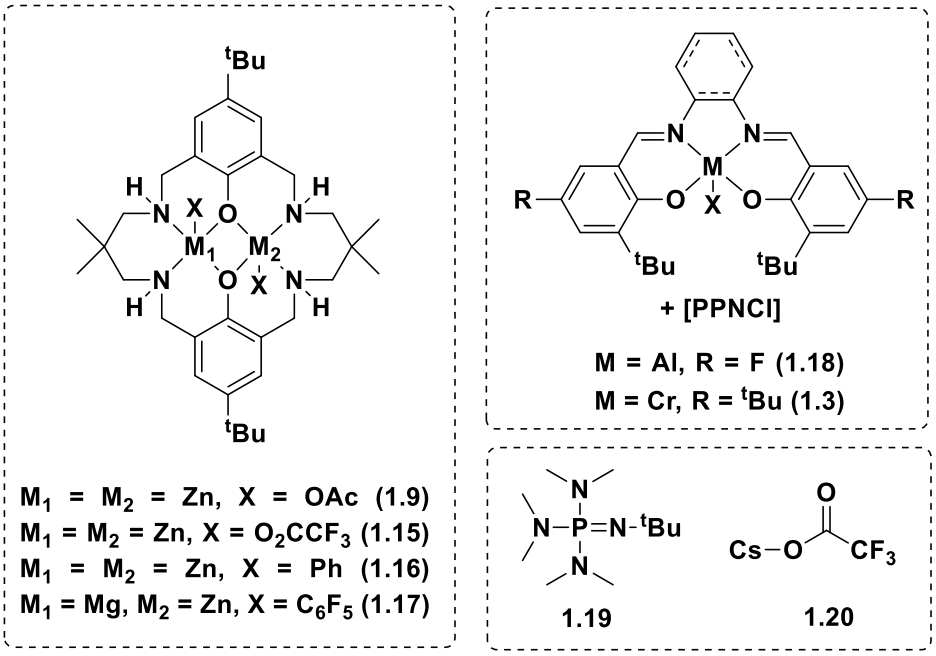


Figure 1.7. Selection of catalysts reported for switchable catalysis.

Subsequent work has demonstrated that a range of block copolymers accessed through switchable catalysis have applications as pressure sensitive adhesives, toughened plastics and thermoplastic elastomers.[19, 85-87] Notably, the catalysts used in this work (**1.16** and **1.17**) feature non-initiating organometallic coligands, which were used in conjunction with bifunctional protic CTAs to deliver, exclusively, triblock copolymers. Good end group control was required to deliver high weight polyesters, which were required to yield phase separated materials that delivered the desired material properties.

1.6 Aims and Objectives

This thesis will focus on the development of homogenous catalysts for polymerisations of oxygenated monomers, with a particular focus on the ROCOP of epoxides and anhydrides. Despite recent strides in catalyst development, there are still several broad issues within the field:

1. Overall catalyst performance. The rates displayed by the best-in-class catalysts are still low when compared to other classes of polymerisation, such as lactide ROP, where TOFs of up to ~800,000 h^{-1} have been obtained.[88] Further, many of the most active epoxide/anhydride ROCOP catalysts display disadvantages to their use, including intolerance to low loadings, use of toxic, expensive and highly coloured metals (such as chromium and cobalt), or require cocatalysts. The use of cocatalysts is undesirable as these compounds are often expensive, may be toxic and corrosive to steel and, further, lead to poor end group control (see point 2).

   The development of catalysts that can utilise cheap, earth abundant and non-toxic metals and function without cocatalyst is hence highly desirable. It is essential to properly understand and study the polymerisation mechanism so as to rationally design for more active, controlled, and selective catalysts in future.
2. End-group control. The vast majority of catalysts reported for the ROCOP of epoxides and anhydrides utilise monofunctional initiators (such as chloride or acetate), present from either coligands or cocatalysts. The presence of adventitious water, or diol impurities present in epoxides, which can act as chain transfer agents (CTAs) lead to bifunctional initiating species. Together, these initiating species result in bimodal polymer molar mass distributions, as the bifunctional chains grow at twice the rate of the monofunctional chains (see Section 1.3.1).

In order to study material properties of polyesters in a controlled fashion, or to achieve selective formation of, for example, triblock over diblock copolymers, catalysts that are able to function without monofunctional cocatalysts or coligands are required.

3. Application of polyesters. Although much research has gone in to catalyst development for polyester ROCOP, there has been much less focus on developing applications for the materials that can be accessed through this methodology. Recent developments in switchable catalysis have shown that block copolymers featuring polyesters can be applied to a range of applications.[67] Further work developing and expanding this range of materials and applications is warranted.

Chapters 2 and 3 will focus on addressing the first challenge, particularly in the context of switchable catalysis. Whilst a range of catalysts have been reported for switchable catalysis, most show low activities for one or both of the two classes of polymerisations (ROCOP and ROP), meaning that overall reaction rates are low. This will be addressed by targeting monometallic M(III) Schiff-base supported catalyst systems, which could be expected to be active for both classes of polymerisation. These complexes will be characterised through NMR spectroscopy, IR spectrometry, SQUID magnetometry, X-ray crystallography and elemental analysis. The activity of these complexes for the ROCOP of PA and CHO, and ROP of ε-DL will be established. Following this, the most effective catalysts will be applied to the one-pot reaction of CHO, PA and ε-DL reaction to target the synthesis of triblock polyesters through switchable catalysis.

Chapter 4 will focus on challenges 1 and 2 through the development of heterodinuclear complexes for the ROCOP of epoxides and anhydrides. Whilst heterodinuclear complexes have previously delivered field-leading rates for epoxide/CO_2 ROCOP, without the use of

cocatalysts, there is no such equivalent catalyst for epoxide/anhydride ROCOP.[55, 89] To this end, combinations of Al(III) with Group 1 metals will be tested. These complexes will be characterised through NMR spectroscopy, X-ray crystallography and elemental analysis. Following this, the activity of the complexes will be established for the ROCOP of PA and CHO. The catalytic mechanism will be investigated through a combined kinetic and computational study.

Chapter 5 will focus on addressing challenges 2 and 3. The heterodinuclear complexes developed in chapter 4 function without a cocatalyst, but feature initiating coligands. By replacing these coligands with non-initiating organometallic groups, good end group control may be achieved through addition of protic CTAs (which act as the sole initiating species by generating alkoxides *in situ*). The novel organometallic catalyst will be characterised using NMR and IR spectroscopy and elemental analysis. Using this catalyst, the synthesis of monodisperse polyesters with high molar masses will be targeted. The thermal and material properties of these polyesters will be measured through DSC, TGA and DMTA.

1.7 References for Chapter 1

1. PlasticsEurope, 2021, https://plasticseurope.org/knowledge-hub/.
2. N. Simon, K. Raubenheimer, N. Urho, S. Unger, D. Azoulay, T. Farrelly, J. Sousa, H. van Asselt, G. Carlini, C. Sekomo, M. L. Schulte, P.-O. Busch, N. Wienrich and L. Weiand, *Science*, 2021, **43**, 43-47.
3. F. Welle, *Resour. Conserv. Recycl.*, 2011, **55**, 865-875.
4. S. Kakadellis and G. Rosetto, *Science*, 2021, **373**, 49-50.
5. G. W. Coates and Y. D. Y. L. Getzler, *Nat. Rev. Mater.*, 2020, **5**, 501-516.
6. I. Vollmer, M. J. F. Jenks, M. C. P. Roelands, R. J. White, T. van Harmelen, P. de Wild, G. P. van der Laan, F. Meirer, J. T. F. Keurentjes and B. M. Weckhuysen, *Angew. Chem. Int. Ed.*, 2020, **59**, 15402-15423.
7. M. Haussler, M. Eck, D. Rothauer and S. Mecking, *Nature*, 2021, **590**, 423-427.
8. E. Barnard, J. J. R. Arias and W. Thielemans, *Green Chem.*, 2021, **23**, 3765-3789.
9. B. A. Abel, R. L. Snyder and G. W. Coates, *Science*, 2021, **373**, 783-789.
10. Y. Q. Zhu, C. Romain and C. K. Williams, *Nature*, 2016, **540**, 354-362.
11. M. Volanti, D. Cespi, F. Passarini, E. Neri, F. Cavani, P. Mizsey and D. Fozer, *Green Chem.*, 2019, **21**, 885-896.
12. G. Odian, *Principles of Polymerization, 4th Ed.*, 2004.
13. S. Paul, Y. Q. Zhu, C. Romain, R. Brooks, P. K. Saini and C. K. Williams, *Chem. Comm.*, 2015, **51**, 6459-6479.
14. P. Olsen, K. Odelius and A. C. Albertsson, *Biomacromolecules*, 2016, **17**, 699-709.
15. M. Vert, 2005, **6**, 538-546.
16. S. Farah, D. G. Anderson and R. Langer, *Adv. Drug Deliv. Rev.*, 2016, **107**, 367-392.
17. J. M. Longo, M. J. Sanford and G. W. Coates, *Chem. Rev.*, 2016, **116**, 15167-15197.
18. C. Romain, J. A. Garden, G. Trott, A. Buchard, A. J. P. White and C. K. Williams, *Chem. Eur. J.*, 2017, **23**, 7367-7376.
19. G. S. Sulley, G. L. Gregory, T. T. D. Chen, L. P. Carrodeguas, G. Trott, A. Santmarti, K. Y. Lee, N. J. Terrill and C. K. Williams, *J. Am. Chem. Soc.*, 2020, **142**, 4367-4378.
20. H. Du, X. Pang, H. Yu, X. Zhuang, X. Chen, D. Cui, X. Wang and X. Jing, *Macromolecules*, 2007, **40**, 1904-1913.
21. W. Gruszka and J. A. Garden, *Nat. Commun.*, 2021, **12**, 3252.
22. A. Nakayama, N. Kawasaki, K. Hayashi, S. Aiba, N. Yamamoto and Y. Maeda, *Polymer*, 1997, **38**, 4718-4725.

23. A. Takasu, T. Bando, Y. Morimoto, Y. Shibata and T. Hirabayashi, *Biomacromolecules*, 2005, **6**, 1707-1712.

24. P. F. Song, M. Xiao, F. G. Du, S. J. Wang, L. Q. Gan, G. Q. Liu and Y. Z. Meng, *J. Appl. Polym. Sci.*, 2008, **109**, 4121-4129.

25. X. Sun, X. Zhang, S. Chen, B. Du, Q. Wang, Z. Fan and G. Qi, *Polymer*, 2010, **51**, 5719-5725.

26. Y. L. Liu, M. Xiao, S. J. Wang, L. Xia, D. M. Hang, G. F. Cui and Y. Z. Meng, *RSC Adv.*, 2014, **4**, 9503-9508.

27. W. Fisch and W. Hofmann, *J. Polym. Sci.*, 1954, **7**, 497-502.

28. W. Fisch, W. Hofmann and J. Koskikallio, *J. App. Chem.*, 1956, **6**, 429-441.

29. E. C. Dearborn, R. M. Fuoss and A. F. White, *J. Polym. Sci.*, 1955, **16**, 201-208.

30. H. K. Weiss, *Ind. Eng. Chem.*, 1957, **49**, 1089-1090.

31. R. F. Fischer, *J. Polym. Sci.*, 1960, **44**, 155-172.

32. V. A. Hilt, K. H. Reichert and H. K., *Macromol. Chem. Phys*, 1967, **101**, 246-270.

33. V. E. Schwenk, K. Gulbins, M. Roth, G. Benzing, R. Maysenhölder and K. Hamann, *Macromol. Chem. Phys*, 1962, **51**, 53-69.

34. T. Tsuruta, K. Kitamura and S. Inoue, *Macromol. Chem. Phys.*, 1969, **126**, 250-265.

35. T. Tsuruta, K. Matsuura and S. Inoue, *Macromol. Chem. Phys.*, 1964, **75**, 211-214.

36. R. J. Kern and J. Schaefer, *J. Am. Chem. Soc*, 1967, **89**, 6-14.

37. T. Aida and S. Inoue, *J. Am. Chem. Soc*, 1985, **107**, 1358-1364.

38. A. Bernard, C. Chatterjee and M. H. Chisholm, *Polymer*, 2013, **54**, 2639-2646.

39. R. C. Jeske, A. M. DiCiccio and G. W. Coates, *J. Am. Chem. Soc.*, 2007, **129**, 11330-11331.

40. D. R. Moore, M. Cheng, E. B. Lobkovsky and G. W. Coates, *J. Am. Chem. Soc*, 2003, **125**, 11911-11924.

41. G. Trott, P. K. Saini and C. K. Williams, *Phil. Trans. R. Soc. A.*, 2016, **374**, 20150085.

42. A. M. DiCiccio and G. W. Coates, *J. Am. Chem. Soc.*, 2011, **133**, 10724-10727.

43. S. Huijser, E. Hosseini Nejad, R. Sablong, C. de Jong, C. E. Koning and R. Duchateau, *Macromolecules*, 2011, **44**, 1132-1139.

44. E. Hosseini Nejad, C. G. W. van Melis, T. J. Vermeer, C. E. Koning and R. Duchateau, *Macromolecules*, 2012, **45**, 1770-1776.

45. D. J. Darensbourg, R. R. Poland and C. Escobedo, *Macromolecules*, 2012, **45**, 2242-2248.

46. M. E. Fieser, M. J. Sanford, L. A. Mitchell, C. R. Dunbar, M. Mandal, N. J. Van Zee, D. M. Urness, C. J. Cramer, G. W. Coates and W. B. Tolman, *J. Am. Chem. Soc.*, 2017, **139**, 15222-15231.

47. B. A. Abel, C. A. L. Lidston and G. W. Coates, *J. Am. Chem. Soc.*, 2019, **141**, 12760-12769.

48. C. A. L. Lidston, B. A. Abel and G. W. Coates, *J. Am. Chem. Soc.*, 2020, **142**, 20161-20169.

49. J. Li, Y. Liu, W.-M. Ren and X.-B. Lu, *J. Am. Chem. Soc.*, 2016, **138**, 11493-11496.

50. L. Cui, B. H. Ren and X. B. Lu, *J. Polym. Sci.*, 2021, DOI: 10.1002/pol.20210334, 10.1002/pol.20210334.

51. B. M. Lipinski, K. L. Walker, N. E. Clayman, L. S. Morris, T. M. E. Jugovic, A. G. Roessler, Y. Getzler, S. N. MacMillan, R. N. Zare, P. M. Zimmerman, R. M. Waymouth and G. W. Coates, *ACS Catal*, 2020, **10**, 8960-8967.

52. L. S. Morris, M. I. Childers and G. W. Coates, *Angew Chem Int Ed Engl*, 2018, **57**, 5731-5734.

53. P. K. Saini, C. Romain, Y. Q. Zhu and C. K. Williams, *Polym. Chem.*, 2014, **5**, 6068-6075.

54. J. A. Garden, P. K. Saini and C. K. Williams, *J. Am. Chem. Soc.*, 2015, **137**, 15078-15081.

55. A. C. Deacy, A. F. R. Kilpatrick, A. Regoutz and C. K. Williams, *Nat. Chem.*, 2020, **12**, 372-380.

56. A. C. Deacy, C. B. Durr, R. W. F. Kerr and C. K. Williams, *Catal. Sci. Technol.*, 2021, **11**, 3109-3118.

57. A. C. Deacy, University of Oxford, 2019.

58. A. C. Deacy, C. B. Durr and C. K. Williams, *Dalton Trans.*, 2020, **49**, 223-231.

59. A. Thevenon, J. A. Garden, A. J. P. White and C. K. Williams, *Inorg. Chem.*, 2015, **54**, 11906-11915.

60. C.-M. Chen, X. Xu, H.-Y. Ji, B. Wang, L. Pan, Y. Luo and Y.-S. Li, *Macromolecules*, 2021, **54**, 713-724.

61. H. Y. Ji, B. Wang, L. Pan and Y. S. Li, *Green Chem.*, 2018, **20**, 641-648.

62. H. Y. Ji, X. L. Chen, B. Wang, L. Pan and Y. S. Li, *Green Chem.*, 2018, **20**, 3963-3973.

63. A. Kummari, S. Pappuru and D. Chakraborty, *Polym. Chem.*, 2018, **9**, 4052-4062.

64. L. F. Hu, C. J. Zhang, H. L. Wu, J. L. Yang, B. Liu, H. Y. Duan and X. H. Zhang, *Macromolecules*, 2018, **51**, 3126-3134.

65. R. Xie, Y. Y. Zhang, G. W. Yang, X. F. Zhu, B. Li and G. P. Wu, *Angew. Chem. Int. Ed.*, 2021, DOI: 10.1002/anie.202104981, 10.1002/anie.202104981.

66. H. Li, H. T. Luo, J. P. Zhao and G. Z. Zhang, *Macromolecules*, 2018, **51**, 2247-2257.

67. A. C. Deacy, G. L. Gregory, G. S. Sulley, T. T. D. Chen and C. K. Williams, *J. Am. Chem. Soc.*, 2021, **143**, 10021-10040.

68. H. Feng, X. Lu, W. Wang, N. G. Kang and J. W. Mays, *Polymers*, 2017, **9**, 494.

69. D. K. Schneiderman and M. A. Hillmyer, *Macromolecules*, 2016, **49**, 2419-2428.

70. M. A. Hillmyer and W. B. Tolman, *Acc. Chem. Res.*, 2014, **47**, 2390-2396.

71. G. P. Wu, D. J. Darensbourg and X. B. Lu, *J. Am. Chem. Soc.*, 2012, **134**, 17739-17745.

72. M. R. Kember, J. Copley, A. Buchard and C. K. Williams, *Polym. Chem.*, 2012, **3**, 1196-1201.

73. C. Romain and C. K. Williams, *Angew. Chem. Int. Ed.*, 2014, **53**, 1607-1610.

74. T. Stößer, T. T. D. Chen, Y. Zhu and C. K. Williams, *Phil. Trans. R. Soc. A.*, 2018, **376**, 20170066.

75. T. Aida, K. Sanuki and S. Inoue, *Macromolecules*, 1985, **18**, 1049-1055.

76. Y. Q. Zhu, C. Romain and C. K. Williams, *J. Am. Chem. Soc.*, 2015, **137**, 12179-12182.

77. C. Romain, Y. Q. Zhu, P. Dingwall, S. Paul, H. S. Rzepa, A. Buchard and C. K. Williams, *J. Am. Chem. Soc.*, 2016, **138**, 4120-4131.

78. S. Paul, C. Romain, J. Shaw and C. K. Williams, *Macromolecules*, 2015, **48**, 6047-6056.

79. H. Y. Ji, B. Wang, L. Pan and Y. S. Li, *Angew Chem Int Ed Engl*, 2018, **57**, 16888-16892.

80. X. Xia, R. Suzuki, K. Takojima, D. Jiang, T. Isono and T. Satoh, *ACS Catal.*, 2021, **11**, 5999-6009.

81. S. Kernbichl, M. Reiter, F. Adams, S. Vagin and B. Rieger, *J. Am. Chem. Soc.*, 2017, **139**, 6787-6790.

82. T. Stößer, D. Mulryan and C. K. Williams, *Angew. Chem. Int. Ed.*, 2018, **57**, 16893-16897.

83. T. Stößer and C. K. Williams, *Angew. Chem. Int. Ed.*, 2018, **57**, 6337-6341.

84. T. Stößer, G. S. Sulley, G. L. Gregory and C. K. Williams, *Nat. Comm.*, 2019, **10**.

85. T. T. D. Chen, L. P. Carrodeguas, G. S. Sulley, G. L. Gregory and C. K. Williams, *Angew. Chem. Int. Ed.*, 2020, **59**, 23450-23455.

86. G. L. Gregory, G. S. Sulley, L. P. Carrodeguas, T. T. D. Chen, A. Santmarti, N. J. Terrill, K. Y. Lee and C. K. Williams, *Chem. Sci.*, 2020, **11**, 6567-6581.

87. L. P. Carrodeguas, T. T. D. Chen, G. L. Gregory, G. S. Sulley and C. K. Williams, *Green Chem.*, 2020, **22**, 8298-8307.

88. R. W. F. Kerr, P. M. D. A. Ewing, S. K. Raman, A. D. Smith, C. K. Williams and P. L. Arnold, *ACS Catal.*, 2021, **11**, 1563-1569.

89. A. C. Deacy, E. Moreby, A. Phanopoulos and C. K. Williams, *J. Am. Chem. Soc.*, 2020, **142**, 19150-19160.

Chapter 2

Monometallic complexes for the ROCOP of epoxides and anhydrides and ROP of lactones

Work described in this chapter appears in "*Ortho-vanillin derived Al(III) and Co(III) catalyst systems for switchable catalysis using ε-decalactone, phthalic anhydride and cyclohexene oxide*"

W. T Diment, T. Stößer, R. W. F. Kerr, A. Phanopoulos, C. B. Durr, C. K. Williams

Catal. Sci. Technol., 2021, **11**, 1737 - 1745

2.1 Introduction

Catalysts with high activities for both the ring-opening copolymerisation (ROCOP) of epoxides and anhydrides, and the ring-opening polymerisation (ROP) of lactones or lactide, are suitable candidates for application to switchable catalysis, where both polymerisations are utilised.[1] In general, however, complexes reported to display high activities as catalysts for both polymerisations are rare.[2-4] For example, Williams and co-workers reported a heterodinuclear Zn(II)Mg(II) macrocyclic complex which displayed a high activity for the ROP of ε-decalactone (ε-DL, TOF = 952 h^{-1}, 0.067 mol% *vs*. lactone, T = 80 °C), but a much lower activity for cyclohexene oxide (CHO)/ phthalic anhydride (PA) ROCOP (TOF = 25 h^{-1}, 0.14 mol% *vs*. anhydride, T = 80 °C).[5]

Many metal(III) salen catalyst systems have been reported for the ROCOP of epoxides with anhydrides (M = Cr, Co or Al) or CO_2 (M = Cr or Co), but only Al(III)-containing systems have significant precedence as catalysts for the ROP of cyclic esters.[2, 6, 7] Aluminium(III) salen catalyst systems are often less active for ROCOP than their cobalt(III)- and chromium(III)-containing analogues, however.[8] In the context of switchable catalysis, the [SalcyCrCl]/PPNCl catalyst system displayed a high activity for CHO/PA ROCOP (TOF = 192 h^{-1}, 0.5% *vs*. anhydride, T = 100 °C), but a very low activity for the ROP of ε-DL (TOF = 3 h^{-1}, 0.5% *vs*. lactone, T = 100 °C).[8, 9]

2.2 Aims

The aim of this work is to develop complexes that show high rates for both the ROCOP of epoxides and anhydrides and the ROP of lactones. Tetradentate and bidentate monometallic bearing *ortho*-vanillin derived ancillary ligands featuring aluminium and titanium, respectively, have been shown to be active catalysts for the ROP of lactide and lactones.[6, 10] The capability of these complexes for ROCOP of epoxides and anhydrides has not been

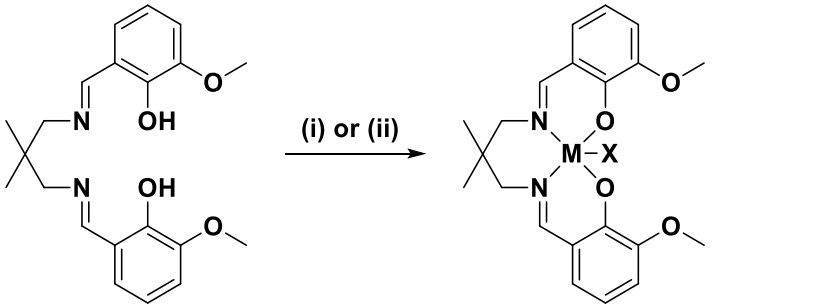
investigated, however. By selection of an ancillary ligand that promotes lactone ROP but applied to a framework (salen-type) that is well known for ROCOP catalysis, it was reasoned that complexes that function as active catalysts for both reactions may result.

To investigate this hypothesis, a series of monometallic (M(III) = Cr, Mn, Fe, Co, Al) complexes featuring tetradentate, *ortho*-vanillin derived, ancillary ligands will be synthesised and characterised *via* NMR and IR spectroscopy, X-ray crystallography and, where appropriate, SQUID magnetometry. A series of metals are targeted as there is substantial precedent for metal selection altering polymerisation activity.[8, 11] Note that some complexes featured have been previously reported, but the aim of this work is to present a systematic study for this novel application.[12, 13]

These complexes will be investigated for the ROCOP of CHO with PA, CHO with CO_2, and the ROP of ε-DL. Each catalysts' performance in these benchmark polymerisations will highlight their respective suitability (or otherwise) for application to switchable catalysis.

2.3 Synthesis and Characterisation of Monometallic Complexes supported by *ortho*-Vanillin Derived Ligands

In order to investigate the application of tetradentate *ortho*-vanillin supported complexes as catalysts ROCOP and ROP, a series of monometallic(III) complexes (Al (**1**), Cr (**2**), Mn (**3**), Fe (**4**), Co(**5**)) were targeted (Scheme 2.1, See Chapter 7 for experimental details).



Scheme 2.1: Synthesis of complexes **1** – **5**. i) $AlEt_3$, THF, -30 °C to RT, 2 h, (68%). ii) $M(OAc)_2$, THF, RT, 2 h followed by exposure to O_2, RT, 24-48 h. Yield = 68% (**1**), 24% (**2**), 61% (**3**), 71% (**4**), 70% (**5**).

The *ortho*-vanillin derived pro-ligand, [$L_{van}H_2$], was synthesised through the Schiff base condensation reactions of *ortho*-vanillin with 2,2-dimethyl-1,3-propanediamine.[14] The aluminium containing compound, [L_{van}AlEt] (**1**), was synthesised through reaction of $AlEt_3$ with [$L_{van}H_2$] in toluene under an inert atmosphere, and was isolated as a yellow powder in 68% yield.[12] Complexes **2** (Cr), **3** (Mn), **4** (Fe) and **5** (Co) were synthesised through reaction of the respective metal(II) acetate salts with [$L_{van}H_2$] in THF under an inert atmosphere, resulting in the formation of the corresponding M(II) adduct. Subsequently, the reaction solutions were exposed to oxygen which, in conjunction with the acetic acid formed from the initial ligand deprotonation, resulted in oxidation of the M(II) species to the corresponding M(III) complexes, which precipitated from the reaction solution over 24 - 48 hours.

In order to directly compare the coordination chemistries of aluminium with the transition metals investigated, [L_{van}AlOAc] (**6**) was also synthesised. Reaction of complex **1** with 1 equivalent of acetic acid, in THF, resulted in the precipitation of the **6** as a pale yellow powder, allowing for its isolation in 79% yield from complex **1**. Alternatively, complex **6** could be synthesised in one-pot from [$L_{van}H_2$]. Firstly, 1 equivalent of $AlEt_3$ was added to [$L_{van}H_2$] in THF under an inert atmosphere, resulting in the formation of **1** *in situ* over 2 hours. Subsequent addition of 1 equivalent of acetic acid resulted in the formation of **6**, which precipitated from the reaction solution over 16 hours. Isolation of the complex *via* this method resulted in 74% yield from [$L_{van}H_2$].

The diamagnetic complexes **5** and **6** were characterised by solution phase NMR spectroscopy, IR spectroscopy and X-ray crystallography. Complex **1** has previously been synthesised in our group, but, where relevant, its characterisation data is discussed for comparison. Complexes **2**, **3** and **4** all contain metals that have unpaired *3d* electrons, hence are paramagnetic, and so characterisation by NMR spectroscopy was unsuitable. These were characterised through SQUID magnetometry, IR spectroscopy and X-ray crystallography. Complex **3** has recently been reported for immobilisation on silica-coated nanoparticles for sulfide and alkene oxidations; the characterisation data presented here is in addition to that already reported in the literature.[13] The bulk purity of all complexes was confirmed through elemental analysis.

2.3.1 X-ray Crystallography

Single crystals, suitable for X-ray diffraction, of all complexes were obtained by layering saturated solutions of the complexes in chloroform (**2**, **3** and **6**), THF (**4**) or dichloromethane (**5**), with hexane at 25 °C (Figure 2.1). The crystal structure of complex **1** has been previously reported by our group but is presented for clarity.[12]

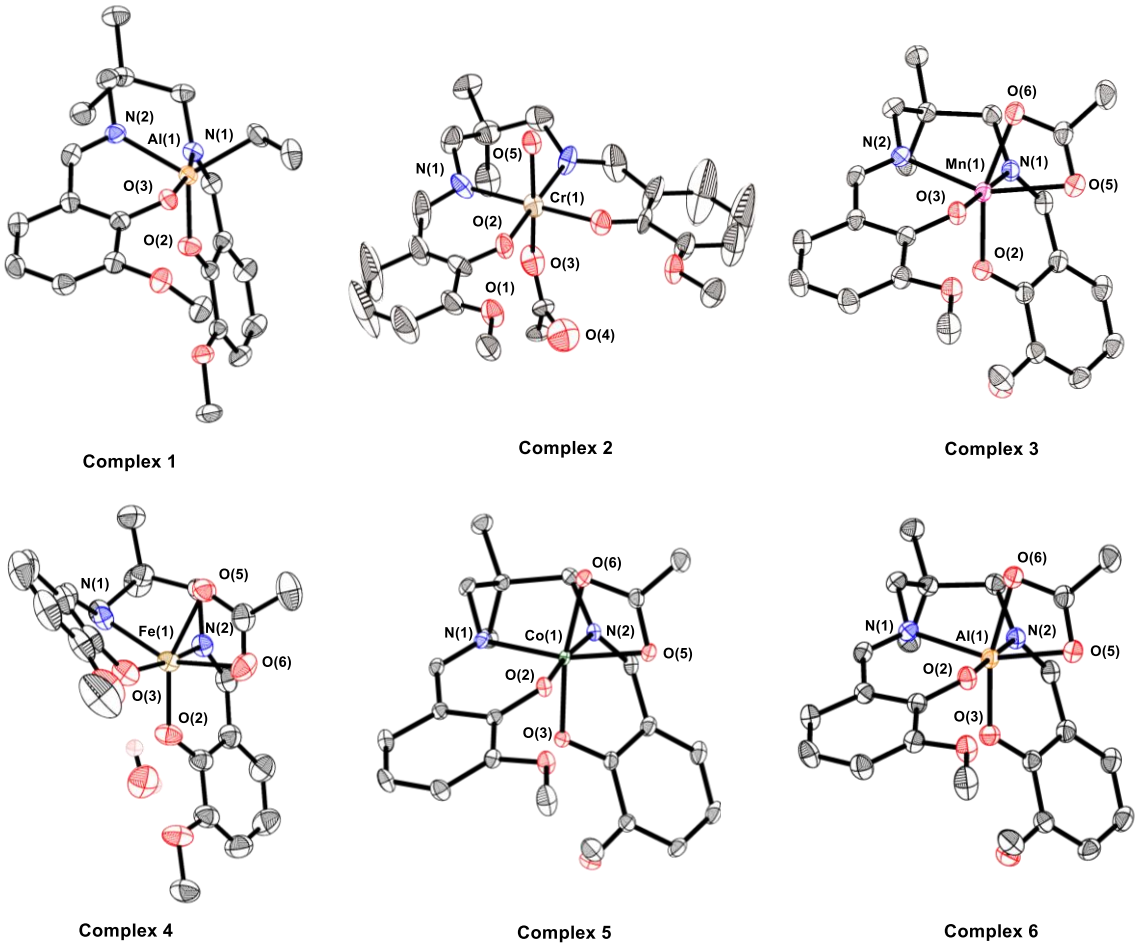


Figure 2.1. Molecular structures (determined by X-ray diffraction, H-atoms omitted for clarity, thermal ellipsoids at 50% probability) of complexes **1** - **6**. Selected bond lengths and angles and crystallographic refinement data are presented in Tables S2.1 – 2.5). For the structure of complex **2** only connectivity is established.

All complexes possess monomeric structures in the solid state. Complex **1** possesses C_1 molecular symmetry, with a pentacoordinate, distorted trigonal bipyramidal geometry around the Al(III) centre [N(1)-Al(1)-O(3) ∠ 167.80°, $\tau_5 = 0.79$].[15] In comparison, in the solid state structures of complexes **3** - **6** the metals possess distorted O_h geometry, with *cis*-β coordinated *ortho*-vanillin ligands and κ^2-acetate coligands and an overall C_1 molecular symmetry.[16] The degree of distortion can be quantified by comparing the *trans*-$O_{phenoxy}$-M(III)-$O_{carboxylate}$ angle, which should be 180° in a perfect octahedron (Table 2.1, Entries 1 - 4). Whilst complex **2** also possesses an O_h geometry around the Cr(III) centre, the *ortho*-

vanillin ligand is *trans*-coordinate, with κ^1-acetate and water coligands, and is C_s symmetric overall.

The structure of complex **4** includes a molecule of water that is hydrogen bonded to the phenoxy oxygens [O(2) and O(3)]. This coordination results in a greater degree of distortion from O_h geometry around the metal centre [*e.g.* O(2)-Fe(1)-O(5) = 153.876(6)° *cf.* O(3)-Co(1)-O(6) = 167.90(5)°]. This may be due to the d^5 configuration of the Fe(III) centre (*vide infra*), which would result in less energetic preference (*via* LFSE) for an octahedral coordination mode.

The average M(III)-$O_{carboxy}$ bond lengths show shorter bonds for complexes **5** and **6** compared to **3** and **4** (Table 2.1, Entries 1 - 4). Such a trend may be rationalised by considering the relative Lewis acidity of the different M(III) centres, and further by LFSE considerations (d^4/d^5 for Mn(III) and Fe(III) would be expected to have smaller contributions to the M-L bond strength). A notable first order Jahn-Teller distortion is also observed for complex **3**. The Mn-$O_{carboxylate}$ bond lengths show a difference of ~0.2 Å [Mn(1)-O(5) = 2.2948(14) Å and Mn(1)-O(6) = 2.0926(14) Å] whilst for complex **4**, the Fe-$O_{carboxylate}$ bond lengths show a difference of ~0.03 Å [Fe(1)-O(5) = 2.1440(14) Å and Fe(1)-O(6) = 2.1147(13) Å].

Table 2.1. Selected bond lengths and angles, obtained from the solid-state molecular structures, of complexes **3** – **6**.

Entry	Complex	Bond	Length (Å)	Bond	Angle (°)
1	**3** (Mn)	Mn(1)-$O_{carboxy}$[a]	2.1934	O(2)-Mn(1)-O(6)	159.79(6)
2	**4** (Fe)	Fe(1)-$O_{carboxy}$[a]	2.1294	O(3)-Fe(1)-O(6)	153.87(6)
3	**5** (Co)	Co(1)-$O_{carboxy}$[a]	1.9689	O(3)-Co(1)-O(6)	167.90(5)
4	**6** (Al)	Al(1)-$O_{carboxy}$[a]	1.9923	O(3)-Al(1)-O(6)	164.69(4)

[a] Average of respective M(III)-O(5) and M(III)-O(6) bonds lengths, obtained from solid state molecular structures.

2.3.2 NMR Spectroscopy

The diamagnetic complexes **1**, **5** and **6** were characterised by ^{1}H, ^{13}C{^{1}H} and, for **1** and **6**, ^{27}Al NMR spectroscopy (Figures S2.1 – S2.17). Complex **1** possesses a ^{1}H NMR spectrum consistent with that previously reported, featuring 9 sharp resonances corresponding the *ortho*-vanillin derived ligand, and 2 resonances corresponding to the ethyl coligand, implying the complex possessed C_s symmetry, and a symmetrically coordinated ligand, in solution (Figure S2.1).[12] The ^{1}H NMR spectrum of complex **6** at room temperature is analogous to that of complex **1**, with 9 sharp resonances corresponding to the *ortho*-vanillin derived ligand, and 1 resonance corresponding to the acetate coligand (Figure 2.2).

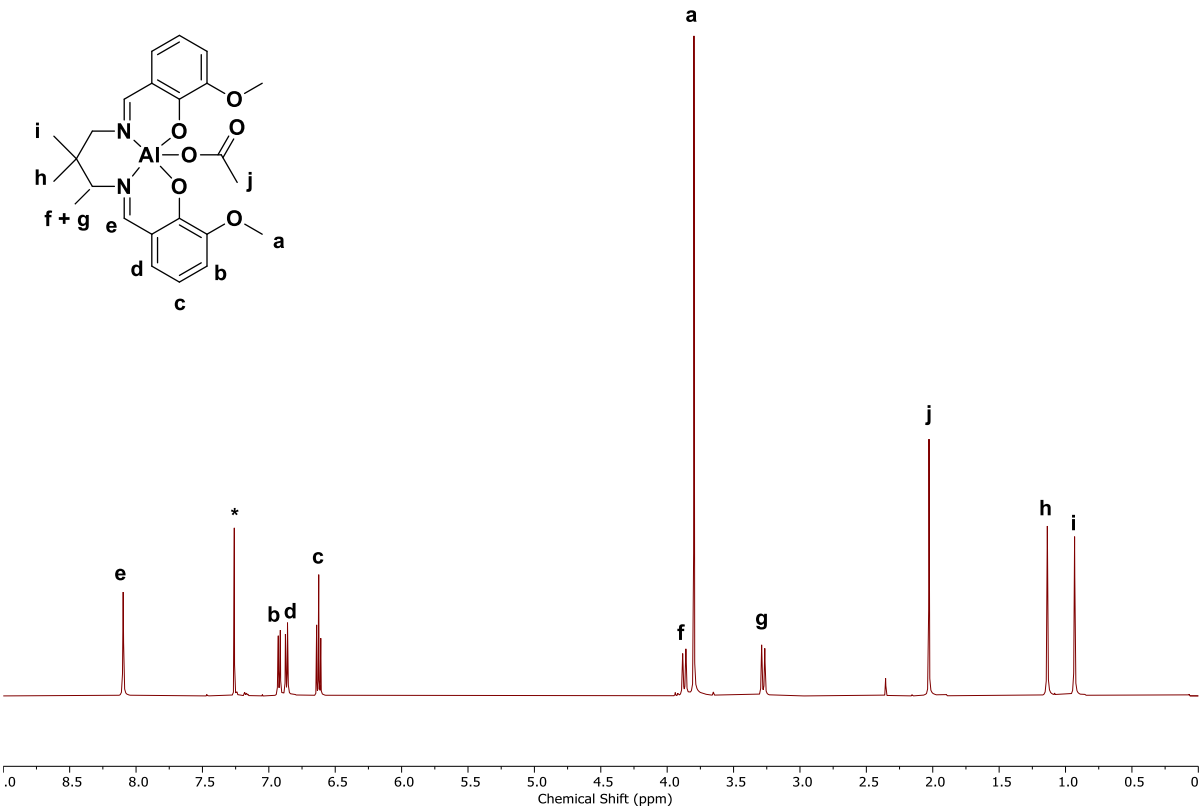


Figure 2.2. ^{1}H NMR spectrum ($CDCl_3$ (*), 400 MHz, 298 K) of complex **6**.

This again suggests a C_s symmetric complex in solution, which could arise from either a κ^1-acetate coligand (and hence a pentacoordinate aluminium centre as in complex **1**), or rapid interconversion of a κ^2-acetate coligand with a low barrier to moving to a κ^1-mode, both of

which allow for interconversion of coordination isomers. Given the crystal structure observed, the latter is proposed. In order to investigate whether interconversion between the coordination isomers could be observed, variable temperature ^{1}H NMR spectroscopy in DCM-d_2 was attempted, but no significant changes in the ^{1}H NMR were observed despite cooling to -80 °C (Figure S2.18).

To further investigate the coordination geometry of complexes **1** and **6** in solution, the complexes were analysed by ^{27}Al NMR. Whilst the ^{27}Al spectrum of complex **1** shows a broad, weak peak at 5.7 ppm, the spectrum of complex **6** shows a sharp, well defined peak at 14.8 ppm (Figure S2.3 and S2.14, respectively). This finding is consistent with an octahedrally coordinated aluminium centre in complex **6**, since ^{27}Al is quadrupolar, and will therefore only give rise to significant resonances if the nucleus is in a high-symmetry environment. Taken together, the ^{1}H and ^{27}Al NMR spectra for complexes **1** and **6** are consistent with rapid interconversion of coordination isomers, which would result in single, time averaged, structures being observed by NMR spectroscopy that maintain the coordination geometry (trigonal bipyramidal and distorted octahedral, respectively) of the aluminium centre.

The ^{1}H NMR spectrum of complex **5** features 16 resonances corresponding to the *ortho*-vanillin ligand, and 1 corresponding to the acetate coligand (Figure 2.3). This suggests an asymmetrically coordinated *ortho*-vanillin derived ligand, and a complex possessing C_1 symmetry, in solution, consistent with the structure observed in the solid state. This implies that, in contrast to complexes **1** and **6**, the interconversion of coordination isomers is not observed in solution. The ^{13}C{^{1}H} spectra of all complexes are consistent with the solution phase structures described.

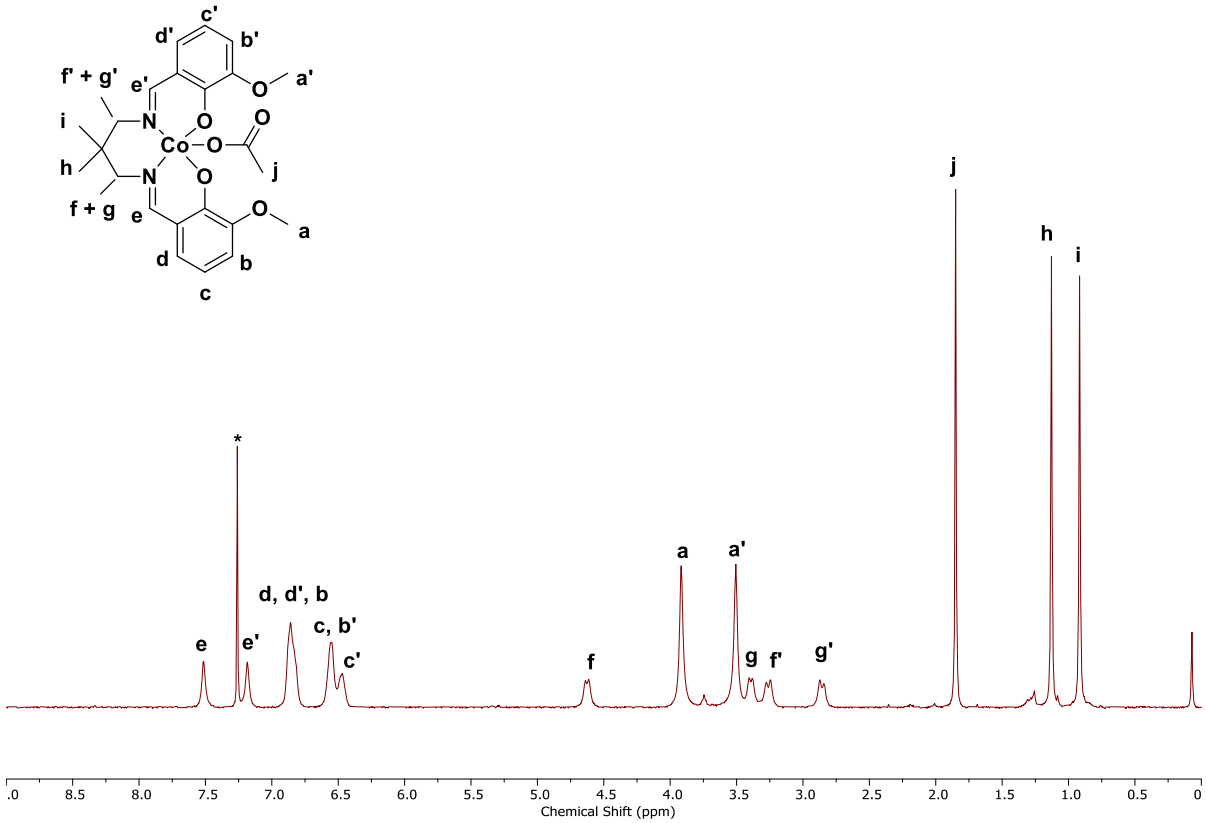


Figure 2.3. ^{1}H NMR spectrum ($CDCl_3$ (*), 400 MHz, 298 K) of complex **3**.

2.3.3 Infrared Spectroscopy

Complexes **2** - **6** were characterised by Fourier transform infrared (FT-IR) spectroscopy, which can be compared to the corresponding spectra obtained for the proligand, [$L_{van}H_2$] (Figure 2.4 and S2.19 – S2.23).

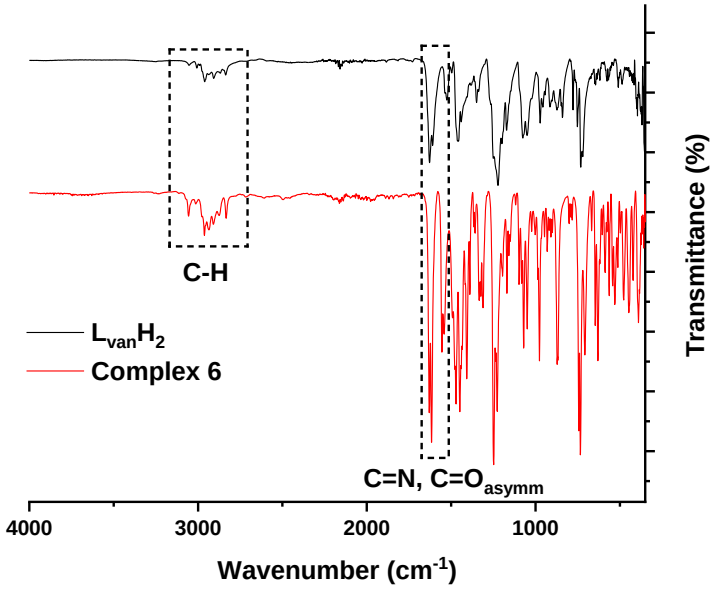


Figure 2.4. Overlaid IR spectra of complex **6** and the pro-ligand, $L_{van}H_2$.

The complexes display IR spectra consistent with the solid-state molecular structures determined by XRD. For complexes **3** – **6**, the absence of any signals in the 1700 cm^{-1} region implies that in all of the complexes a chelating carboxylate is observed, consistent with solid state crystal structures obtained. By comparison with the spectra of [$L_{van}H_2$], resonances between 1650 – 1500 cm^{-1} can be assigned to both the imine (C=N) and asymmetric carboxylate (C=O) stretches.

In addition to the above resonances, the IR spectrum of complex **2** displays O-H (3260 cm^{-1}) and C=O (1728 cm^{-1}) stretches. This is consistent with the solid-state molecular structure which features a coordinated water molecule, and unidentate acetate coligand, which would be expected to have a stronger C=O bond in comparison to a chelating acetate.

2.3.4 Superconducting Quantum Interference Device (SQUID) Magnetometry

In order to determine the number of unpaired electrons, and hence oxidation and spin state, of the paramagnetic complexes **2 - 4**, Superconducting Quantum Interference Device (SQUID) magnetometry was carried out. The measurements were carried out by Gloria Rosetto at the University of Oxford. By plotting the inverse of molar magnetic susceptibility (χ_{mol}^{-1}) against temperature, the Curie and Weiss constants can be extracted (Figure 2.5).

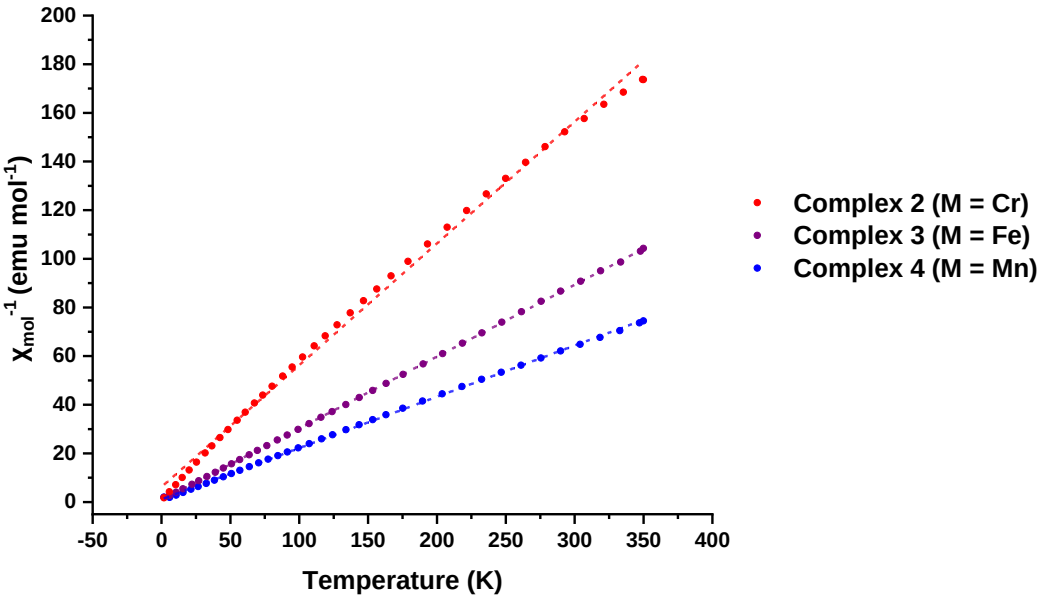


Figure 2.5. Plot of χ_{mol}^{-1} *vs.* Temperature for complexes **2 - 4**.

By extracting the molar magnetic susceptibility per magnetic centre, $\chi_m = \frac{\chi_{mol}}{n}$ (where n is the number of magnetic centres per formula unit, n = 1 for complexes **2 - 4**), at the desired temperature, the effective magnetic moment per magnetic centre, μ_{eff}, can be calculated (Table 2.2).[17] Comparison between the values of μ_{eff} and μ_{so}, the expected magnetic moment if only electron spin is considered, allows for evaluation of the spin state of the complexes. A 'spin only' approximation is reasonable provided there is no ground state angular momentum, which is observed for complexes in *T* electronic ground states.

Table 2.2. Magnetometry data for complexes **2** - **4**.

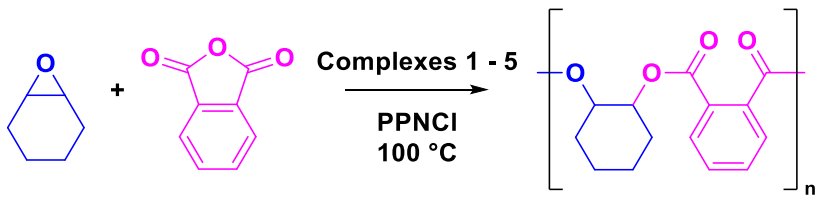
Entry	Complex	C^a (emu K mol^{-1})	θ^b (K)	$\mu_{eff}{}^c$	S^d	$\mu_{SO}{}^e$
1	**2** (Cr)	2.00	-12.41	3.92	3/2	3.87
2	**3** (Mn)	3.37	-1.43	5.18	2	4.90
3	**4** (Fe)	4.74	-5.38	6.10	5/2	5.92

[a] Curie constant is extracted from a plot of $\chi_{mol}{}^{-1}$ *vs*. temperature for each complex (Figure 2.5). From a linear fit of the data, $\chi_{mol}{}^{-1} = \alpha T + \beta,\ C = 1/\alpha$. [b] Weiss constant is extracted from a plot of $\chi_{mol}{}^{-1}$ *vs*. temperature for each complex (Figure 2.5). From a linear fit of the data, $\chi_{mol}{}^{-1} = \alpha T + \beta,\ \ \theta = x$ intercept. [c] Experimentally determined effective magnetic moment; $\mu_{eff} = 2.828\sqrt{\chi_m T}$ where $\chi_m = \frac{C}{T-\theta}$, T = 300 K. [d] Total spin quantum number, assuming high spin M(III) complexes. [e] Theoretical magnetic moment calculated from spin angular momentum only; $\mu_{so} = 2\sqrt{S(S+1)}$, which assumes complete quenching of *d* orbital angular momentum.

Complexes **2**, **3** and **4** displayed μ_{eff} values of 3.92, 5.18 and 6.10, respectively (Table 2.2, Entries 1 - 3). Comparison of these values with μ_{so} for 3, 4 and 5 unpaired electrons, respectively, shows good agreement. This suggests that all complexes are in the +3 oxidation state and, further, are high spin. This is in contrast to the low spin Co(III) complex **5**, which is diamagnetic. The high- to low-spin crossover in going from iron to cobalt is also observed for the hexaaqua complexes ($[M(H_2O)_6]^{3+}$).[18, 19]

2.4 ROCOP of CHO and PA, and ε-DL ROP, with Complexes 1 - 5

Following the successful synthesis and characterisation of the monometallic complexes, investigation of their capability to catalyse the ROCOP of epoxides and anhydrides was carried out. For this purpose, cyclohexene oxide (CHO) and phthalic anhydride (PA) were selected as monomers as they are frequently used as benchmark monomers, allowing for ready comparison between a range of catalyst systems (Scheme 2.2, Table 2.3).



Scheme 2.2. ROCOP of PA and CHO to form poly(cyclohexene phthalate) (PCHPE) with complexes **1** – **5**.

The commercial [SalcyCrCl]/PPNCl catalyst systems, previously reported by our group for switchable catalysis, was also tested under equivalent conditions. In all reactions, PPNCl was used as a cocatalyst, since its use enhances rates, and polyester selectivity, in salen-type catalyst systems.[8] Cyclohexene diol (CHD) was added as a chain transfer agent to confirm that all complexes were compatible with its presence, as use of CHD would be required in later work (see Chapter 3).

Table 2.3. Data for the ROCOP of CHO and PA using complexes **1** - **5** and [SalcyCrCl].[a]

Entry	Catalyst	Conv.[b] (%)	Selectivity[c] (%)	TOF[d] (h^{-1})	$M_{n,\ GPC}$ [Đ][e] (kg mol^{-1})	$M_{n,\ Theory}$[f] (kg mol^{-1})
1	**1** (Al)	29	>99	348	2.2 [1.11]	2.4
2	**2** (Cr)	>99	>99	1200	3.6 [1.29]	6.2
3	**3** (Mn)	14	>99	172	1.2 [1.18]	0.9
4	**4** (Fe)	22	>99	261	1.4 [1.20]	1.4
5	**5** (Co)	43	>99	516	3.5 [1.12]	2.7
6	[SalcyCrCl]	97	>99	1160	5.1 [1.17]	6.1

[a] Catalysis conditions: [Cat]:[PPNCl]:[CHD]:[PA]:[CHO] = 1:1:2:100:500, T = 100 °C, Time = 5 m. [b] Determined by comparison of ^{1}H NMR integrals corresponding to PCHPE (7.65-7.30 ppm) and PA (8.10-7.85 ppm). [c] Selectivity for polyester over polyether, determined by comparison of ^{1}H NMR integrals corresponding to PCHPE (5.22-5.06 ppm) and PCHO (3.60 - 3.20 ppm). [d] TOF (turnover frequency) = TON per unit time. TON (turnover number) = Number of moles of monomer consumed/number of moles of catalyst. Determined by GPC in THF, at 30 °C, using narrow dispersity polystyrene standards. [f] Theoretical M_n values. Determined through (TON*M_n(Repeat Unit))/ (number of equivalents of CHD + number of equivalents of PPNCl + number of equivalents of catalyst (except for complex **1**, which does not feature an initiating coligand)).

All of the novel complexes, as well as the commercial [SalcyCrCl], were found to be capable catalysts for the ROCOP of CHO and PA, displaying good activities and perfect selectivities (>99%) for polyester linkages. By comparing conversions at a fixed timepoint it was found that complex **2** was most active (TOF = 1200 h^{-1}), displaying a similar activity to that obtained for the commercial catalyst [SalcyCrCl] (TOF = 1160 h^{-1}) (Table 2.3, Entries 2 and 6). Good activities were also obtained for complexes **5** (TOF = 516 h^{-1}) and **1** (TOF = 348 h^{-1}) (Table 2.3, Entries 5 and 1). Full conversion of PA could be obtained for all complexes investigated by leaving the reactions for a longer time period (Table S2.6).

It should be noted that the TOF obtained for SalcyCrCl (1160 h^{-1}, 1% *vs*. anhydride, 100 °C) is significantly higher than that reported in the literature (TOF = 245 h^{-1}, 0.4% *vs*. anhydride, 110 °C) by Duchateau and co-workers.[8] In the original report, the reactions were run with stoichiometric epoxide (*i.e.* [PA]:[CHO] = 1:1), whilst in this work, and most contemporary reports, reactions are typically run with epoxide as the solvent, and in significant excess. As reactions typically show a 1st order dependence on epoxide concentration, an excess of epoxide results in a zero order reaction, and hence higher observed TOFs.[2] For this reason, when comparing the activity of [SalcyCrCl] to the novel complexes developed here, the TOF reported here is a significantly more accurate value.

Previous reports on monometallic salen catalysts systems have found that, for polyester ROCOP, metal reactivity typically follows the trend Cr > Co > Al, although application of other transition metals within these ligand frameworks is often not reported.[8] Recent work by Coates and co-workers included catalysts featuring both iron and manganese, but these metals demonstrated very low activities when compared to the aluminium, chromium and cobalt-containing analogues.[20] Of the novel complexes described here, the most active (**1**, **2** and **5**) follow the previously reported metal reactivity series. However, the manganese- and iron-containing complexes (**3** and **4**) also show significant activities (TOF = 172 and 261 h^{-1}, respectively), which should promote further research on complexes featuring these metals (Table 2.3, Entries 3 and 4) .

There is an inverse correlation between the average M(III)-$O_{carboxylate}$ bond length and activities of these monometallic catalyst systems where M(III)-$O_{carboxylate}$: Mn > Fe > Al > Co and TOF(CHO/PA): Mn < Fe < Al < Co (*vide supra*). Given that the proposed mechanism for monometallic salen-type systems involves the activation of an epoxide monomer by the M(III) species during the rate determining step, the relative weakness of

the M(III)-coligand bond may be indicative of weaker activation of the epoxide monomer during this key intermediate.[21]

All of the polymer molar mass distributions were bimodal (Figure 2.6 and S2.24). This bimodality arises due to the presence of initiating coligands (*i.e.* acetate) and cocatalysts (*i.e.* chloride in PPNCl) as both ring open CHO to give a monofunctional alkoxide species, which acts as an initiator for the polymerisation (see Chapter 1), leading to α-chloride(or acetate)-ω-hydroxy terminated polymers. The presence of CHD, a bifunctional initiator, gives rise to a second, higher molar mass, distribution featuring α,ω-hydroxy terminated polymers.[22] The use of CHD to obtain monomodal distributions, as well as further discussion about the initiating species present, will be described in Chapter 3.

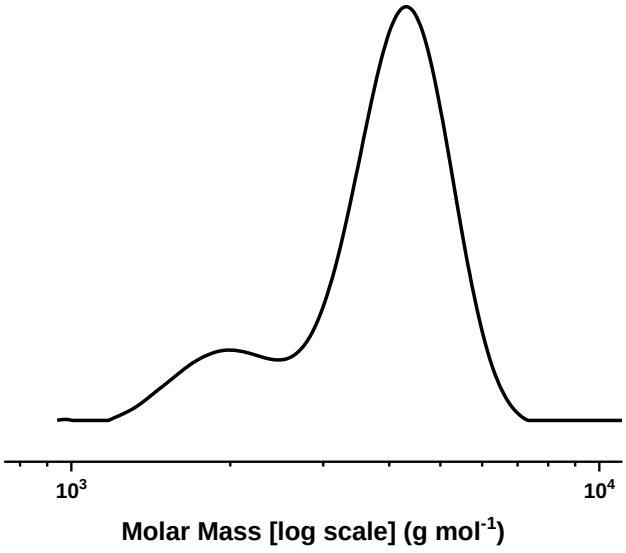
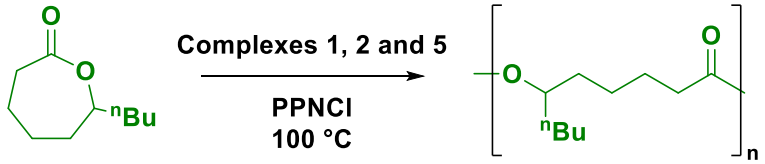


Figure 2.6. GPC trace of PCHPE obtained with complex **5** corresponding to Table 2.3, Entry 5.

The three most active complexes (**1, 2** and **5**) were also tested for the ROP of ε-DL (Scheme 2.3).



Scheme 2.3. ROP of ε-DL to form poly(decalactone) (PDL) with complexes **1**, **2** and **5**.

ε-DL was selected as it provides access to an elastomeric, low glass transition temperature (T_g = -50 °C) homopolymer (PDL). Further, the ε-substitution aids in supressing transesterification reactions that can occur in unsubstituted lactones, such as ε-caprolactone.[23] Block copolymers derived from PDL with rigid, high T_g polymers, such as PCHPE or PCHC, are thermoplastic elastomers with high tensile strength, strain at break and elastic recovery.[5, 22] Such copolymers can be accessed in one-pot through switchable catalysis, which will be discussed in Chapter 3. The catalysts were tested under conditions identical to those use for the CHO/PA ROCOP polymerisations, as these would be the conditions used in the one-pot process (Table 2.4).

Table 2.4. Data for the ROP of ε-DL with complexes **1**, **2**, **5** and SalcyCrCl.[a]

Entry	Catalyst	Time (h)	Conv.[b] (%)	TON[c]	TOF[d] (h^{-1})	$M_{n,\,GPC}$ [Đ][e] (kg mol^{-1})	$M_{n,\,Theory}$[f] (kg mol^{-1})
1	**1** (Al)	0.5	82	162	330	15.6 [1.19]	9.3
2	**2** (Cr)	72	63	126	2	4.1 [1.25]	7.1
3	**5** (Co)	3	96	192	64	12.2 [1.27]	8.1
4	SalcyCrCl	72	94	188	3	7.1 [1.30]	8

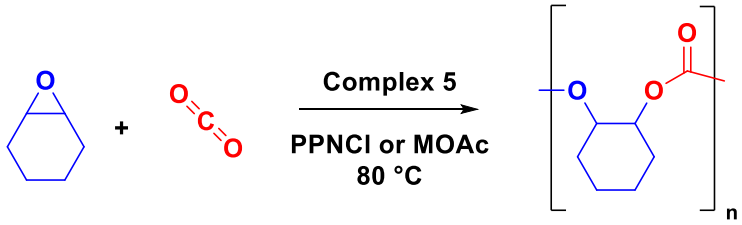
[a] Catalysis conditions: [Cat]:[PPNCl]:[CHD]:[ε-DL]:[CHO] = 1:1:2:200:500, T = 100 °C. [b] Determined by comparison of ^{1}H NMR integrals corresponding to PDL (4.85 – 4.55 ppm) and ε-DL (4.30 – 4.15 ppm). [c] Turnover number (TON) = number of moles of monomer consumed/ number of moles of catalyst. [d] TOF (turnover frequency) = TON per unit time. TON (turnover number) = Number of moles of monomer consumed/number of moles of catalyst. [e] Determined by GPC, in THF, using narrow dispersity polystyrene standards. [f] Theoretical M_n values. Determined through (TON*M_n(Repeat Unit))/ (number of equivalents of CHD + number of equivalents of PPNCl + number of equivalents of catalyst (except for complex **1**, which does not feature and initiating coligand)).

Of the novel complexes, **1** was found to be most active (TOF = 330 h^{-1}), with **5** being significantly slower (TOF = 64 h^{-1}), and **2** displaying very low activity (TOF = 2 h^{-1}) (Table 2.4, Entries 1 - 3). Overall, an inverse reactivity ratio compared to PA/CHO ROCOP is observed, where TOF(**2**) > TOF(**5**) > TOF(**1**). The commercial catalyst SalcyCrCl also showed very low activities (TOF = 3 h^{-1}, Table 2.4, Entry 4). It should be noted that, owing to the larger hydrodynamic radius of PDL *cf.* equivalent weight polystyrene standards, the polymer molar mass measured by GPC can be higher than the mass obtained from theoretical calculations.[23] As observed for the PCHPE obtained from PA/CHO ROCOP, bimodal polymer molar mass distributions were observed in all cases owing to the presence of both mono- and bifunctional initiators (Figure S2.25).

This initial catalyst screening demonstrated that complexes **1** and **5** were capable catalysts for both the ROCOP of PA and CHO and the ROP of ε-DL, and so would be suitable for application to switchable catalysis involving both polymerisations.

2.5 ROCOP of CHO and CO_2 with Complex 5

Monometallic cobalt salen catalyst systems are well known to be effective catalysts for CO_2/epoxide ROCOP.[24] Whilst prior work in our group has shown that monometallic [L_{van}AlOR]-type complexes (which feature the same propagating species as complex **1**) are unsuccessful in catalysing the ROCOP of CO_2 with limonene oxide (LO), PO or CHO, cobalt analogues of these complexes have not been explored.[12] It was therefore of interest to determine whether the cobalt containing complex **5** was capable of polymerising the ROCOP of CO_2 with CHO, which would allow for the application of these monometallic complexes to the synthesis of triblock copolymers involving polycarbonate blocks (Scheme 2.4).



Scheme 2.4. ROCOP of CHO and CO_2 to form PCHC with complex **5**.

Complex **5** was initially screened for the ROCOP of CO_2 and CHO under conditions typical for the literature (T = 80 °C, $p(CO_2)$ = 1 or 20 bar) utilising co-catalytic PPNCl as it enhances both selectivity for polycarbonate, and rate of reaction (Table 2.5).[24]

Table 2.5. Data for the ROCOP of CHO and CO_2 with complex **5**.[a]

Entry	Cocat.	Time (h)	Conv.[b] (%)	CO_2[c] (%)	Polym.[d] (%)	TON_{PCHC}[e]	TOF_{PCHC}[f]	$M_{n,\,GPC}$[Đ][g] (kg mol^{-1})
1	None	20	0	-	-	-	-	*N.d.*
2	PPNCl	20	3	>99	0	-	-	*N.d.*
3	PPNCl[h]	48	30	>99	0	-	-	*N.d.*
4	NaOAc	20	2.5	>99	>99	25	1	*N.d.*
5	NaOAc	48	12	>99	>99	120	3	1.6 [1.20]
6	NaOAc	72	21	>99	99	199	3	2.0 [1.21]
7	NaOAc	96	22	>99	99	217	-	1.9 [1.31]
8	NaOAc[i]	20	30	>99	90	270	14	6.4 [1.33]

[a] Catalysis conditions: [Cat]:[Cocat]:[CHO] = 1:x:1000, x = 1 for PPNCl and 2 for NaOAc, T = 80 °C, $p(CO_2)$ = 1 bar. [b] Conversion of CHO, determined by comparison of relative ^{1}H NMR integrals of CHO (1.27-1.17 ppm) with the sum of the relative integrals of polycarbonate (4.72-4.55 ppm), polyether (3.5-3.0 ppm) and cyclic carbonate products (*cis*-CHC, 4.69-4.64 ppm; *trans*-CHC, 4.04-3.96 ppm). [c] Percentage of CHO consumed that yields CO_2 containing products. Determined by comparison of relative ^{1}H NMR integrals corresponding to polycarbonate and cyclic carbonate with polyether. [d] Selectivity for PCHC over cyclic carbonate, determined by comparison of relative ^{1}H NMR integrals. [e] Turnover number for polycarbonate production = number of moles of CHO consumed to yield polycarbonate products/ number of moles of catalyst. [f] Turnover frequency for polycarbonate production = TON_{PCHC} per unit time. [g] Determined by GPC, in THF, using narrow dispersity polystyrene standards. [h] Catalysis conditions: [Cat]:[PPNCl]:[CHD]:[CHO] = 1:1:2:1000, T = 80 °C, $p(CO_2)$ = 40 bar. [i] Catalysis conditions: [Cat]:[NOAc]:[CHO] = 1:2:1000, T = 100 °C.

Complex **5** was found to be unable to catalyse the ROCOP of CHO and CO_2 at 1 bar of CO_2 pressure, although when cocatalytic PPNCl was utilised the slow ($TOF_{cyclic\ carbonate}$ = 1.5 h^{-1}) formation of *cis*-cyclohexene carbonate (CHC) was observed (Table 2.5, Entries 1 and 2). At 40 bar CO_2 pressure, with PPNCl, no PCHC was formed, and instead both *cis*- and *trans*-CHC were observed (91% *cis*-CHC, 9% *trans*-CHC, Entry 3).

Concurrent with this work, our group reported that combining Co(III) with Group 1 Metals within a macrocyclic ligand framework resulted in active and selective catalysts for the ROCOP of epoxides and CO_2 (Figure 2.7).[25, 26] With this in mind, it was found that the addition of cocatalytic NaOAc resulted in the slow (TOF_{PCHC} *ca*. 3 h^{-1}), but selective (>99%), formation of PCHC (Table 2.5, Entries 4 - 6). This catalyst system remained active for up to 72 hours, although was observed to decompose after this point, as judged by a halt in further CHO consumption after 96 hours (Table 2.5, Entry 7). Carrying out the polymerisation at a higher temperature (100 °C) resulted in the expected increase in TOF_{PCHC} (14 h^{-1}), but also resulted in lower selectivity (90%) for PCHC, with *trans*-CHC being formed as a side product (Table 2.5, Entry 8).

The promotion of activity for CO_2/epoxide ROCOP in salen-type catalyst systems through addition of Group 1 Metal acetate cocatalysts has not previously been reported. In comparison to PPNCl, Group 1 Metal acetate complexes are both significantly cheaper and less toxic, and so efficient catalyst systems featuring these cocatalysts would be of significant interest. By analogy with the heterodinuclear cobalt/Group 1 Metal macrocyclic complexes, it is likely that the addition of a NaOAc leads to the formation of a heterodinuclear [$L_{van}CoNa(OAc)_2$] active species *in situ* (Figure 2.7).[25]

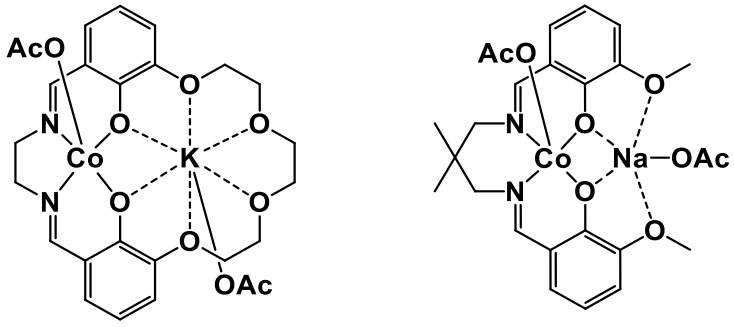


Figure 2.7. A heterodinuclear complex, [$LCoK(OAc)_2$] reported for CO_2/epoxide ROCOP (LHS) and the proposed dinuclear active species for the **5**/NaOAc catalyst system (RHS).

Following this initial result, different Group 1 metal acetates were trialled as cocatalysts in order to investigate whether this could yield more effective catalysts systems, in terms of both activity and catalyst stability (Table 2.6).

Table 2.6. Data for the ROCOP of CHO and CO_2 with **5**/MOAc catalyst systems.[a]

Entry	Cocat.[a]	Time (h)	Conv.[b] (%)	CO_2[c] (%)	Polym[d] (%)	TON_{PCHC}[e]	TOF_{PCHC}[f] (h^{-1})	$M_{n,\,GPC}$ [Đ][g] (kg mol^{-1})
1	KOAc	1	6.9	>99	95	66	66	3.0 [1.09]
2	KOAc	3	8.6	>99	95	82	27	3.5 [1.08]
3	RbOAc	1	11.5	>99	99	110	110	3.8 [1.08]
4	RbOAc	3	12	>99	98	120	40	3.9 [1.08]
5	CsOAc	1	3.5	>99	93	32	32	1.5 [1.15]
6	CsOAc	3	4.2	>99	84	35	15	1.6 [1.15]

[a] Catalysis conditions: [Cat]:[Cocat]:[CHO] = 1:2:1000, $p(CO_2)$ = 1 bar, T = 80 °C [b] Conversion of CHO, determined by comparison of relative ^{1}H NMR integrals of CHO (1.27-1.17 ppm) with the sum of the relative integrals of polycarbonate (4.72-4.55 ppm), polyether (3.5-3.0 ppm) and cyclic carbonate products (*cis*-CHC, 4.69-4.64 ppm; *trans*-CHC, 4.04-3.96 ppm). [c] Percentage of CHO consumed that yields polymeric products. Determined by comparison of relative ^{1}H NMR integrals corresponding to polycarbonate and cyclic carbonate products. [d] Selectivity for PCHC over cyclic carbonate, determined by comparison of relative ^{1}H NMR integrals. [e] Turnover number for polycarbonate production = number of moles of CHO consumed to yield polycarbonate products/ number of moles of catalyst. [f] Turnover frequency for polycarbonate production = TON_{PCHC} per unit time. [g] Determined by GPC, in THF, using narrow dispersity polystyrene standards.

It was found that variation of the Group 1 Metal acetate (MOAc) resulted in increased activities, but reduced lifetimes, of the catalytic species. In comparison to NaOAc, use of either KOAc or RbOAc, resulted in significant increases in TOF (67 h^{-1} and 110 h^{-1} respectively, Table 2.6, Entries 1 and 3). Further, excellent selectivities for PCHC over cyclic carbonate (>95%), and polyether linkages (>99%), were observed in both cases. An enhanced rate of catalyst decomposition, as determined by a distinct decrease in further CHO consumption after the 1 hour timepoint, was observed, however. (Table 2.6, Entry 1 *cf.* 2 for KOAc, and Entry 3 *cf.* 4 for RbOAc). When CsOAc was used as a cocatalyst, both lower TOFs (32 h^{-1}) and selectivities (93%) were observed compared to KOAc and RbOAc (Entry 5). Catalyst decomposition was again observed after 1 hour (Table 2.6, Entry 6).

In order to rule out catalyst decomposition occurring during the aliquoting process, the reaction with KOAc was repeated, and the conversion was measured after 3 hours, without any aliquoting. It was found that conversion was 9%, implying that the aliquoting process did not significantly affect catalyst decomposition. To ensure that complex **5** was thermally stable, it was heated for 20 hours at 100 °C in $CDCl_3$; comparison of the ^{1}H NMR spectra before and after this period showed no significant decomposition (Figure S2.26). It should also be noted that complex **5** is stable for at least 3 hours whilst polymerising the ROP of ε-DL (*vide supra*). From these results, it could be confirmed that this catalyst decomposition is unique to the **5**/MOAc systems, and not inherent to complex **5**.

In order to probe whether catalyst decomposition could be suppressed, the effect of temperature of the **3**/KOAc system was subsequently investigated (Table 2.7).

Table 2.7 Data for the ROCOP of CHO and CO_2 with **5**/KOAC at varied temperatures. [a]

Entry	Temp. (°C)	Time (h)	Conv.[b] (%)	CO_2[c] (%)	Polym.[d] (%)	TON_{PCHC}[e]	TOF_{PCHC} [f] (h^{-1})	$M_{n,\,GPC}$ [Đ][g] (kg mol^{-1})
1	60	1	6.7	>99	>99	67	67	4.7 [1.11]
2	60	3	6.7	>99	>99	67	27	4.8 [1.12]
3	40	1	1.3	>99	>99	13	13	1.6 [1.10]
4	40	3	4.4	>99	>99	44	15	3.5 [1.14]
5	40	6	4.4	>99	>99	44	7	3.8 [1.10]

[a] Catalysis conditions: [Cat]:[KOAc]:[CHO] = 1:2:1000, $p(CO_2)$ = 1 bar, T = 80 °C [b] Conversion of CHO, determined by comparison of relative ^{1}H NMR integrals of CHO (1.27-1.17 ppm) with the sum of the relative integrals of polycarbonate (4.72-4.55 ppm), polyether (3.5-3.0 ppm) and cyclic carbonate products (*cis*-CHC, 4.69-4.64 ppm; *trans*-CHC, 4.04-3.96 ppm). [c] Percentage of CHO consumed that yields polymeric products. Determined by comparison of relative ^{1}H NMR integrals corresponding to polycarbonate and cyclic carbonate products. [d] Selectivity for PCHC over cyclic carbonate, determined by comparison of relative ^{1}H NMR integrals. [e] Turnover number for polycarbonate production = number of moles of CHO consumed to yield polycarbonate products/ number of moles of catalyst. [f] Turnover frequency for polycarbonate production = TON_{PCHC} per unit time. [g] Determined by GPC, in THF, using narrow dispersity polystyrene standards.

Lowering the temperature to 60 °C saw an increase in selectivity for PCHC over *trans*-CHC (>99%) when compared to the equivalent polymerisation at 80 °C (Table 2.7, Entry 1). The TOF after 1 hour was found to be similar (67 h^{-1} for 60 °C compared to 69 h^{-1} for 80 °C) although, as observed previously, no further conversion was observed after 3 hours,

implying catalyst decomposition (Table 2.7, Entries 1 and 2). Although, typically, a decrease in temperature would be expected to yield a lower activity, in this case it is possible that this effect is counteracted by increased catalyst lifetimes at the lower temperature of 60 °C. In comparison, when the polymerisation is carried out at 40 °C, the expected decrease in TOF is observed (*ca.* 15 h^{-1}), but the catalyst remains active for 3 hours (Table 2.7, Entries 3 - 5). Despite the improved lifetimes, the significantly lower activity at this temperature means that overall TON of CHO is lower compared to results at higher temperatures.

This work demonstrates the possibility of *in situ* formation of heterodinuclear Co(III)/M(I) catalysts that are capable of catalysing the ROCOP of epoxides and CO_2. Unfortunately, and in contrast to the stable macrocyclic analogues, these catalyst systems display limited lifetimes under the reaction conditions investigated.[25, 26] For investigation of switchable catalysis featuring polycarbonates, the macrocyclic complexes would be the most suitable.

2.6 Conclusion and Outlook

A series of six monometallic complexes supported by a tetradentate *ortho*-vanillin derived ancillary ligands were synthesised and characterised. Subsequently, these complexes, alongside the commercial [SalcyCrCl], were investigated for the ROCOP of PA and CHO, ROP of ε-DL. Complexes **1** (Al) and **5** (Co) were found to be the most effective for the ROCOP of CHO and PA, and ROP ε-DL. Application of these complexes to switchable catalysis utilising these three monomers will be explored in Chapter 3.

Complex **5** was also applied to the ROCOP of CHO and CO_2. It was found to be inactive both by itself and with PPNCl, however, addition of group 1 metal acetate salts was found to result in active (TOF = 120 h^{-1}) and selective systems. Despite this promising discovery, the catalyst systems were found to be relatively unstable, resulting in low overall TONs. The application of this finding will be further explored in Chapter 4, with heterodinuclear complexes based on Al(III) instead of Co(III); complexes based on Al could be expected to be more stable owing to their lack of potential redox chemistry.

2.7 References for Chapter 2

1. T. Stößer, T. T. D. Chen, Y. Zhu and C. K. Williams, *Phil. Trans. R. Soc. A*, 2018, **376**, 20170066.
2. S. Paul, Y. Q. Zhu, C. Romain, R. Brooks, P. K. Saini and C. K. Williams, *Chem. Comm.*, 2015, **51**, 6459-6479.
3. O. Dechy-Cabaret, B. Martin-Vaca and D. Bourissou, *Chem. Rev.*, 2004, **104**, 6147-6176.
4. N. Ajellal, J. C. Carpentier, C. Guillaume, S. M. Guillaume, M. Helou, V. Poirier, Y. Sarazina and A. Trifonov, *Dalton Trans.*, 2010, **39**, 8363-8376.
5. G. L. Gregory, G. S. Sulley, L. P. Carrodeguas, T. T. D. Chen, A. Santmarti, N. J. Terrill, K.-Y. Lee and C. K. Williams, *Chem. Sci.*, 2020, **11**, 6567-6581.
6. A. Rae, A. J. Gaston, Z. Greindl and J. A. Garden, *Eur. Polym. J.*, 2020, **138**.
7. M. J. Stanford and A. P. Dove, *Chem. Soc. Rev.*, 2010, **39**, 486-494.
8. E. Hosseini Nejad, C. G. W. van Melis, T. J. Vermeer, C. E. Koning and R. Duchateau, *Macromolecules*, 2012, **45**, 1770-1776.
9. T. Stößer and C. K. Williams, *Angew. Chem. Int. Ed.*, 2018, **57**, 6337-6341.
10. C. B. Durr and C. K. Williams, *Inorg. Chem.*, 2018, **57**, 14240-14248.
11. B. A. Abel, C. A. L. Lidston and G. W. Coates, *J. Am. Chem. Soc.*, 2019, **141**, 12760-12769.
12. T. Stößer, Doctoral Thesis, University of Oxford, 2018.
13. S. Rayati, E. Khodaei, P. Nafarieh, M. Jafarian, B. Elmi and A. Wojtczak, *RSC Adv.*, 2020, **10**, 17026-17036.
14. A. Thevenon, J. A. Garden, A. J. White and C. K. Williams, *Inorg. Chem.*, 2015, **54**, 11906-11915.
15. A. W. Addison, T. N. Rao, J. Reedijk, J. van Rijn and G. C. Verschoor, *J. Chem. Soc., Dalton Trans.*, 1984, 1349-1359.
16. A. L. Gavrilova and B. Bosnich, *Chem. Rev.*, 2004, **104**, 349−383.
17. A. C. Deacy, University of Oxford, 2019.
18. W. Kläui, W. Eberspach and P. Gütlichl, *Inorg. Chem.*, 1987, **26**, 3977-3982.
19. N. J. Hair and J. K. Beattie, *Inorg. Chem.*, 1977, **16**, 245-250.
20. B. A. Abel, C. A. L. Lidston and G. W. Coates, *J. Am. Chem. Soc.*, 2019, **141**, 12760-12769.
21. M. E. Fieser, M. J. Sanford, L. A. Mitchell, C. R. Dunbar, M. Mandal, N. J. Van Zee, D. M. Urness, C. J. Cramer, G. W. Coates and W. B. Tolman, *J. Am. Chem. Soc.*, 2017, **139**, 15222-15231.

22. G. S. Sulley, G. L. Gregory, T. T. D. Chen, L. Pena Carrodeguas, G. Trott, A. Santmarti, K. Y. Lee, N. J. Terrill and C. K. Williams, *J. Am. Chem. Soc.*, 2020, **142**, 4367-4378.

23. M. T. Martello, D. K. Schneiderman and M. A. Hillmyer, *ACS Sustain. Chem. Eng.*, 2014, **2**, 2519-2526.

24. X. B. Lu and D. J. Darensbourg, *Chem. Soc. Rev.*, 2012, **41**, 1462-1484.

25. A. C. Deacy, E. Moreby, A. Phanopoulos and C. K. Williams, *J. Am. Chem. Soc.*, 2020, **142**, 19150-19160.

26. W. Lindeboom, D. A. X. Fraser, C. B. Durr and C. K. Williams, *Chem. Eur. J.*, 2021, **27**, doi.org/10.1002/chem.202101140.

Chapter 3

Monometallic complexes for the switchable catalysis of epoxides, anhydrides and lactones

Work described in this chapter appears in "*Ortho-vanillin derived Al(III) and Co(III) catalyst systems for switchable catalysis using ε-decalactone, phthalic anhydride and cyclohexene oxide*"

W. T Diment, T. Stößer, R. W. F. Kerr, A. Phanopoulos, C. B. Durr, C. K. Williams

Catal. Sci. Technol., 2021, **11**, 1737 - 1745

3.1 Introduction

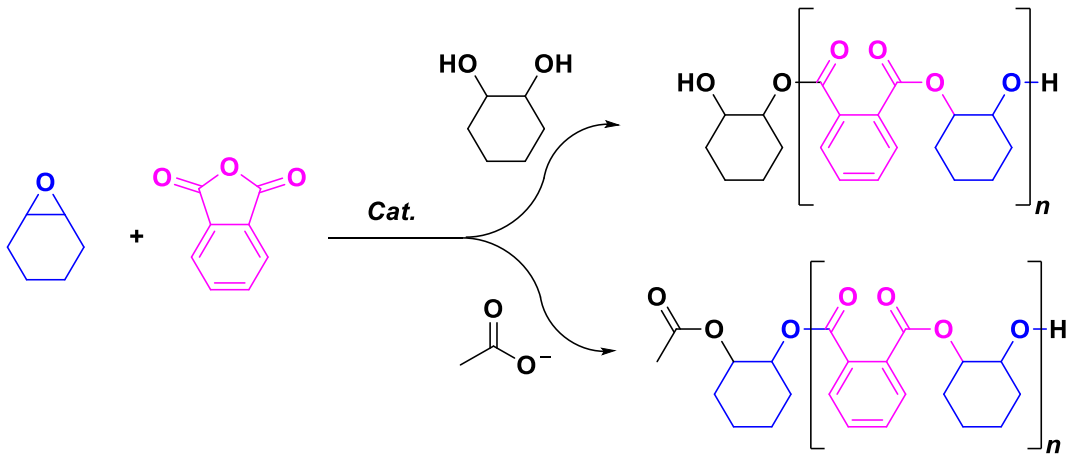
The synthesis of triblock copolymers *via* switchable catalysis presents a novel route to these materials.[1] A key target of this process is to access block copolymers with sufficient polymer molar masses in order to yield microphase-separated materials, which is essential in providing the enhanced material properties typically observed for block copolymers over polymer blends with equivalent compositions.[2] Despite this, many triblock copolymers synthesised previously *via* switchable catalysis are amorphous, block miscible, polyols with relatively low molar masses (*ca*. 10 kg mol^{-1}), and hence are unsuited to serving as materials with useful mechanical properties.[3-5] By utilising catalysts that display enhanced rates of catalysis, and tolerance for lower catalyst loadings, higher molar mass triblock copolymers can be effectively targeted.

3.2 Aims

The primary objective of the work in this chapter is to target the synthesis of triblock copolyesters with sufficiently high molar masses to observe microphase-separation. Hence, the application of complexes **1** and **5**, which showed high activities for both the ROCOP of CHO and PA, and ROP of ε-DL, to the 'one-pot' switchable catalysis of these monomers will be explored. Firstly, in order to achieve selective triblock synthesis, it will be necessary to optimise the amount of bifunctional chain transfer agent (CTA) used in the targeted catalyst systems. Following this, it will be established that these catalyst systems operate through the switchable catalysis mechanism, which is required to ensure efficient block copolymers formation. In order to target block copolymers with increasing molar mass, the catalyst systems will be tested under a series of lowered catalyst loadings. The application of complex **1** with a bifunctional cocatalyst will also be investigated, as it may provide access to triblock copolymers whilst requiring fewer equivalents of bifunctional CTA.

3.3 Chain Transfer Agent Optimisation

The selective synthesis of triblock copolymers *via* switchable catalysis requires a high degree of chain end control. Importantly, the initially formed polymer, which subsequently functions as a macroinitiator, must be telechelic in order to yield triblock copolymers (Scheme 3.1).



Scheme 3.1. Initiators determine which polymeric species are obtained. The synthesis of telechelic poly(cyclohexene phthalate) (PCHPE) is required to yield triblock copolymers, and is achieved using bifunctional initiating species such as cyclohexene diol (CHD, top). Monofunctional initiators, such as acetate (bottom) or chloride, yield monochelic PCHPE.

Hence, before complexes **1** and **5** were applied to the switchable catalysis of CHO, PA and ε-DL, it was necessary to optimise the amount of CTA required to yield monomodal polymer molar mass distributions consisting of majority telechelic α,ω-hydroxy terminated polymers. Whilst ensuring selectivity for hydroxy-terminated telechelic chains is essential for the successful synthesis of triblock copolymers, doing so with as few equivalents as possible of CTA is necessary if higher polymer molar masses are to be achieved. In previous work utilising a [SalcyCrCl]/PPNCl catalyst system, 15 equivalents of CHD were required to yield monomodal molar mass distributions of triblock copolymers, which contributed to the relatively low molar mass of the block copolymers obtained in this work.[5]

Given that in previous reports, from a one-pot mixture of a ε-DL, CHO, and PA, epoxide/anhydride ROCOP occurs before lactone ROP, this optimisation was carried out for the former polymerisation (Figure 3.1 (**1**) and S3.1 (**5**)) [6, 7]

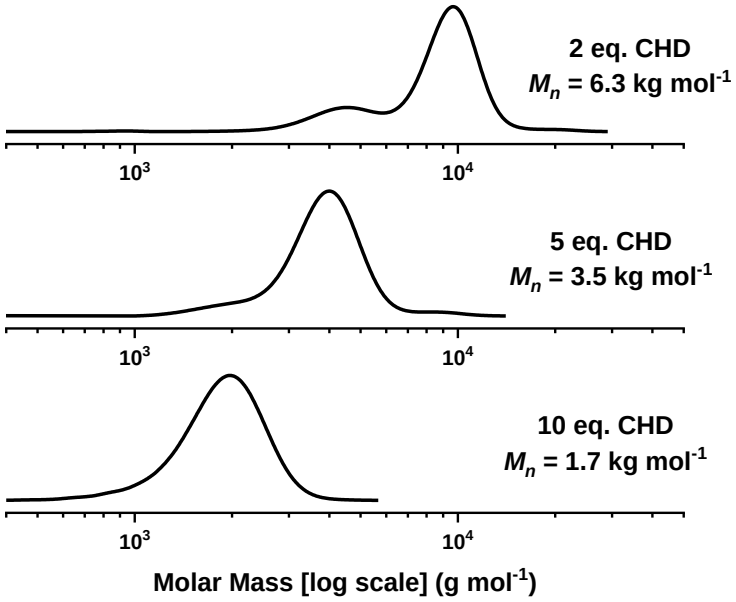


Figure 3.1. GPC traces of of PCHPE obtained with complex **1**/PPNCl at full PA conversion. 10 equivalents of CHD are necessary to yield monomodal molecular weight distributions. Catalysis conditions: [**1**]:[PPNCl]:[CHD]:[PA]:[CHO] = 1:1:*x*:100:500, 100 °C.

For both complexes **1** and **5**, the bimodality of the polymer molar mass distributions was partially supressed with 5 equivalents of CHD, whilst 10 equivalents were required to yield monomodal distributions. The addition of increasing equivalents of CHD also resulted in the expected decrease in polymer molar mass. Analysis of the PCHPE obtained with 10 equivalents of CHD *via* MALDI-ToF spectrometry confirmed that the end groups were the desired telechelic α,ω-hydroxy-end capped polymers (Figure 3.2 (**1**) and S3.2 (**5**)).

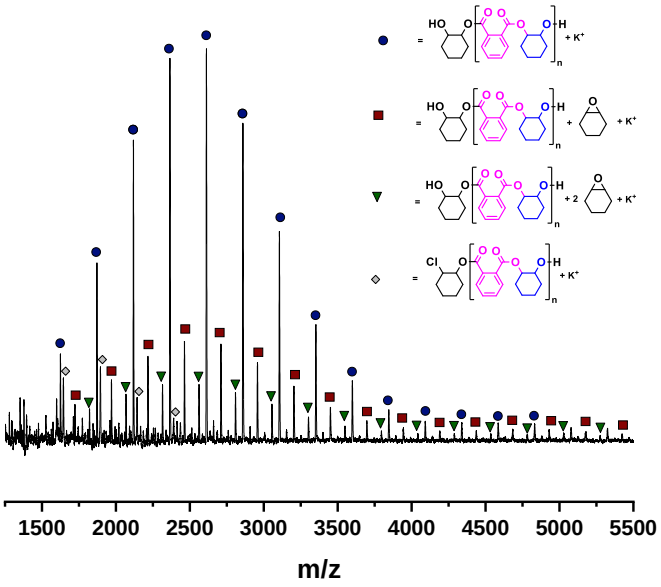
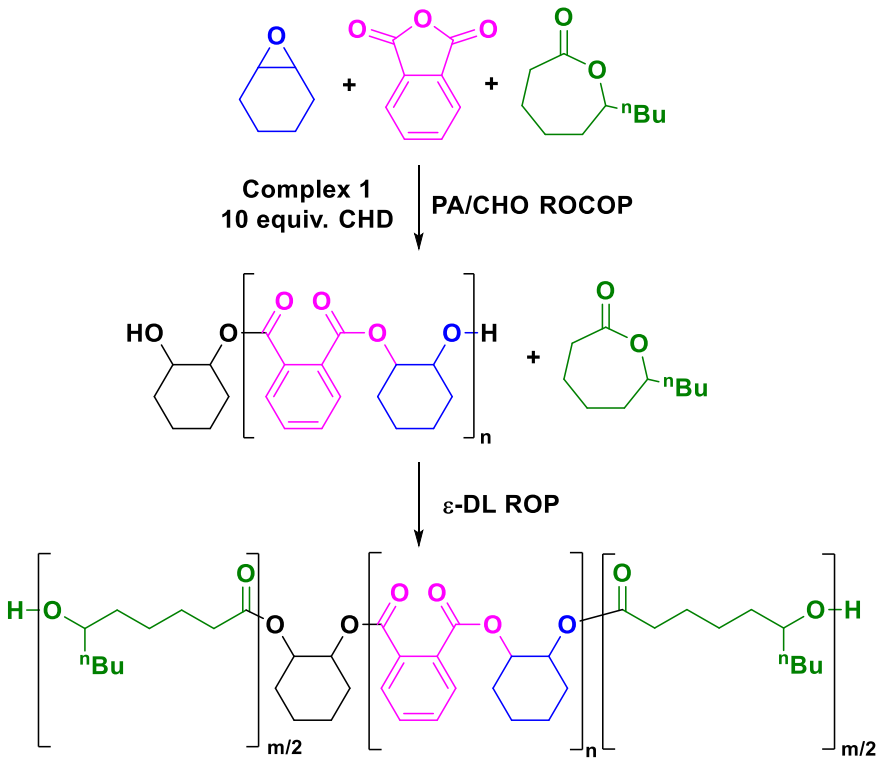


Figure 3.2. MALDI-ToF spectrum of PCHPE obtained with complex **1**/PPNCl and 10 equivs. of CHD.

A minor impurity of α-chloro-ω-hydroxy (and, when complex **5** was used, α-acetate-ω-hydroxy) terminated polymers could also be observed in the tail of the distributions. As both systems contain at least 1 equivalent of a monofunctional initiator, owing to the use of PPNCl, minor monochelic impurities will always be present. Nevertheless, it was demonstrated that for both catalyst systems, effective end group control could be obtained, which should lead to triblock copolymers when applied to switchable catalysis.

3.4 Switchable Catalysis from a One-Pot Mixture of CHO, PA, and ε-DL

Following this initial optimisation study, complex **1** was applied to the one-pot reaction of PA, CHO and ε-DL using 10 equivalents of CHD to test whether these novel catalysts systems could operate *via* the switchable catalysis mechanism (Scheme 3.2).



Scheme 3.2. One pot reaction of CHO, PA and ε-DL to yield triblock copolymers. Typical conditions: [**1**]:[PPNCl]:[CHD]:[PA]:[DL]:[CHO] = 1:1:10:100:200:500, T = 100 °C.

By monitoring the reaction in a Schlenk flask fitted with an *in situ* ATR-IR probe it was found, consistent with previous reports, that the ROCOP of CHO and PA proceeded first, and then latterly ε-DL ROP occurred (Figure 3.3).[5, 8, 9]

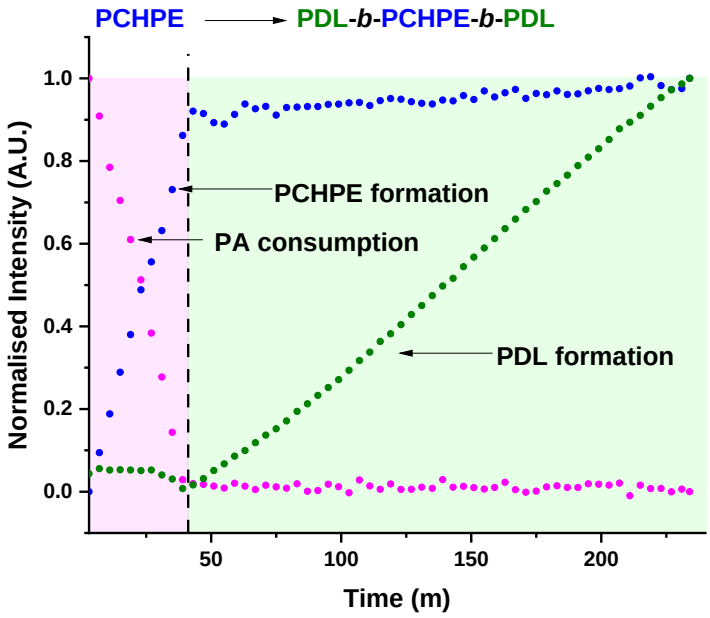


Figure 3.3. Data collected using ATR-IR spectroscopy illustrating switchable catalysis. Conditions: [**1**]:[PPNCl]:[CHD]:[PA]:[DL]:[CHO] = 1:1:10:100:200:650, T = 100 °C.

In the first stage of the reaction selective formation of PCHPE can be observed (1582 cm $^{-1}$), with concurrent consumption of PA (1856 cm^{-1}). Following full consumption of the PA monomer, formation of PDL is subsequently observed (1231 cm^{-1}; *n.b.* the intensity of this absorption increases for both PCHPE formation and PDL formation due to band overlap. The latter increase in intensity of this band can be assigned to PDL formation as other bands associated with PCHPE formation (*e.g.* 1582 cm^{-1}) do not grow in intensity during the same time period).

To further confirm the chemoselective reactivity, aliquots of the reaction were analysed by ^{1}H NMR spectroscopy and GPC. GPC analysis of the aliquots showed that a single, monomodal, polymer molar mass distribution was observed throughout the course of the reaction (Figure 3.4). Consistent with the results of *in situ* IR monitoring, ^{1}H NMR spectroscopy demonstrated that consumption of PA (and CHO) occurred first, with ε-DL subsequently being consumed (Figure S3.3). Collectively, these results demonstrate that the PCHPE formed initially in the one-pot reaction is able to function as a macroinitiator for the

ROP of ε-DL, implying that formation of block copolymers occurs, as opposed to the formation of a mixture of two homopolymers.

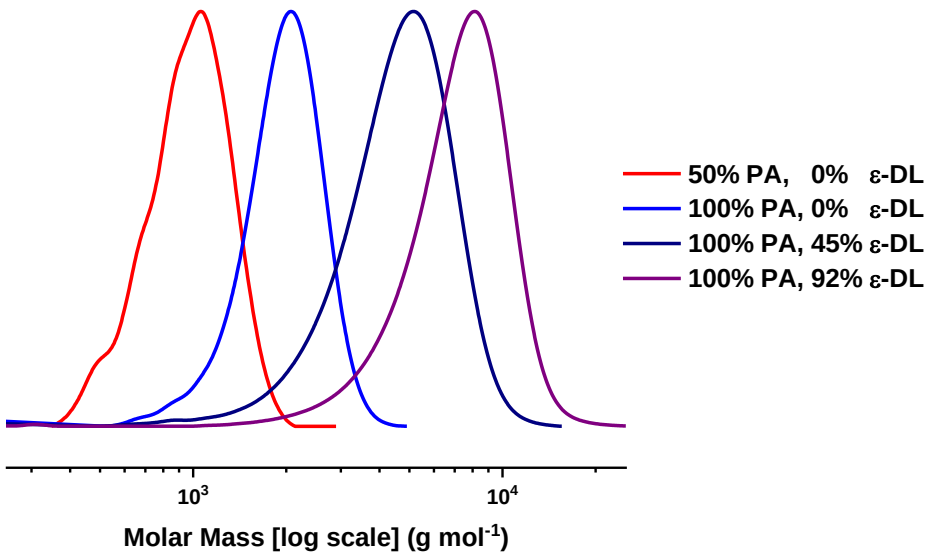


Figure 3.4. GPC traces of triblock copolymers obtained from aliquots taken during switchable catalysis with complex **1**. Percentage conversions of monomers determined by ^{1}H NMR spectroscopy of aliquots taken from the reaction mixture.

Isolation of the polymer, *via* precipitation from methanol, allowed for further analysis. Reaction of the hydroxyl polymer chain end groups with a phosphorus reagent allows for characterisation of the end group *via* $^{31}P\{^{1}H\}$ NMR spectroscopy (See Chapter 7 for experimental details).[10] Comparison of the $^{31}P\{^{1}H\}$ resonances observed for the block copolymer to that obtained when the equivalent test is performed on both PCHPE and PDL homopolymers showed that only PDL end groups are present in the triblock copolymer synthesised. This confirms efficient initiation by the PCHPE initially synthesised from the one-pot mixture, and further supports the selective synthesis of PDL-*b*-PCHPE-*b*-PDL copolymers (Figure 3.5).

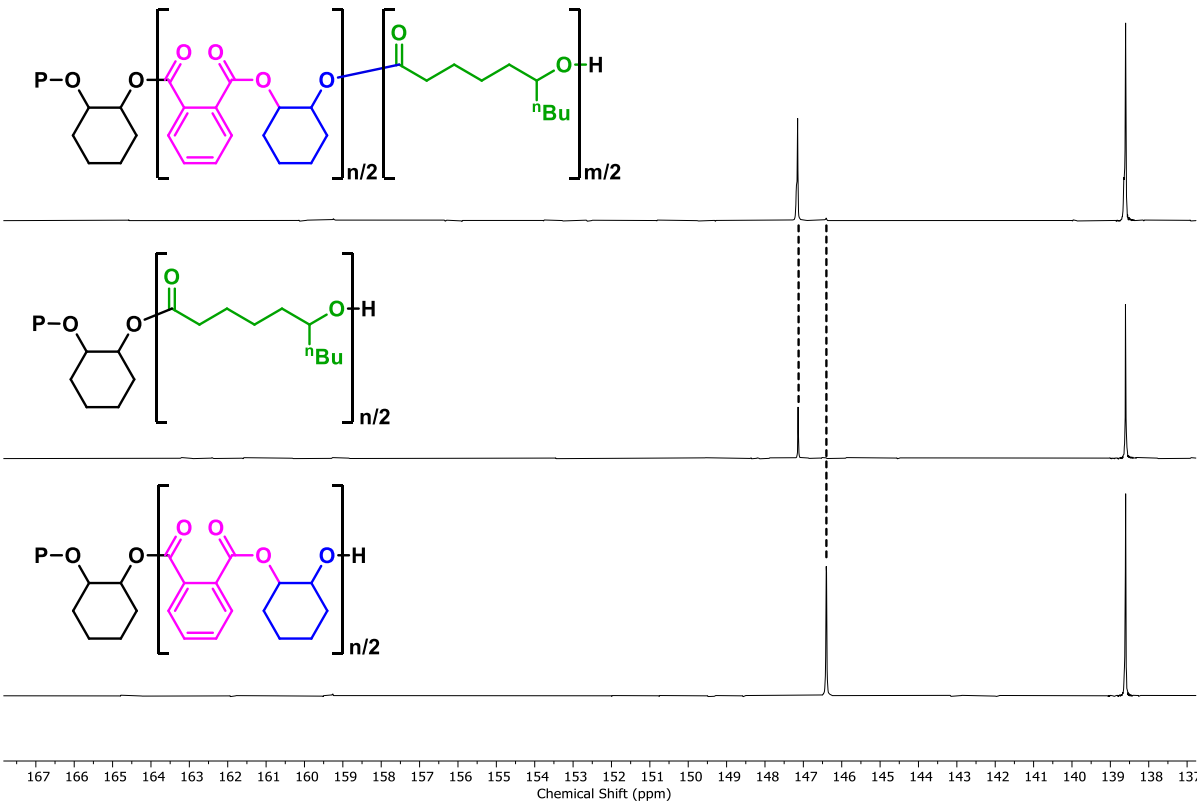


Figure 3.5. $^{31}P\{^{1}H\}$ NMR spectra of (from top to bottom) PDL-*b*-PCHPE-*b*-PDL, PDL and PCHPE, showing that only PDL end groups are present in the triblock copolymer.

Further analysis of the triblock copolymer by ^{1}H DOSY confirmed that all signals observed in the ^{1}H NMR spectrum of the polymer possessed the same diffusion coefficient, and so could be assigned to the same polymeric species (Figure S3.4). It has previously been demonstrated that a mixture of PDL and PCHPE homopolymers of similar molar masses display two separate diffusion coefficients.[8]

Taken together, these results are consistent with the catalysts operating through the previously reported 'switch' mechanism, and that selective synthesis of triblock copolymers is being achieved.

3.5 Synthesis of High Molar Mass Triblock Polyesters

Following this initial investigation, complexes **1** and **5** were subsequently applied to the switchable catalysis of PA, CHO and ε-DL at a range of different catalyst loadings in order to access triblock copolymers of increasing molar masses (Table 3.1).

Table 3.1. Data for switchable polymerisations of CHO, PA and ε-DL utilising complexes **1** and **5**.[a]

Entry	Catalyst	Loading (%)	[CHD]	Time (h)	Conv. (PA, DL)[b] (%)	$M_{n,\,GPC}$ [Đ][c] (kg mol^{-1})	T_g[d] (°C)
1	**1**	1	10	2	100, 94	6.5 [1.16]	-26
2	**5**	1	10	4.5	100, 96	6.3 [1.16]	*N.d.*
3	[SalcyCrCl][d]	0.5	15	>24	100, 100	6.2 [1.20]	*N.d.*
4	**1**	0.2	10	7	100, 93	33.0 [1.14]	-51
5	**1**	0.1	10	18	100, 92	57.1 [1.07]	-50
6	**1**	0.1	15	18	100, 90	42.8 [1.07]	*N.d.*

[a] Catalysis conditions: [Cat]:[PPNCl]:[CHD]:[PA]:[DL]:[CHO] = 1:1:10:x:y:z, where [PA]:[DL]:[CHO] = 1:2:5 and x is given as loading, T = 100 °C. [b] Determined by comparison of relative ^{1}H NMR integrals of resonances corresponding to the respective monomer and polymer unit (See Chapter 2). [c] Determined by GPC, in THF, using narrow dispersity polystyrene standards. [d] Catalysis conditions: [Cat]:[PPNCl]:[CHD]:[PA]:[DL]:[CHO] = 1:1:15:200:200:250, 2.2 mL Toluene, 100 °C.[5] [d] Determined by DSC.

At catalyst loadings of 1 mol% *vs*. anhydride, it was found that complex **1** reached complete monomer conversion significantly faster than complex **5** (Table 3.1, Entries 1 *cf*. 2). This was attributed to the significantly higher TOF for ε-DL ROP observed for complex **1** (see Chapter 2). Despite this, the time taken for both novel complexes to reach polyesters with a molar mass of *ca.* 6 kg mol^{-1} marks a significant improvement on that previously reported by our group when utilising the commercial [SalcyCrCl] catalyst system, where over 24 hours were required (Table 3.1, Entry 3).[5]

Following this, utilising the more active complex **1,** the catalyst loading was sequentially reduced from 1% to 0.2% and 0.1% (Table 3.1, Entries 4 and 5). The catalyst system remained active under these challenging conditions, allowing access to triblock copolymers of weights up to 57.1 kg mol^{-1}, whilst maintaining low dispersities and monomodal molar

mass distributions (Figure 3.6). Further, by increasing the equivalents of chain transfer agent utilised, a polymer of 42.8 kg mol^{-1} could be obtained over the same time period, allowing for tuning of the polymer molar masses obtained (Table 3.1, Entry 6).

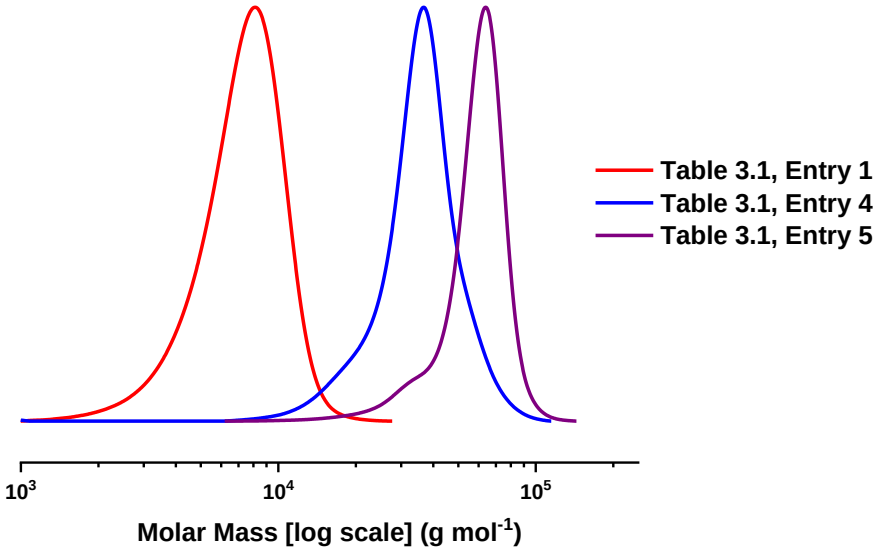


Figure 3.6. GPC traces of of PDL-*b*-PCHPE-*b*-PDL prepared with complex **1**, corresponding to Table 3.1, Entries 1, 4 and 5. Measured by GPC at 30 °C with THF eluent.

The polymer obtained from the reaction at 0.1% *vs*. anhydride catalyst loading displayed a minor low molar mass shoulder. Analysis of aliquots of PCHPE formed in the initial stages of this polymerisation through MALDI-ToF revealed that both α-chloro-ω-hydroxy- and α,ω-hydroxy-end capped PCHPE were present (Figure S3.5). A secondary monochelic species of α-cyclohexanol-ω-hydroxy-PCHPE was also observed, which arises from mono-cyclohexanol impurities that are often present in CHO.[11] These monochelic homopolymers subsequently lead to both di- and triblock copolymers being present in the final polymeric product, albeit with only ~5 Wt.% of the former species.

Previous monometallic catalysts reported for these polymerisations frequently struggle to access block copolymers with molar masses > 30 kg mol^{-1}, owing to both low TOFs for one or both of the component polymerisations and high equivalents of CTA needed to yield

monomodal polymer molar mass distributions.[4, 5, 12] It has been demonstrated that, for block polymers consisting of PCHPE and PDL, molar masses in excess of 30 kg mol^{-1} are required to yield full phase separation of the different blocks.[6, 9] Complex **1** is capable of tolerating loadings of up to 0.1% *vs.* anhydride and 0.02% *vs.* epoxide, whilst still delivering the high TOFs observed for higher loadings, allowing access to higher molar mass polymers.

Thus, to confirm that the block polyesters synthesised were phase separated, the triblock copolymers synthesised in Table 3.1, Entries 1, 4 and 5, were analysed by DSC to investigate whether two separate glass transition temperatures (T_g) could be observed, which is indicative of phase separation of the polymer (Figure 3.7).

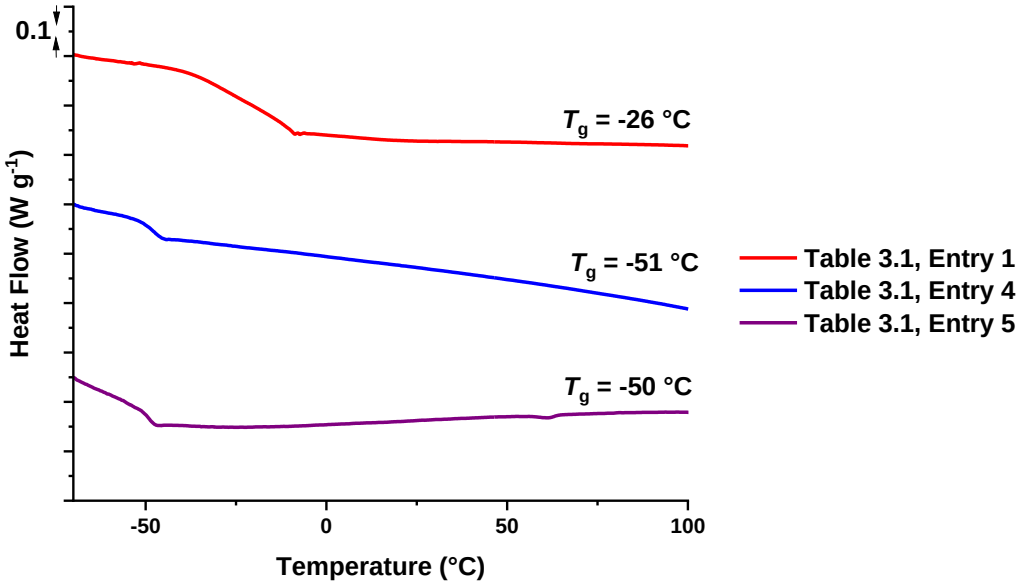


Figure 3.7. DSC plots of triblock copolymers corresponding to Table 3.1, Entries 1, 4 and 5.

In all cases, a lower T_g that could be assigned to the PDL 'soft' block was observed, although no upper glass transition was observed. The difficulty in observing a T_g that can be assigned to PCHPE in triblock copolymers *via* DSC has been previously reported.[8] The lowest molar mass triblock copolymer (6 kg mol^{-1}) displayed a T_g of -25 °C, suggesting it was not fully phase separated (Table 3.1, Entry 1). In comparison, the two higher molar mass polymers (33.0 kg mol^{-1} and 57.1 kg mol^{-1}) displayed T_gs of -50 °C and -51 °C, respectively, consistent

with the T_g (-51 °C) reported for the PDL homopolymer (Table 3.1, Entries 4 and 5).[13] These results suggest that, whilst the lowest weight triblock copolymer is amorphous, the higher weight samples are phase separated, emphasising the need to access high weight triblock copolymers in order to attain improved mechanical properties.[14, 15]

3.6 A Bifunctional PPN-based Cocatalyst

The use of PPNCl as a cocatalyst results in formation of monofunctional alkoxide initiators, which, in combination with residual mono-alcohol impurities, results in bimodal polymer molar mass distributions (*vide supra*). As a result, if triblock copolyesters are to be selectively obtained, multiple equivalents of CHD are typically required to suppress initiation by these monofunctional species, in turn leading to lower polymer molar masses for a given catalyst loading.

In order to reduce the amount of CHD used to obtain selective synthesis of telechelic α,ω-hydroxy-terminated polymers, use of a bifunctional initiating cocatalyst was targeted. Recently, Coates and co-workers reported use of a bifunctional cocatalyst, PPN_2ADC (ADC = 1,3-adamantine dicarboxylate), in conjunction with a non-initiating aluminium salen catalyst to synthesise a range of polyesters *via* ROCOP of epoxides with anhydrides.[16] Polyesters with monomodal molar mass distributions up to 20 kg mol^{-1} were obtained with only 2 equivalents of a bifunctional CTA. These systems were not applied to lactone ROP, nor switchable catalysis.

In order to develop a system suitable for application to switchable catalysis, the PPN-based salt PPN_2PA (PA = phthalate) was targeted, as it was hypothesised that the phthalate dianion would be able to ring open CHO, given its similarity to the propagating phthalate species present in the ROCOP of CHO and PA. Synthesis of PPN_2PA was achieved through addition of K_2PA to a solution of PPNCl in water at 80 °C, which resulted in the precipitation of

PPN_2PA as a white powder (See Chapter 7 for experimental details, Figures S3.6 – S3.7 for associated spectra).

Catalyst **1** was selected for use with this novel cocatalyst, as it does not possess an initiating coligand. The ROCOP of PA and CHO and ROP of ε-DL by **1** with PPN_2PA was subsequently investigated under identical conditions to those utilised for **1** with PPNCl (Table 3.2).

Table 3.2. Data for the ROCOP of CHO and PA, and ROP of ε-DL, using complex **1** with PPN_2PA.[a]

Entry	Mon.	Time (min)	Conv.[b] (%)	TON[c]	TOF[d] (h^{-1})	M_n [Đ][e] (kg mol^{-1})	$M_{n,\ Theory}$[f] (kg mol^{-1})
1	PA	5	77	77	924	4.5 [1.23]	8.2
2	DL	180	79	158	53	12.3 [1.09]	17.0

[a] Catalysis conditions: [**1**]:[PPN_2PA]:[CHD]:[Mon]:[CHO] = 1:1:2:x:500, where x = 100 for PA and 200 for ε-DL, T = 100 °C. [b] Determined by relative ^{1}H NMR integrals of respective monomer and polymer. [c] TON (turnover number) = Number of moles of monomer consumed/number of moles of catalyst. [d] TOF (turnover frequency) = TON per unit time. [e] Determined by SEC, in THF, using narrow dispersity polystyrene standards. [f] Theoretical M_n values. Determined through (TON*M_n(Repeat Unit))/ (Number of equivalents of CHD + Number of equivalents of PPN_2PA) for Entry 1 and (TON*M_n(Repeat Unit))/ (Number of equivalents of CHD) for Entry 2 (*vide infra*).

In comparison to the polymerisations where PPNCl was used, PPN_2PA resulted in a higher activity (TOF = 924 h^{-1}) and equivalent selectivity for polyester linkages (>99%) for the ROCOP of PA and CHO (Table 3.2, Entry 1 *cf.* Table 2.1, Entry 1). A reduced activity for the ROP of ε-DL (TOF = 53 h^{-1}) was obtained, however (Table 3.2, Entry 2 *cf.* Table 2.4, Entry 1). This increased activity for ROCOP of PA and CHO is possibly due to the presence of 2 equivalents of the $[PPN]^+$ cation present for each equivalent of PPN_2PA. The suppression of ε-DL ROP activity was unexpected but could be due to competition between the phthalate dianion and ε-DL binding to the catalyst. Analysis of the PDL produced in this reaction *via* MALDI-ToF spectroscopy showed no incorporation of the PA moiety within the end group of the PDL obtained in these reactions, implying it was not involved with the initiation, and so was likely present throughout the reaction (Figure S3.8).

In comparison to the polymers obtained when PPNCl was used as a cocatalyst, no low weight shouldering in the polymer molar mass distributions of either PCHPE or PDL was observed, demonstrating that effective end group control could be obtained with only 2 equivalents of CHD (Figure (PCHPE) and Figure S3.9 (PDL)).

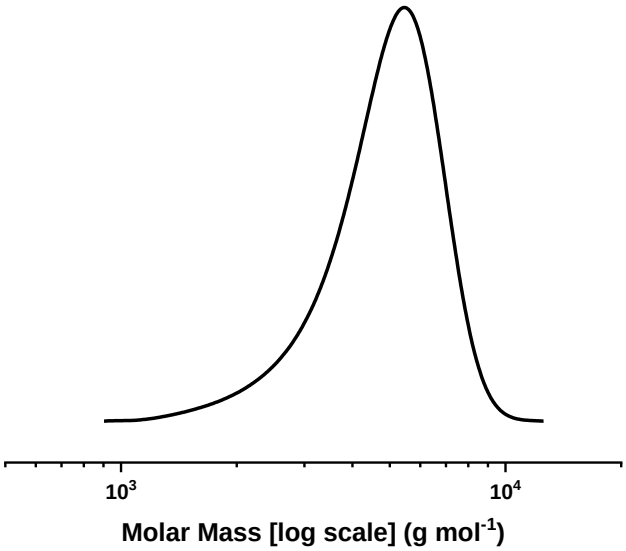


Figure 3.8. GPC trace of PCHPE corresponding to Table 3.2, Entry 1.

MALDI-ToF spectroscopy of the PCHPE confirmed that the majority of the polymeric species were α,ω-hydroxy-end capped (Figure S3.10). Minor series of both α-chloride-ω-hydroxy- and α-cyclohexanol-ω-hydroxy-end capped PCHPE were also observed but were effectively suppressed by the CHD added, as evidenced by the obtained GPC trace.

The presence of the minor α-chloride-ω-hydroxy-end capped series revealed that chloride anions were still present in the catalyst system, albeit in a far reduced quantity. The cocatalyst, PPN_2PA, which was synthesised from PPNCl, was subsequently tested by anion chromatography for chloride anions, revealing a 65.2 ppm w/w chloride impurity. Despite this minor impurity, the ability of this catalyst system to obtain monomodal polymer molar

mass distributions of PCHPE and PDL with 2 equivalents of CHD marks a significant improvement over the 10 equivalents of CHD required when PPNCl is used as a cocatalyst.

Subsequently, the novel bicomponent catalyst system was applied to the one pot reaction of PA, CHO and ε-DL, in order to investigate whether higher molar mass triblock copolymers could be obtained in comparison to those synthesised with the **1**/PPNCl catalyst system (Table 3.3).

Table 3.3. Data for switchable polymerisations of CHO, PA and ε-DL utilising complex **1** with PPNCl and PPN_2PA.[a]

Entry	Cocat.	Loading (%)	[Cat]:[CHD]	Time (h)	Conv. (PA, DL)[b] (%)	$M_{n,\,GPC}$ [Đ][c] (kg mol^{-1})
1	PPN_2PA	1	2	3	100, 93	15.6 [1.18]
2	PPNCl	1	10	2	100, 94	6.5 [1.16]
3	PPN_2PA	0.2	2	20	100, 97	35.9 [1.23]

[a] Catalysis conditions: [**1**]:[PPNCl]:[CHD]:[PA]:[DL]:[CHO] = 1:1:2:*x*:*y*:*z*, where [PA]:[DL]:[CHO] = 1:2:5 and *x* is given as loading, T = 100 °C. [b] Determined by comparison of relative ^{1}H NMR integrals of resonances corresponding to the respective monomer and polymer unit (*vide supra*). [c] Determined by SEC, in THF, using narrow dispersity polystyrene standards.

When using PPN_2PA it was found that, for a given catalyst loading, higher polymer molar masses were obtained when compared to reactions using PPNCl, owing to the fewer equivalents of CHD required to yield monomodal distributions when the former is used (Table 3.3, Entry 1 *cf.* 2). Longer reaction times were observed, however, owing to the suppression of catalyst activity for ε-DL ROP by PPN_2PA. When the catalyst loading is reduced to 0.2 mol% *vs*. anhydride, a significant low weight shouldering is observed in the polymer molar mass distribution (Table 3.3, Entry 3 and Figure S3.11). This is attributed to both the aforementioned residual PPNCl and monofunctional alcohol impurities present in CHO.[11] For a given catalyst loading, the effect of impurities on the polymer molar mass distributions is more pronounced in reactions where fewer equivalents of CTA are used, as impurities make up a greater proportion of the initiating species. As a result, although this cocatalyst provides a superior alternative for targeting higher weight molecular weight

triblock copolymers at high catalyst/cocatalyst loadings (1% *vs.* anhydride), when the loading is reduced this advantage is lost, and, owing to the suppression of ε-DL ROP activity by PPN_2PA, use of PPNCl is more effective.

3.7 Discussion

In order to assess the effectiveness of the monometallic catalyst systems developed here, it is important to compare the results obtained with a range of catalysts have been reported for switchable catalysis in the literature (Figure 3.9). Where possible, examples using the same monomers and reactions temperatures are used as altering these would be expected to have a significant impact on overall catalytic activity. To aid in this comparison, the measure of M_n / hour (kg mol^{-1} h^{-1}) is introduced as the selective production of block copolymers requires both high catalytic activity and good end group control.

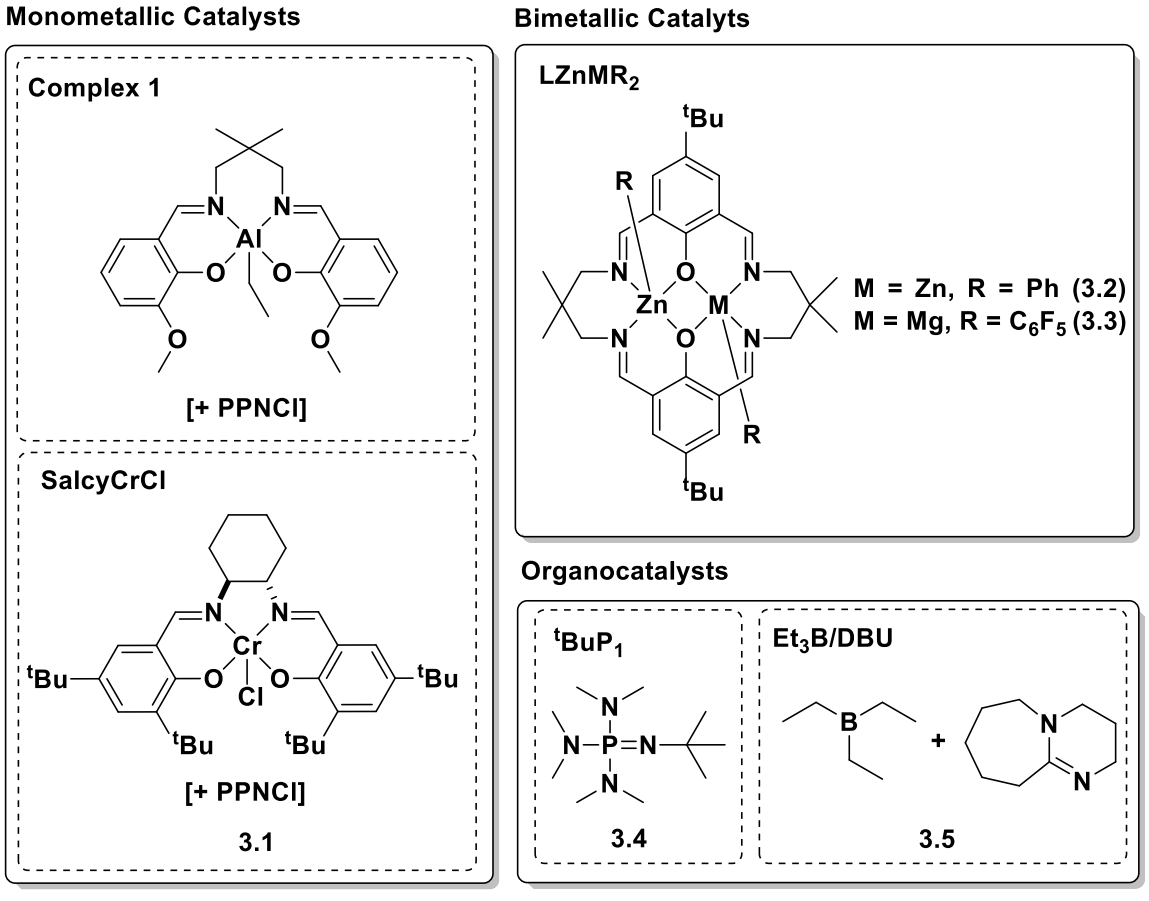


Figure 3.9. Catalysts reported for switchable catalysis of epoxides, anhydrides and lactones.

Table 3.4. Data for catalysts applied to the switchable catalysis of epoxides, anhydrides and lactones.

Entry	Catalyst[a]	Monomers	Temp (°C)	Time (h)	$M_{n,\,GPC}$ [Đ][b] (kg mol^{-1})	$M_{n,\,GPC}$ / hour[c] (kg mol^{-1} h^{-1})
1[d]	**1**/PPNCl	CHO/PA/DL	100	18	57.1 [1.07]	3.2
2[e]	[SalcyCrCl]/PPNCl (**3.1**)	CHO/PA/DL	100	>24	6.2 [1.20]	0.26
3[f]	[LZn_2Ph_2] (**3.2**)	CHO/PA/DL	100	4	34.6 [1.19]	6.2
4[g]	[$LZnMg(C_6F_5)_2$] (**3.3**)	CHO/PA/DL	80	36	108 [<1.10]	3
5[h]	$^tBuP_1$ (**3.4**)	CHO/PA/LA	100	8	6.6 [1.18]	0.83
6[i]	Et_3B/DBU (**3.5**)	PO/PA/DL	60	3	6.4 [1.12]	2.1

[a] Representative conditions as reported for each catalyst. [b] As reported under conditions described in respective literature. [c] Molar mass of block polymer per unit time. [d] [1]:[PPNCl]:[CHD]:[CHO]:[PA]:[DL] = 1:1:10:5000:1000:2000. [e] [SalcyCrCl]: [SalcyCrCl]:[PPNCl]:[CHD]:[CHO]:[PA]:[DL] = 1:1:15:250:200:200, 2.2 mL Toluene.[5] [f] [LZn_2Ph_2]:[CHD]:[CHO]:[PA]:[DL] = 1:2:800:100:100.[9] [g] [$LZnMg(C_6F_5)_2$]:[1,4-BDM]:[CHO]:[PA]:[DL] = 1:4:1050:700:1500.[8] [h] [$^tBuP_1$]:[BDM]:[CHO]:[PA]:[LA] = 1:2:500:100:100.[17] [i] [Et_3B]:[DBU]:[CTA]:[PO]:[PA]:[LA] = 3:1:5:500:100:100.[18]

Complex **1** shows good activity for switchable catalysis using CHO, PA and ε-DL, yielding triblock PDL-*b*-PCHPE-*b*-PDL copolymers with molar masses of 57.1 kg mol^{-1} in 18 hours (an M_n / hour of 3.2 kg mol^{-1} h^{-1}) (Table 3.4, Entry 1). It significantly outperforms the [SalcyCrCl] catalyst system (**3.1**), which has an activity of 0.26 kg mol^{-1} h^{-1} for the same triblock copolymer (Table 3.4, Entry 2).[5] This is attributed to the 110-fold increase in activity that complex **1** displays for the ROP of ε-DL over **3.1** (TOF = 330 h^{-1} and 3 h^{-1}, respectively, 0.5% *vs.* lactone, T = 100 °C). Both catalysts require excess equivalents of a bifunctional CTA (10 for complex **1** and 15 for [SalcyCrCl]) to yield selective triblock formation, on account of their initiating coligands and use of cocatalyst (PPNCl), however.

Emphasising the advantages of good end group control, one of the best performing catalysts is a homodinuclear [LZn_2Ph_2] complex (**3.2**), which bears non-initiating organometallic coligands. These coligands are readily protonated by bifunctional protic CTAs, generating bifunctional alkoxide initiating species. As a result, complex **3.2** could achieve selective

formation of triblock PDL-*b*-PCHPE-*b*-PDL with only 2 equivalents of CHD at a rate of 6.2 kg mol^{-1} h^{-1} (Table 3.4, Entry 3).[6, 9] This high rate is obtained in spite of the lower activity of **3.2** for both the ROCOP of PA and CHO (TOF = 25 h^{-1}, 1% *vs*. anhydride, T = 100 °C) and ROP of ε-DL (TOF = 160 h^{-1}, 0.5% *vs*. lactone, T = 100 °C) when compared to complex **1**.[6] With complex **3.2**, triblock polyesters obtained had molar masses of 34.6 kg mol^{-1} and required chain extension to yield multiblock copolymers of 56.6 kg mol^{-1}. In comparison, complex **1** is able to achieve triblock copolymers of equivalent molar masses without chain extension, owing to its good loading tolerance and higher catalytic activity, demonstrating one potential advantage of the use of complex **1**.

Recently, Williams and co-workers reported the heterodinuclear [$LZnMg(C_6F_5)_2$] complex (**3.3**) which, similar to **3.2** featured non-initiating coligands that could be protonated by bifunctional CTAs.[14, 15] Complex **3.3** was hence capable of accessing triblock PCHPE-*b*-PDL-*b*-PCHPE with molar masses of up to 108 kg mol^{-1}, at a rate of 3 kg mol^{-1} h^{-1}, a similar activity to that obtained with complex **1** (Table 3.4, Entry 4).

Organocatalysts have also been applied to switchable catalysis, including $^tBuP_1$ (**3.4**) and Et_3B/DBU (**3.5**). In the former case, triblock copolymers of PLA-*b*-PCHPE-*b*-PLA were obtained from one-pot mixtures of LA, CHO and PA at a rate of 0.83 kg mol^{-1} h^{-1} (Table 3.4, Entry 5).[17] Similar to the dinuclear complexes bearing non-initiating organometallic coligands, **3.4** is non-initiating and functions without a cocatalyst and so can achieve selective triblock formation with only 2 equivalents of 1,4-benzene dimethanol. However, its relatively low activities for the ROCOP of CHO and PA (TOF = 30 h^{-1}, 1% *vs*. anhydride, T = 100 °C) and ROP of LA (TOF = 10 h^{-1}, 1% *vs*. lactide, T = 100 °C) prevent the faster formation of triblock copolymers. The application of **3.5**, with a chain transfer agent possessing a functional chain end-group, to the one pot reaction of LA, PO, PA and methyl methacrylate (MMA) resulted in the efficient production of diblock P(PO-*alt*-PA)-*b*-PLA

that was concurrently used as a macroinitiator for the RAFT polymerisation of MMA, yielding PMMA-*b*-P(PO-*alt*-PA)-*b*-PLA.[18] A relatively high activity for formation of the polyester diblock polymer was obtained (2.1 kg mol^{-1} h^{-1}, Table 3.4, Entry 6).

3.8 Conclusion and Outlook

Two novel monometallic complexes, **1** and **5**, in conjunction with cocatalytic PPNCl, were applied to the one pot reaction of PA, CHO and ε-DL, yielding triblock copolymers *via* switchable catalysis. Complex **1** was found to be the most active owing to its high activity for the ROP of ε-DL (TOF = 330 h^{-1}, 0.5% *vs.* lactone, T = 100 °C) and was subsequently applied to the synthesis of triblock copolymers with molar masses of up to 57.1 kg mol^{-1}. The use of a bifunctional cocatalyst, PPN_2PA, in conjunction with complex **1**, was also explored. With this catalyst system, at 1% *vs.* anhydride loading, selective synthesis of triblock copolymers with only 2 equivalents of CHD was possible. However, when the catalyst loading of this system was reduced to 0.2% *vs*. anhydride, a low molar mass shouldering consisting of diblock copolymers was observed, which was attributed to the presence of monofunctional initiators.

The work presented here demonstrates the effectiveness of applying catalysts that possess high activities for both the ROCOP of epoxides and anhydrides and the ROP of lactones to switchable catalysis. Such systems show good activities for the selective synthesis of triblock copolymers, comparable to the best reported systems to date. Future work, however, should target the synthesis of triblock copolymers with molar masses up to 100 kg mol^{-1}, which have been demonstrated to show improved material properties over analogues at around 60 kg mol^{-1}.[15]

In particular, work with the bifunctional cocatalyst PPN_2PA shows promise, as the selective formation of triblock copolymers with only 2 equivalents of CHD should allow for the synthesis of high molar mass polyesters in low reaction times, provided sufficient cocatalyst and monomer purity can be achieved. Further work on purification of PPN_2PA should be undertaken or, if the residual chloride impurity (which is already low) cannot be removed,

the synthesis of an alternate bifunctional cocatalyst that can be more effectively purified should be investigated.

A further target should be the synthesis of multiblock copolymers using switchable catalysis. A study which systematically synthesises a series of multiblock copolymers (*i.e.* tri-, penta- and heptablocks) of equivalent molecular weights and subsequently examines their respective thermal and mechanical properties would be highly informative in establishing whether such multiblocks can lead to enhanced mechanical properties over triblock copolymers.

3.9 References for Chapter 3

1. A. C. Deacy, G. L. Gregory, G. S. Sulley, T. T. D. Chen and C. K. Williams, *J. Am. Chem. Soc.*, 2021, **143**, 10021-10040.
2. H. Feng, X. Lu, W. Wang, N. G. Kang and J. W. Mays, *Polymers*, 2017, **9**, 494.
3. T. Stößer, T. T. D. Chen, Y. Zhu and C. K. Williams, *Phil. Trans. R. Soc. A*, 2018, **376**, 20170066.
4. T. Stößer, D. Mulryan and C. K. Williams, *Angew. Chem. Int. Ed.*, 2018, **57**, 16893-16897.
5. T. Stößer and C. K. Williams, *Angew. Chem. Int. Ed.*, 2018, **57**, 6337-6341.
6. Y. Q. Zhu, C. Romain and C. K. Williams, *J. Am. Chem. Soc.*, 2015, **137**, 12179-12182.
7. C. Romain, Y. Q. Zhu, P. Dingwall, S. Paul, H. S. Rzepa, A. Buchard and C. K. Williams, *J. Am. Chem. Soc.*, 2016, **138**, 4120-4131.
8. G. L. Gregory, G. S. Sulley, L. P. Carrodeguas, T. T. D. Chen, A. Santmarti, N. J. Terrill, K.-Y. Lee and C. K. Williams, *Chem. Sci.*, 2020, **11**, 6567-6581.
9. Y. Zhu, M. R. Radlauer, D. K. Schneiderman, M. S. P. Shaffer, M. A. Hillmyer and C. K. Williams, *Macromolecules*, 2018, **51**, 2466-2475.
10. A. Spyros, D. S. Argyropoulos and R. H. Marchessault, *Macromolecules*, 1997, **30**, 327-329.
11. J. Deng, M. Ratanasak, Y. Sako, H. Tokuda, C. Maeda, J. Y. Hasegawa, K. Nozaki and T. Ema, *Chem. Sci.*, 2020, **11**, 5669-5675.
12. T. Stößer, G. S. Sulley, G. L. Gregory and C. K. Williams, *Nat. Comm.*, 2019, **10**.
13. M. T. Martello, D. K. Schneiderman and M. A. Hillmyer, *ACS Sustainable Chem. Eng.*, 2014, **2**, 2519-2526.
14. G. S. Sulley, G. L. Gregory, T. T. D. Chen, L. P. Carrodeguas, G. Trott, A. Santmarti, K. Y. Lee, N. J. Terrill and C. K. Williams, *J. Am. Chem. Soc.*, 2020, **142**, 4367-4378.
15. G. L. Gregory, G. S. Sulley, L. P. Carrodeguas, T. T. D. Chen, A. Santmarti, N. J. Terrill, K. Y. Lee and C. K. Williams, *Chem. Sci.*, 2020, **11**, 6567-6581.
16. M. J. Sanford, N. J. Van Zee and G. W. Coates, *Chem. Sci.*, 2018, **9**, 134-142.
17. H. Y. Ji, B. Wang, L. Pan and Y. S. Li, *Angew Chem Int Ed Engl*, 2018, **57**, 16888-16892.
18. S. Zhu, Y. Zhao, M. Ni, J. Xu, X. Zhou, Y. Liao, Y. Wang and X. Xie, *ACS Macro Lett.*, 2020, **9**, 204-209.

Chapter 4

Heterodinuclear Al(III)/M(I) complexes for ROCOP of epoxides and anhydrides

Work described in the chapter appears in "*Catalytic Synergy Using Al(III) and Group 1 Metals to Accelerate Epoxide and Anhydride Ring Opening Copolymerizations*"

W. T Diment, G. L. Gregory, R. W. F. Kerr, A. Phanopoulos, A. Buchard, C. K. Williams

ACS Catal., 2021, **11**, 12532 - 12542

4.1 Introduction

The controlled synthesis of polyesters *via* the ring-opening copolymerisation (ROCOP) of epoxides and anhydrides could be an important contributor in the development of the post-petrochemical plastic economy. Many mono- and multi-metallic catalysts have been reported for the ROCOP of epoxides and anhydrides, but most require the use of a cocatalyst.[1] These cocatalysts can be expensive, toxic and corrosive to steel. Further, many of these catalyst systems show intolerance to low catalyst loadings, which is in part attributed to the formation of catalyst/cocatalyst ion pairs.[2, 3]

The use of dinuclear complexes avoids many of these issues; chain shuttling mechanisms obviate the need for cocatalyst, and previously reported complexes, when applied to the ROCOP of epoxides and CO_2, have demonstrated high tolerance to low catalyst loadings, with a first order dependence on catalyst concentration observed over a large concentration range.[4-6]

Despite this, there are few reports on the application of dinuclear catalysts to the ROCOP of epoxides and anhydrides.[7-9] Of these, the most active is a homodinuclear zinc complex, [$L_{van}Zn_2OAc_2$], which displays moderate rates (TOF = 198 h^{-1}, 1% *vs*. anhydride, T = 100 °C). Although a heterodinuclear macrocyclic complex, [$LZnMgBr_2$] (See Chapter 1 for structure) displayed elevated activities in comparison to homodinuclear zinc and magnesium analogues (*i.e* [LZn_2Br_2] and [LMg_2Br_2]), it displayed a lower activity (TOF = 188 h^{-1}, 1% *vs*. anhydride, T = 100 °C) than the homodinuclear zinc *ortho*-vanillin based complex. There are no heterodinuclear complexes capable of delivering the exceptional activities that have been obtained by such complexes for epoxide/CO_2 ROCOP.[4, 5]

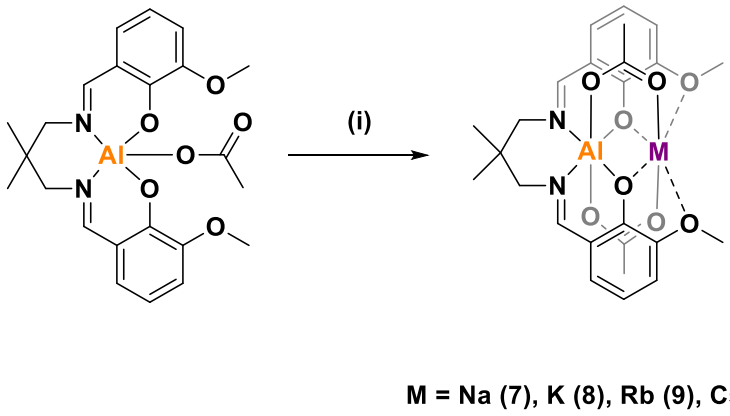
4.2 Aims

This chapter details the synthesis and characterisation of a series of heterodinuclear complexes and their subsequent application to the ROCOP of epoxides and anhydrides. In Chapter 2, the monometallic complex [L_{van}AlEt] (**1**), in conjunction with cocatalytic PPNCl, was found to be an effective catalyst for the ROCOP of PA and CHO and ROP of ε-DL. In this work, the *N*,*N*,*O*,*O*-Schiff base donor pocket was targeted for coordination to a metal ion. *Ortho*-vanillin derived ancillary ligands have an extensive, and well reported, coordination chemistry which employs both the *O*,*O*,*O*,*O*-pocket and the *N*,*N*,*O*,*O*-Schiff base pocket to selectively coordinate different metal ions, allowing access to heterodinuclear complexes.[10]

In this chapter, these coordination environments will be exploited to target a series of heterodinuclear Al(III)/M(I) complexes. The use of earth-abundant, non-toxic and colourless metals in the development of catalysts is a key goal, as many prior catalysts utilise metals that feature expensive, toxic and highly coloured metals such as Co(III) and Cr(III). In order to establish whether heterodinuclear complexes can act as active catalysts for the ROCOP of epoxides and anhydride, this series will first be tested for a benchmark copolymerisation of CHO and PA, which allows for comparison with other contemporary catalysts. It is also important to establish the mechanism by which the catalysis occurs. To this end, kinetic investigations will be carried out, and computational studies will be undertaken, to rationalise the role of the metals within the complex. It is also important that any novel catalyst can be applied to the synthesis of a range of polyesters, hence the complexes will be tested for the ROCOP of a range of epoxides and anhydrides.

4.3 Synthesis and Characterisation of Heterodinuclear Al(III)/M(I) Complexes

In order to investigate the capability of aluminium-containing heterodinuclear complexes for polyester ROCOP, a series of Al(III)/M(I) (M = Na (**7**), K (**8**), Rb (**9**), Cs (**10**)) were targeted (Scheme 4.1).



Scheme 4.1. Synthesis of heterodinuclear complexes **7** - **10**. (i) 1.0 equiv. MOAc (M = Na, K, Rb, Cs), $CHCl_3$, RT, 16 h. Yields = 64% (**7**), 98% (**8**), 86% (**9**), 99% (**10**).

The synthesis of complexes **7** - **10** was achieved through reaction of [L_{van}AlOAc] (**6**) with the corresponding Group 1 metal acetates in chloroform under an inert atmosphere. The complexes were isolated as yellow powders, in good yields, and were subsequently characterised by solution-phase NMR spectroscopy and X-ray crystallography. The bulk purity of all complexes was confirmed by elemental analysis.

4.3.1 X-ray Crystallography

Single crystals, suitable for X-ray diffraction, of all complexes were obtained by layering saturated solutions of the complexes in dichloromethane (**7**) or chloroform (**8** - **10**) with hexane at 25 °C. The representative structure of complex **8** is presented below; the structures of complexes **7**, **9** and **10** are presented in the Appendix (Figures 4.1 and S4.1 – S4.3. Selected bond angles and crystallographic refinement data are presented in Tables S4.1 – S4.4 and S4.6).

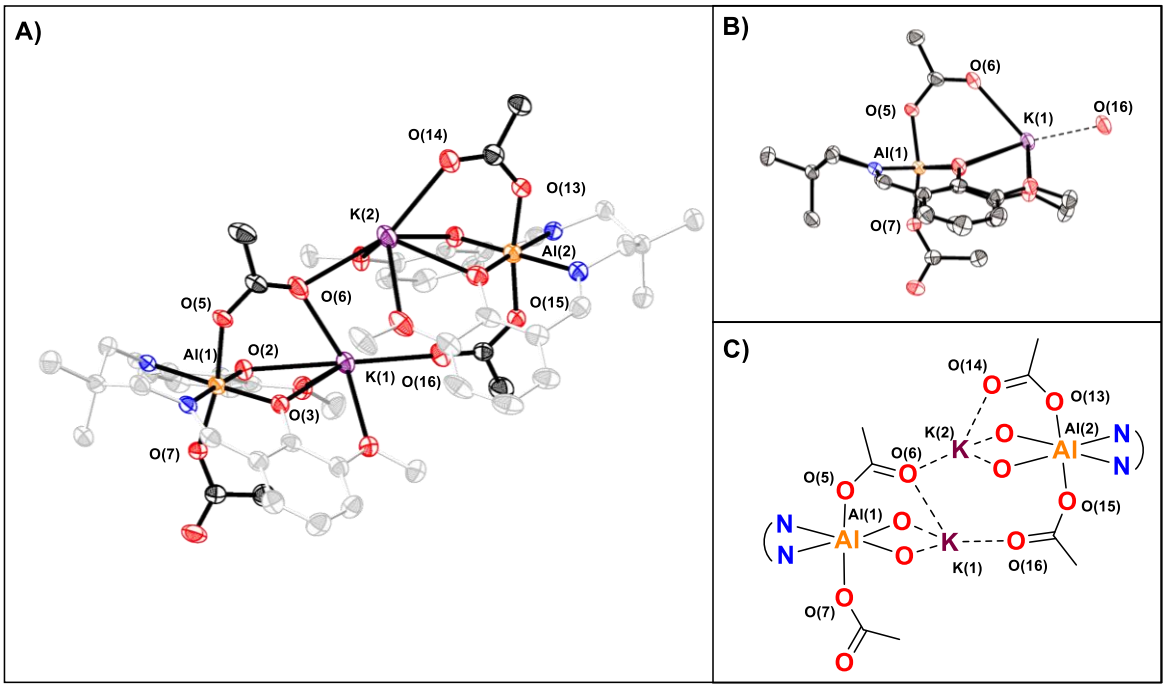


Figure 4.1. Molecular structure of complex **8·chloroform** (H-atoms omitted for clarity, thermal ellipsoids at 50% probability; atom colour scheme: aluminium (orange), potassium (purple), oxygen (red), nitrogen (blue), carbon (black/greyscale). A) Total dimeric structure of the complex, displaying the bridging acetate coligands. B) Structure of the monomeric Al(III)/K(I) unit, displaying the aluminate centre and K^+ ion displaced above the ligand plane. C) Schematic representation of the crystal structure, displaying key binding modes of both metals and acetate groups.

The solid-state molecular structures of complexes **7** - **10** confirmed their heterodinuclear nature, with the Al atom coordinated in the *N*,*N*,*O*,*O*-pocket and the Group 1 metal atom coordinated in the *O*,*O*,*O*,*O*-pocket in all cases. Complexes **7** - **9** show dimeric molecular structures, whilst complex **10** shows an extended polymeric molecular structure (Figure 4.1A). For all complexes, aggregation is facilitated by bonding between the acetate coligands and Group 1 Metals.

The complexes exhibit distorted octahedral geometry at the aluminium centre with typical *trans*-$O_{carboxy}$(5)-Al(1)-$O_{carboxy}$(7) bond angles of ~167° (Table 4.1, Entries 1 - 4). Further, the two Al(III)-$O_{carboxy}$ bond lengths are very similar [for complex **8**: Al(1)-O(5) = 1.905(2) Å, Al(1)-O(7) = 1.869(2) Å] (Figure 4.1B). As one of the acetates is unidentate, it is implied that both of the acetates are coordinated in an anionic fashion to Al(1), and hence the K(1)-O(8) interaction of the bidentate acetate can be considered dative-covalent. The Al(III)-

$O_{Phenoxy}$ bonds also show similar lengths [for complex **8**: Al(1)-O(2) = 1.842(2) Å, Al(1)-O(3) = 1.854(2) Å], which are significantly shorter than the corresponding K(I)-$O_{Phenoxy}$ bonds [K(1)-O(2) = 2.7220(19) Å, K(1)-O(3) = 2.738(2) Å]. Taken together, these findings suggest that the aluminium-centres observed in the solid-state molecular structures are best described as mono-anionic aluminates. It is important to emphasise that aluminate species have been proposed as key mechanistic intermediates in ROCOP catalysis, but thus far structural evidence supporting their formation using ligands relevant to this catalysis has been lacking.[2]

In complexes **8** – **10**, the Group 1 Metal ion is displaced above the plane of the ligand (*e.g.* Figure 4.1B). The degree of displacement increases with increasing ionic radii of the metal ion, consequently increasing the Al(III)-M(I) separation (Table 4.1, Entries 1 - 4). Only for complex **7**, which features the smallest cation (Na^+), does the metal ion sit 'inside' the tetra-oxy ligand donor pocket.

Table 4.1. Selected bond lengths and angles, obtained from the solid-state molecular structures, of complexes **7** – **10**.

Entry	Complex	Bond	Length (Å)	Bond	Angle (°)
1	**7**	Al(1)-Na(1)	3.284	O(5)-Al(1)-O(7)	169.21(7)
2	**8**	Al(1)-K(1)	3.665	O(5)-Al(1)-O(7)	167.84(10)
3	**9**	Al(1)-Rb(1)	3.819	O(5)-Al(1)-O(7)	167.42(7)
4	**10**	Al(1)-Cs(1)	3.979	O(5)-Al(1)-O(7)	165.76(7)

4.3.2 NMR Spectroscopy

Complex **7** – **10** were characterised by ^1H, $^{13}C\{^1H\}$ and ^{27}Al NMR spectroscopy (Figures S4.4 – S4.27). In all cases the NMR data supports the formation of the desired heterodinuclear species; the representative NMR spectroscopy data for complex **8** is discussed.

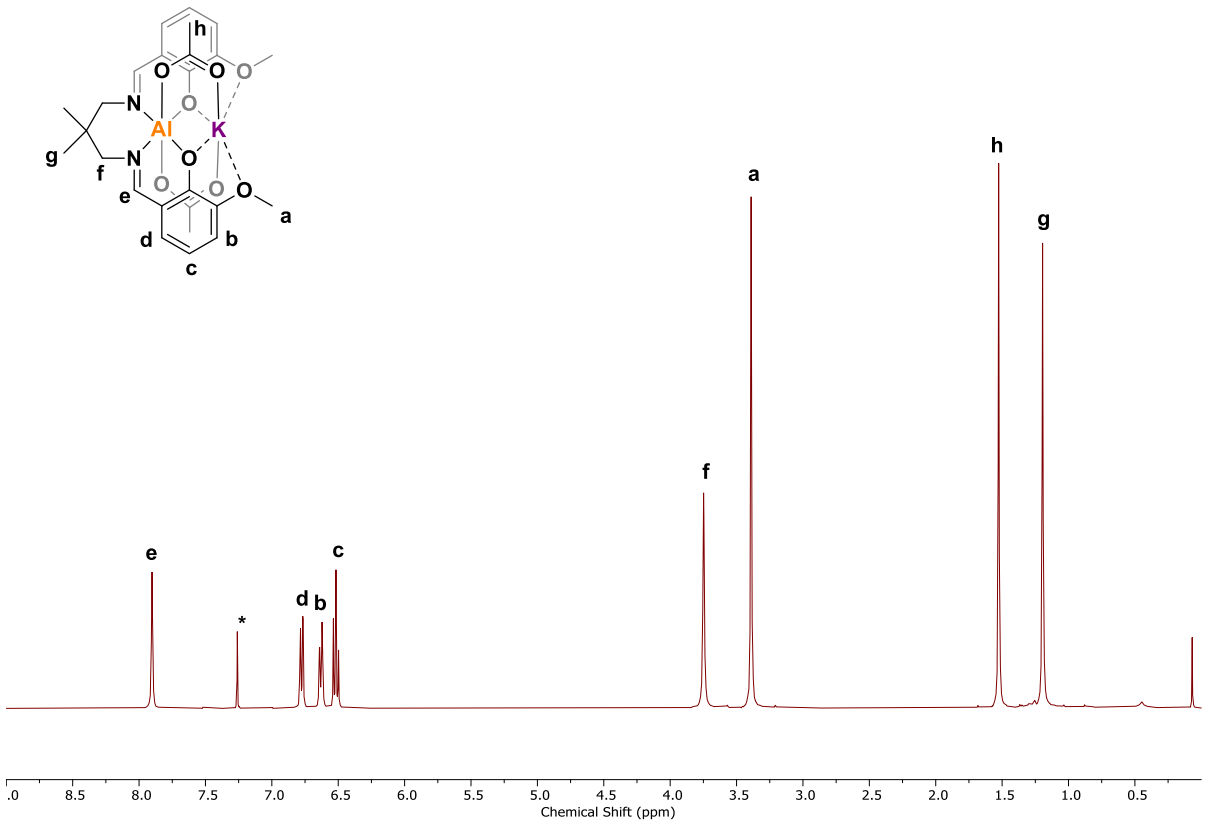


Figure 4.2. ^{1}H NMR spectrum ($CDCl_3$(*), 400 MHz, 298 K) of complex **8**. Spectra assigned as monomeric unit as, at room temperature, fluxional processes renders the two molecules within the dimer equivalent.

Complex **8** displays 7 resonances corresponding to the *ortho*-vanillin derived ligand, and 1 corresponding to the acetate coligand (Figure 4.2). In comparison to the monometallic complex **6**, complex **8** shows diagnostic shifts in the imine and *ortho*-methoxy protons from 8.10 and 3.80 ppm to 7.90 and 3.39 ppm, respectively. Further, in the ^{1}H NMR spectrum of complex **6**, the methylene protons and methyl groups of the ligand backbone are diastereotopic, whilst in complex **8** these groups give rise to a single resonance each, consistent with the coordination of a Group 1 metal rendering the two faces of the molecule equivalent.

The ^{27}Al NMR also shows a diagnostic shift from 14.8 ppm for complex **6** to -1.2 ppm for complex **8**, with the sharp resonances in both cases being consistent with octahedrally coordinated aluminium centre. The ^{13}C{^{1}H} spectrum is consistent with the solution phase structure described.

In order to investigate complex solution nuclearity, and in light of the dimeric crystal structure obtained, DOSY NMR was performed on the complex **8**, which displayed the best catalytic performance, *vide infra*. Room temperature DOSY NMR in chloroform, using *tetrakis*(trimethylsilyl)silane as an internal standard, revealed a diffusion coefficient of 6.9×10^{-10} m^2 sec^{-1} (Figure S4.28). Application of the Stokes-Einstein equation revealed a solvation radius, r_{solv}, of 6.0 Å, in comparison to the radius of the dimeric molecular structure, $r_{crystal,}$ of 6.0 Å suggesting that, in chloroform at 25 °C, complex **8** is dimeric.

In light of these results, the highly symmetric ^{1}H NMR for complex **8** implies that rapid fluxional processes must occur in order to give rise to equivalence of several proton environments (H^f, H^g, H^h). To test this, low temperature (-80 °C) ^{1}H NMR spectroscopy of complex **8** was undertaken (Figure 4.3).

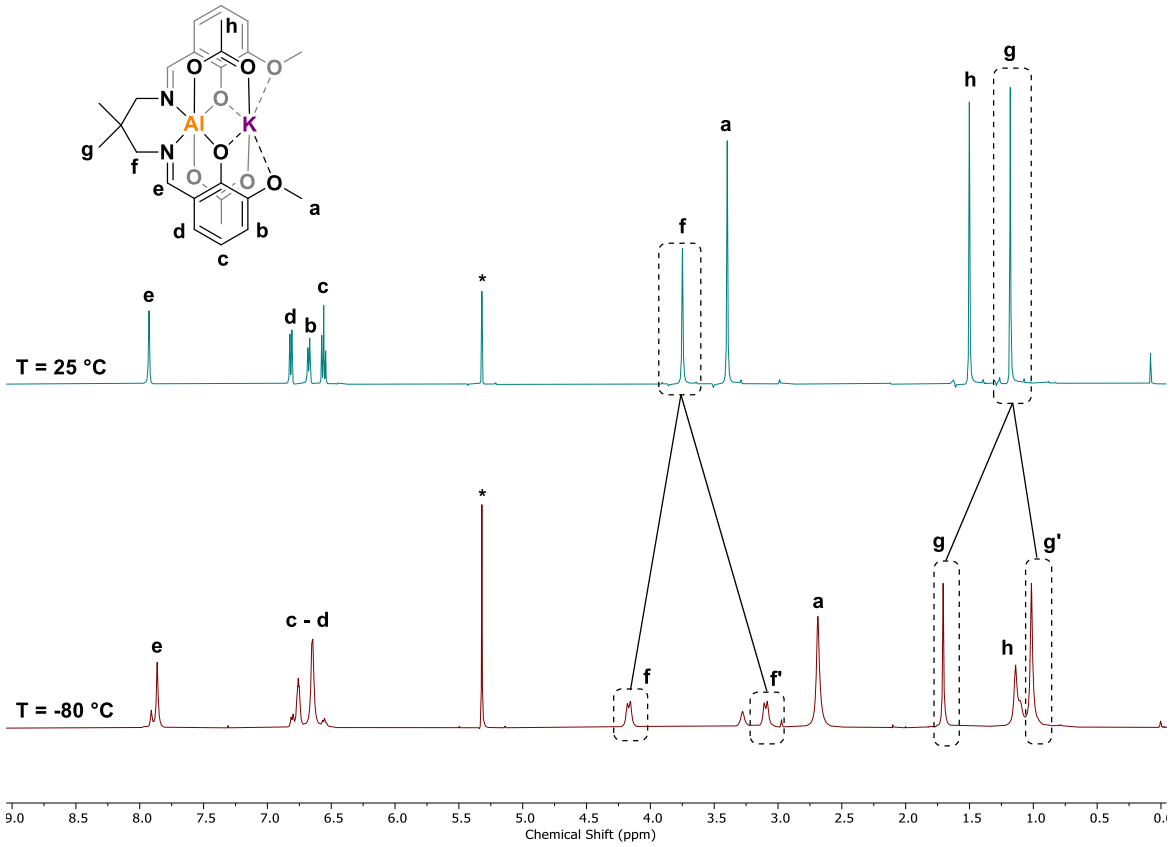
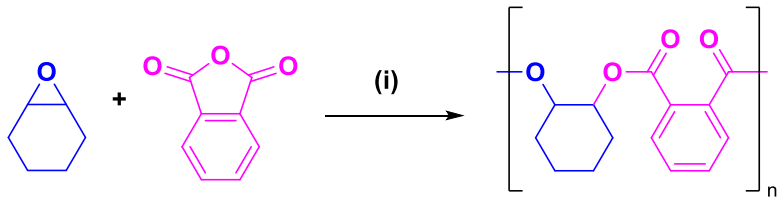


Figure 4.3. ^{1}H NMR spectrum (CD_2Cl_2(*), 500 MHz) of complex **8** at 298 K (25 °C) and 173 K (-80 °C).

A splitting of the methylene (H^f) and methyl (H^g) protons was observed. This suggests that, at -80 °C, the two faces of each monomer unit are no longer equivalent, rendering the solution structure closer to that of the solid-state molecular structure of complex **8**. In comparison to the solid-state structure however, where the two molecules within the dimer are asymmetric, the individual molecules of complex **8** cannot be resolved within the dimeric unit, implying some fluxionality is still present.

4.4 ROCOP of CHO and PA with Complexes 7 - 10

Following the successful synthesis of complexes **7 - 10**, testing for the ROCOP of CHO and PA was carried out in order to determine the most active catalyst (Scheme 4.2).



Scheme 4.2. ROCOP of CHO and PA to form PCHPE with complexes **7** – **10**. (i) [Cat]:[PA]:[CHO] = 1:400:2000, T = 100 °C.

For each of the polymerisations, aliquots were taken in order to obtain a k_{obs} and TOF for each complex (Figure 4.4 and Table S4.7). Each reaction was repeated in triplicate, with average values of $[PA]_t$ plotted for each time point. Experimental errors were determined by $\pm\sigma/\sqrt{n}$ where σ is the experimental standard deviation and n is the number of measurements (=3).

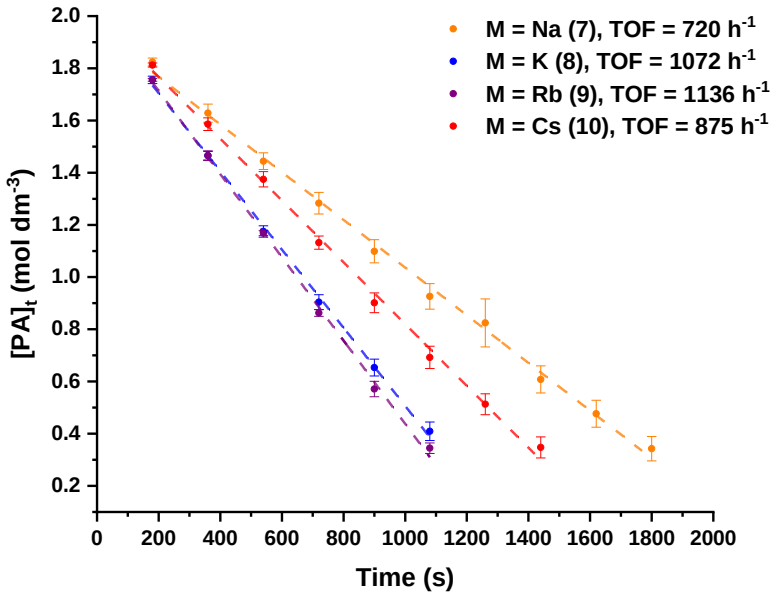


Figure 4.4. Plot showing $[PA]_t$ *vs*. Time for complexes **7 - 10**. Each reaction repeated in triplicate, with average $[PA]_t$ plotted, and errors plotted as $\pm\sigma/\sqrt{n}$, where n = 3.

It was found that complexes **8** and **9** were the most active, with TOFs of 1072 ± 6 h^{-1} (k_{obs} = 1.50 ± 0.03 x 10^{-3} s^{-1}) and 1136 ± 6 h^{-1} (k_{obs} = 1.53 ± 0.03 x 10^{-3} s^{-1}), respectively. Complex **10** was the next most active (TOF = 875 ± 8 h^{-1}, k_{obs} = 1.18 ± 0.03 x 10^{-3} s^{-1}), with complex **7** proving the least active (TOF = 720 ± 9 h^{-1}, k_{obs} = 9.1 ± 0.2 x 10^{-4} s^{-1}). The trends observed in TOF were replicated in k_{obs}, confirming that the observed difference in activity were a result of propagation rates. All complexes were found to be perfectly selective for polyester, with no polyether linkages being observed in any case (Figure S4.29, Table S4.7). The activities, and polyester selectivities, for all complexes under these conditions are exceptional and comparable to the best reported catalysts to date, *vide infra*.

Given the similarity in rate between complexes **8** and **9**, but significantly higher earth abundance and lower weight of potassium over rubidium, complex **8** was selected for further investigation. GPC analysis of aliquots taken throughout the polymerisations demonstrated that it proceeded with good control, with a narrow dispersity maintained throughout (Đ < 1.10) (Figure 4.5A).

Furthermore, the polymerisations were living, with a linear increase in polymer molar mass with PA conversion being observed.

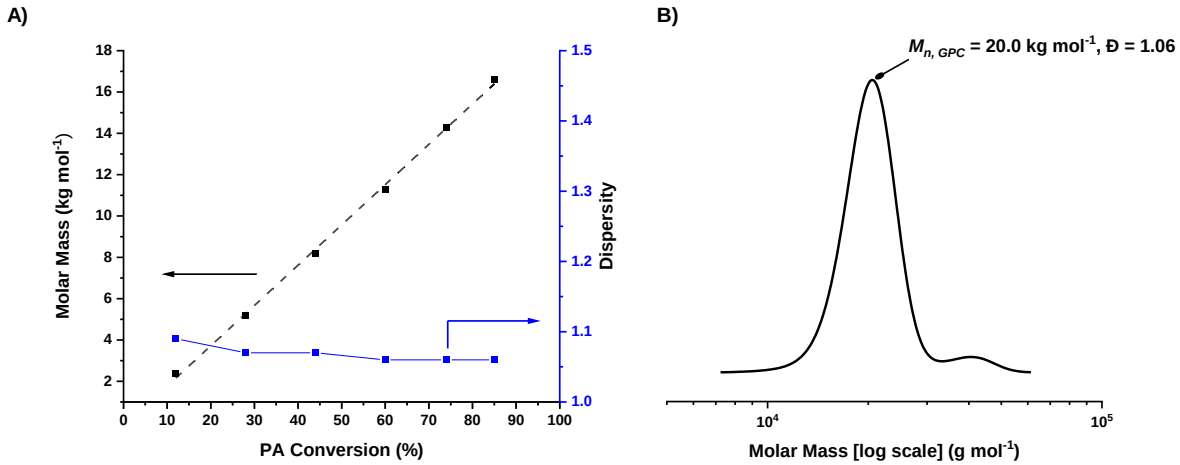


Figure 4.5. A) Plot of PCHPE molar mass and dispersity against PA conversion. B) GPC trace of PCHPE obtained with complex **8** at full PA conversion.

The poly(cyclohexene oxide-*alt*-phthalate) (PCHPE) obtained displayed a minor high weight shoulder, which was attributed to the presence of residual diols in the epoxide used (Figure 4.5B). MALDI-ToF spectrometry confirmed that the principal initiating species was the acetate coligand, which gives rise to α-acetate-ω-hydroxy capped PCHPE (Figure S4.30).

A common issue for many complexes applied to the ROCOP of epoxides and anhydrides is an intolerance to low catalyst loadings, which results in lower catalytic activities. With this in mind, complex **8** was also tested at 0.025% *vs*. anhydride (*i.e.* [**8**]:[PA]:[CHO] = 1:4000:20000). A TOF of 1010 h^{-1} was observed, which is very similar to the TOF at 0.25% *vs*. anhydride (1072 h^{-1}), demonstrating an exceptional resilience to low loading for this complex.

In order to establish the effect of the heterodinuclear combination of metals within complex **8**, the catalytic activities of the individual components of complex **8** (the monometallic precursor (complex **6**) and KOAc) were compared under equivalent conditions.[11] An

aluminium salen complex, [L_{sal}Al(OAc)] (**11**, see Chapter 7 for experimental details, Figures S4.31 – S4.36 for associated spectra), was also trialled to investigate the role of the second coordination environment in complex **8** (Figure 4.6, Table 4.2).

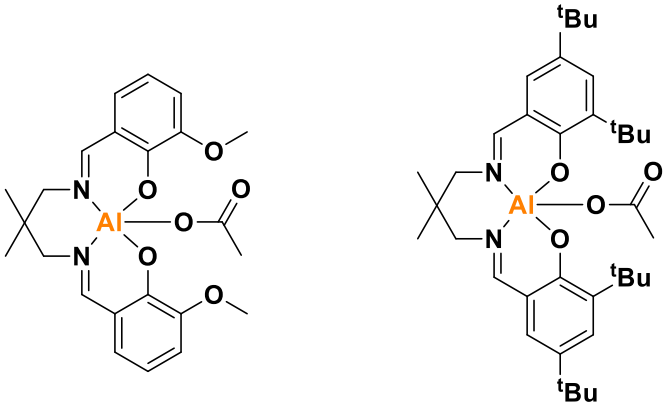


Figure 4.6. Complexes utilised to investigate the effects of metallic synergy in ROCOP catalysis.

Table 4.2. Data for the ROCOP of CHO and PA using complexes **6**, **8**, and **11**.[a]

Entry	Catalyst	Time (m)	TON_{PCHPE}[b]	TOF_{PCHPE}[c] (h^{-1})	Selectivity[d] (%)	$M_{n,\,GPC}$ [Đ][e] (kg mol^{-1})
1[f]	**8**	15	268	1072	>99	14.3 [1.06]
2	**6**	30	83	168	22	3.7 [1.86]
3[g]	KOAc	60	23	23	>99	4.0 [1.27]
4	**6**/KOAc	5	89	1068	>99	7.4 [1.07]
5	**11**	60	8	8	4	*N.d.*
6	**11**/KOAc	60	32	32	>99	*N.d.*

[a] General conditions: [Cat]:[PA]:[CHO] = 1:100:500, T = 100 °C. [b] Turnover number (TON) for polyester formation = number of moles of PA consumed/number of moles of catalyst. Determined by comparison of ^{1}H NMR integrals corresponding to PCHPE (7.65 – 7.30 ppm) and PA (8.10 – 7.85 ppm). [c] Turnover Frequency for polyester formation, TOF = TON/time(h). [d] Selectivity for polyester over polyether, determined by comparison of ^{1}H NMR integrals corresponding to PCHPE (5.22-5.06 ppm) and PCHO (3.60 - 3.20 ppm). [e] Determined by GPC in THF, at 30 °C, using narrow dispersity polystyrene standards. [f] Conditions: [Cat]:[PA]:[CHO] = 1:400:2000, T = 100 °C. [g] Conditions: [KOAc]:[PA]:[CHO] = 1:100:500, T = 110 °C.[11]

The monometallic complex **6** displays a relatively high activity (TOF = 168 h^{-1}) but low selectivity (22%) for polyester formation (Table 4.2, Entry 2). In comparison, KOAc shows a low activity (TOF = 23 h^{-1}) but is fully selective (>99%) for polyester formation (Table 4.2, Entry 3).[11] Combining the two components *in situ* yields an active (TOF = 1068 h^{-1}), and fully selective (>99% for polyester), catalyst system, with a nearly identical TOF to that

obtained from the isolated complex **8** (Table 4.2, Entry 1 *cf.* 4). These results suggest that when complex **6** and KOAc are combined in a polymerisation, complex **8** is rapidly formed *in situ*.

In comparison, complex **11** displayed a very low selectivity (4%) and activity (TOF_{PCHPE} = 4 h^{-1}) for polyester formation (Table 4.2, Entry 5). Interestingly, the combination of **11**/KOAc saw an increase in polyester selectivity (>99%), although no significant increase in activity was observed (Table 4.2, Entry 6). The suppression of ether linkage formation in this case is attributed to *in situ* aluminate formation, which reduces the aluminium centre's Lewis acidity and slows/inhibits sequential epoxide ring-opening reactions. However, without an adjacent *O,O,O,O*-pocket to coordinate a potassium cation, no heterodinuclear complex can be formed and hence catalytic activities remain very low.

Complex **8** displays a 6-fold increase in activity and 5-fold increase in selectivity in comparison to complex **6**, and a 50-fold increase in activity when compared to KOAc. In comparison to the [L_{sal}Al(OAc)]/KOAc catalyst system, complex **8** delivers equivalent selectivities but with a 33-fold increase in activity. These findings indicate a clear heterometallic synergy within the novel complexes that cannot be replicated without an ancillary coligand capable of supporting both metals.

It should be noted, however, that previous work with the same *ortho*-vanillin derived ancillary ligand has demonstrated that not all heterodinuclear combinations are successful.[9] In this prior work, a range of M(II)/Group 1 metal complexes were investigated, but all were found to be less active than the homodinuclear Zn(II) analogue.[7] These results ultimately highlight the need for insight into the catalytic mechanism and the role of metals within heterometallic frameworks, which should lead to better, and more efficiently targeted, catalyst design.

4.5 Kinetic Investigation of ROCOP of CHO and PA with Complex 8

In order to establish a mechanism for this new series of highly active complexes, a kinetic investigation was carried out with complex **8**. In general, the rate law for CHO/PA copolymerisation takes the form:

$$rate = k[\mathbf{8}]^l[CHO]^m[PA]^n$$

$$\text{where } rate = \frac{d[Polymer]}{dt} = -\frac{d[PA]}{dt}$$

In reactions that are performed in bulk epoxide (such as those in section 4.4), both [**8**] and [CHO] are constant, and hence can be subsumed into the rate constant yielding $k_{obs} = k[\mathbf{8}]^l[CHO]^m$. This results in a rate law of:

$$-\frac{d[PA]}{dt} = k_{obs}[PA]^n$$

If the reaction is zero order with respect to [PA] (i.e. $n = 0$), then the observed rate law simplifies to:

$$\frac{d[PA]}{dt} = -k_{obs}$$

Rearranging this result leads to a differential equation, which can be solved, leading to:

$$\int_{[PA]_o}^{[PA]_t} d[PA] = -k_{obs}\int_0^t dt$$

$$[PA]_t = -k_{obs}t + [PA]_0$$

Therefore, by plotting $[PA]_t$ *vs.* time, a linear plot with a gradient of $-k_{obs}$ will be obtained if the reaction is zero order with respect to [PA]. In section 4.4, linear plots of $[PA]_t$ *vs.* time were obtained for all complexes, hence demonstrating a zero-order dependence on [PA] (Figure 4.4).

Next, the reactions' dependence on [CHO] was examined by performing the polymerisations without excess (bulk) epoxide. Under these conditions, the rate law takes the form:

$$rate = \frac{d[P]}{dt} = -\frac{d[CHO]}{dt} = k_{cat}[CHO]^m$$

where $k_{cat} = k[\mathbf{8}]^l$. Should the reaction prove to be first order with respect to [CHO] (m = 1), the rate law can be rearranged and the differential equation solved, leading to:

$$-\frac{d[CHO]}{dt} = k_{cat}[CHO]$$

$$\int_{[CHO]_o}^{[CHO]_t} \frac{d[CHO]}{[CHO]} = -k_{cat}\int_0^t dt$$

$$\ln\left(\frac{[CHO]_t}{[CHO]_0}\right) = -k_{cat}t$$

This result indicates that a plot of $\ln\left(\frac{[CHO]_t}{[CHO]_0}\right)$ *vs*. time will yield a linear dependence with a gradient of k_{cat} if the reaction is first order with respect to [CHO]. A first order dependence on [CHO] was revealed by carrying out polymerisations using stoichiometric quantities of epoxide, with toluene as the solvent, and plotting the resultant $[CHO]_t$ as described above (Figure 4.7).

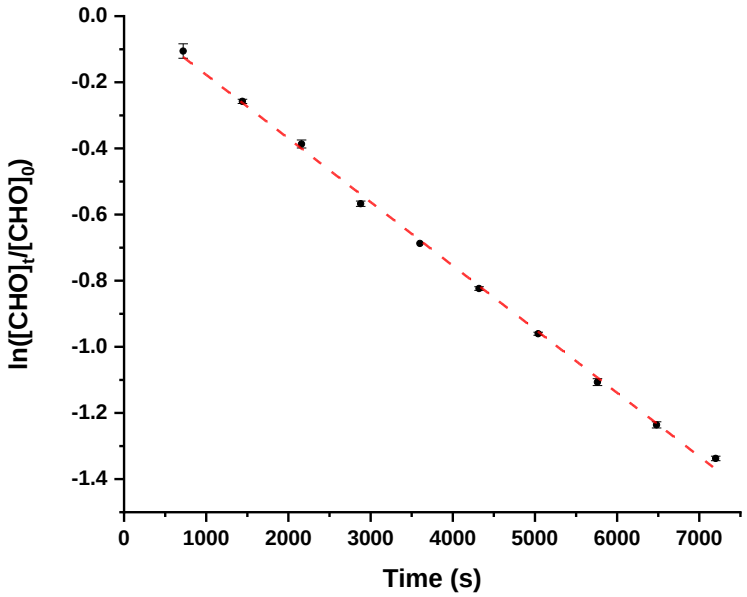


Figure 4.7. Plot of ln $\left(\frac{[CHO]_t}{[CHO]_0}\right)$ *vs.* time (m) obtained with complex **8**. Conditions: [**8**]:[PA]:[CHO] = 1:400:500 = 1:400:500, 0.75 mL toluene, [**8**] = 4.9 mmol, T = 100 °C. Reaction repeated in duplicate with average $[CHO]_t$ plotted. Errors plotted as $\pm(\frac{\Delta x}{x})$ where Δx is the error of $[CHO]_t$ and x is the value of $[CHO]_t$.

Finally, the dependence on catalyst concentration was investigated. For reactions run in bulk epoxide:

$$k_{obs} = k[\mathbf{8}]^l[CHO]$$

$$\ln(k_{obs}) = \ln(k[\mathbf{8}]^l[CHO])$$

$$\ln(k_{obs}) = l.\ln([\mathbf{8}]) + \ln(k[CHO])$$

Revealing that a plot of $\ln(k_{obs})$ against $\ln([\mathbf{8}])$ will have a gradient of l, which is the reaction order with respect to [**8**]. To investigate this, polymerisations were carried out at 4 different concentrations of [**8**], with each result repeated in triplicate (Figure S4.37). A k_{obs} was extracted for each concentration, which was then plotted against [**8**] as described above (Figure 4.8).

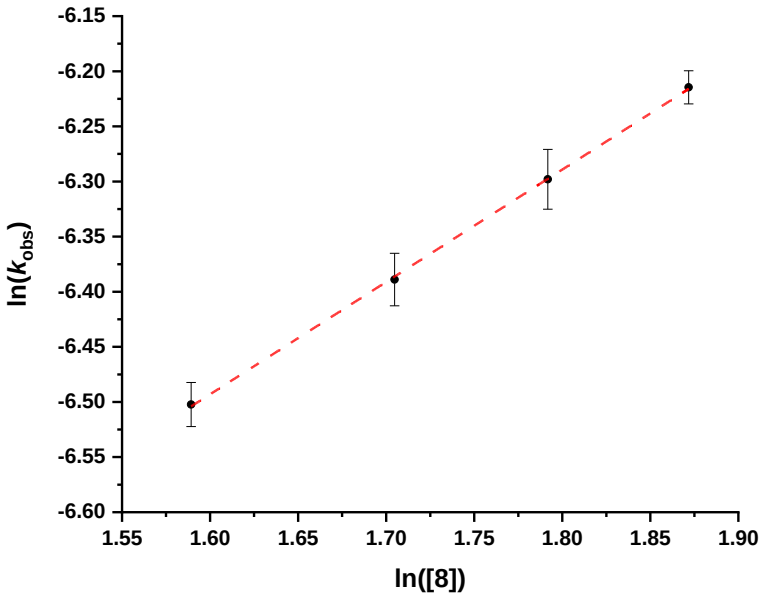


Figure 4.8. Plot of ln(k_{obs}) *vs.* ln([**8**]) at various concentrations of complex **8**. Errors plotted as $\pm(\frac{\Delta x}{x})$ where Δx is the error of k_{obs} and x is the value of k_{obs}. k_{obs} extracted from plots of $[PA]_t$ *vs.* time for each concentration (Figure S4.37).

A gradient of 1.02 ± 0.01 was obtained, indicating a first order dependence on [**8**]. Overall, the rate law for the polymerisation was found to be:

$$rate = k[\mathbf{8}]^1[CHO]^1[PA]^0$$

Significantly, no monomer ⇌ dimer equilibrium is observed, as a more complex dependence on catalyst concentration would be observed in such a case. Therefore, a first order dependence on catalyst concentration is observed as a result of a catalyst system that is either consistently monomeric or dimeric during the catalysis. The catalyst nuclearity under the conditions of catalysis is tentatively ascribed as monomeric, owing to the high temperatures (100 °C) and highly coordinating solvents (bulk epoxide) that are utilised, both of which would favour a monomeric catalyst. However, a dimeric structure, analogous to that observed in the solid-state structure of **8**, is also viable. In this case it should be noted that, due to the first order dependence on [CHO], the rate law would require that only half of the dimer is catalytically active at any one time.

A secondary key observation from this rate law is that, in common with many other complexes, the rate determining step of the reaction is epoxide ring opening. Importantly, as this ring opening must occur from a carboxylate chain-end, the catalyst resting state is likely to be very similar to the solid-state molecular structure of complex **8**. This provides new supporting evidence for the importance of aluminate (metallate) intermediates in this catalysis. Further, it allows for computational calculations to be carried out using the molecular structure of **8** as a starting point.

4.6 DFT Studies of Mechanism for ROCOP Catalysis

In order to elucidate the roles of the separate metals in complex **8** during ROCOP catalysis, a computational study was performed. All computational work described in this section was carried out by Dr. Georgina Gregory (University of Oxford) and Prof. Antoine Buchard (University of Bath).

As the ring-opening of epoxide had been shown to be the rate determining step, a monomeric model (Species I) based on the solid-state molecular structure of complex **8** was used, with the minor modification of replacing one acetate coligand with a benzoate coligand to better represent the polymer chain's end group (Figures 4.9 and S4.38 – S4.42 and Tables S4.8 – S4.9, see Appendix for computational details).

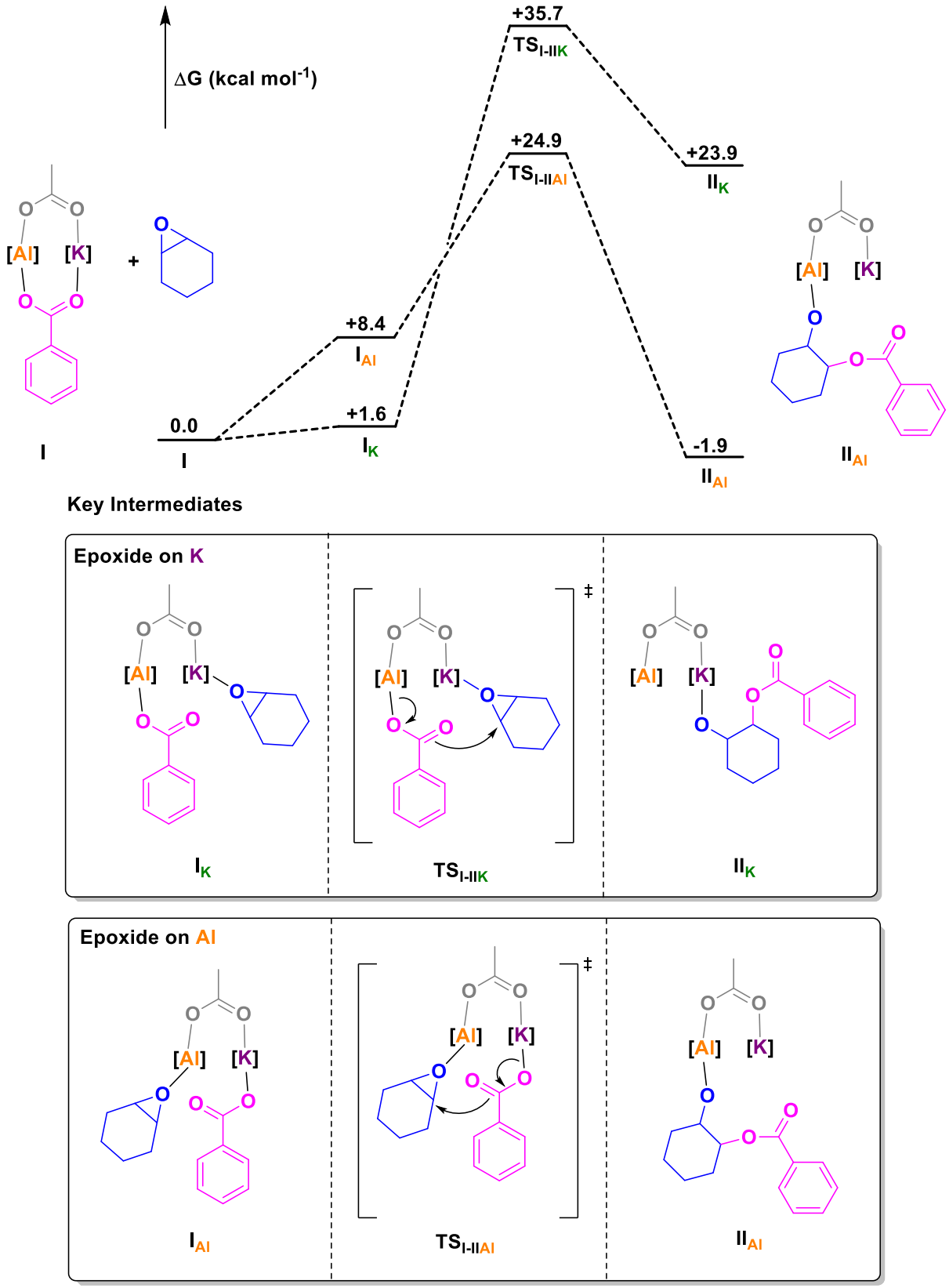


Figure 4.9. Density Functional Theorem calculations for two possible propagation pathways (through epoxide binding to potassium (top), or aluminium (bottom)) for complex **8**. Ancillary ligand omitted for clarity.

From species I, two possible propagation mechanism are likely; an equivalent of epoxide can bind to either potassium (I_k) or aluminium (I_{Al}), which results in its activation and susceptibility to nucleophilic attack from the polymer carboxylate chain end. This attack will occur through the corresponding transition state ($TS_{I\text{-}IIK}$ or $TS_{I\text{-}IIAl}$), resulting in an alkoxide species bound to the metal which initially activated the epoxide (II_K or II_{Al}).

It was found that, initially, epoxide coordination to potassium was favoured over aluminium [$\Delta G(I\text{-}I_k)$ = +1.6 kcal *vs*. $\Delta G(I\text{-}I_{Al})$ = +8.4 kcal]. Experimentally, this notion was tested through the synthesis of [$L_{van}AlK(OBz)_2$] (**12**) (See Chapter 7 for experimental details, and Figure S4.43 for ^{1}H NMR spectrum). Recrystallisation of **12** *via* layering a saturated solution of **12** in THF with hexane at 25 °C yielded a dimeric structure with one molecule of THF bound to one of the potassium cations, which could mimic epoxide binding (Figure 4.10).

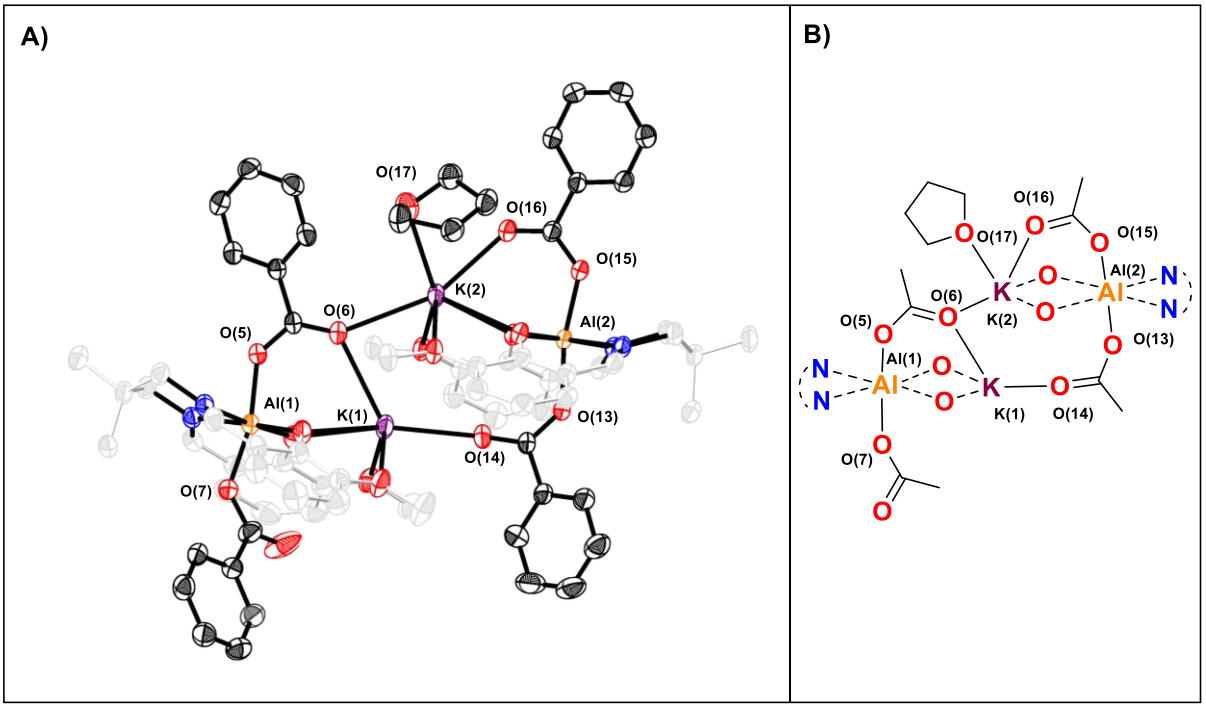


Figure 4.10. Molecular structure of complex **12** (H-atoms omitted for clarity, thermal ellipsoids at 50% probability; atom colour scheme: aluminium (orange), potassium (purple), oxygen (red), nitrogen (blue), carbon (black/greyscale). A) Total dimeric structure of the complex, displaying the bridging acetate coligands and THF coordination to K(2). B) Schematic representation of the crystal structure, displaying key binding modes of both metals and acetate groups.

Despite this initial binding preference, it was found that the subsequent ring opening of the epoxide was both kinetically [$\Delta G(\text{I-TS}_{\text{I-IIK}})$ = +35.7 kcal *vs*. $\Delta G(\text{I-TS}_{\text{I-IIAl}})$ = +24.9 kcal] and thermodynamically [$\Delta G(\text{I-II}_{\text{K}})$ = +23.9 kcal *vs*. $\Delta G(\text{I-II}_{\text{Al}})$ = -1.9 kcal] more favourable to proceed *via* initial epoxide binding to aluminium. This energetic preference can be rationalised by considering the greater Lewis acidity Al(III) over K(I); binding to aluminium will result in much greater degree of epoxide activation when compared to potassium. As part of this pathway, whilst the aluminium binds and activates the epoxide, the potassium binds the polymer chain, keeping it in close proximity to the activated epoxide, potentially promoting insertion. In this regard, the potassium centre may be acting in a similar fashion to the cocatalytic moieties that have been applied to generate some of the most active catalysts for the ROCOP of epoxides with both anhydrides and/or CO_2.[1, 3]

Comparison of this proposed mechanism with the observed activity values of complexes **7** – **10** allows for further mechanistic insight that could help direct future catalyst design. Since the role of the Group 1 metal ion appears to be principally to tether the carboxylate group, reducing the barrier to insertion into the aluminium-bound epoxide, it is likely that the intermetallic (Al(III)-M(I)) separation is important in lowering transition state energies. As described in Section 4.3.1, in the solid-state molecular structures of complexes **7** – **10,** the Al(III)-M(I) separation increases in the order Al(III)-Na(I) < Al(III)-K(I) < Al(III)-Rb(I) < Al(III)-Cs(I). Another important aspect of the transition state is the breaking of the M(I)-$O_{\text{carboxylate}}$ bond, the strength of which will be dependent on the Lewis acidity of M(I). Considering this, it could be expected that reactivity would follow the order Cs (**10**) > Rb (**9**) > K (**8**) > Na (**7**). In contrast, the intermetallic separation would suggest that complex **7** should be most active. Complexes **8** and **9** are experimentally most active, which suggests that counterbalancing these two opposing mechanistic demands is important to achieve the maximal rate.

4.7 Scope of Catalysis

Given the excellent performance of complex **8** in the ROCOP of CHO and PA, further work was carried out to determine the scope of the catalysis possible (Figure 4.11, Table 4.3).

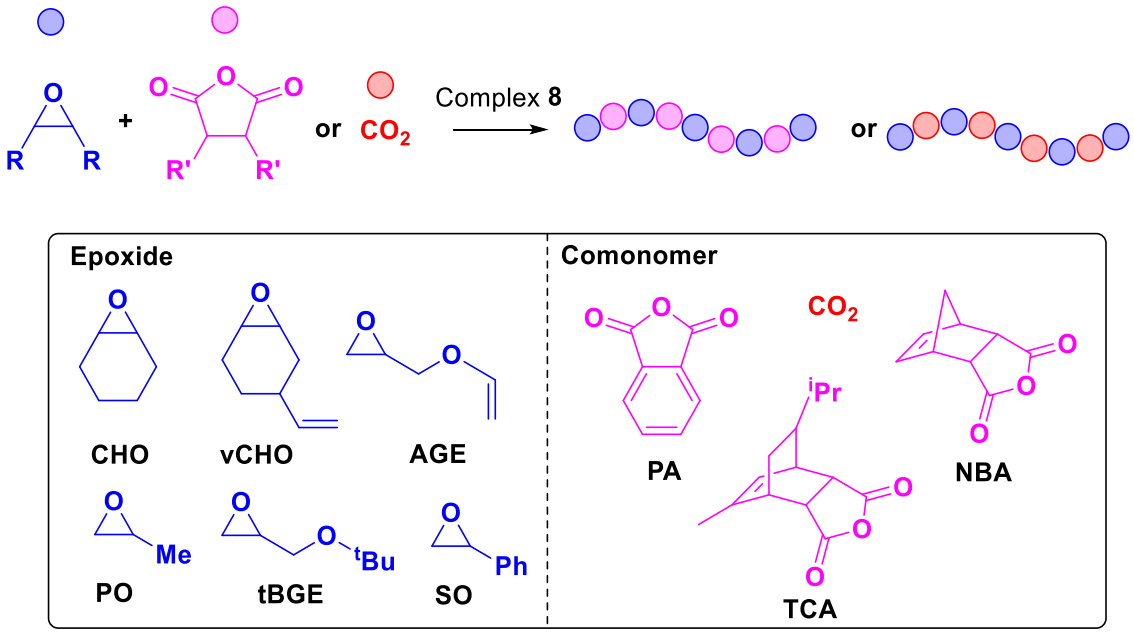


Figure 4.11. Epoxide and anhydride (or CO_2) comonomers tested with complex **8**.

Table 4.3 Data for the ROCOP of a range of epoxides and comonomers with complex **8**.[a]

Entry	Monomers	Time (m)	TON[b]	TOF[c] (h^{-1})	$M_{n,\,GPC}$ [Đ][d] (kg mol^{-1})
1	CHO/PA	15	268	1072	14.3 [1.06]
2	CHO/TCA	30	144	288	4.7 [1.22]
3	CHO/NBA	30	133	266	4.5 [1.10]
4	tBGE/PA	30	160	320	7.9 [1.24]
5	SO/PA	30	76	152	3.2 [1.24]
6	PO/PA	1200	400	20	33.2 [1.13]
7	vCHO/PA	30	296	592	42.9 [1.06]
8	AGE/PA	30	136	272	8.2 [1.20]
9[e]	CHO/CO_2	60	58	58	3.5 [1.18]
10[f]	CHO/CO_2	120	1010	505	23.4 [1.21]

[a]Conditions for anhydride: [**8**]:[Anhydride] = 1:400, 1 mL epoxide (= [**8**]:[CHO] = 1:2000), [**8**] = 4.9 mmol, 100 °C. Conditions for CO_2: [**8**]:[CHO] = 1:2000, 100 °C. [b]Turnover number = moles of epoxide consumed (=moles of anhydride consumed, when present)/ moles of catalyst. Determined by ^{1}H NMR spectroscopy (Figures S4.44 - S4.52). For entries 9 and 10, TON is for polycarbonate formation. [c]Turnover frequency = TON/time (hours). [d]Determined by GPC in THF, at 30 °C, using narrow dispersity polystyrene standards. [e]Reaction run at 60 °C. [g] $p(CO_2)$ = 1 bar. [f] $p(CO_2)$ = 20 bar.

In each case, a single monomer was varied from the initial CHO/PA combination to allow for ready comparison. Complex **8** remained highly active for a range of epoxides and anhydrides, and in all cases quantitative selectivity (>99% within the limits of the detection method) for polyester over polyether formation was observed. In comparison to PA, lower activities were obtained for the sterically hindered tricylic anhydride (TCA, TOF = 288 h^{-1}) and norbornene anhydride (NBA, TOF = 266 h^{-1}), although the observed rates were still relatively high (Table 4.3, Entries 2 and 3). Complex **8** was also capable of polymerising a range of challenging epoxides, including *tert*-butyl glycidyl ether (tBGE, TOF = 320 h^{-1}), styrene oxide (SO, TOF = 152 h^{-1}) and propylene oxide (PO, TOF = 20 h^{-1}) with high activities (Table 4.3, Entries 3, 4 and 5). High activities were also obtained for monomers with pendant vinyl groups, namely vinyl-cyclohexene oxide (vCHO, TOF = 592 h^{-1}) and allyl-glycidyl ether (AGE, TOF = 272 h^{-1}) (Table 4.3, Entries 7 and 8).

Complete anhydride conversion was obtained in all cases, leading to the formation of polyesters with molar masses between 15 – 55 kg mol^{-1} (Table S4.10). Transesterification was not observed for any monomer combination during the reaction, but occurred after complete anhydride conversion for monomer combinations featuring terminal epoxides (*e.g.* PO, AGE, tBGE). In all cases the polymers displayed bimodal molar mass distributions, owing to the presence of both monofunctional (*i.e.* acetate) and bifunctional (residual diol) initiators (Figure S4.53).

The broad scope of the catalysis indicates that complex **8** can be utilised for the synthesis of a range of polyesters. Rigid polyesters show promising applications as 'hard', high T_g blocks within thermoplastic elastomers.[12-14] Polyesters with vinyl group side chains, such as those containing vCHO and AGE, are candidates for post-functionalisation, allowing for modification of a range of properties including solubility, ion-conductivity and

hydrophilicity.[15-17] Elastomeric polyesters of PO/PA and tBGE/PA could be utilised as 'soft', lower T_g blocks in switchable catalysis.[18]

Given the impressive capability of complex **8** in the ROCOP of polyesters, it was also investigated for polycarbonate ROCOP utilising CHO/CO_2 (Table 4.3, Entries 9 and 10). At 1 bar of CO_2 pressure, a moderate activity (TOF_{PCHC} = 58 h^{-1}) and selectivity over cyclic carbonate ($Selectivity_{PCHC}$ = 50%) was observed. At 20 bar of CO_2 pressure, the expected increase in both activity (TOF_{PCHC} = 505 h^{-1}) and selectivity ($Selectivity_{PCHC}$ = 88%) was observed. No CHO polyether was formed in either reaction.

Complex **8** shows promising activity and selectivity for CHO/CO_2 ROCOP, particularly under 20 bar CO_2 pressure. In comparison to the more commonly utilised chromium and cobalt-containing catalysts, aluminium is cheaper, earth-abundant and non-toxic, making aluminium-containing complexes a desirable target for the copolymerisation of epoxides and CO_2. These results should inspire further catalyst development, as few catalysts containing aluminium are currently reported.[19-22]

4.8 Discussion

It is important to compare the performance of complex **8** to a range of catalysts reported in the literature (Table 4.4, for catalyst structures see Figure S4.54). Comparisons with other catalysts can be challenging owing to the lack of a standard set of conditions utilised within the field. Nevertheless, comparisons are generally feasible for a standard CHO/PA monomer set at temperatures of *ca.* 100 °C and catalyst loadings of ≤1% *vs*. anhydride.

Table 4.4. Comparisons between complex **8** and a selection of literature complexes.

Entry	Catalyst	Mon.	Time (h)	TON[a]	TOF[b] (h^{-1})	$M_{n,\,GPC}$ [Đ][c] (kg mol^{-1})
1[d]	[L_{van}AlK$(OAc)_2$] (**8**)	CHO/PA	0.25	268	1072	14.3 [1.06]
2[e]	[$L_{van}Zn_2(OAc)_2$] (**4.1**)	CHO/PA	0.5	99	198	5.3 [1.23]
3[f]	$^tBuP_1$	CHO/PA	2	96	48	18.4 [1.06]
4[g]	KOAc	CHO/PA	1	23	23	4.0 [1.27]
5[g]	$Cs(O_2C(CF_3))$	CHO/PA	1	92	92	6.0 [1.20]
6[h]	R_2B-$(CH_2)_5$-NR_3Cl (**4.2**)	CHO/PA	0.66	172	258	24.5 [1.18]
7[i]	[LAlCl] (**4.3**)	NBA/CHO	6	51	34	8.2 [1.24]
8[j]	[LAlCl] (**4.3**)	PA/PO	4	>99	>99	22.1 [1.14]
9[k]	[SalcyCrCl]/PPNCl (**4.4**)	CHO/PA	0.083	97	1164	5.1 [1.17]
10[l]	[LFe_2]/PPNCl (**4.5**)	CHO/PA	0.5	290	588	5.7 [1.30]
11[m]	[LAl_2]/PPNCl (**4.6**)	CHO/PA	0.3	225	750	9.8 [1.14]
12[n]	$Zn(C_6F_5)_2$/DMAP	CHO/PA	0.8	92	116	5.6 [1.20]
13[o]	DBU/BEt_3	PO/PA	3	80	27	13.2 [1.14]
14[p]	[LCr_3]/PPNCl (**4.7**)	CHO/PA	0.33	3540	10620	12.3 [1.21]

[a] Turnover Number (TON) = number of moles of anhydride consumed/ number of moles of catalyst, as reported in respective literature. [b] Turnover Frequency (TOF) = TON/time (hours), as reported in respective literature. [c] Under conditions described in respective literature. [d]Conditions: [Cat]:[PA]:[CHO] = 1:400:2000, T = 100 °C. [e]Conditions: [Cat]:[PA]:[CHO] = 1:100:800, T = 100 °C.[7] [f]Conditions: [Cat]:[BnOH]:[PA]:[CHO] = 1:2:100:150, T = 100 °C.[23] [g]Conditions: [Cat]:[PA]:[CHO] = 1:100:500, T = 110 °C.[11] [h]Conditions: [Cat]:[PA]:[CHO] = 1:200:400, T = 120 °C.[24] [i]Conditions: [Cat]:[NBA]:[CHO] = 1:400:2000, T = 60 °C.[3] [j]Conditions: [Cat]:[PA]:[PO] = 1:400:2000, T = 60 °C.[3] [k]Conditions: [Cat]:[PPNCl]:[CHD]:[PA]:[CHO] = 1:1:2:100:500, T = 100 °C, See Chapter 2. [l]Conditions: [Fe]:[PPNCl]:[PA]:[CHO] = 1:1:1000:5000, T= 100 °C.[25] All values reported per metal centre as an analogous monometallic complex was shown to have equivalent TOF when the number of metal centres was accounted for. [m]Conditions: [Cat]:[PPNCl]:[PA]:[CHO] = 1:2:250:1000, T = 50 °C.[26] [n]Conditions: [$Zn(C_6F_2)_2$]:[DMAP]:[PA]:[CHO] = 1:2:100:500, T = 110 °C.[27] [o]Conditions: [DBU]:[BEt_3]:[PA]:[PO] = 1:1:100:500, T = 60 °C.[28] [p]Conditions: [Cat]:[PPNCl]:[PA]:[CHO] = 1:3:6000:30000, T = 100 °C.[29]

Catalysts reported for the ROCOP of epoxides and anhydrides can be divided into two classes: those that function effectively without cocatalysts (monocomponent systems) and those that require cocatalysts to either function, or significantly enhance performance (bicomponent systems). Whilst bicomponent systems can display high activities, they are often intolerant to low catalyst loadings.[3] As a result, the design of catalysts that avoid their use is highly desirable.

Simple metal acetate catalysts, such as KOAc, whilst cheap and non-toxic, show low activities (TOF = 23 h^{-1}, 1% *vs*. anhydride, T = 110 °C) (Table 4.4, Entry 4).[11] This activity can be improved through optimisation of the metal carboxylate utilised (*e.g.* $Cs(O_2CCF_3)$, TOF = 92 h^{-1}, 1% *vs*. anhydride, T = 110 °C, Table 4.5, Entry 5). However, in doing so, the principle appeal of these simple catalysts, namely low catalyst molecular weight and cost, is lost. Monocomponent organobase catalysts, such as $^tBuP_1$, also show low activities (TOF = 48 h^{-1}, 1% *vs*. anhydride, T = 100 °C), although compatibility with a wide range of epoxides and anhydrides is possible (Table 4.3, Entry 3).[23]

The current best-performing monocomponent systems are those that feature covalently tethered cocatalytic moieties - a design strategy that has been applied to both organocatalyst and monometallic complexes (See Chapter 1). A tethered organoboron complex (**4.2**) displayed high activities (TOF = 258 h^{-1}, 0.5% *vs*. anhydride, T = 120 °C), but it is clear that rates will be higher at such elevated operating temperatures (Table 4.4, Entry 6).[24] The field-leading monocomponent system is an aluminium salen complex featuring a tethered cocatalytic moiety (**4.3**) reported by Coates and co-workers.[3, 30] Complex **4.3** shows impressive activity for the ROCOP of PO with PA (TOF = 99 h^{-1}, 0.25% *vs*. anhydride, 60 °C) and CHO with NBA (TOF = 34 h^{-1} 0.25% *vs*. anhydride, 60 °C) at low temperatures, as well as exceptional tolerance to low (0.025% *vs*. anhydride) catalyst loadings (Table 4.4, Entries 7 and 8).

An alternate strategy to the use of covalently-tethered cocatalytic moieties is the development dinuclear complexes, many of which function through dinuclear chain shuttling mechanisms which obviates the need for cocatalysts. Although heterodinuclear complexes have shown exceptional capabilities when applied to the ROCOP of epoxides and CO_2, prior to this work, no effective heterodinuclear complexes were reported with high activities for the ROCOP of epoxides and anhydrides.[4, 5] The best-performing dinuclear complex is the homodinuclear complex [$L_{van}Zn_2OAc_2$] (**4.1**), which shows moderate activities [TOF = 198 h^{-1}, 1% *vs*. anhydride, T = 100 °C] for the ROCOP of PA and CHO (Table 4.4, Entry 2).[7]

Compared to monocomponent systems, higher activities are often observed for bicomponent systems. The most effective bicomponent organocatalyst system, $Zn(C_6F_5)_2$/DMAP, shows moderate activities (TOF = 116 h^{-1}, 1% *vs.* anhydride, T = 110 °C) for the ROCOP of CHO and PA (Table 4.4, Entry 13).[27] This activity is higher than the metal acetate and organobase catalysts discussed above, and equivalent to complex **4.2**, when operating temperature is accounted for. Use of DBU/BEt_3 gives a catalyst system with moderate activities for the ROCOP of PO and PA (TOF = 27 h^{-1}, 1% *vs*. anhydride, T = 60 °C) (Table 4.4, Entry 12).[28] However, the best activities for the ROCOP of epoxides and anhydrides result from bicomponent systems that utilise metal-containing complexes with PPNCl as a cocatalyst. In Chapter 2, the widely-used, commercially available [SalcyCrCl]/PPNCl (**4.4**) catalyst system was shown to be highly active (TOF = 1164 h^{-1}, 1% *vs*. anhydride, T = 100 °C) (Table 4.4, Entry 9). This activity is significantly higher than the initially reported activity for this catalytic system (TOF = 250 h^{-1}, 0.4% *vs*. anhydride, T = 110 °C), which was not performed in bulk epoxide.[31] In comparison to many metal-containing catalysts reported for polyester ROCOP, which produce polyether when no cocatalyst is present, **4.4** can function without a cocatalyst, although activity is significantly improved when one is used.[31] As

discussed above, the bicomponent nature of the catalysis renders this complex sensitive to catalyst loadings, and the disadvantages of using a chromium-based complex include its toxicity, colour, and cost.

Even higher activities have been obtained by utilising ligands that tether multiple metal centres together, allowing for synergy between the individual metal centres. In order to assess whether the metal centres in such multi-metallic catalysts display inter-metallic synergy, it is essential to compare their activities to monometallic analogues. For example, a bimetallic Fe(III) complex (**4.5**) shows very high activities (TOF = 588 h^{-1}, 0.1% *vs.* anhydride, T = 100 °C). However, when the number of metal centres are accounted for, the activity is equivalent to the analogous monometallic complex, showing that little-to-no inter-metallic synergy takes place (Table 4.4, Entry 10). A bimetallic Al(III) complex (**4.6**) also displays very high activities (TOF = 750 h^{-1}, 0.4% *vs*. anhydride) but in this case comparisons to analogous monometallic Al(III) complexes were not performed (Table 4.4, Entry 11). Complex **4.6** is highly dependent on use of PPNCl, as without it only polyether was obtained. Very recently a trimetallic Cr(III) complex (**4.7**) was reported, which shows exceptional activities and tolerance to low loadings (TOF = 10,620 h^{-1}, 0.017% *vs*. anhydride, T = 100 °C), although without PPNCl cocatalyst it again produces only polyether (Table 4.4, Entry 14). Complex **4.6** was shown to exhibit a significant degree of intermetallic synergy: the TOF, when normalised for the number of metal centres in each complex, was found to be *ca*. 50x higher for the trimetallic complex when compared to a monometallic analogue.

Complex **8** is one of the best reported catalysts for the ROCOP of CHO with PA, recording the highest reported TOF for this reaction for a monocomponent system. It shows a 5-fold increase in reactivity compared to the previous best dinuclear catalyst **4.1** and a 4-fold increase in reactivity compared to the best-in-class organocatalyst **4.2**, at a lower operating

temperature. When compared to complex **4.3**, complex **8** shows a *ca*. 8-fold increase in activity for the ROCOP of CHO with NBA, albeit at a higher temperature, although **4.3** does display a higher activity for the ROCOP of PO and PA. One advantage of complex **8** over **4.3** is its relative ease of synthesis; complex **8** can be synthesised in 3 steps in 73% overall yield from commercially available starting materials, whilst the synthesis of **4.3** requires 8 steps in 9% overall yield. Complex **8** is also *ca*. 2x lighter than **4.3**, which is desirable when considering g/g activity - an industrially relevant measure.

In comparison to bicomponent systems, complex **8** shows 2-fold higher activities than the bimetallic Fe(III) complex (**4.5**) at equivalent and lower catalyst loadings, and equivalent activities to **4.4** at up to 40-fold lower loadings. Complex **4.6** displays a similar activity to complex **8**, but at a significantly lower operating temperature (50 °C *cf.* 100 °C). Only complex **4.7** shows significantly higher activities than **8** whilst also displaying an impressive tolerance to low loadings. In comparison to the best reported bimetallic systems, use of complex **8** obviates the need for cocatalyst, presenting one clear advantage for its use. All of the high performing systems require extensive ligand synthesis, as the ligands required to coordinate the multi-metallic systems are necessarily more complex. As a corollary, use of these ligands results in significantly increased catalyst molecular weights, which again would be expected to decrease g/g activity.

4.9 Conclusion and Outlook

Four novel heterodinuclear complexes were synthesised, characterised and subsequently tested for the ROCOP of PA and CHO. Complexes **8** and **9** were found to be most active, with TOFs of >1000 h^{-1} (0.25% *vs.* anhydride, T = 100 °C). Further kinetic studies with complex **8**, combined with a computational study, enabled elucidation of the catalytic mechanism which should provide insight into future catalyst designs. The broad catalytic scope was also established, showing that these heterodinuclear complexes could be applied to the synthesis of a broad range of polyesters.

There remain several avenues for subsequent investigation (Figure 4.12). Firstly, it was demonstrated that the role of the M(III) ion is to bind and activate an epoxide molecule. Therefore, a study which varies the M(III) ion should be undertaken in order to understand how changing the Lewis acidity, or altering the degree of covalency in metal-epoxide coordination in the case of transition metals, influences the activity of these heterodinuclear species. An investigation into the *ortho*-vanillin derived diamine ligand backbone should also be undertaken, as multiple studies have demonstrated that the appropriate ligand backbone can significantly enhance catalytic activity.[1, 31]

A final future objective should be to use the heterodinuclear framework described here to develop a dinuclear catalyst with non-initiating coligands. As demonstrated with the **1**/PPNCl system in Chapter 3, any system that relies on a monofunctional initiating cocatalyst will require multiple equivalents of CTA to yield monomodal polymer molar mass distributions. Dinuclear catalysts, such as complex **8**, do not require cocatalysts to function and so, provided the monofunctional initiating coligands (*e.g.* acetate) can be replaced with non-initiating analogues, these catalysts are ideal for the synthesis of high weight polyesters.

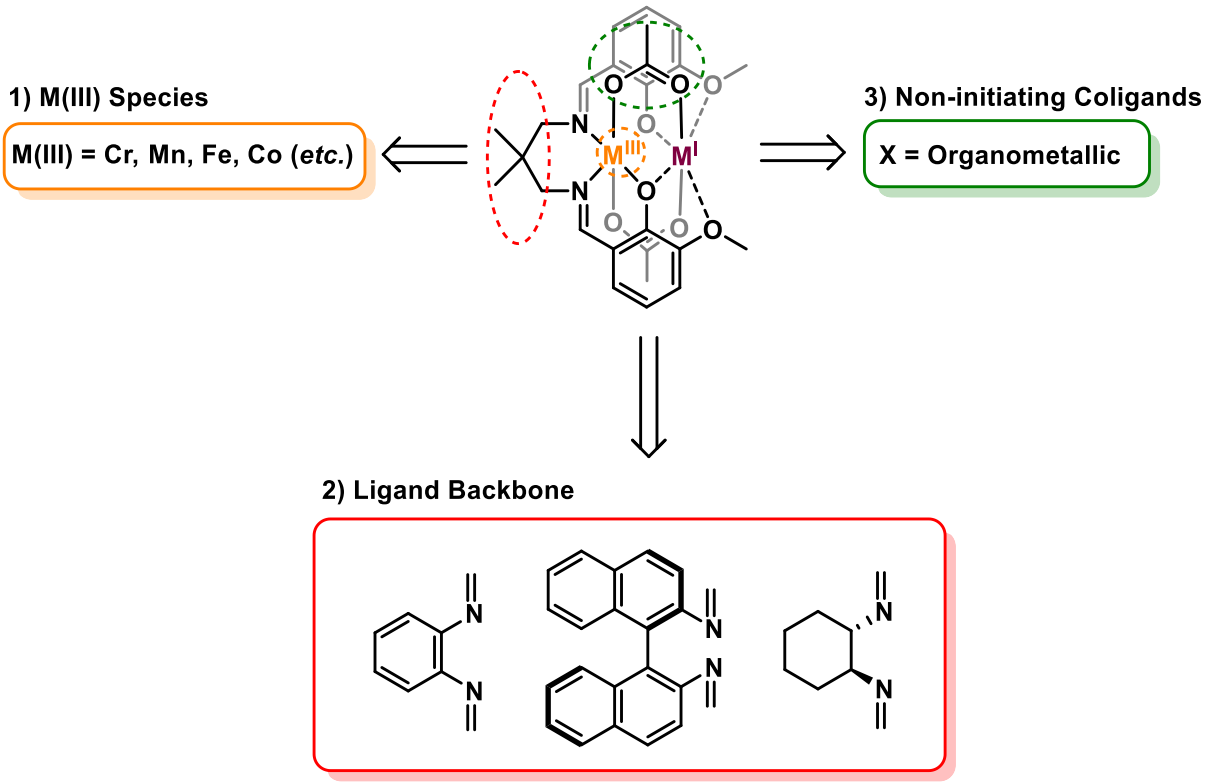


Figure 4.12. Future catalyst design directions.

4.10 References for Chapter 4

1. S. Paul, Y. Q. Zhu, C. Romain, R. Brooks, P. K. Saini and C. K. Williams, *Chem. Comm.*, 2015, **51**, 6459-6479.
2. M. E. Fieser, M. J. Sanford, L. A. Mitchell, C. R. Dunbar, M. Mandal, N. J. Van Zee, D. M. Urness, C. J. Cramer, G. W. Coates and W. B. Tolman, *J. Am. Chem. Soc.*, 2017, **139**, 15222-15231.
3. B. A. Abel, C. A. L. Lidston and G. W. Coates, *J. Am. Chem. Soc.*, 2019, **141**, 12760-12769.
4. A. C. Deacy, E. Moreby, A. Phanopoulos and C. K. Williams, *J. Am. Chem. Soc.*, 2020, **142**, 19150-19160.
5. A. C. Deacy, A. F. R. Kilpatrick, A. Regoutz and C. K. Williams, *Nat. Chem.*, 2020, **12**, 372-380.
6. W. Lindeboom, D. A. X. Fraser, C. B. Durr and C. K. Williams, *Chem. Eur. J.*, 2021, **27**, doi.org/10.1002/chem.202101140.
7. A. Thevenon, J. A. Garden, A. J. P. White and C. K. Williams, *Inorg. Chem.*, 2015, **54**, 11906-11915.
8. J. A. Garden, P. K. Saini and C. K. Williams, *J. Am. Chem. Soc.*, 2015, **137**, 15078-15081.
9. A. C. Deacy, C. B. Durr, R. W. F. Kerr and C. K. Williams, *Catal. Sci. Technol.*, 2021, **11**, 3109-3118.
10. M. Andruh, *Dalton Trans.*, 2015, **44**, 16633-16653.
11. C.-M. Chen, X. Xu, H.-Y. Ji, B. Wang, L. Pan, Y. Luo and Y.-S. Li, *Macromolecules*, 2021, **54**, 713-724.
12. G. L. Gregory, G. S. Sulley, L. P. Carrodeguas, T. T. D. Chen, A. Santmarti, N. J. Terrill, K. Y. Lee and C. K. Williams, *Chem. Sci.*, 2020, **11**, 6567-6581.
13. M. J. Sanford, L. Peña Carrodeguas, N. J. Van Zee, A. W. Kleij and G. W. Coates, *Macromolecules*, 2016, **49**, 6394-6400.
14. L. Peña Carrodeguas, C. Martín and A. W. Kleij, *Macromolecules*, 2017, **50**, 5337-5345.
15. N. Yi, T. T. D. Chen, J. Unruangsri, Y. Zhu and C. K. Williams, *Chem. Sci.*, 2019, **10**, 9974-9980.
16. T. T. D. Chen, Y. Q. Zhu and C. K. Williams, *Macromolecules*, 2018, **51**, 5346-5351.
17. M. J. Sanford, N. J. Van Zee and G. W. Coates, *Chem. Sci.*, 2018, **9**, 134-142.
18. T. Stößer, D. Mulryan and C. K. Williams, *Angew. Chem. Int. Ed.*, 2018, **57**, 16893-16897.
19. D. R. Billodeauz and D. J. Darensbourg, *Inorg. Chem.*, 2005, **44**, 1433-1442.

20. K. Nishioka, H. Goto and H. Sugimoto, *Macromolecules*, 2012, **45**, 8172-8192.

21. N. Kindermann, À. Cristòfol and A. W. Kleij, *ACS Catal.*, 2017, **7**, 3860-3863.

22. J. Deng, M. Ratanasak, Y. Sako, H. Tokuda, C. Maeda, J. Y. Hasegawa, K. Nozaki and T. Ema, *Chem. Sci.*, 2020, **11**, 5669-5675.

23. H. Li, H. T. Luo, J. P. Zhao and G. Z. Zhang, *Macromolecules*, 2018, **51**, 2247-2257.

24. R. Xie, Y. Y. Zhang, G. W. Yang, X. F. Zhu, B. Li and G. P. Wu, *Angew. Chem. Int. Ed.*, 2021, DOI: 10.1002/anie.202104981, 10.1002/anie.202104981.

25. Z. Shi, Q. Z. Jiang, Z. Z. Song, Z. H. Wang and C. L. Gao, *Polym. Chem.*, 2018, **9**, 4733-4743.

26. J. Li, Y. Liu, W.-M. Ren and X.-B. Lu, *J. Am. Chem. Soc.*, 2016, **138**, 11493-11496.

27. H. Y. Ji, B. Wang, L. Pan and Y. S. Li, *Green Chem.*, 2018, **20**, 641-648.

28. S. Zhu, Y. Wang, W. Ding, X. Zhou, Y. Liao and X. Xie, *Polym. Chem.*, 2020, **11**, 1691-1695.

29. L. Cui, B. H. Ren and X. B. Lu, *J. Polym. Sci.*, 2021, DOI: 10.1002/pol.20210334, 10.1002/pol.20210334.

30. C. A. L. Lidston, B. A. Abel and G. W. Coates, *J. Am. Chem. Soc.*, 2020, **142**, 20161-20169.

31. E. Hosseini Nejad, C. G. W. van Melis, T. J. Vermeer, C. E. Koning and R. Duchateau, *Macromolecules*, 2012, **45**, 1770-1776.

Chapter 5

Synthesis of high molar mass polyesters using non-initiating heterodinuclear complexes

5.1 Introduction

Despite the recent advances in catalyst development for the ROCOP of epoxides and anhydrides, there remains limited understanding about the materials that can be accessed *via* this methodology beyond the field of polyols (low molar mass polymers with hydroxyl end-groups).[1-4] One major challenge remains access to polyesters of sufficiently high molar mass, *i.e.* above full entanglement. Other problems include mixed end-groups and multimoldal molar mass distributions which prevent correlation of structure-property relationships. Yet another problem lies in the fact that some of the rigid, semi-aromatic polymer backbones are very difficult to process.

Overall, the impact of polymer molar mass, dispersity, and distribution modality on material properties has yet to be fully explored. The failure to understand the impact of these important properties stems from the lack of catalysts capable of synthesising high molar mass (>50 kg mol^{-1}), monodisperse polyester samples. Of the limited number of catalysts capable of synthesising polyesters with high molar masses, the vast majority give rise to bimodal polymer molar mass distributions which prohibits proper systematic investigation.[3, 5-7] To date, there is only a single catalyst reported to deliver high molar mass, monodisperse, polyesters: a phosphazene organobase, $^{t}BuP_1$.[6] Although this catalyst does exhibit good end group control, as a result of initiation occurring solely through the alcohol groups of the added chain transfer agent, it shows low activity (*e.g.* $TOF_{PA/CHO}$(**8**) = 1072 h^{-1}, $TOF_{PA/CHO}(^{t}BuP_1)$ = 48 h^{-1}, T = 100 °C). In the work describing this catalyst, there was no attempt to ascertain the material properties of the polymers produced beyond glass transition temperature (T_g). There has yet to be a catalyst that combines the required degree of end group control with high activities, which would allow for full evaluation and understanding of the properties of the resulting alternating polyesters.

5.2 Aims

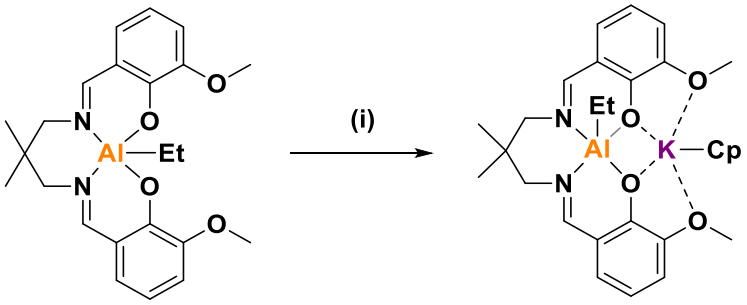
This chapter details the synthesis, characterisation, and application to alternating polyester synthesis of a heterodinuclear Al(III)/K(I) catalyst bearing organometallic coligands. In Chapter 4, a series of Al(III)/M(I) complexes were developed and shown to be highly active for the ROCOP of epoxides and anhydrides. However, these previous catalysts featured acetate coligands, which resulted in bimodal polymer molar mass distributions. This phenomenon is very common in the field of catalysis and arises from difficulties removing (at ppm level) residual water/protic impurities from the monomers.

One solution to the issue of polyester bimodality is to develop catalysts featuring organometallic coligands, since such ligands are not capable by themselves of initiating polymerizations. Rather, they must react with protic species (chain transfer agents, (CTAs)) to form *in situ* metal-alkoxide initiators.[8, 9] Provided that the CTAs selected are bifunctional, then monodisperse polymer molar mass distributions result (as the dominant monomer impurity is a diol formed by reaction of trace quantities of water with the epoxide). By exploiting this strategy, a series of monodisperse polyesters with increasing molar masses are targeted. Provided that the organometallic catalyst shows equivalent loading tolerance to the acetate complexes, it should be feasible to properly explore the thermal and material properties of these polyesters and to understand the correlation with polymer molar mass.

Another concept to test is whether, by utilising ratios of monofunctional and bifunctional alcohol CTAs, it may be possible to deliberately prepare multimodal molar mass distributions. Such a study could have several useful outcomes: firstly, it may allow deliberate targeting of the empirically obtained molar mass distributions in this field and secondly, it may allow plasticization of the higher molar mass distributions by lower mass chains and improve processability and properties of those samples.

5.3 Synthesis and Characterisation of an Organometallic Heterodinuclear Complex

In order to access a non-initiating heterodinuclear catalyst, complex **13**, featuring the same ancillary ligand and metal combinations as complex **8** but with organometallic coligands, was targeted. A synthesis route from complex **1**, which features Al(III) coordinated to an ethyl coligand was explored (Scheme 5.1). Potassium cyclopentadiene was utilised as the second organometallic species as it is both less basic and less nucleophilic than other common potassium organometallic reagents (*e.g.* KCp*, KBn). It is important to manage this nucleophilicity since there is precedent for side-reactions between nucleophilic organometallic species and the Schiff-base imines.[10]



Scheme 5.1. Synthesis of complex **13**. (i) 1.0 eq KCp, THF, RT, 30 m. Yield = 99%.

The synthesis of complex **13** was achieved through reaction of complex **1** with KCp in THF, under an inert atmosphere. The reaction progressed rapidly at room temperature, with a colour change from yellow to orange. Removal of the THF under vacuum resulted in the isolation of complex **13** as an orange powder in quantitative yield. Complex **13** was characterised by ^{1}H and ^{13}C{^{1}H} NMR and IR spectroscopy (Figures S5.1 – S5.6). Bulk purity was confirmed through elemental analysis.

The ^{1}H NMR spectrum of complex **13** is consistent with the formation of a heterodinuclear complex (Figure 5.1).

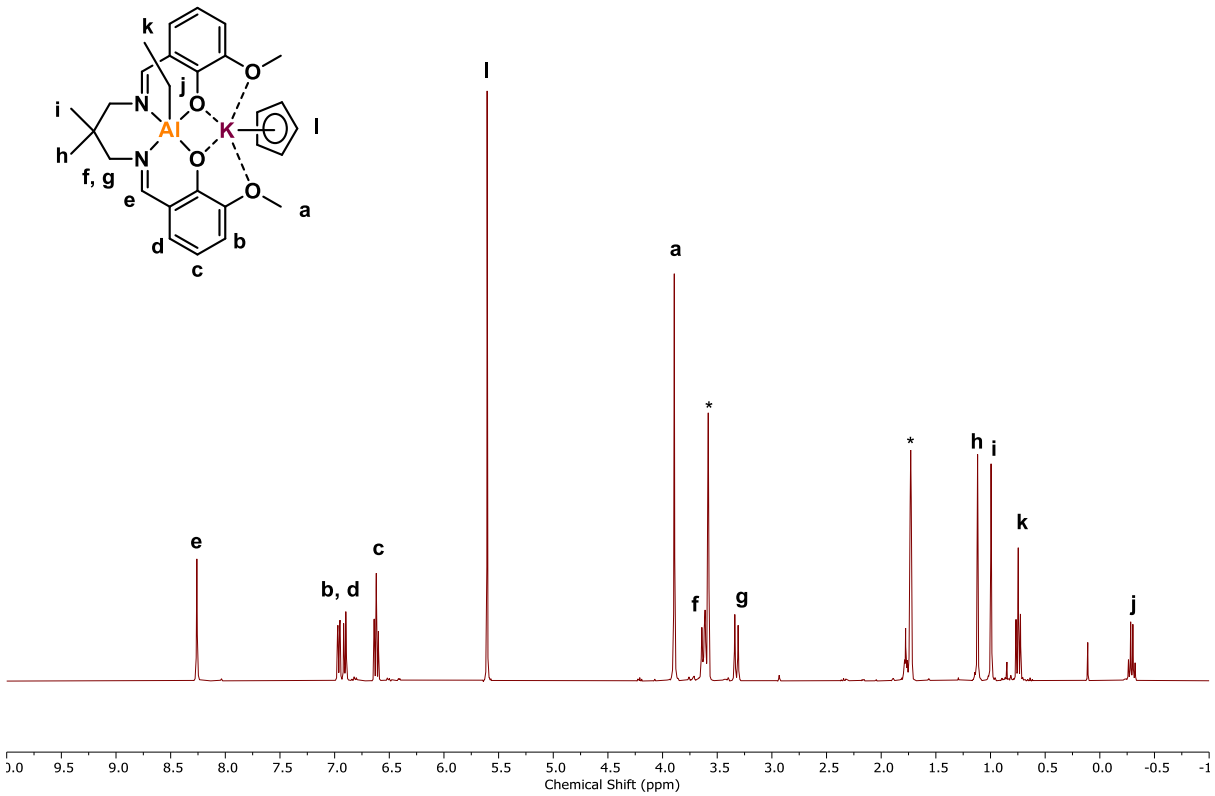
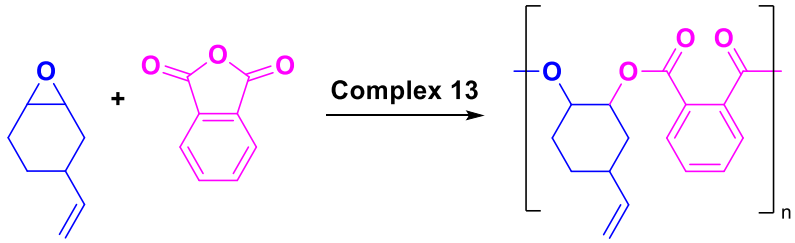


Figure 5.1. ^{1}H NMR spectrum (THF-d_8 (*), 400 MHz, 298 K) of complex **13**.

There are 9 resonances corresponding to the *ortho*-vanillin ancillary ligand, two corresponding to the ethyl coligand, and a single resonance corresponding to the cyclopentadienyl protons, suggesting an η^5-coordination mode of the latter coligand. In comparison to the ^{1}H NMR spectrum of complex **1** (in THF-d_8), there is a shift in the ethyl proton resonances from 0.97 and 0.03 ppm to 0.75 and -0.29 ppm, suggesting greater anionic character to the ethyl moiety (Figure S5.7). In comparison to complex **8**, where the two acetate coligands render both faces of the complex equivalent at room temperature, the methylene and methyl protons of the ligand backbone in complex **13** are diastereotopic, as the cyclopentadiene and ethyl coligands are different. ^{27}Al NMR spectroscopy revealed no observable aluminium resonance, suggesting that the aluminium is not in a (pseudo)octahedral coordination environment as would be expected with different coligands. The ^{13}C{^{1}H} NMR data is consistent with the proposed structure.

5.4 ROCOP of vCHO and PA with Complex 13

As the goal of developing an organometallic catalyst was to target high molar mass polyesters, it was essential to select a monomer combination that delivered experimental molar masses close to their theoretical values. In Chapter 4, Section 7, it was shown that complex **8** was capable of polymerising a wide range of epoxides and anhydrides. Many, however, showed polymer molar masses below their theoretical values. The discrepancy may be attributed to the presence of mono- and bifunctional CTAs that are present as impurities in the epoxides and anhydrides. Notably, the combinations of propylene oxide (PO) or vinyl cyclohexene oxide (vCHO) with PA both delivered polyesters with experimental polymer molar masses close to the theoretical values, indicating these monomers show relatively higher purity. With this in mind, and considering the relative activities reported for complex **8** for the two monomer combinations ($TOF_{PO/PA}$ = 25 h^{-1}, T = 60 °C; $TOF_{vCHO/PA}$ = 572 h^{-1}, T = 100 °C), the monomer combination of vCHO and PA was selected for further testing (Scheme 5.2).



Scheme 5.2. ROCOP of PA and vCHO to form poly(vinyl-cyclohexene phthalate) (PvCHPE) with complex **13**.

Firstly, it was necessary to ensure that controlled initiation from complex **13** could be achieved using bifunctional alcohol CTAs. Previous work with catalysts featuring organometallic coligands have typically utilised 4 equivalents of CTA to obtain good end group control.[8, 9] Using this starting point, copolymerisations of vCHO and PA were run with 4 equivalents of 1,4-benzenedimethanol (1,4-BDM). In order to obtain poly(vinyl-cyclohexene-*alt*-phthalate) (PvCHPE) with a molar mass suitable for MALDI-ToF

spectrometry a high (1% *vs*. anhydride) catalyst loading was used. Under these conditions, a monodisperse polyester with the expected low molar mass and low dispersity (Đ = 1.07) was obtained (Figure 5.2A). MALDI-ToF spectrometry confirmed that the polymerisation was initiated only from 1,4-BDM, and the only series of chains were α,ω-hydroxy end capped (Figure 5.2B).

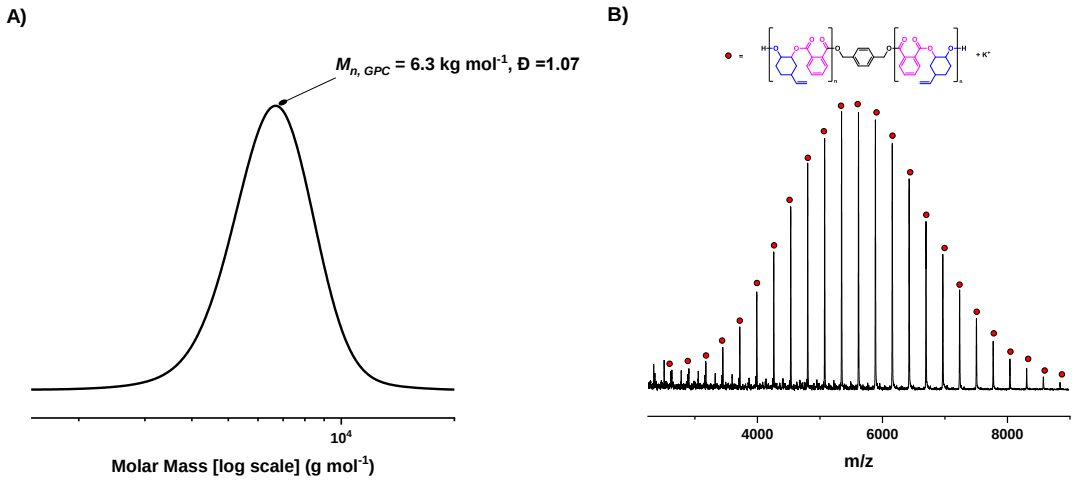


Figure 5.2. A) GPC trace of PvCHPE obtained with complex **13**. B) MALDI-ToF spectrum of PvCHPE obtained using complex **13**. Reaction conditions: [**13**]:[BDM]:[PA]:[CHO] = 1:4:100:2000, T = 100 °C.

Next, complex **13** was tested under progressively lower catalyst loadings in order to target higher molar mass polyesters (Table 5.1).

Table 5.1. Data for the ROCOP of vCHO and PA with complex **13**.[a]

Entry	[**13**]:[PA]	Time (h)	Conv.[b] (%)	TOF[c] (h^{-1})	$M_{n,\ GPC}$ [Đ][d] (kg mol^{-1})	$M_{n,\ Th.}$[e] (kg mol^{-1})	$M_{n,\ Th.\ Adj.}$[f] (kg mol^{-1})
1	400	1.25	>99	320	23.5 [1.06]	27.2	24.2
2	800	2	>99	400	43.5 [1.06]	54.5	43.6
3	1600	4	>99	400	70.1 [1.07]	108.9	72.6
4	2400	7.5	>99	320	91.0 [1.08]	163.4	93.4
5[g]	2400	4.33	99	554	92.4 [1.05]	160.1	91.5

[a] Conditions: [**13**]:[BDM]:[PA]:[vCHO] = 1:4:x:y where x is given, and x: y = 1:5, T = 100 °C. [b] Conversion of PA, determined by comparison of ^{1}H NMR resonances corresponding to PvCHPE (7.77-7.37 ppm) and PA (8.07-7.87 ppm). [c] TOF = TON/time (h), where TON = Conversion(%)*[PA], as given in table. [d] Determined by GPC in THF, at 30 °C, using narrow dispersity polystyrene standards. [e] Theoretical molar mass. Calculated *via* $M_{n,\ Th.}$ = M_n(repeat unit)*TON/[BDM]. [f] Theoretical molar weight adjusted for residual CTA. Calculated *via* $M_{n,\ Th.}$ = M_n(repeat unit)*TON/[BDM]+$[CTA]_{Residual}$, where $[CTA]_{Residual}$ is calculated to be $[CTA]_{Residual}$ [PA]:[vCHO] = 1:800:4000. [g] Reaction repeated on 1 mL epoxide scale.

All reactions were performed on a bulk scale (*ca*. 1g PA, 4.5 mL CHO) in order to prepare sufficient PvCHPE for material testing, *vide infra*. Complex **13** remained active, and displayed quantitative selectivity for polyester over polyether, at all loadings investigated, consistent with the high tolerance to catalyst loading displayed by complex **8** (Table 5.1, Entries 1 - 4). In comparison to complex **8**, slightly lower activities (TOF = 300 - 400 h^{-1} *cf*. 572 h^{-1}) were obtained which is attributed to minor issues with stirring and heating at larger scale (note these experiments were conducted at 5-fold larger scale than for **8**). When the reaction at [**13**]:[PA] = 1:2400 was repeated on an equivalent scale to that utilised for complex **8** (1 mL epoxide), an equivalent activity (TOF = 554 h^{-1}) for complex **13** was obtained, confirming that the same active species was present (Table 5.1, Entries 4 *cf*. 5).

In all cases the polyesters remained monodisperse with low dispersities (Figure 5.3). At the lowest catalyst loading, a minor shoulder in the GPC trace could be observed, attributed to initiation from a monofunctional initiator impurity, possibly vinyl-cyclohexanol, an analogue of the known cyclohexanol impurity often found in CHO.[11]

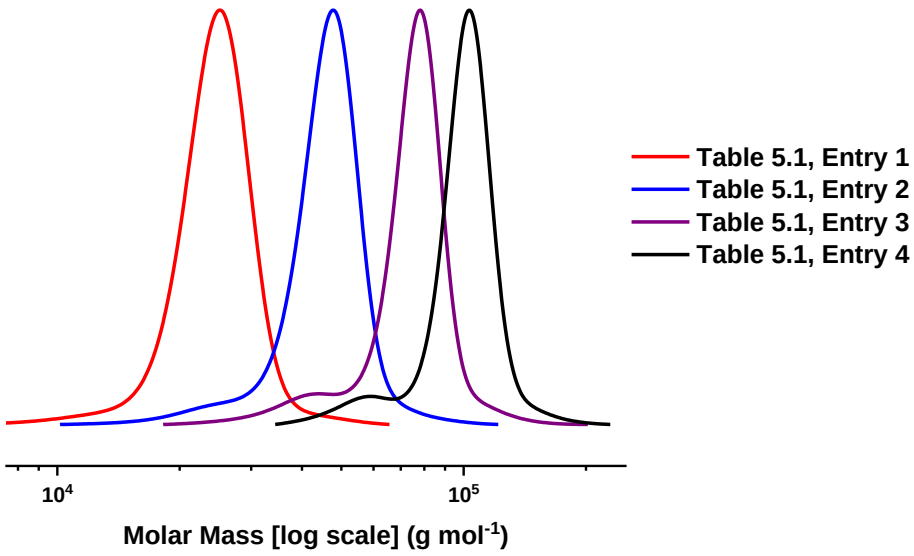


Figure 5.3. GPC traces for PvCHPE synthesised at different catalyst loadings, corresponding to Table 5.1, Entries 1 – 4.

An increasing discrepancy between the observed and theoretical molar masses was observed with progressively lower catalyst loadings, which was attributed to residual alcohols present in the monomers (Table 5.1, Entry 1 *cf.* Entry 2, 3 and 4). In order to quantify this, the ratio between the theoretical and obtained molar mass values was used to calculate the proportion of residual CTA impurities present (Figure S5.8). It was found that there was an approximate residual CTA ratio of $[CTA]_{Residual}$:[PA]:[vCHO] = 1:800:4000 (*N.b.* that since residual impurities could be introduced from either the epoxide or anhydride, the ratio of both is necessary). When this additional residual CTA was accounted for in theoretical molar mass calculations, an excellent agreement between the experimental and theoretical polymer molar masses was observed. This indicates that deviations from theoretical molar mass are due to the effect of residual CTA impurities, and are not a limit of the catalyst itself. Given that, at the lowest catalyst loadings, a minor low weight shouldering is observed, it is proposed that these residual impurities feature both mono- and bifunctional alcohol impurities.

The synthesis of polymers with monodisperse molar mass distributions and the molar masses achieved here are scarcely reported in the field. The high activity, tolerance to low loading, and excellent end group control of complex **13** allows for the controlled synthesis of these materials at gram scale, in turn allowing for study on the impact of increasing polymer molar mass on the physical and mechanical properties of these polyesters.

5.5 Thermal Properties and Processing of PvCHPE

Following the synthesis of the monodisperse molar mass series, the polyester samples were purified by precipitation (once in acidified methanol, then twice in methanol). Solvent casting of the polyesters from dichloromethane was subsequently attempted, but was unsuccessful as the polyesters were highly brittle and could not be removed from the moulds

without shattering. It should be noted that. for other high glass transition temperature polymers, processing without plasticizers/additives is very challenging.[12, 13] To investigate further, the processing of the polyesters was undertaken using a hot press. In order to ensure that the polymers would be stable to the conditions used in their processing, the polyesters' thermal properties were first investigated.

Firstly, in order to measure the glass transition temperature (T_g), and hence establish the temperatures required to process the PvCHPE, the polyesters were analysed by DSC (Figure 5.4).

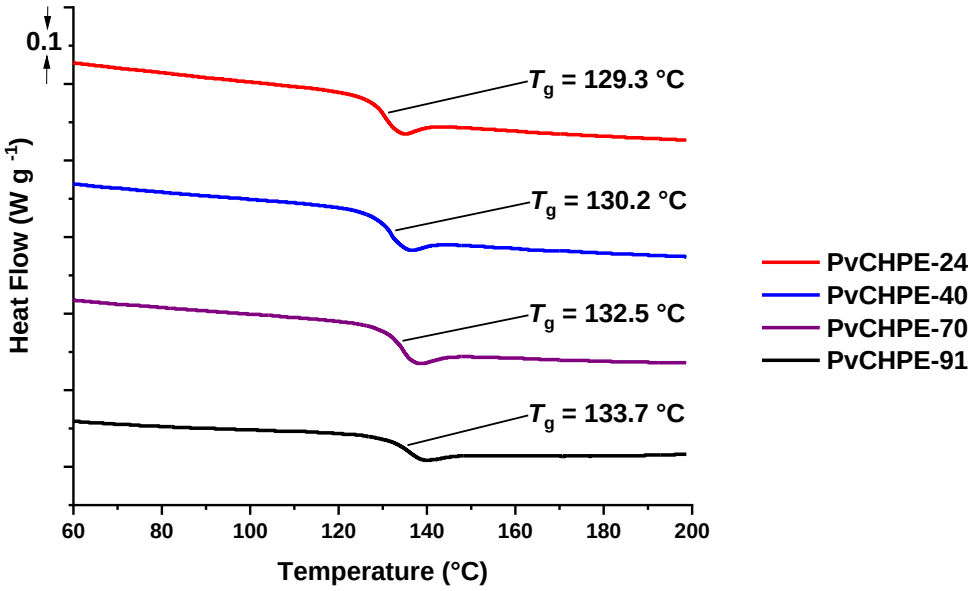


Figure 5.4. DSC traces of the PvCHPE weight series. PvCHPE-24 refers to Table 5.1, Entry 1, where a polymer with $M_{n,\,GPC}$ = 24 kg mol^{-1} (to 2 s.f.) was obtained, *etc.*

A small, but consistent increase in T_g with molar mass with observed. This finding suggested that full entanglement of the polyesters had not been achieved, indicating that there may be an improvement in the material properties across the molar mass series.

Further analysis through TGA was undertaken in order to assess the decomposition temperature ($T_{d,5\%}$) of the polyesters, and to ensure that they were suitably purified (Figures S5.9 – S5.12). A $T_{d,5\%}$ of 290 – 303 °C was obtained for all samples, confirming both that

the catalyst had been successfully removed from all samples, and also indicating that a processing window of *ca*. 150 °C (T_g ~ 130 °C, $T_{d,5\%}$ ~ 290 °C) was feasible for these polyesters.

Following this the polyesters were processed *via* hot-press. A temperature of 140 °C was used, and 4 metric tonnes of pressure applied, to a mould with 4 x ~300 mg of polyester sample for 45 minutes, which resulted in the clean formation of processed film. From these films, uniform bars with dimensions of ~15 mm * ~5 mm * ~0.3 mm (l*w*d) were prepared for all polyester samples except for PvCHPE-24, which was too brittle to be cut, and shattered readily (Figure 5.5).

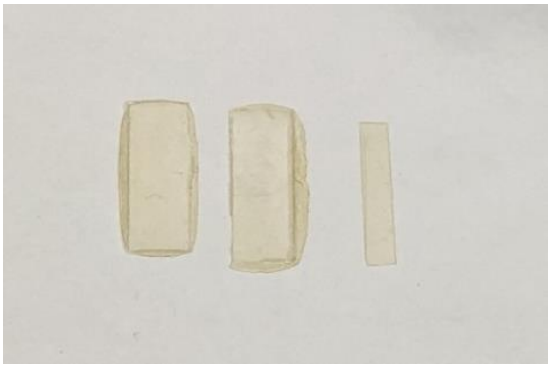


Figure 5.5. Polymer films of PvCHPE-91 obtained *via* hot press. LHS: Films obtained directly from hot press. RHS: typical bar used in DMTA analysis (*vide infra*).

It was important to establish that the polymers had not been adversely affected by the processing conditions applied. Comparison of the ^{1}H NMR resonances associated with the vinyl protons of the vCHO within the polyester before and after hot pressing saw no reduction in their intensity relative to the aliphatic protons within the polymer chain, indicating no significant cross linking had occurred (Figures S5.13 – S5.16). GPC analysis of these samples confirmed that minimal sample degradation had occurred. (Figures 5.6 and S5.17 – S5.19).

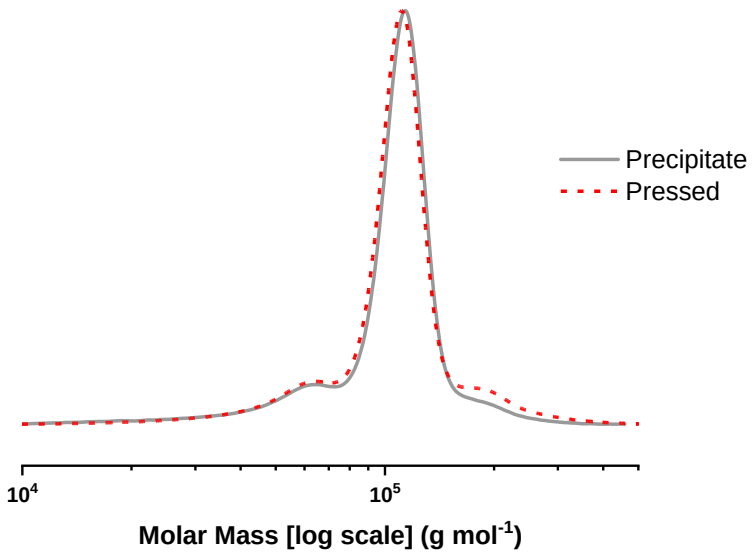


Figure 5.6. GPC Trace of PvCHPE-91 before and after processing *via* hot press.

5.6 Mechanical Properties of PvCHPE

The successful production of films for PvCHPE-44, -70 and -91 allowed for mechanical testing. The samples were subsequently applied to DMTA to measure the storage and loss moduli and hence tan(δ). The representative DMTA data for PvCHPE-91 is presented (Figure 5.7 and S5.20 – S5.21 and Table 5.2).

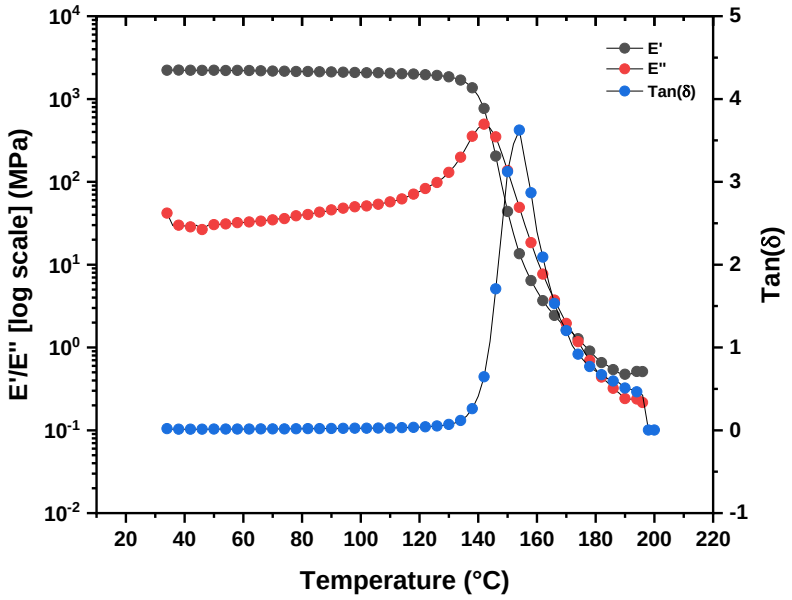


Figure 5.7. Results from DMTA of PvCHPE-91 between 30 – 200 °C. Storage Modulus (E'), Loss Modulus (E''), and Tan(δ) presented. See Appendix for DMTA plots corresponding to other PvCHPE samples.

Table 5.2. Data for PvCHPE weight series from DMTA.

Entry	Polymer	Storage Modulus[a] (GPa)	Loss Modulus[b] (MPa)	$T_{g,\ Tan(\delta)}$[c] (°C)	$T_{g,\ E''}$[d] (°C)
1	PvCHPE-24	-	-	-	
2	PvCHPE-44	1.71 ± 0.07	53.6 ± 13.9	*N.d.*	*N.d.*
3	PvCHPE-70	2.01 ± 0.10	35.9 ± 9.1	152	140
4	PvCHPE-91	2.12 ±0.08	26.7 ± 3.2	153	142

[a] Measured at 60 °C, each measurement repeated in triplicate, average values reported with error $\pm\sigma/\sqrt{n}$. [b] Measured at 60 °C, each measurement repeated in triplicate, average values reported with error $\pm\sigma/\sqrt{n}$. [c] T_g estimated from the peak in Tan(δ). [d] T_g estimated from the peak of the loss modulus.

The materials were found to display very high storage moduli (>1 GPa), and low loss moduli (<100 MPa), and as such fall into the sub-class of rigid plastics. A 25% increase in storage modulus was observed with increasing molar mass (PvCHPE-44 to PvCHPE-91), demonstrating the importance of this catalysis strategy in optimizing material performance (Table 5.3, Entry 2 *cf.* 4). For PvCHPE-91 and PvCHPE-70 the T_g as estimated through tan(δ) was ~152 °C (Table 5.2, Entries 3 and 4). The T_g as estimated through the peak in loss modulus is found to be around 10 degrees lower (Table 5.33, Entries 3 and 4), closer to the values obtained from DSC. In both cases the trends follow those observed with DSC *i.e.*

a small increase with increasing polymer molar mass. The T_g for PvCHPE-44 could not be established through DMTA due to sample yielding (Figure S5.20).

The increase in storage modulus demonstrates an advantage of synthesising high weight polyesters, which is consistent with the notion that full entanglement has not been reached, even at polymer molar masses of 100 kg mol^{-1}. The application of these materials to triblock copolymers should be explored; it has previously been demonstrated that triblock PCHPE-*b*-PDL-*b*-PCHPE saw significant increases in material properties in increasing weights from *ca*. 60 kg mol^{-1} to 100 kg mol^{-1}.[14] Use of complex **13** should allow access to significantly higher weight triblock copolymers than those developed in this work (*ca*. 100 kg mol^{-1} hard block alone), and the work presented here demonstrates that there is an impact on material properties with increasing the molar mass of hard-block segments.

5.7 Controlling Bimodality in Epoxide/Anhydride ROCOP

A further area of polyester chemistry that currently remains unexplored is the impact of bimodality on polymer properties. Although many catalysts yield bimodal polymer molar mass distributions as a result of monofunctional initiating coligands and cocatalysts, they are not able to achieve any particular control over this bimodality. Given that complex **13** was capable of obtaining monodisperse polymer molar mass distributions with 4 equivalents of 1,4-BDM, it was reasoned that, by adding a monofunctional alcohol, the degree of bimodality could be effectively controlled. To investigate this, polymerisation of PA and vCHO were run with varying ratios of methylbenzyl alcohol (MBA) and 1,4-BDM (Table 5.3).

Table 5.3. Controlled bimodality using various ratios of mono- and bifunctional CTAs.[a]

Entry	[MBA]:[BDM]	$M_{n,\,GPC}$ [Đ][b] (kg mol^{-1})	Wt.%$_{GPC}$[c]	Wt.%$_{Th.}$[d]
1	0:4	43.5 [1.08]	100	100
2	1.5:4	20.6 [1.04], 45.1 [1.05]	18, 82	16, 84
3	4.5:2.5	21.3 [1.04], 43.5 [1.03]	46, 54	47, 53

[a] Conditions: [**13**]:[MBA]:[BDM]:[PA]:[vCHO] = 1:x:y:800:4000, where x and y are given, T = 100 °C, 1 mL vCHO, reactions run to complete PA conversion. [b] Determined by GPC in THF, at 30 °C, using narrow dispersity polystyrene standards. [c] Experimental weight percentage of the lower and upper (respectively) polymer molar mass peaks. Determined by GPC in THF, at 30 °C. [d] Theoretical weight percentage of lower and upper polymer molar mass peaks. Determined *via* Wt%$_{upper}$ = ([BDM]*2/[BDM]*2+[MBA])*100. Wt%$_{lower}$ = 100-Wgt%$_{upper}$.

It was demonstrated that effective control of the bimodality could be obtained through control of the feed ratios of CTA (Figure 5.8). Excellent agreement between the experimental and theoretical weight percentages were found in all cases (Table 5.3, Entries 2 and 3). The ability to synthesise controlled bimodal distributions in one-pot, simply by altering the ratios of CTA applied, has not previously been reported. It provides a route to a range of polymer distributions where previously manual blending of polymer samples was required.[15]

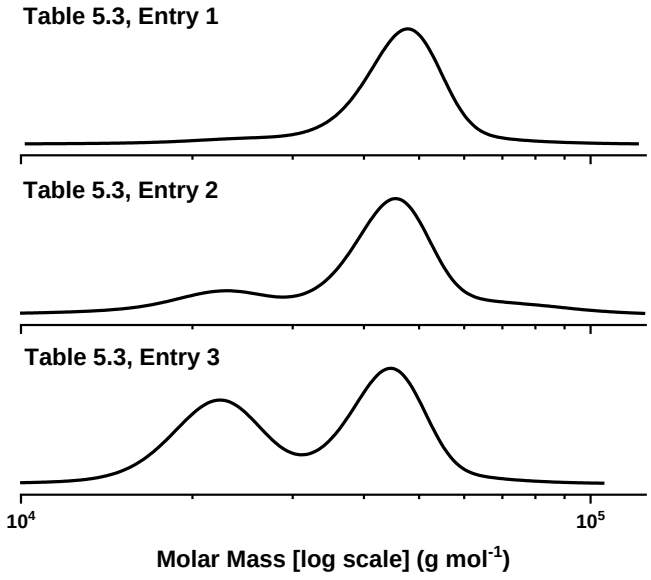


Figure 5.8. GPC traces of bimodal PvCHPE corresponding to Table 5.3, Entries 1, 2 and 3.

5.8 Conclusion and Outlook

A novel heterodinuclear complex with organometallic coligands (**13)** was synthesised and characterised. It was subsequently applied to the ROCOP of vCHO and PA, and it was demonstrated that monodisperse polymer molar mass distributions could be obtained with four equivalents of 1,4-BDM, a bifunctional alcohol CTA. Subsequent application of complex **13** to progressively lower catalyst loadings resulted in the synthesis of PvCHPE with a series of increasing molar masses. The thermal and mechanical properties of these polyesters were investigated to establish whether significant improvements in properties were obtained by accessing higher weight materials. It was also demonstrated that complex **13**, in conjunction with a mixed CTA system (MBA/1,4-BDM) could be used to generate bimodal polymer molar mass distributions with controlled degrees of the two different molar mass distributions.

The work presented in this Chapter presents a proof-of-concept study in the application of heterodinuclear complexes with organometallic coligands to the controlled synthesis of polyesters. There exist several areas of further research that should be explored to build on the results presented. Firstly, further mechanical testing should be carried out on the different polymer molar mass series synthesised here to help further establish the properties for these products. In particular, tensile testing would be valuable, but issues with processing suitable 'dog-bones' have prevented progress in these investigations so far. Following this, mechanical testing should be carried out on a series of polyesters with varied bimodal distributions in order to determine whether any self-plasticisation is observed – such a phenomenon could prove quite useful in reducing the need for additives. One major problem of small-molecule plasticizers is their mobility which compromises properties over time; the major problem of polymeric plasticizers is ensuring sufficient compatibility with the host polymer – both problems would be overcome by self-plasticization.

A further application of controlled bimodality is to combine the concept with switchable catalysis. Many commercial thermoplastic elastomers comprise mixtures of both triblock and diblock polymers, with the diblock components plasticising the majority triblock component.[16] Triblock copolymers of PCHPE-*b*-PDL-*b*-PCHPE have recently been shown to be effective thermoplastic elastomers.[14] Complex **13** could be utilised with a mixed CTA feedstock of both mono- and bifunctional alcohols (such as MBA and 1,4-BDM used herein) to deliver multimodal distributions of these thermoplastic elastomers (*i.e.* PCHPE-b-PDL and PCHPE-b-PDL-b-PCHPE), in order to establish how this impacts the material properties of these polyesters.

5.9 References for Chapter 5

1. J. M. Longo, M. J. Sanford and G. W. Coates, *Chem. Rev.*, 2016, **116**, 15167-15197.
2. C. A. L. Lidston, B. A. Abel and G. W. Coates, *J. Am. Chem. Soc.*, 2020, **142**, 20161-20169.
3. B. A. Abel, C. A. L. Lidston and G. W. Coates, *J. Am. Chem. Soc.*, 2019, **141**, 12760-12769.
4. L. Cui, B. H. Ren and X. B. Lu, *J. Polym. Sci.*, 2021, DOI: 10.1002/pol.20210334, 10.1002/pol.20210334.
5. R. Xie, Y. Y. Zhang, G. W. Yang, X. F. Zhu, B. Li and G. P. Wu, *Angew. Chem. Int. Ed.*, 2021, DOI: 10.1002/anie.202104981, 10.1002/anie.202104981.
6. H. Li, H. T. Luo, J. P. Zhao and G. Z. Zhang, *Macromolecules*, 2018, **51**, 2247-2257.
7. X. Yu, J. Jia, S. Xu, K. U. Lao, M. J. Sanford, R. K. Ramakrishnan, S. I. Nazarenko, T. R. Hoye, G. W. Coates and R. A. DiStasio, Jr., *Nat. Commun.*, 2018, **9**, 2880.
8. G. S. Sulley, G. L. Gregory, T. T. D. Chen, L. P. Carrodeguas, G. Trott, A. Santmarti, K. Y. Lee, N. J. Terrill and C. K. Williams, *J. Am. Chem. Soc.*, 2020, **142**, 4367-4378.
9. T. T. D. Chen, Y. Q. Zhu and C. K. Williams, *Macromolecules*, 2018, **51**, 5346-5351.
10. H. Yang, Y. Ingen, B. Blom, S. Rastogi and D. Romano, *ChemCatChem*, 2020, **12**, 5209-5220.
11. J. Deng, M. Ratanasak, Y. Sako, H. Tokuda, C. Maeda, J. Y. Hasegawa, K. Nozaki and T. Ema, *Chem. Sci.*, 2020, **11**, 5669-5675.
12. C. Koning, J. Wildeson, R. Partona, B. Pluma, P. Steemana and D. D. J., *Polymer*, 2001, **42**, 3995-4004.
13. O. Hauenstein, S. Agarwal and A. Greiner, *Nat Commun*, 2016, **7**, 11862.
14. G. L. Gregory, G. S. Sulley, L. P. Carrodeguas, T. T. D. Chen, A. Santmarti, N. J. Terrill, K. Y. Lee and C. K. Williams, *Chem. Sci.*, 2020, **11**, 6567-6581.
15. R. Whitfield, N. P. Truong and A. Anastasaki, *Angew Chem Int Ed Engl*, 2021, **60**, 19383-19388.
16. Kraton Polymer Data Documents, 2021, https://www.kraton.com/products/KRATON_D_SIS.php.

Chapter 6

Thesis conclusions and outlook

6.1 Thesis Summary

The thesis has principally detailed the development of catalysts for the ROCOP of epoxides and anhydrides (Figure 6.1). Application of these catalysts to the ROP of ε-DL, and hence switchable catalysis, was also explored. The work presented expands on existing catalyst performance in two main areas:

1) Monometallic catalysts for the switchable catalysis of epoxides, anhydrides and lactones.

   A series of monometallic(III) (M = Al, Cr, Mn, Fe, Co) Schiff-base complexes were developed and characterised. It was found that catalyst systems containing the Al(III) and Co(III) complexes were active for both the ROCOP of CHO and PA (TOFs = 348 and 516 h^{-1} respectively, 1% *vs*. anhydride, T = 100 °C), and the ROP of ε-DL (TOFs = 330 and 64 h^{-1} respectively, 0.5% *vs*. lactone, T = 100 °C), and hence were capable of yielding triblock copolymers from a one-pot reaction of the three monomers *via* switchable catalysis. Using the Al(III) catalyst, triblock copolymers with molecular masses up to 57 kg mol^{-1} were obtained in significantly reduced reaction times compared to many other catalysts reported for switchable catalysis. These results highlight the importance of developing catalysts that are efficient at catalysing both polymerisation cycles used in switchable catalysis (epoxide/anhydride ROCOP and lactone ROP).

2) Heterodinuclear catalysts for the ROCOP of epoxides and anhydrides.

   A series of heterodinuclear Al(III)/M(I) (M = Na, K, Rb, Cs) complexes were developed and characterised. All complexes displayed very high activity for the ROCOP of CHO and PA, with the best performing being the Al(III)/K(I) and Al(III)/Rb(I) congeners (TOFs = 1072 and 1136 h^{-1} respectively, 0.25% *vs*. anhydride, T = 100 °C). In further studies with the Al(III)/K(I) complex, an exceptional loading tolerance and broad scope for the ROCOP of a range of epoxides with anhydrides or CO_2 was demonstrated. A mechanism involving the Al(III) binding and activating an epoxide molecules, with the K(I) ion binding the

carboxylate polymer chain in close proximity before insertion, during the rate determining step was proposed based on combined kinetic, structure-activity and DFT studies. These results establish the effectiveness of heterodinuclear catalysts for the ROCOP of epoxides and anhydrides.

Subsequent work developed an analogue of the novel heterodinuclear Al(III)/K(I) complex that possessed organometallic coligands. Use of this complex, in combination with bifunctional protic CTAs, allowed for the synthesis of high molecular mass polyesters with monodisperse molecular mass distributions. In turn, this allowed for investigation in to the impact of molecular mass on polyester properties.

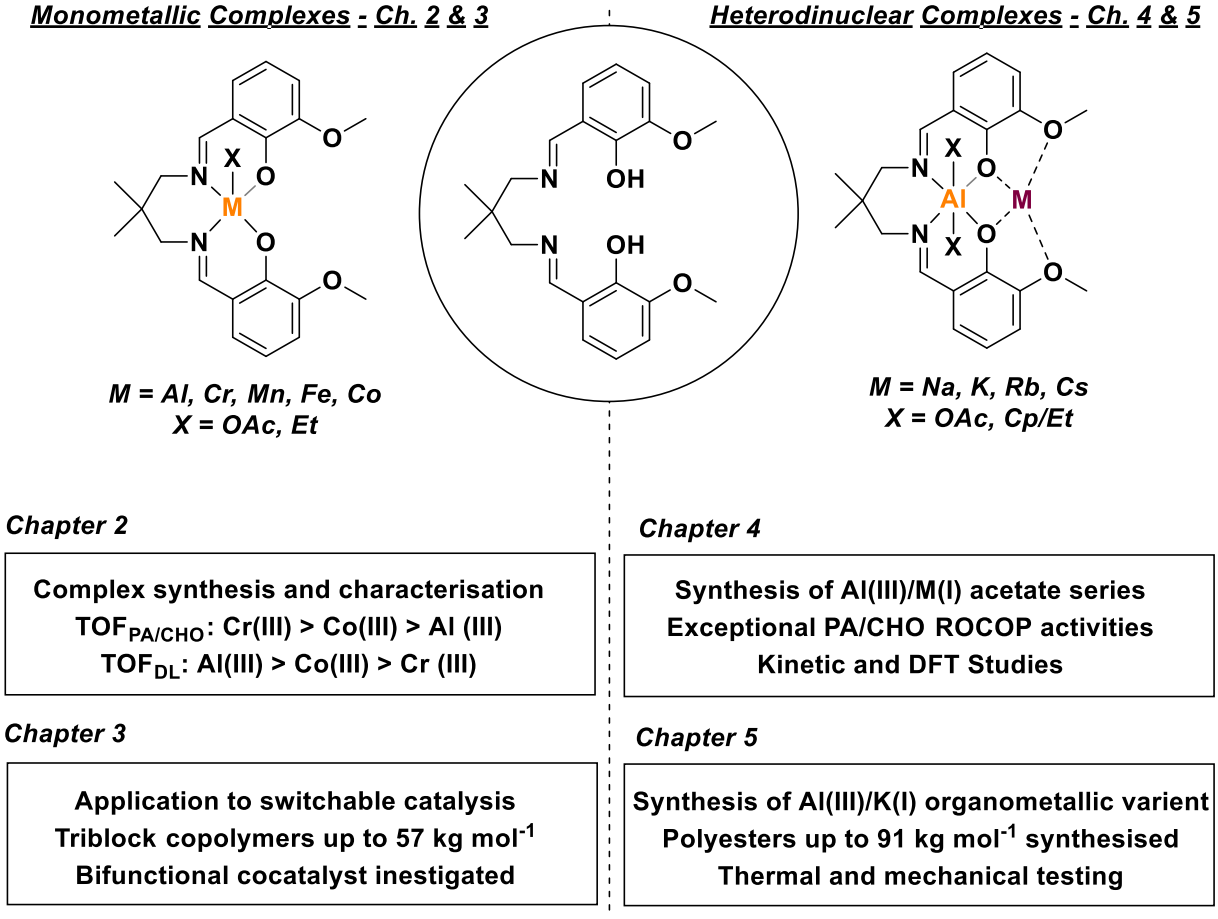


Figure 6.1. Thesis summary

6.2 Outlook

6.2.1 Future Catalyst Design

The work in this thesis shows the significant potential for heterodinuclear catalysts for the ROCOP of epoxide and anhydrides. Alongside the alterations proposed to the current ligand/metal set that are proposed in Chapter 4, Section 9, which would serve to optimise catalytic activities, other aspects catalyst designs should be probed (Figure 6.2).

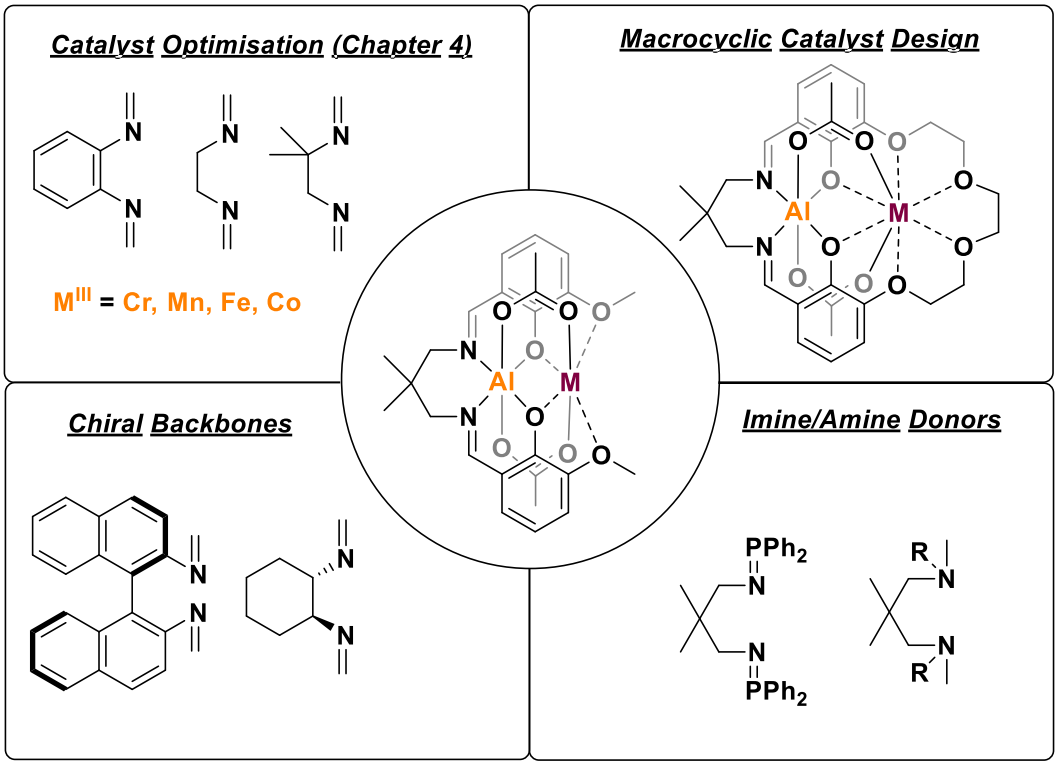


Figure 6.2. Proposed future catalyst designs. Top left: Initial optimisation of catalyst based on simple ligand backbone and metal alterations. Top right: macrocyclic analogue of complex **8**. Bottom left: development of complexes with chiral backbones. Bottom right: altering the donor capacity of the ligand.

Heterodinuclear Co(III)/M(I) complexes have been shown to be highly active for the ROCOP of epoxides and CO_2.[1, 2] Synthesis of a series of complexes featuring Al(III)/M(I) should be targeted since the ancillary ligands appears successful in enabling dinuclear complex formation. Such dinuclear catalysts should be investigated for the ROCOP of epoxides and anhydrides. It seems likely that such catalysts would show both greater temperature stability, in comparison to Co(III) containing catalysts, and allow for investigation into the effect of

macrocyclic coordination environments on catalytic activity, especially in contrast to the more 'open' coordination environment of the *ortho*-vanillin derived ligand used in this work.

There are several further alterations that could be made to the ligand design to allow for more complex applications of these novel heterodinuclear systems. Firstly, the development of complexes with chiral diamine backbones should be investigated. These complexes should be applied to stereoselective polymerisations or those using pro-chiral monomers, e.g. using propylene oxide. In addition, the capability for the complexes to enantioselectively polymerise monomers from racemic mixtures should be targeted.[3, 4] This could potentially allow for the formation of isotactic polyesters which may be semi-crystalline and even stereoblock polyesters (from *rac*-monomer with stereo-controlled catalysts).

Further ligand modifications should involve altering the donor capacity of the nitrogen atoms.[5-7] Given that it is proposed that the M^{III} centre of the heterodinuclear complex binds, and activates the epoxide during the rate determining step, altering the Lewis acidity of the metal is expected to offer significant differences in activity. These catalysts should also be trialled for epoxide/CO_2 ROCOP as altering the metal Lewis acidity would be expected to affect the selectivity for polycarbonate over cyclic carbonate by-products.[7]

6.2.2 Advanced Polyester Synthesis and Further Application

Although recent strides have been made with regards to catalysts for polyester production *via* ROCOP, a key issue remains in establishing the application of the materials that can be accessed with this methodology. To this end, there are several important areas that should be investigated (Figure 6.3). Utilising the organometallic complex **13** described in Chapter 5 will be an important aspect of this work, as its combined exceptional activity and tolerance to low catalyst loadings allows for the synthesis of polyesters with both molar masses and dispersity control that is currently unmatched.

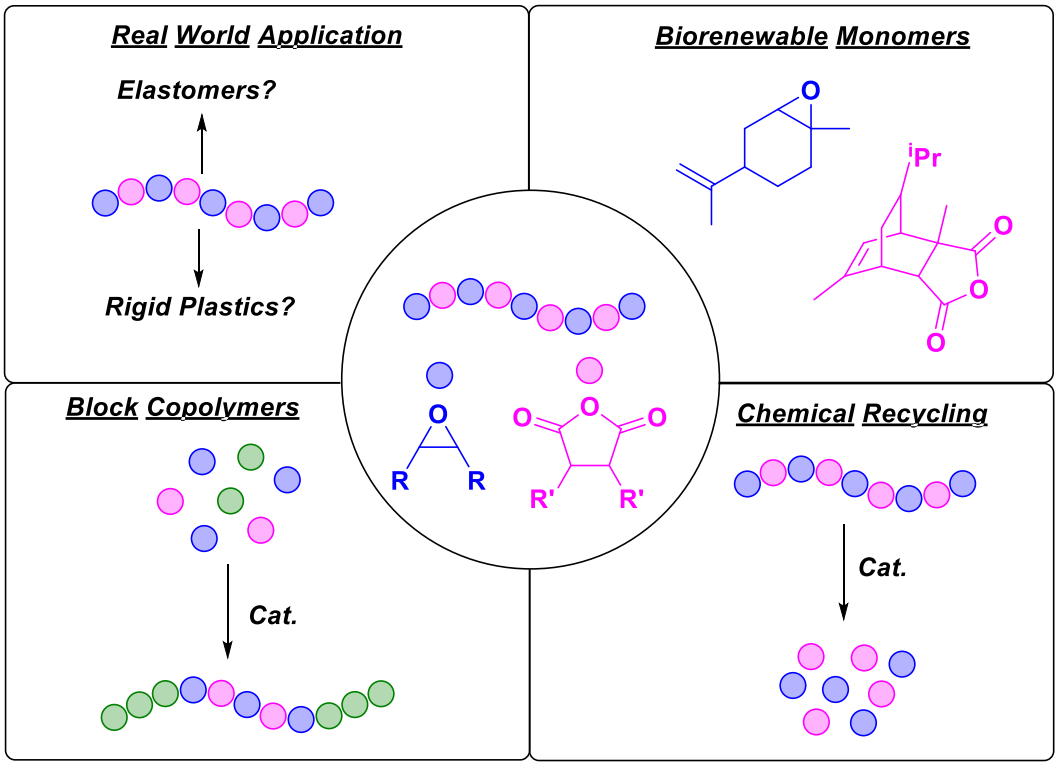


Figure 6.3. Proposed future research on polyesters. Top Left: Applications of polyesters. Top Right: Biorenewable monomers that should be incorporated in to polyester materials. Bottom Left: Block copolymers featuring high weight ROCOP derived polyesters. Bottom Right: Chemical recycling to monomer (CRM) of polyesters.

There should be further investigation into application of the alternating polyesters derived from epoxide/anhydride ROCOP, with a particular focus on establishing the impact of molecular mass and dispersity on overall polymer properties. In addition to this, there should be a renewed focus on accessing polymers with biorenewable monomers (such as limonene oxide and tricyclic anhydrides). Demonstrating that appropriate polyester materials can replace current polyolefin derived plastics, in tandem with utilising monomers that are not derived from petrochemicals, would be a significant development.[8]

Alongside, this investigation, application of these high molecular mass polymers should be applied to the formation of block copolymers, both through switchable catalysis with epoxide/anhydride/lactone and terpolymerisations of with epoxide/anhydride/CO_2.[9] Previous work has established the use of triblock polyesters as thermoplastic elastomers, but using the

catalysts developed here even higher weights of block copolymer, and block polymers with targeted multimodal distributions, could be accessed.[10]

A further target for investigation should be the application of CRM (chemical recycling to monomer) to ROCOP polyesters. Although it has been demonstrated that triblock PCHPE-*b*-PDL-*b*-PCHPE can be decomposed using relatively mild conditions (2 wt% polymer in toluene, 6 mM *para*-toluenesulphonic acid, 60 °C) the products were largely oligomeric chains over the base feedstock molecules.[10] Investigations into the application of catalysts to depolymerisation of polyesters is well warranted, as it would provide a further motivation for use of polyesters over traditional polyolefin-based materials.[11]

6.3 References for Chapter 6

1. A. C. Deacy, E. Moreby, A. Phanopoulos and C. K. Williams, *J. Am. Chem. Soc.*, 2020, **142**, 19150-19160.
2. W. Lindeboom, D. A. X. Fraser, C. B. Durr and C. K. Williams, *Chem. Eur. J.*, 2021, **27**, doi.org/10.1002/chem.202101140.
3. J. Li, Y. Liu, W.-M. Ren and X.-B. Lu, *J. Am. Chem. Soc.*, 2016, **138**, 11493-11496.
4. J. Li, B. H. Ren, Z. Q. Wan, S. Y. Chen, Y. Liu, W. M. Ren and X. B. Lu, *J. Am. Chem. Soc.*, 2019, **141**, 8937-8942.
5. N. Yuntawattana, T. M. McGuire, C. B. Durr, A. Buchard and C. K. Williams, *Catal. Sci. Technol.*, 2020, **10**, 7226-7239.
6. A. Thevenon, A. Cyriac, D. Myers, A. J. P. White, C. B. Durr and C. K. Williams, *J Am Chem Soc*, 2018, **140**, 6893-6903.
7. A. Thevenon, J. A. Garden, A. J. P. White and C. K. Williams, *Inorg. Chem.*, 2015, **54**, 11906-11915.
8. T. T. D. Chen, L. P. Carrodeguas, G. S. Sulley, G. L. Gregory and C. K. Williams, *Angew. Chem. Int. Ed.*, 2020, **59**, 23450-23455.
9. G. Rosetto, A. C. Deacy and C. K. Williams, *Chemical Science*, 2021, DOI: 10.1039/d1sc03856g, 10.1039/d1031sc03856g.
10. G. L. Gregory, G. S. Sulley, L. P. Carrodeguas, T. T. D. Chen, A. Santmarti, N. J. Terrill, K. Y. Lee and C. K. Williams, *Chem. Sci.*, 2020, **11**, 6567-6581.
11. S. Kakadellis and G. Rosetto, *Science*, 2021, **373**, 49-50.

Chapter 7

Experimental details

7.1 General Considerations

All manipulations, unless otherwise stated, were carried out under an inert atmosphere utilising a dual manifold vacuum-nitrogen Schlenk line or nitrogen-filled glovebox. Solvents used for air-sensitive synthesis were collected from a solvent purification system (SPS), degassed with freeze-pump-thaw cycles and stored over 3 Å molecular sieves, under an inert atmosphere.

Triethyl aluminium (Sigma Aldrich 93%), chromium acetate monohydrate dimer (Insight Biotechnology), manganese(II) acetate (98%, Sigma Aldrich), iron(II) acetate (95%, Sigma Aldrich) and cobalt (II) acetate tetrahydrate (99.999%, Sigma Aldrich) were used as received. Group 1 Metal acetate salts (M = Na, K, Rb, Cs) were purchased from Sigma Aldrich or Acros Organics and dried under vacuum at 100 °C for 16 hours before use. All materials were stored under a nitrogen atmosphere, in a glovebox.

The *ortho*-vanillin derived proligand, [$L_{van}H_2$], used throughout this thesis was synthesised through a Schiff base condensation of 2,2-dimethyl-1,3-propanediamine and *ortho*-vanillin.[1] The salen proligand, [$L_{sal}H_2$], utilised in Chapter 4 was synthesised following a literature procedure.[2]

Potassium cyclopentadiene was synthesised following a literature procedure.[3] At room temperature, under an inert atmosphere, freshly cut metallic potassium was slowly added to neat dicyclopentadiene (Sigma Aldrich) in a 3-necked Schlenk flask with reflux condenser attached under continuous nitrogen flow. This mixture was subsequently heated to 160 °C. Under these conditions, the dicyclopentadiene undergoes a retro-cycloaddition, resulting in the formation of cyclopentadiene. This cyclopentadiene reacts with the metallic potassium, generating potassium cyclopentadiene which precipitates from the reaction solution, with concomitant hydrogen gas evolution. The reaction was left until evolution of hydrogen was observed to have stopped, and then heated for a further 30 minutes to ensure complete

potassium consumption. The remaining reaction solution was filtered, and the precipitate washed with pentane before being dried under vacuum, yielding potassium cyclopentadiene as a pale pink powder.

7.2 General Polymerisation Procedures

Inside a nitrogen filled glovebox, the catalyst and desired monomers were added to a dried vial equipped with a magnetic stirrer bar. The vial was sealed with a melamine-cap containing a Teflon inlay, and further sealed with first Parafilm M and then electrical insulation tape. This sealed vial was then heated to 100 °C for the time stated. Aliquoting was performed by first cooling the polymerisation vial in a cold water bath, before removing *ca.* 10 μL of the polymerisation mixture with a syringe in the glovebox. The polymerisations were quenched by exposing the reaction mixture to air, followed by removal of volatiles. A 1H NMR spectrum of the crude product was measured in CDCl3. GPC samples were prepared by dissolving *ca.* 10 mg of the crude product in 1 mL HPLC grade THF and filtered before use. Polymers were purified by precipitation from methanol and dried under vacuum at 40 °C.

7.3 End Group Analysis by $^{31}P\{^{1}H\}$ NMR Spectroscopy

Analysis of the hydroxyl polymer end groups was carried out following a reported procedure.[4] In an NMR tube, the triblock polyester (40 mg), purified via precipitation from methanol, was added to a stock solution (40 μL of a solution make from pyridine (10 mL), bisphenol A (400 mg) and $Cr(acac)_3$ (5.5 mg) and 2-chloro-4,4,5,5- tetramethyldioxaphospholane (40 mg), in $CDCl_3$ (0.5 mL). The mixture was allowed to react at room temperature for 6 hours before $^{31}P\{^{1}H$ NMR spectra were recorded.

7.4 Monomer Purification Procedures

Epoxides (cyclohexene oxide (CHO, Acros Organics), propylene oxide (PO, Sigma Aldrich), vinyl cyclohexene oxide (vCHO, Sigma Aldrich), *tert*-butyl glycidyl ether (tBGE, Sigma Aldrich), allyl glycidyl ether (AGE, Sigma Aldrich) and styrene oxide (SO, Sigma Aldrich) were purified by stirring over calcium hydride followed by fractional distillation. For CHO further purification, necessary for the synthesis of the high molar mass block copolymers in Chapter 3 was, was carried out according to the method reported by Greiner and co-workers.[5] Firstly, sodium hydride was added to CHO under an inert atmosphere, and the solution stirred for 30 minutes at 0 °C. Subsequently, methyl iodide was added and the suspension was stirred overnight at room temperature, before being fractionally distilled to isolate the CHO. The sodium hydride acts as both a drying agent, and deprotonates any residual alcohols present, which are methylated upon addition of methyl iodide. The collected CHO was then further purified by twice repeated stirring over calcium hydride and fractional distillation.

Epsilon-decalactone (ε-DL, Sigma Aldrich) was purified by stirring over calcium hydride, followed by fraction distillation at 130 °C under reduced pressure.

Phthalic anhydride (PA, Sigma Aldrich) was purified through a three-step procedure. Under inert conditions, PA (15 g) was stirred in dry toluene (500 mL) for 16 hours at room temperature. The supernatant was filtered, and solvent removed to yield a white powder. This white powder was recrystallised from hot (60 °C) chloroform, and subsequently sublimed under vacuum at 80 °C. Norbornene anhydride (NBA, Acros Organics) was purified by recrystallisation from dry ethyl acetate, followed by sublimation under vacuum at 80 °C. Tricyclic anhydride (TCA) was synthesised according to the method reported by Mathers and co-workers was purified by recrystallisation from dry hexane followed by sublimation under vacuum at 80 °C.[6]

Research-grade carbon dioxide (BOC, 99.99%) was passed through a drierite column and then two subsequent drying columns (Micro Torr, Model No: MC1-804FV) before use in copolymerisations.

7.5 Methods

NMR Spectroscopy: ^{1}H, ^{27}Al and ^{31}P NMR spectra were obtained using a Bruker AV III HD 400 instrument. ^{13}C NMR spectra were obtained using either a Bruker AV III 500, a Bruker NEO 600, or a Bruker AV III 700 instrument.

IR Spectroscopy: Carried out on a Shimadzu IRSpirit FT-IR spectrometer equipped with a single reflection ATR (attenuated total reflectance) accessory, in a nitrogen filled glovebox.

Superconducting Quantum Interference Device (SQUID) Magnetometry: SQUID Data was collected and analysed by Gloria Rosetto (Oxford University). Measurements were carried out on powdered samples using a Quantum Design MPMS-3 Magnetometer, with a field of 0.1 T, at temperatures of 2 - 300 K. All magnetic susceptibility values were corrected using the diamagnetic Pascal constants.

Elemental Analysis: Carried out by either Mr. Stephen Boyer at London Metropolitan University (complexes **1**, **5** and **6**) or Elemental Microanalysis Ltd., 1 Hameldown Road, Okehamptom, Devon, EX20 1UB (all other complexes).

X-Ray Crystallography: Crystallographic data were collected, and structures solved, by Dr. Ryan Kerr and Dr. Andreas Phanopolous. Air sensitive samples were isolated in a nitrogen filled glovebox and immersed in fluorinated oil before analysis. Crystalline samples were mounted on a MiTeGen Micromount and cooled to 150 K with dry nitrogen using an Oxford Cryostream.[7] Data was collected with an Oxford Diffraction Supernova diffractometer using Cu K_α (λ = 1.5417 Å) or Mo K_α (λ = 0.7107 Å) radiation. The resulting reflection data was

processed with CrysAlis Pro.[8] Structures were solved using the SHELXT program and least-square refined using the SHELXL program within the Olex2 system suite.[9-11]

Ion Chromatography: Carried out by Exeter Analytical UK Ltd., The Venture Centre, University of Warwick Science Park, Sir William Lyons Road, Coventry, CV4 7EZ. The assay was performed on a Dionex IC system, with a carbonate/bicarbonate mobile phase (1mL min^{-1}), Dionex IonPac AS17 column (equilibrated for carbonate/bicarbonate) and using conductivity detection. Quantification was obtained by comparison of peak areas with standard solutions of potassium chloride.

GPC analysis: Carried out on a Shimadzu LC-20AD instrument, equipped with a Refractive Index (RI) detector and two PSS SDV 5 μm linear M columns, with an eluent of HPLC-grade THF, heated to 30 °C and with a flow rate of 1.0 mL min^{-1}.

MALDI-ToF spectrometry: Carried out on a Bruker Autoflex Speed MALDI-ToF instrument. A 1:4:1 solution of polymer (10 mg mL^{-1} in THF), dithranol (10 mg mL^{-1} in THF) and KTFA or NaTFA (10 mg mL^{-1} in THF) was prepared and spotted twice on a MALDI plate. The samples were allowed to dry completely before being subjected to analysis.

Differential Scanning Calorimetry (DSC): Carried out using either a DSC3+ (Mettler-Toledo Ltd.) or a DSC 25 (TA Instruments). For samples described in chapter 3 the following procedure was applied: samples were heated to 200 °C for 5 minutes to remove thermal history, before heating and cooling from -80 °C to 200 °C at a rate of 10 °C min^{-1}. Each sample was run for three heating and cooling cycles. For samples described in chapter 5 the following procedure was applied: samples were heated to 200 °C for 5 minutes to remove thermal history, before heating and cooling from 30 °C to 200 °C at a rate of 10 °C min^{-1}. Glass transition temperatures (T_g) were recorded from the midpoint of the transition during the third heating curve.

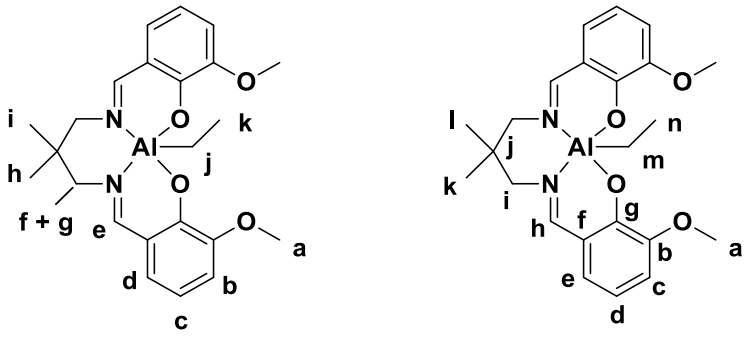
Thermal Gravimetric Analysis (TGA): Carried out using a TGA/DSC 1 (Mettler-Toledo Ltd.) instrument. Samples were heated from 30 °C to 500 °C, under continuous N_2 flow, at a rate of 5 °C min^{-1}.

Dynamic Mechanical Thermal Analysis (DMTA): Carried out on a DMA Q800 (TA Instruments). Samples were heated from 30 °C to 180 °C at 3 °C min^{-1} and oscillated at a frequency of 1 Hz with 0.05% strain.

7.6 Characterising Data for Chapter 2

Complex 1: This complex was synthesised following an adapted literature procedure. Characterising data presented here is in addition to that already reported.[12] Under inert conditions, $AlEt_3$ (0.17 g, 1.5 mmol) was added dropwise to a stirring solution of [$L_{van}H_2$] (0.57 g, 1.5 mmol) in anhydrous toluene (10 mL) at -30 °C. The reaction mixture was allowed to warm to room temperature, and then stirred for 1 hour. A yellow powder precipitated from the reaction mixture, which was isolated via centrifuge, washed with toluene (3 x 10 mL) and hexane (1 x 10 mL) and subsequently dried under vacuum to give 1 as a yellow powder (0.39 g, 1.0 mmol, 68%). X-ray diffraction quality crystals were grown from a saturated solution of **1** in THF, layered with hexane.

^{1}H NMR Notation ***^{13}C NMR Notation***



^{1}H NMR ($CDCl_3$, 400 MHz, 298 K); δ 8.07 (2H, s, H^e), 6.92 (2H, dd, *J* = 7.7 , 1.6 Hz, H^b), 6.80 (2H, dd, *J* = 7.7, 1.6 Hz, H^d), 6.60 (2H, t, *J* = 7.7 Hz, H^c), 3.96 (2H, d, *J* = 12.0 Hz, H^f), 3.85 (6H, s, H^a) 3.22 (2H, d, *J* = 12.0 Hz, H^g), 1.14 (3H, s, H^h), 0.95 (3H, s, H^i), 0.88 (3H, t, *J* = 8.0 Hz, H^k), -0.01 (2H, q, *J* = 8.0 Hz, H^j) ppm. **^{13}C NMR** ($CDCl_3$, 126 MHz, 298 K); δ 169.0 (C^h), 157.7 (C^g), 151.8 (C^b), 124.8 (C^e), 119.0 (C^f), 117.9 (C^c), 115.6 (C^d), 71.0 (C^i), 56.9 (C^a), 36.1 (C^j), 26.0 (C^k), 23.2 (C^l), 10.0 (C^n), 1.2 (C^m) ppm. **^{27}Al NMR** ($CDCl_3$, 104 MHz, 298 K): 5.8 ppm. **IR**: 343, 352, 367, 375, 382, 389, 397, 459, 499, 520, 565, 580, 592, 615, 628, 649, 673, 741, 752, 866, 975, 986, 1045, 1071, 1087, 1235, 1251, 1311, 1324, 1392, 1404, 1414,

1440, 1450, 1468, 1478, 1555, 1614, 1628, 2785, 2848, 2924, 2959, 3059 cm^{-1}. **Anal. Calc.** ($C_{23}H_{29}AlN_2O_4$); C, 65.08; H, 6.89; N, 6.60 %. Found: C, 64.95; H, 6.69; N, 6.56 %.

For associated spectra see Appendix.

Complex 2: Under inert conditions, $[Cr(OAc)_2.H_2O]_2$ (0.26 g, 0.7 mmol) was added to a stirred solution of $[L_{van}H_2]$ (0.51 g, 1.4 mmol) in anhydrous THF (10 mL) at 25 °C, resulting in a rapid colour change from yellow to red. The solution was stirred under an inert atmosphere for 2 hours before being exposed to air and stirred at room temperature for 72 hours, resulting in precipitation of an orange powder. The precipitate was isolated via centrifuge and was subsequently washed sequentially with toluene (3 x 10 mL) and hexane (3 x 10 mL) before being dried under vacuum to give **2**•H_2O as an orange powder (0.17 g, 0.35 mmol, 24%). X-ray diffraction quality crystals were grown from a saturated solution of **2**•H_2O in chloroform layered with hexane.

IR. 349, 357, 370, 385, 396, 459, 538, 563, 620, 643, 673, 696, 726, 742, 861, 936, 966, 985, 1029, 1069, 1081, 1175, 1191, 1199, 1222, 1245, 1279, 1315, 1367, 1378, 1394, 1437, 1451, 1468, 1548, 1613, 1728, 2904, 3267. **Anal. Calc.** ($C_{23}H_{29}CrN_2O_7$): C, 55.53; H, 5.88; N, 5.63 %. Found: C; 54.51, H, 5.61; N, 5.32 %.

For associated spectra see appendix. Complex **2** was further characterised by SQUID magnetometry (see Chapter 2) and X-ray crystallography (see Chapter 2 and Appendix).

Complex 3: Under inert conditions, $[Mn(OAc)_2]$ (0.24 g, 1.4 mmol) was added to a stirred solution of $[L_{van}H_2]$ (0.52 g, 1.4 mmol) in anhydrous THF (10 mL) at 25 °C. The solution was stirred under an inert atmosphere for 2 hours before being exposed to air and stirred at room temperature for 72 hours, resulting in precipitation of a green powder. The precipitate was isolated via centrifuge and was subsequently washed sequentially with THF (3 x 10 mL) and hexane (3 x 10 mL) before being dried under vacuum to give **3** as a green powder (0.410 g, 1.3

mmol, 61%). X-ray diffraction quality crystals were grown from a saturated solution of **3** in chloroform, layered with hexane.

IR: 343, 349, 395, 423, 430, 459, 476, 523, 559, 573, 618, 623, 640, 679, 723, 735, 742, 788, 798, 859, 904, 914, 935, 969, 975, 998, 1046, 1068, 1081, 1091, 1169, 1222, 1231, 1251, 1295, 1315, 1355, 1387, 1395, 1428, 1434, 1468, 1547, 1610, 1620, 2833, 2894, 2934, 2959, 3052 cm^{-1}. **Anal. Calc.** ($C_{23}H_{27}MnN_2O_6$): C, 57.26; H, 5.64; N 5.81 %. Found: C, 56.46; H, 5.45; N 5.73 %.

For associated spectra see appendix. Complex **3** was further characterised by SQUID magnetometry (see Chapter 2) and X-ray crystallography (see Chapter 2 and Appendix).

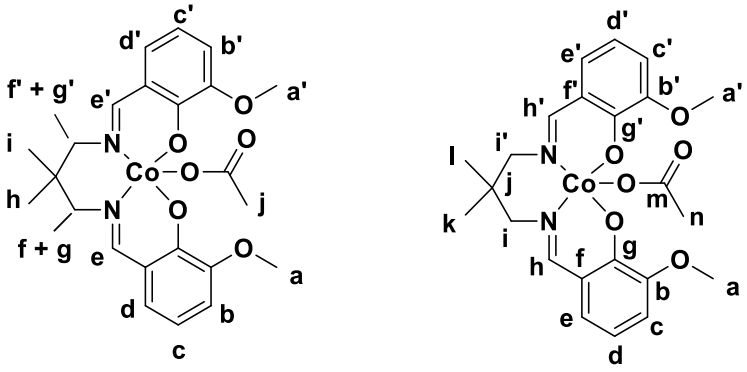
Complex 4: Under inert conditions, [$Fe(OAc)_2$] (0.25 g, 1.4 mmol) was added to a stirred solution of [$L_{van}H_2$] (0.53 g, 1.4 mmol) in anhydrous THF (10 mL) at 25 °C. The solution was stirred under an inert atmosphere for 2 hours before being exposed to air and stirred at room temperature for 72 hours, resulting in precipitation of a purple powder. The precipitate was isolated via centrifuge and was subsequently washed sequentially with THF (1 x 10 mL), toluene (3 x 10 mL) and hexane (3 x 10 mL) before being dried under vacuum to give **4** as a purple powder (0.49 g, 1.0 mmol, 71%). X-ray diffraction quality crystals were grown from a saturated solution of **4** in THF, layered with hexane.

IR: 343, 347, 357, 369, 406, 419, 455, 506, 556, 565, 592, 612, 619, 634, 688, 723, 733, 742, 859, 866, 908, 912, 944, 972, 1046, 1068, 1079, 1092, 1159, 1169, 1192, 1221, 1231, 1248, 1301, 1325, 1357, 1365, 1387, 1397, 1408, 1432, 1445, 1462, 1520, 1548, 1605, 1618, 2833, 2898, 2932, 2959, 3052 cm^{-1}. **Anal. Calc.** ($C_{23}H_{27}FeN_2O_6$): C, 57.16; H, 5.63; N 5.80 %. Found: C, 57.14; H, 5.53; N 5.99 %.

For associated spectra see appendix. Complex **4** was further characterised by SQUID magnetometry (see Chapter 2) and X-ray crystallography (see Chapter 2 and Appendix).

Complex 5: Under inert conditions, [Co(OAc)$_2$.4H$_2$O] (0.45 g, 1.8 mmol) was added to a stirred solution of [L$_{van}$H$_2$] (0.67 g, 1.8 mmol) in anhydrous THF (10 mL) at 25 °C, resulting in a rapid colour change from yellow to brown. The solution was stirred under an inert atmosphere for 2 hours before being exposed to air and stirred at room temperature for 48 hours, resulting in precipitation of a green powder. The precipitate was isolated via centrifuge and was subsequently washed sequentially with THF (3 x 10 mL) and hexane (3 x 10 mL) before being dried under vacuum to give **5** as a green powder (0.54 g, 1.3 mmol, 70%). X-ray diffraction quality crystals were grown from a saturated solution of **5** in dichloromethane, layered with hexane.

^{1}H NMR Notation ***^{13}C NMR Notation***



^{1}H NMR ($CDCl_3$, 400 MHz, 298 K); δ 7.52 (1H, s, H^e), 7.18 (1H, s, H$^{e'}$), 6.92-6.87f (3H, m, H^d, H$^{d'}$, H^b), 6.56-6.55 (2H, m, H^c and H$^{b'}$), 6.47 (1H, m, H$^{c'}$), 4.63 (1H, d, *J* = 10.5 Hz, H^f), 3.88 (s, 3H, H^a), 3.56 (s, 3H, H$^{a'}$), 3.40 (1H, d, *J* = 10.5 Hz, H^g), 3.28 (1H, d, *J* = 13.0 Hz, H$^{f'}$), 2.87 (1H, d, *J* = 13.0 Hz, H$^{g'}$), 1.85 (3H, s, H^j), 1.17 (3H, s, H^h), 0.92 (3H, s, H^i) ppm. **^{13}C NMR** ($CDCl_3$, 126 MHz, 298 K); δ 193.5 (C^m), 168.4 (C^h), 166.8 (C$^{h'}$), 160.4 (C^f), 157.9 (C$^{f'}$), 155.3 (C^b), 154.4 (C$^{b'}$), 125.8 (C^e), 124.7 (C^g), 124.3 (C$^{e'}$), 122.2 (C$^{g'}$), 117.7 (C^d), 117.1 (C$^{d'}$), 115.7 (C^c), 114.9 (C$^{c'}$), 70.5 (C^i and C$^{i'}$), 57.4 (C^a), 56.7 (C$^{a'}$), 35.4 (C^j), 25.9 (C^k), 23.8 (C^n), 23.3 (C^l) ppm. **IR:** 345, 349, 353, 356, 362, 373, 382, 389, 415, 427, 452, 480, 490, 539, 548, 572, 635, 652, 688, 732, 742, 862, 954, 968, 978, 986, 1048, 1068, 1082, 1097, 1168, 1199, 1228, 1245,

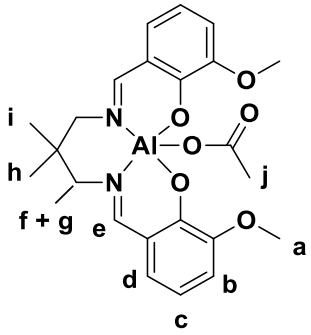
1301, 1330, 1352, 1367, 1387, 1395, 1410, 1437, 1468, 1547, 1601, 1618, 2832, 2911, 2929, 3054 cm^{-1}. **Anal. Calc.** ($C_{23}H_{29}AlN_2O_4$); C, 56.79; H, 5.60; N, 5.76 %. Found: C, 56.40; H, 5.85; N, 5.59 %.

For associated spectra see appendix. Complex **5** was further characterised by X-ray crystallography (see Chapter 2 and Appendix).

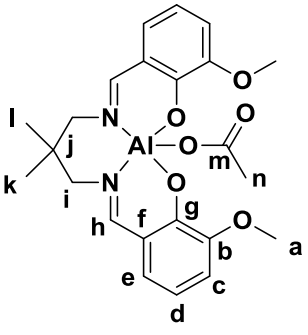
Complex 6: Method 1: Under inert conditions, glacial acetic acid (0.01 mL, 0.19 mmol) was added to a stirred solution of **1** (80 mg, 0.19 mmol) in anhydrous THF (10 mL) at 25 °C. The reaction mixture was stirred for 2 hours, resulting in the precipitation of a yellow powder. The precipitate was isolated via centrifuge, before being dried under vacuum to yield **6** as a pale yellow powder (70 mg, 0.15 mmol, 79%). X-ray Diffraction quality crystals were grown from a saturated solution of **5** in chloroform, layered with hexane.

Method 2: Under inert conditions, $AlEt_3$ (191 mg, 1.67 mmol) was added to a stirred solution of $L_{van}H_2$ (550 mg, 1.48 mmol) in anhydrous THF (5 mL) at room temperature, and stirred for 2 hours. Subsequently, glacial acetic acid (85 μL, 1.48 mmol) was added, and the reaction was stirred for 16 hours at room temperature, resulting in the formation of a yellow precipitate. The precipitate was isolated via centrifuge, and subsequently washed with THF (1 x 10 mL) and hexane (1 x 10 mL) before being dried under vacuum, to give **6** as a pale-yellow powder (496 mg, 1.09 mmol, 74%).

^{1}H NMR Notation



^{13}C NMR Notation



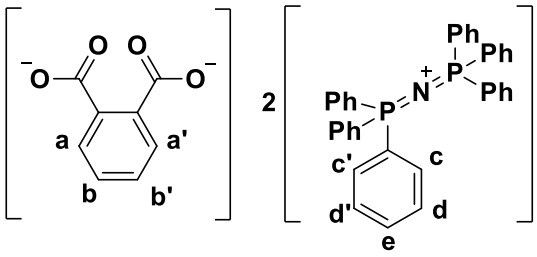
^{1}H NMR ($CDCl_3$, 400 MHz, 298 K); δ 8.10 (2H, s, H^e), 6.92 (2H, dd, *J* = 7.7, 1.6 Hz, H^b), 6.87, (2H, dd, *J* = 7.7, 1.6 Hz, H^d), 6.62 (2H, t, *J* = 7.7 Hz, H^c), 3.87 (2H, d, *J* = 11.9 Hz, H^f), 3.80 (6H, s, H^a), 3.28 (2H, d, *J* = 11.9 Hz, H^g), 2.03 (3H, s, H^j), 1.14 (3H, s, H^h), 0.93 (3H, s, H^i) ppm. **^{13}C NMR** ($CDCl_3$, 126 MHz, 298 K); δ 181.1 (C^m), 169.4 (C^h), 158.1 (C^g), 152.0 (C^b), 125.3 (C^e), 119.6 (C^f), 118.0 (C^c), 115.8 (C^d), 69.8 (C^i), 56.8 (C^a), 36.8 (C^j), 25.9 (C^k), 24.7 (C^l), 20.5 (C^n) ppm. **^{27}Al NMR** ($CDCl_3$, 104 MHz, 298 K): 14.8 ppm. **IR:** 390, 447, 477, 512, 530, 543, 563, 588, 630, 646, 708, 735, 743, 872, 976, 1049, 1071, 1082, 1098, 1169, 1227, 1248, 1311, 1324, 1334, 1390, 1407, 1448, 1471, 1541, 1555, 1617, 1630, 2833, 2875, 2909, 2935, 2962, 3056 cm^{-1}. **Anal. Calc.** ($C_{23}H_{29}AlN_2O_4$); C, 60.79 H, 5.99; N, 6.16 %. Found: C, 60.77; H, 6.12; N, 6.05 %.

For associated spectra see appendix. Complex **6** was further characterised by X-ray crystallography (see Chapter 2 and Appendix).

7.7 Characterising Data for Chapter 3

PPN$_2$PA: This complex was synthesised following a modified literature procedure.[13] Bis(triphenylphosphine)iminium chloride (2.17 g, 3.8 mol) was dissolved in 50 mL of H_2O at 80 °C. To this stirred solution, a solution of dipotassium phthalate (0.46 g, 1.9 mmol) in 10 mL H_2O was added dropwise, resulting in precipitation of a white solid. The reaction mixture was stirred for 1 hour, before being allowed to cool, resulting in the precipitation of a white solid. The suspension was filtered through a sinter funnel and the precipitate retained. This precipitation process was repeated a further two times. The residual white solid was then washed with water (1 x 50 mL) and diethyl ether (1 x 50 mL), yielding a white powder which was dried under vacuum at 60 °C for 6 hours, giving **4** in 31% yield.

^{1}H NMR Notation

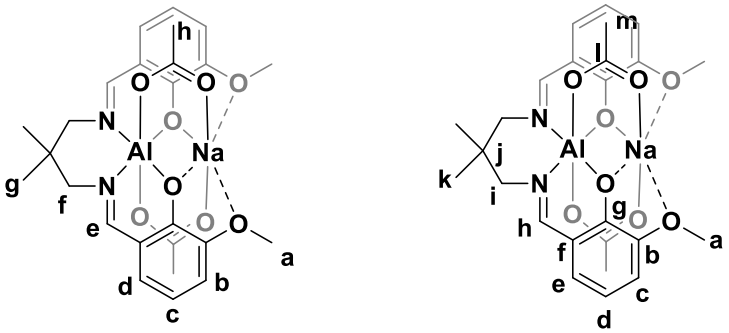


^{1}H NMR (400 MHz, 298 K, MeCN-d_3); δ 7.68-7.64 (12 H, m, H^e), 7.60-7.55 (24 H, m, H$^{d/d'}$ or H$^{c/c'}$), 7.50-7.45 (24 H, m, H$^{d/d'}$ or H$^{c/c'}$), 7.20-7.18 (2H, m, H$^{a/a'}$), 6.95-6.93 (2H, m, H$^{b/b'}$) ppm. **^{31}P{^{1}H} NMR** (162 MHz, 298 K, MeCN-d_3); δ 20.77 ppm. **Anal. Calc.** ($C_{80}H_{64}N_2O_4P_4$): C, 77.41; H, 5.20; N, 2.26 %. Found: C, 77.32; H, 5.28; N, 2.27 %.

7.8 Characterising Data for Chapter 4

Complex 7: Under inert conditions, NaOAc (17 mg, 0.21 mmol) was added to a stirred solution of complex **6** (95 mg, 0.21 mmol) in anhydrous chloroform (5 mL) at room temperature, and stirred for 16 hours. The solvent was removed, and the crude product purified by recrystallisation from a saturated solution of dichloromethane layered with hexane, to give complex **7** as pale-yellow crystals. (72 mg, 0.13 mmol, 64%). Diffraction quality crystals were obtained through the same recrystallisation method.

^{1}H NMR Notation ***^{13}C NMR Notation***

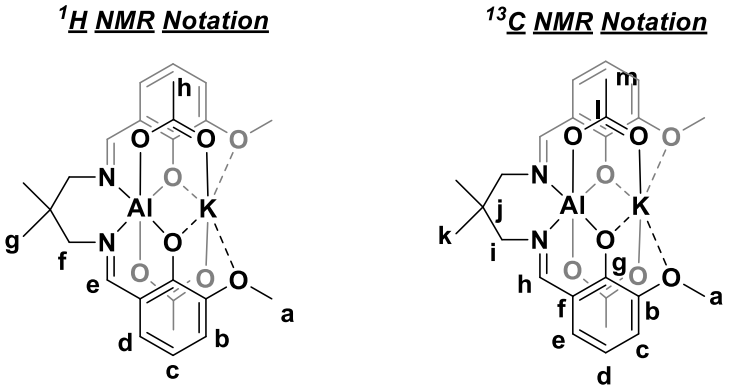


^{1}H NMR (CD_2Cl_2, 400 MHz, 298 K): 7.94 (2H, s, H^e), 6.81 (2H, d, J = 7.6 Hz, H^d), 6.65 (2H, d, J = 7.6 Hz, H^b), 6.60 (2H, t, J = 7.6 Hz, H^c), 3.70 (4H, s, H^f), 3.23 (6H, s, H^a), 1.57 (6H, s, H^h), 1.15 (6H, s, H^g) ppm. **^{13}C NMR** (CD_2Cl_2, 176 Hz, 298 K): 174.2 (C^l), 167.5 (C^h), 155.7 (C^g), 150.8 (C^b), 125.6 (C^e), 119.5 (C^f), 114.4 (C^d or C^c), 114.5 (C^d or C^c), 74.3 (C^i), 55.5 (C^a), 35.2 (C^j), 25.0 (C^m), 24.7 (C^k) ppm. **^{27}Al NMR** (CD_2Cl_2, 104 MHz, 298 K): -1.0 ppm. **Anal. Calc.** ($C_{25}H_{30}AlNaN_2O_8$); C, 55.97; H, 5.64; N, 5.22. Found: C, 56.25; H, 5.48; N, 5.29.

For associated spectra see appendix. Complex **7** was further characterised by X-ray crystallography (see Chapter 4 and Appendix).

Complex 8: Under inert conditions, KOAc (18 mg, 0.18 mmol) was added to a stirred solution of complex **6** (85 mg, 0.18 mmol) in anhydrous chloroform at room temperature, and stirred for 16 hours. Subsequently, the solution was filtered, and the solvent removed under vacuum to give **8** as

a pale-yellow powder (102 mg, 0.18 mmol, 98%). Diffraction quality crystals were grown from a saturated solution of **8** in $CHCl_3$, layered with hexane.

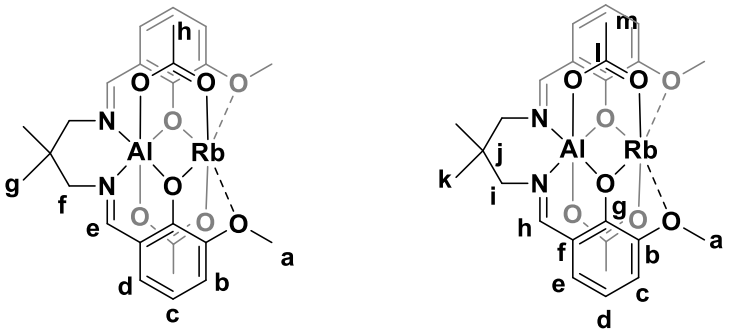


^{1}H NMR ($CDCl_3$, 400 MHz, 298 K): 7.90 (2H, s, H^e), 6.78 (2H, dd, J = 7.9, 1.2 Hz, H^d), 6.63 (2H, d, J = 7.9 Hz, H^b), 6.52 (2H, t, J = 7.9 Hz, H^c), 3.75 (4H, s, H^f), 3.39 (6H, s, H^a), 1.53 (6H, s, H^h), 1.20 (6H, s, H^g) ppm. **^{13}C NMR** ($CDCl_3$, 151 MHz, 298 K): 173.5 (C^l), 166.7 (C^h), 156.4 (C^g), 151.1 (C^b), 125.2 (C^e), 120.0 (C^f), 114.1 (C^d), 113.7 (C^c), 74.0 (C^i), 55.2 (C^a), 35.6 (C^j), 24.9 (C^k), 24.2 (C^m) ppm. **^{27}Al NMR** ($CDCl_3$, 104 MHz, 298 K): -1.2 ppm. **Anal. Calc.** ($C_{25}H_{30}AlKN_2O_8$); C, 54.34; H, 5.47; N, 5.07. Found: C, 54.70; H, 5.59; N, 4.74.

For associated spectra see appendix. Complex **8** was further characterised by X-ray crystallography (see Chapter 4 and Appendix).

Complex 9: Under inert conditions, RbOAc (16 mg, 0.11 mmol) was added to a stirred solution of complex **6** (55 mg, 0.11 mmol) in anhydrous chloroform at room temperature, and stirred for 16 hours. Subsequently, the solution was filtered, and the solvent removed under vacuum. The crude product was washed with toluene (1 x 10 mL), and subsequently dried under vacuum to give **9** as a pale-yellow powder (57 mg, 0.95 mmol, 86%). Diffraction quality crystals were grown from a saturated solution of **6** in chloroform, layered with hexane.

^{1}H NMR Notation ***^{13}C NMR Notation***

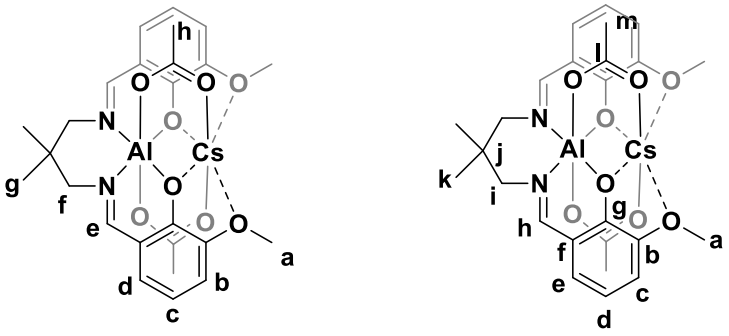


^{1}H NMR ($CDCl_3$, 400 MHz, 298 K): 7.92 (2H, s, H^e), 6.79 (2H, d, *J* = 7.9 Hz, H^d), 6.66 (2H, d, *J* = 7.9 Hz, H^b), 6.53 (2H, t, *J* = 7.9 Hz, H^c), 3.73 (4H, s, H^f), 3.46 (6H, s, H^a), 1.59 (6H, s, H^h), 1.18 (6H, s, H^g) ppm. **^{13}C NMR** ($CDCl_3$, 126 MHz, 298 K): 173.9 (C^l), 167.0 (C^h), 156.4 (C^g), 151.1 (C^b), 125.3 (C^e), 120.0 (C^f), 114.4 (C^d). 114.0 (C^c), 73.4 (C^i), 55.0 (C^a), 35.7 (C^j), 25.1 (C^k), 23.8 (C^m) ppm. **^{27}Al NMR** ($CDCl_3$, 104 MHz, 298 K): -2.1 ppm. **Anal. Calc.** ($C_{25}H_{30}AlRbN_2O_8$); C, 50.13; H, 5.05; N, 4.68. Found: C, 50.17; H, 4.8.; N, 4.61.

For associated spectra see appendix. Complex **9** was further characterised by X-ray crystallography (see Chapter 4 and Appendix).

Complex 10: Under inert conditions, CsOAc (39 mg, 0.20 mmol) was added to a stirred solution of complex **6** (95 mg, 0.20 mmol) in anhydrous chloroform at room temperature, and stirred for 16 hours. Subsequently the solvent was removed under vacuum to give **10** as a pale-yellow powder (131 mg, 0.20 mmol, 99%). Diffraction quality crystals were grown from a saturated solution of **10** in chloroform, layered with hexane.

^{1}H NMR Notation ***^{13}C NMR Notation***

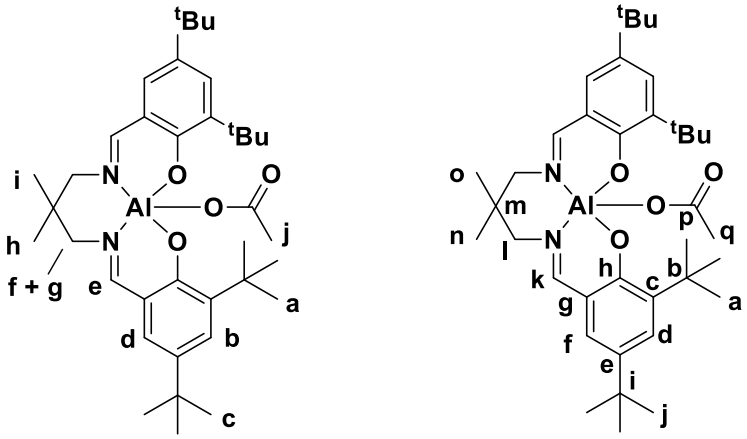


^{1}H NMR ($CDCl_3$, 400 MHz, 298 K): 7.94 (2H, s, H^e), 6.80 (2H, d, *J* = 7.9 Hz, H^d), 6.71 (2H, d, *J* = 7.9 Hz, H^b), 6.54 (2H, t, *J* = 7.9 Hz, H^c), 3.71 (4H, s, H^f), 3.51 (6H, s, H^a), 1.58 (6H, s, H^h), 1.18 (6H, s, H^g) ppm. **^{13}C NMR** ($CDCl_3$, 126 MHz, 298 K): 174.1 (C^l) 167.4 (C^h), 156.4 (C^g), 151.1 (C^b), 125.6 (C^e), 120.2 (C^f), 114.6 (C^d), 114.2 (C^c), 72.8 (C^i), 54.8 (C^a), 35.7 (C^j), 25.5 (C^k), 23.9 (C^m) ppm. **^{27}Al NMR** ($CDCl_3$, 104 MHz, 298 K): -2.5 ppm. **Anal. Calc.** ($C_{25}H_{30}AlCsN_2O_8$); C, 46.45; H, 4.68; N, 4.33. Found: C, 46.85; H, 4.55; N, 4.38.

For associated spectra see appendix. Complex **10** was further characterised by X-ray crystallography (see Chapter 4 and Appendix).

Complex 11: [L_{sal}AlEt] was synthesised following an adapted literature procedure.[14] Under inert conditions, $AlEt_3$ (113 mg, 0.99 mmol) was added to a stirred solution of SaldpnH_2 (493 mg, 0.92 mmol) in anhydrous hexane (5 mL) at room temperature, and stirred for 16 hours, resulting in the formation [L_{sal}AlEt] as a yellow precipitate. The precipitate was isolated *via* centrifuge, and a crude yield was recorded (137 mg, 0.23 mmol, 25%). The crude product was subsequently dissolved in toluene before glacial acetic acid (15 μL, 0.23 mmol) was added, and the reaction was stirred for 16 hours at room temperature, resulting in the formation of a yellow precipitate. The precipitate was isolated *via* centrifuge, and subsequently washed with hexane (1 x 10 mL) before being dried under vacuum, to give **11** as a pale-yellow precipitate (0.117 g, 0.19 mmol, 83%).

^{1}H NMR Notation ***^{13}C NMR Notation***



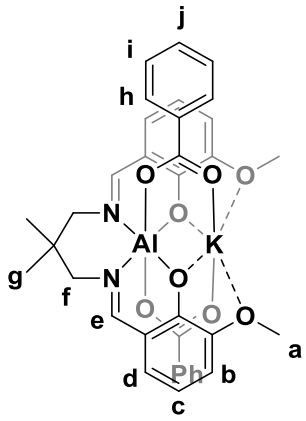
^{1}H NMR ($CDCl_3$, 400 MHz, 298 K): δ 8.11 (2H, s, H^e), 7.48 (2H, d, *J* = 2.6 Hz, H^b), 7.06 (2H, d, *J* = 2.6 Hz, H^d), 3.53 (2H, d, *J* = 11.5 Hz, H^f), 3.32 (2H, d, *J* = 11.5 Hz, H^g), 1.90 (3H, s, H^j), 1.40 (9H, s, H^c), 1.30 (9H, s, H^d), 1.15 (3H, s, H^h), 0.98 (3H, s, H^i) ppm. **^{13}C NMR** ($CDCl_3$, 176 MHz, 298 K): δ 186.7 (C^p), 170.0 (C^k), 163.9 (C^h), 140.8 (C^c), 137.4 (C^e), 130.6 (C^d), 127.5 (C^f), 118.5 (C^g), 67.9 (C^l), 36.8 (C^m), 35.4 (C^n), 34.1 (C^i), 31.6 (C^a), 29.7 (C^j), 26.3 (C^n or C^o), 25.7 (C^n or C^o), 20.5 (C^q) ppm. **^{27}Al NMR** ($CDCl_3$, 104 MHz, 298 K): 16.3 ppm. **Anal. Calc.** ($C_{25}H_{30}AlNaN_2O_8$); C, 71.81; H, 8.96; N, 4.53. Found: C, 70.43; H, 8.92; N, 4.13.

For associated spectra see appendix.

Complex 12: Under inert conditions, benzoic acid (57 mg, 0.47 mmol) was added to a stirred solution of **1** (198 mg, 0.47 mmol) in anhydrous THF (5 mL) and heated for 16 hours at 60 °C, resulting in the formation of a yellow precipitate. The precipitate was isolated *via* centrifuge and washed with hexane (1 x 5 mL) to yield [L_{van}AlOBz] as a yellow powder (202 mg, 0.39 mmol, 84%), which was used without further purification. Under inert conditions, KOBz (35 mg, 0.22 mmol) was added to a stirred solution of [L_{van}AlOBz] (113 mg, 0.22 mmol) in dry chloroform at room temperature, and stirred for 16 hours. Subsequently, the reaction solution was filtered, and the solvent removed under vacuum to give **12** as a pale yellow powder (127 mg, 0.19 mmol, 86%). A ^{1}H NMR was taken of the crude product to confirm formation. Diffraction quality crystals were

grown from a saturated solution of **12** in THF layered with hexane. This complex was not utilised in catalysis and so further characterisation was not undertaken.

^{1}H NMR Notation



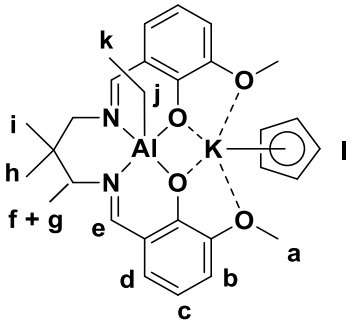
^{1}H NMR ($CDCl_3$, 400 MHz, 298 K): δ 8.01 (2H, s, H^e), 7.73 (4H, d, *J* = 7.4 Hz, H^h), 7.31 (2H, t, H^j), 7.23 (4H, t, *J* = 7.4 Hz, H^i), 6.71 (2H, d, *J* = 7.7 Hz, H^d or H^b), 6.45 (2H, d, *J* = 7.7 Hz, H^d or H^b), 6.37 (2H, t, *J* = 7.7 Hz, H^c), 3.96 (4H, s, H^f), 3.30 (6H, s, H^a), 1.35 (6H, s, H^g) ppm.

For associated spectra see appendix.

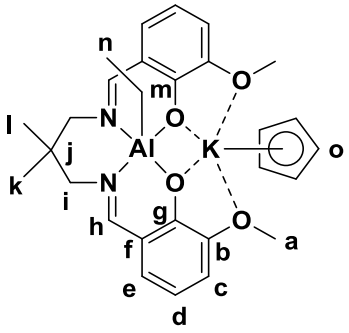
7.9 Characterising Data for Chapter 5

Complex 13: Under inert conditions, KCp (11 mg, 0.11 mmol) was added to a stirred solution of complex **1** (46 mg, 0.11 mmol) in anhydrous THF at room temperature, and was stirred for 30 minutes. Subsequently the solvent was removed under vacuum to give **13** as a pale orange powder (56 mg, 0.11 mmol, 99%). The complex was stored at -30 °C, under an inert atmosphere.

^{1}H NMR Notation



^{13}C NMR Notation



^{1}H NMR: (THF-d_8, 400 MHz, 298 K): δ 8.25 (2H, s, H^e), 6.96 (2H, dd, J = 7.8, 1.4 Hz, H^b), 6.91 (2H, dd, J = 7.8, 1.4 Hz, H^d), 6.62 (2H, t, J = 7.8 Hz, H^c), 5.60 (5H, s, H^l), 3.89 (6H, s, H^a), 3.63 (2H, d, J = 12.2 Hz, **^{13}C NMR:** (THF-d_8, 126 MHz, 298 K): δ 171.6 (C^h), 157.1 (C^f), 152.3 (C^b), 125.9 (C^e), 120.4 (C^g), 117.5 (C^c), 116.6 (C^d), 104.7 (C^o), 69.3 (C^i), 56.9 (C^a), 36.7 (C^j), 26.4(C^k), 24.6 (C^l), 10.6 (C^n), 7.0 (C^m) ppm. **IR**: 347, 356, 363, 370, 379, 392, 460, 477, 512, 626, 649, 701, 739, 859, 976, 1005, 1069, 1082, 1169, 1198, 1231, 1247, 1304, 1340, 1391, 1401, 1452, 1480, 1555, 1615, 2793, 2855, 2928, 3055 cm^{-1}. **Anal. Calc.** ($C_{28}H_{34}AlKN_2O_4$); C, 63.61; H, 6.48; N, 5.30 %. Found: C, 62.38; H, 6.24; N, 5.24 %.

For associated spectra see appendix.

7.10 References for Chapter 7

1. A. Thevenon, J. A. Garden, A. J. P. White and C. K. Williams, *Inorg. Chem.*, 2015, **54**, 11906-11915.
2. G. R. J. Artus, M. U. Rauch and W. A. Herrman, *Inorg. Chem.*, 1996, **35**, 1988-1991.
3. T. K. Panda, M. T. Gamer and P. W. Roesky, *Organometallics*, 2003, **22**, 877-878.
4. A. Spyros, D. S. Argyropoulos and R. H. Marchessault, *Macromolecules*, 1997, **30**, 327-329.
5. O. Hauenstein, M. Reiter, S. Agarwal, B. Rieger and A. Greiner, *Green Chem.*, 2016, **18**, 760-770.
6. D. Dakshinamoorthy, A. K. Weinstock, K. Damodaran, D. F. Iwig and R. T. Mathers, *ChemSusChem*, 2014, **7**, 2923-2929.
7. J. Cosier and A. M. Glazer, *J. Appl. Cryst.*, 1986, **19**, 105-107.
8. CrysAlisPRO, Oxford Diffraction /Agilent Technologies UK Ltd, Yarnton, England.
9. G. M. Sheldrick, *Acta Cryst.*, 2015, **C71**, 3-8.
10. a) SHELXTL v5.1, Bruker AXS, Madison, WI, 1998 b) Sheldrick, G. M., *Acta Cryst.*, 2015, **A71**, 3-8.
11. O. V. Dolomanov, L. J. Bourhis, R. J. Gildea, J. A. K. Howard and H. Puschmann, *J. Appl. Cryst.*, 2009, **42**, 339-341.
12. T. Stößer, *DPhil. Thesis*, University of Oxford, 2018.
13. M. J. Sanford, N. J. Van Zee and G. W. Coates, *Chem. Sci.*, 2018, **9**, 134-142.
14. H. Du, X. Pang, H. Yu, X. Zhuang, X. Chen, D. Cui, X. Wang and X. Jing, *Macromolecules*, 2007, **40**, 1904-1913.

Appendix

Supplementary Figures and Data for Chapter 2 192

Table S2.1. Selected bond lengths and angles for complex **3**. 192

Table S2.2. Selected bond lengths and angles for complex **4**. 192

Table S2.3. Selected bond lengths and angles for complex **5**. 193

Table S2.4. Selected bond lengths and angles for complex **6**. 193

Table S2.5. Summary of crystallographic refinement data for complexes **2** – **6.** 194

Figure S2.1. ^{1}H NMR Spectrum (400 MHz, 298 K, $CDCl_3$(*)) of complex **1**. 195

Figure S2.2. ^{13}C NMR Spectrum (126 MHz, 298 K, $CDCl_3$(*)) of complex **1**. 195

Figure S2.3. ^{27}Al NMR Spectrum (104 MHz, 298 K, CDCl3(*)) of complex **1**. 196

Figure S2.4. ^{1}H COSY NMR Spectrum (400 MHz, 298 K, $CDCl_3$) of complex **1**. 196

Figure S2.5. ^{1}H-^{13}C HSQC NMR Spectrum (298 K, $CDCl_3$) of complex **1**. 197

Figure S2.6. ^{1}H-^{13}C HMBC NMR Spectrum (298 K, $CDCl_3$) of complex **1**. 197

Figure S2.7. ^{1}H NMR Spectrum (400 MHz, 298 K, $CDCl_3$(*)) of complex **5**. 198

Figure S2.8. ^{13}C NMR Spectrum (126 MHz, 298 K, $CDCl_3$(*)) of complex **5**. 198

Figure S2.9. ^{1}H COSY NMR Spectrum (400 MHz, 298 K, $CDCl_3$) of complex **5**. 199

Figure S2.10. ^{1}H-^{13}C HSQC NMR Spectrum (298 K, $CDCl_3$) of complex **5**. 199

Figure S2.11. ^{1}H-^{13}C HMBC NMR Spectrum (298 K, $CDCl_3$) of complex **5**. 200

Figure S2.12. ^{1}H NMR Spectrum (400 MHz, 298 K, $CDCl_3$(*)) of complex **6**. 200

Figure S2.13. ^{13}C NMR Spectrum (126 MHz, 298 K, $CDCl_3$(*)) of complex **6**. 201

Figure S2.14. ^{27}Al NMR Spectrum (104 MHz, 298 K, CDCl3(*)) of complex **6**. 201

Figure S2.15. ^{1}H COSY NMR Spectrum (400 MHz, 298 K, $CDCl_3$) of complex **6**. 202

Figure S2.16. ^{1}H-^{13}C HSQC NMR Spectrum (298 K, $CDCl_3$) of complex **6**. 202

Figure S2.17. ^{1}H-^{13}C HSQC NMR Spectrum (298 K, $CDCl_3$) of complex **6**. 203

Figure S2.18. Variable temperature ^{1}H NMR spectra (400 MHz, CD_2Cl_2) of complex **6**. 204

Figure S2.19. Infrared spectrum of complex **2**. 204

Figure S2.20. Infrared spectrum of complex **3**. 205

Figure S2.21. Infrared spectrum of complex **4**. 205

Figure S2.22. Infrared spectrum of complex **5**. 206

Figure S2.23. Infrared spectrum of complex **6**. 206

Table S2.6. Data for the ROCOP of CHO and PA at complete PA conversion for complexes **1** – **5** and [SalcyCrCl]. 207

Figure S2.24. GPC trace of PCHPE obtained with complexes **1** – **5** and [SalcyCrCl], corresponding to Table 2.3, Entries 1 – 6. 207

Figure S2.25. GPC trace of PDL obtained with complexes **1**, **2**, **5** and [SalcyCrCl], corresponding to Table 2.4, Entries 1 – 4. 208

Figure S2.26. Temperature stability of complex **5**. 208

Supplementary Figures and Data for Chapter 3 209

Figure S3.1. Polymer molecular mass distributions of PCHPE copolymers synthesised with complex **5**/PPNCl, ... 209

Figure S3.2 MALDI-ToF spectrum of PCHPE obtained with **5**/PPNCl and 10 equivs. of CHD. 209

Figure S3.3. ^{1}H NMR spectra ($CDCl_3$, 400 MHz, 298 K) of aliquots taken during switchable polymerisation. 210

Figure S3.4. ^{1}H DOSY ($CDCl_3$, 400 MHz, 298 K) of PDL-*b*-PCHPE-*b*-PDL. 210

Figure S3.5. MALDI-ToF spectrum of PCHPE synthesised during switchable catalysis (Table 2.1, Entry 5) before initiation of ε-DL ROP, showing the low weight shoulder is due to initiation from chloride anions. 211

Figure S3.6. ^{1}H NMR spectrum (400 MHz, 298 K, MeCN-d_3(*)) of PPN_2PA 211

Figure S3.7. $^{31}P\{^{1}H\}$ NMR spectrum (162 MHz, 298K, MeCN-d_3) of PPN_2PA. 212

Figure S3.8. MALDI-ToF spectrum of PDL obtained with **1**/PPN_2PA and 2 equivs. of CHD. 212

Figure S3.9. Polymer molecular mass distributions of PDL prepared with complex **1**/PPN_2PA. 213

Figure S3.10. MALDI-ToF spectrum of PCHPE obtained with **1**/PPN_2PA and 2 equivs. of CHD. 213

Figure S3.11. Polymer molecular mass distributions of PDL-b-PCHPE-b-PDL prepared with complex **1**/PPN_2PA 214

Supplementary Figures and Data for Chapter 4 215

Figure S4.1. Molecular structure of complex **7**. 215

Figure S4.2. Molecular structure of complex **9**. 215

Figure S4.3. Molecular structure of complex **10**. 216

Table S4.1. Selected bond lengths and angles for complex **7** 217

Table S4.2. Selected bond lengths and angles for complex **8**. 218

Table S4.3. Selected bond lengths and angles for complex **9** 219

Table S4.4. Selected bond lengths and angles for complex **10** 220

Table S4.5. Selected bond lengths and angles for complex **12** 221

Table S4.6.. Summary of crystallographic refinement data for complexes **7** – **10** & **12.**..... 222

Figure S4.4. ^{1}H NMR Spectrum (400 MHz, 298 K, CD_2Cl_2(*)) of complex **7**. 223

Figure S4.5. ^{13}C NMR Spectrum (176 MHz, 298 K, CD_2Cl_2(*)) of complex **7**. 223

Figure S4.6. ^{27}Al NMR Spectrum (104 MHz, 298 K, CD_2Cl_2) of complex **7**..... 224

Figure S4.7. ^{1}H COSY NMR Spectrum (400 MHz, 298 K, CD_2Cl_2) of complex **7**. 224

Figure S4.8. ^{1}H-^{13}C HSQC NMR Spectrum (298 K, CD_2Cl_2) of complex **7**. 225

Figure S4.9. ^{1}H-^{13}C HMBC NMR Spectrum (298 K, CD_2Cl_2) of complex **7**. 225

Figure S4.10. ^{1}H NMR Spectrum (400 MHz, 298 K, $CDCl_3$(*)) of complex **8**. 226

Figure S4.11. ^{13}C NMR Spectrum (151 MHz, 298 K, $CDCl_3$(*)) of complex **8**. 226

Figure S4.12. ^{27}Al NMR Spectrum (104 MHz, 298 K, $CDCl_3$) of complex **8**. 227

Figure S4.13. ^{1}H COSY NMR Spectrum (400 MHz, 298 K, $CDCl_3$) of complex **8**. 227

Figure S4.14. ^{1}H-^{13}C HSQC NMR Spectrum (298 K, $CDCl_3$) of complex **8**. 228

Figure S4.15. ^{1}H-^{13}C HMBC NMR Spectrum (298 K, $CDCl_3$) of complex **8**. 228

Figure S4.16. ^{1}H NMR Spectrum (400 MHz, 298 K, $CDCl_3$(*)) of complex **9**. 229

Figure S4.17. ^{13}C NMR Spectrum (400 MHz, 298 K, $CDCl_3$(*)) of complex **9**. 229

Figure S4.18. ^{27}Al NMR Spectrum (104 MHz, 298 K, $CDCl_3$) of complex **9**. 230

Figure S4.19. ^{1}H COSY NMR Spectrum (400 MHz, 298 K, $CDCl_3$) of complex **9**. 230

Figure S4.20. ^{1}H-^{13}C HSQC NMR Spectrum (298 K, $CDCl_3$) of complex **9**. 231

Figure S4.21. ^{1}H-^{13}C HMBC NMR Spectrum (298 K, $CDCl_3$) of complex 3. 231

Figure S4.22. ^{1}H NMR Spectrum (400 MHz, 298 K, $CDCl_3$(*)) of complex **10**. 232

Figure S4.23. ^{13}C NMR Spectrum (126 MHz, 298 K, $CDCl_3$(*)) of complex **10**. 232

Figure S4.24. ^{27}Al NMR Spectrum (104 MHz, 298 K, $CDCl_3$) of complex **10**. 233

Figure S4.25. ^{1}H COSY NMR Spectrum (400 MHz, 298 K, $CDCl_3$) of complex **10**. 233

Figure S4.26. ^{1}H-^{13}C HSQC NMR Spectrum (298 K, $CDCl_3$) of complex **10**. 234

Figure S4.27. ^{1}H-^{13}C HMBC NMR Spectrum (298 K, $CDCl_3$) of complex **10**. 234

Figure S4.28. DOSY NMR spectrum (500 MHz, $CDCl_3$, 298K) of complex **8**. 235

Table S4.7. Data for the ROCOP of CHO and PA with complexes **7** – **10**..... 235

Figure S4.29. ^{1}H NMR spectrum (400 MHz, $CDCl_3$, 298 K) of reaction mixture of CHO and PA. 236

Figure S4.30. MALDI-ToF spectrum of PCHPE obtained with complex 2. 236

Figure S4.31. ^{1}H NMR Spectrum (400 MHz, 298 K, $CDCl_3$(*)) of complex **11**. 237

Figure S4.32. ^{13}C NMR Spectrum (176 MHz, 298 K, $CDCl_3$(*)) of complex **11**. 237

Figure 4.33. ^{27}Al NMR Spectrum (104 MHz, 298 K, $CDCl_3$) of complex **11**. 238

Figure S4.34. ^{1}H COSY NMR Spectrum (400 MHz, 298 K, $CDCl_3$) of complex **11**. 238

Figure S4.35. ^{1}H-^{13}C HSQC NMR Spectrum (298 K, $CDCl_3$) of complex **11**. 239

Figure S4.36. ^{1}H-^{13}C HMBC NMR Spectrum (298 K, $CDCl_3$) of complex **11**. 239

Figure S4.37. Plot of $[PA]_t$ *vs*. Time at a range of [**8**] 240

Computational Details for Chapter 4 241

Table S4.8. Summary of uncorrected computed structures. 242

Table S4.9. Correction computed structures 242

Figure S4.38. Computed Reaction Profile for epoxide ring-opening. 243

Figure S4.39. IRC for $TS_{I\text{-}IIK}$ showing connected intermediates either side. 244

Figure S4.40. IRC for $TS_{I\text{-}IIAl}$ showing connected intermediates either side. 244

Figure S4.41. Computed Pathways for lowest free enthalpy TS 245

Figure S4.42. Computed Pathways for lowest free enthalpy TS 246

Figure S4.43. ^{1}H NMR spectrum (400 MHz, $CDCl_3$(*), 298 K) of complex **12**. 247

Figure S4.44. ^{1}H NMR spectrum (400 MHz, $CDCl_3$, 298 K) of reaction mixture of CHO and TCA. 248

Figure S4.45. ^{1}H NMR spectrum (400 MHz, $CDCl_3$, 298 K) of reaction mixture of CHO and NBA. 248

Figure S4.46. ^{1}H NMR spectrum (400 MHz, $CDCl_3$, 298 K) of reaction mixture of tBGE and PA. 249

Figure S4.47. ^{1}H NMR spectrum (400 MHz, $CDCl_3$, 298 K) of reaction mixture of SO and PA. 249

Figure S4.48. ^{1}H NMR spectrum (400 MHz, $CDCl_3$, 298 K) of reaction mixture of PO and PA. 250

Figure S4.49. ^{1}H NMR spectrum (400 MHz, $CDCl_3$, 298 K) of reaction mixture of vCHO and PA. 250

Figure S4.50. ^{1}H NMR spectrum (400 MHz, $CDCl_3$, 298 K) of reaction mixture of AGE and PA. 251

Figure S4.51. ^{1}H NMR spectrum (400 MHz, $CDCl_3$, 298 K) of reaction mixture of CHO and CO_2 (1 bar). 252

Figure S4.52. ^{1}H NMR spectrum (400 MHz, $CDCl_3$, 298 K) of reaction mixture of CHO and CO_2 (1 bar). 253

Figure S4.53. GPC traces for polymers corresponding to Table 4.3, Entries 1-10. 254

Table S4.10. Data for the ROCOP of epoxide and anhydrides with complex 2 at full anhydride conversion. 254

Figure S4.54. Structure of catalysts reported for epoxide/anhydride ROCOP 255

Supplementary Figures and Data for Chapter 5 256

Figure S5.1. ^{1}H NMR spectrum (400 MHz, 298 K, THF-d_8) of complex **13**. 256

Figure S5.2. ^{13}C NMR spectrum (126 MHz, 298 K, THF-d_8) of complex **13**. 257

Figure S5.3. ^{1}H COSY NMR Spectrum (400 MHz, 298 K, THF-d_8) of complex **13**. 257

Figure S5.4. ^{1}H-^{13}C HSQC NMR Spectrum (298 K, THF-d_8) of complex **13**. 258

Figure S5.5. ^{1}H-^{13}C HMBC NMR Spectrum (298 K, THF-d_8) of complex **13**. 258

Figure S5.6. Infrared spectrum of complex **13**. 259

Figure S5.7. ^{1}H NMR spectra (400 MHz, 298 K, $CDCl_3$) of complexes **1** and **13**. 259

Figure S5.8. Calculation of residual CTA equivalents. 260

Figure S5.9. TGA trace for PvCHPE-24 260

Figure S5.10. TGA trace for PvCHPE-44 261

Figure S5.11. TGA trace for PvCHPE-70 261

Figure S5.12. TGA trace for PvCHPE-91 262

Figure S5.13. ^{1}H NMR spectrum (400 MHz, 298 K,$CDCl_3$) of PvCHPE-24 before and after hot pressing. 262

Figure S5.14. ^{1}H NMR spectrum (400 MHz, 298 K,$CDCl_3$) of PvCHPE-44 before and after hot pressing. 263

Figure S5.15. ^{1}H NMR spectrum (400 MHz, 298 K,$CDCl_3$) of PvCHPE-70 before and after hot pressing. 263

Figure S5.16. ^{1}H NMR spectrum (400 MHz, 298 K,$CDCl_3$) of PvCHPE-91 before and after hot pressing. 264

Figure S5.17. GPC Trace of PvCHPE-24 before and after processing *via* hot press. 264

Figure S5.18. GPC Trace of PvCHPE-44 before and after processing *via* hot press. 265

Figure S5.19. GPC Trace of PvCHPE-70 before and after processing *via* hot press. 265

Figure S5.20. Results from DMTA of PvCHPE-44 between 30 – 200 °C 266

Figure S5.21. Results from DMTA of PvCHPE-70 between 30 – 200 °C. 266

References for Appendix 267

Supplementary Figures and Data for Chapter 2

Table S2.1. Selected bond lengths and angles for complex **3**.

Bond	Bond Length (Å)	Bond	Bond Angle (°)
N(1) – Mn(1)	1.9904(17)	N(1) – Mn(1) – N(2)	90.95(6)
N(2) – Mn(1)	2.1319(16)	N(1) – Mn(1) – O(2)	87.88(7)
O(2) – Mn(1)	1.9105(14)	N(1) – Mn(1) – O(3)	179.15(6)
O(3) – Mn(1)	1.8676(15)	N(1) – Mn(1) – O(5)	90.66(6)
O(5) – Mn(6)	2.2941(14)	N(1) – Mn(1) – O(6)	88.30(6)
O(6) – Mn(6)	2.0926(14)	N(2) – Mn(1) – O(2)	107.76(6)
		N(2) – Mn(1) – O(3)	88.88(6)
		N(2) – Mn(1) – O(5)	151.75(6)
		N(2) – Mn(1) – O(6)	92.14(6)
		O(2) – Mn(1) – O(3)	91.38(6)
		O(2) – Mn(1) – O(5)	100.49(6)
		O(2) – Mn(1) – O(6)	159.79(6)

Table S2.2. Selected bond lengths and angles for complex **4**.

Bond	Bond Length (Å)	Bond	Bond Angle (°)
N(1) – Fe(1)	2.1016(14)	N(1) – Fe(1) – N(2)	83.36(6)
N(2) – Fe(1)	2.1155(14)	N(1) – Fe(1) – O(2)	114.17(6)
O(2) – Fe(1)	1.8964(14)	N(1) – Fe(1) – O(3)	86.68(6)
O(3) – Fe(1)	1.9225(13)	N(1) – Fe(1) – O(5)	91.37(5)
O(5) – Fe(6)	2.1440(13)	N(1) – Fe(1) – O(6)	152.48(6)
O(6) – Fe(6)	2.1147(14)	N(2) – Fe(1) – O(2)	87.70(6)
		N(2) – Fe(1) – O(3)	169.54(6)
		N(2) – Fe(1) – O(5)	90.02(6)
		N(2) – Fe(1) – O(6)	93.12(6)
		O(2) – Fe(1) – O(3)	93.50(6)
		O(2) – Fe(1) – O(5)	153.87(6)
		O(2) – Fe(1) – O(6)	92.86(6)

Table S2.3. Selected bond lengths and angles for complex **5**.

Bond	Bond Length (Å)	Bond	Bond Angle (°)
N(1) – Co(1)	1.9119(13)	N(1) – Co(1) – N(2)	93.09(6)
N(2) – Co(1)	1.9159(14)	N(1) – Co(1) – O(2)	92.84(5)
O(2) – Co(1)	1.8904(12)	N(1) – Co(1) – O(3)	95.12(5)
O(3) – Co(1)	1.8812(12)	N(1) – Co(1) – O(5)	163.39(5)
O(5) – Co(1)	1.9849(11)	N(1) – Co(1) – O(6)	96.80(5)
O(6) – Co(6)	1.9529(11)	N(2) – Co(1) – O(2)	173.83(5)
		N(2) – Co(1) – O(3)	90.14(5)
		N(2) – Co(1) – O(5)	89.43(5)
		N(2) – Co(1) – O(6)	91.26(5)
		O(2) – Co(1) – O(3)	87.65(5)
		O(2) – Co(1) – O(5)	85.37(5)
		O(2) – Co(1) – O(6)	89.72(5)
		O(3) – Co(1) – O(6)	167.90(5)

Table S2.4. Selected bond lengths and angles for complex **6**.

Bond	Bond Length (Å)	Bond	Bond Angle (°)
N(1) – Al(1)	1.9977(9)	N(1) – Al(1) – N(2)	89.93(4)
N(2) – Al(1)	2.0127(9)	N(1) – Al(1) – O(2)	90.81(3)
O(2) – Al(1)	1.8240(8)	N(1) – Al(1) – O(3)	103.42(4)
O(3) – Al(1)	1.8162(8)	N(1) – Al(1) – O(5)	157.05(4)
O(5) – Al(6)	1.9935(8)	N(1) – Al(1) – O(6)	91.35(3)
O(6) – Al(6)	1.9910(8)	N(2) – Al(1) – O(2)	178.63(4)
		N(2) – Al(1) – O(3)	87.67(4)
		N(2) – Al(1) – O(5)	89.94(4)
		N(2) – Al(1) – O(6)	88.35(4)
		O(2) – Al(1) – O(3)	91.03(4)
		O(2) – Al(1) – O(5)	89.83(3)
		O(2) – Al(1) – O(6)	92.79(3)
		O(3) – Al(1) – O(6)	164.69(4)

Table S2.5. Summary of crystallographic refinement data for complexes **2** – **6.**

Complex	**2**	**3**	**4**	**5**	**6**
Local Code	035rwfk21	019rwfk21	005rwfk21	027ap19	008rwfk20
CCDC Deposition Number	-	-	-		
Crystal data					
Chemical formula	$C_{23}H_{29}CrN_2O_7 \cdot 2(CHCl_3)$	$C_{23}H_{27}MnN_2O_6$	$2(C_{23}H_{27}FeN_2O_6) \cdot 2(H_2O)$	$C_{23}H_{27}CoN_2O_6$	$C_{23}H_{27}AlN_2O_6$
M_r	736.22	482.40	1002.66	486.39	454.44
Crystal system, space group	Monoclinic, *C*2/*m*	Monoclinic, $P2_1/c$	Monoclinic, $P2_1/c$	Monoclinic, $P2_1/c$	Monoclinic, $P2_1/c$
a, *b*, *c* (Å)	17.182 (5), 20.689 (4), 8.951 (2)	9.0541 (1), 12.7892 (2), 19.3938 (3)	10.1973 (2), 13.5163 (2), 19.0660 (4)	8.99960(10) 12.8364(2) 19.0472(3)	8.99580(10) 12.88180(10) 19.2304(2)
β (°)	99.23 (3)	96.494 (1)	99.524 (2)	96.7450(10)	96.6150(10)
V (Å^3)	3140.6 (13)	2231.29 (6)	2591.64 (9)	2185.15(5)	2213.62(4)
Z	4	4	2	4	4
Radiation type	Cu *K*α	Cu *K*α	Cu *K*α	Cu *K*α	Cu *K*α
μ (mm^{-1})	8.09	5.17	5.03	6.53	1.17
Data collection					
Absorption correction	Multi-scan *CrysAlis PRO* 1.171.39.46 (Rigaku Oxford Diffraction, 2018) Empirical absorption correction using spherical harmonics, implemented in SCALE3 ABSPACK scaling algorithm.				
T_{min}, T_{max}	0.115, 1.000	0.893, 1.000	0.488, 1.000		0.874, 1.000
No. of measured, independent and observed [$I > 2\sigma(I)$] reflections	6240, 2840, 1494	12066, 4600, 3975	13959, 5365, 4846	12050, 4529, 4158	23912, 4605, 4294
R_{int}	0.267	0.043	0.029	0.031	0.028
$(\sin\theta/\lambda)_{max}$ (Å^{-1})	0.630	0.629	0.630	0.630	0.630
Refinement					
$R[F^2 > 2\sigma(F^2)]$, $wR(F^2)$, *S*	0.212, 0.538, 1.12	0.038, 0.098, 1.05	0.040, 0.111, 1.04	0.034, 0.083, 1.07	0.031, 0.083, 1.05
No. of reflections	2840	4600	5365	4529	4605
No. of parameters	229	294	306	294	294
No. of restraints	6	0	0	0	0
$(\Delta/\sigma)_{max}$	0.869	0.001	0.002	0.000	0.001
$\Delta\rangle_{max}$, $\Delta\rangle_{min}$ (e Å^{-3})	0.64, -0.65	0.41, -0.45	0.33, -0.41	0.34, -0.57	0.28, -0.22

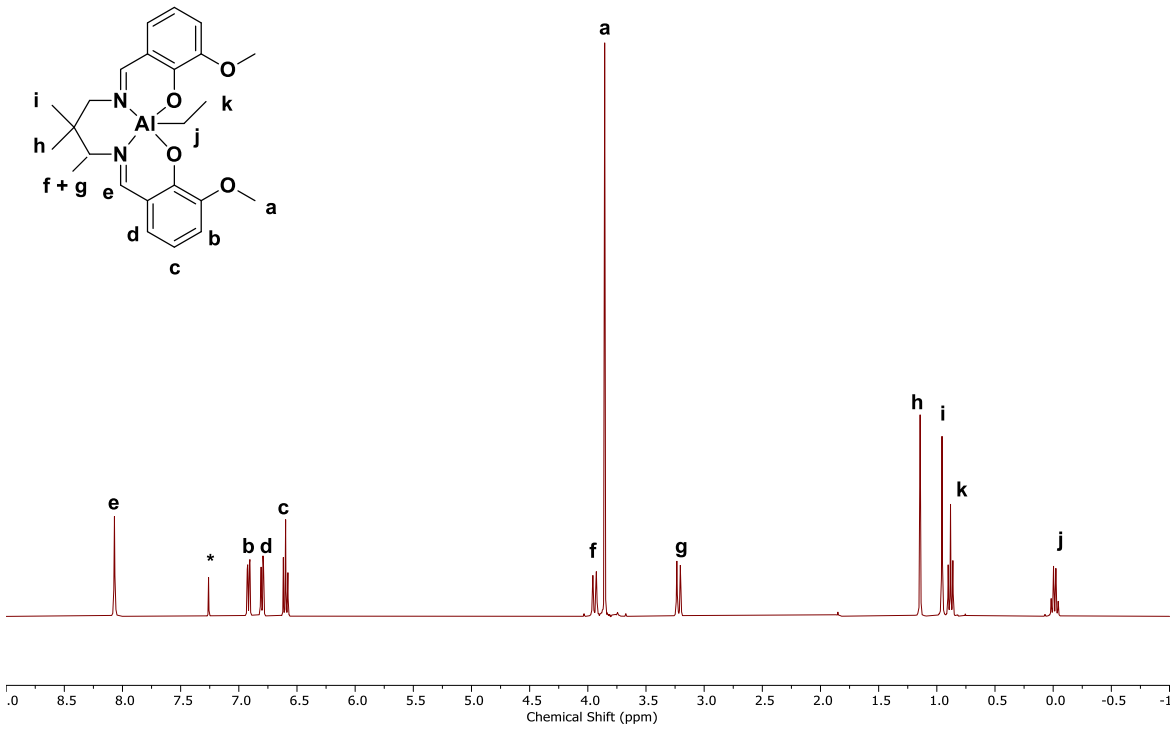


Figure S2.1. ^{1}H NMR Spectrum (400 MHz, 298 K, $CDCl_3$(*)) of complex **1**.

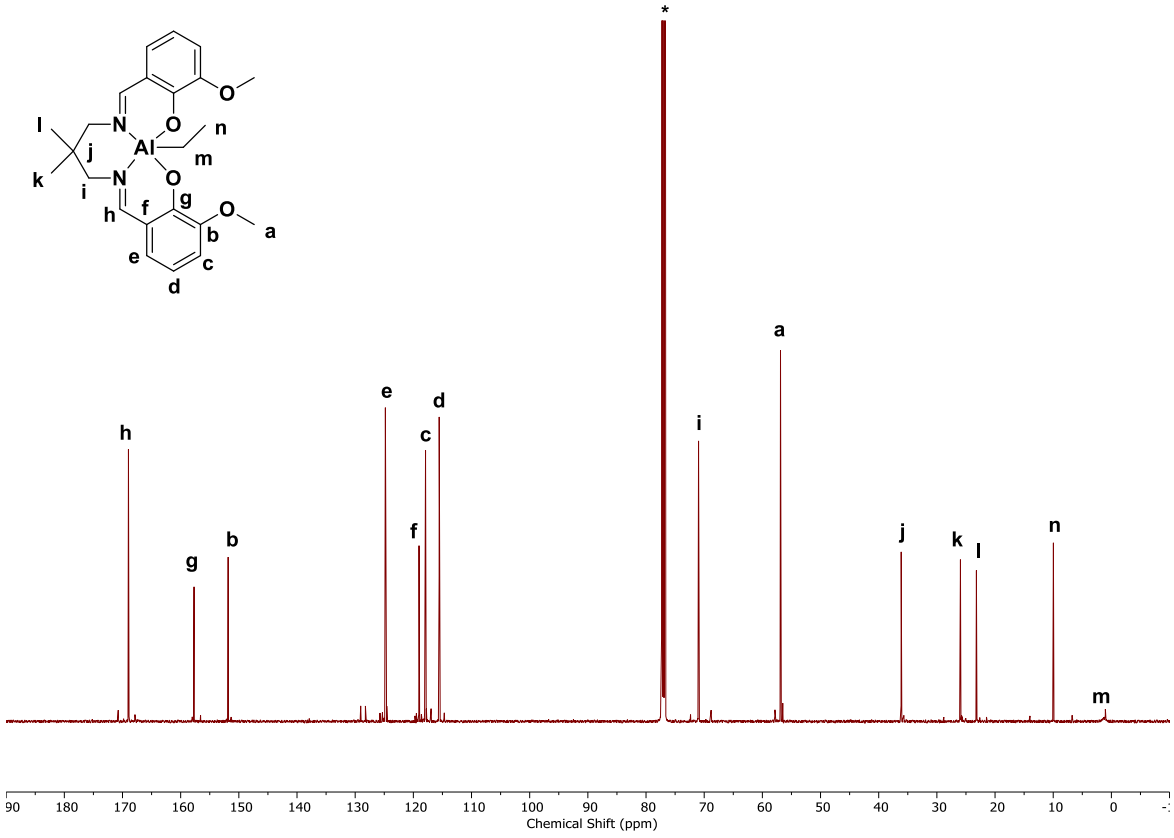


Figure S2.2. ^{13}C NMR Spectrum (126 MHz, 298 K, $CDCl_3$(*)) of complex **1**.

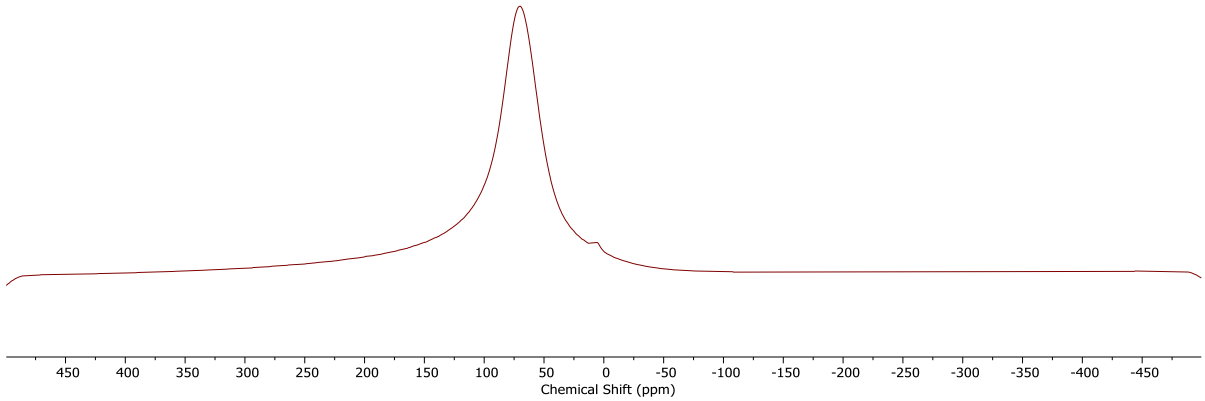


Figure S2.3. ^{27}Al NMR Spectrum (104 MHz, 298 K, CDCl3(*)) of complex **1.**

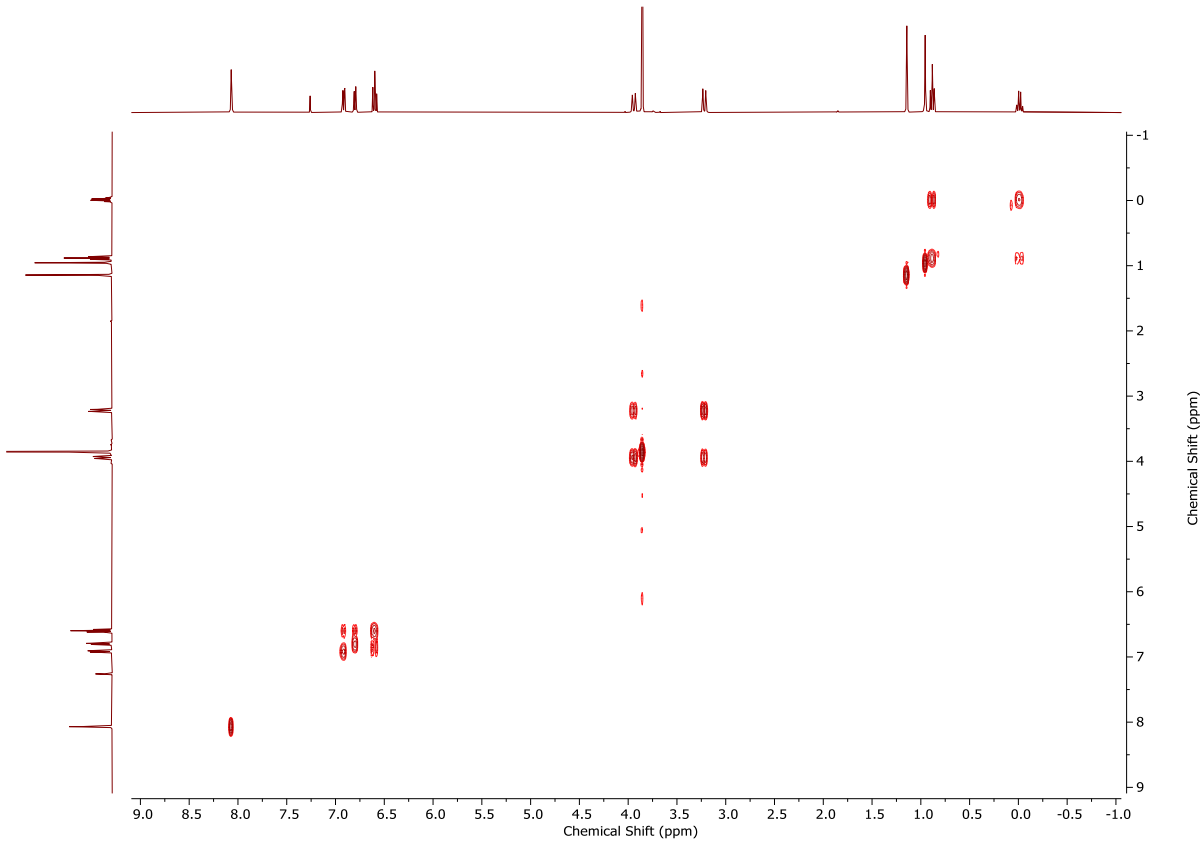


Figure S2.4. ^{1}H COSY NMR Spectrum (400 MHz, 298 K, $CDCl_3$) of complex **1**.

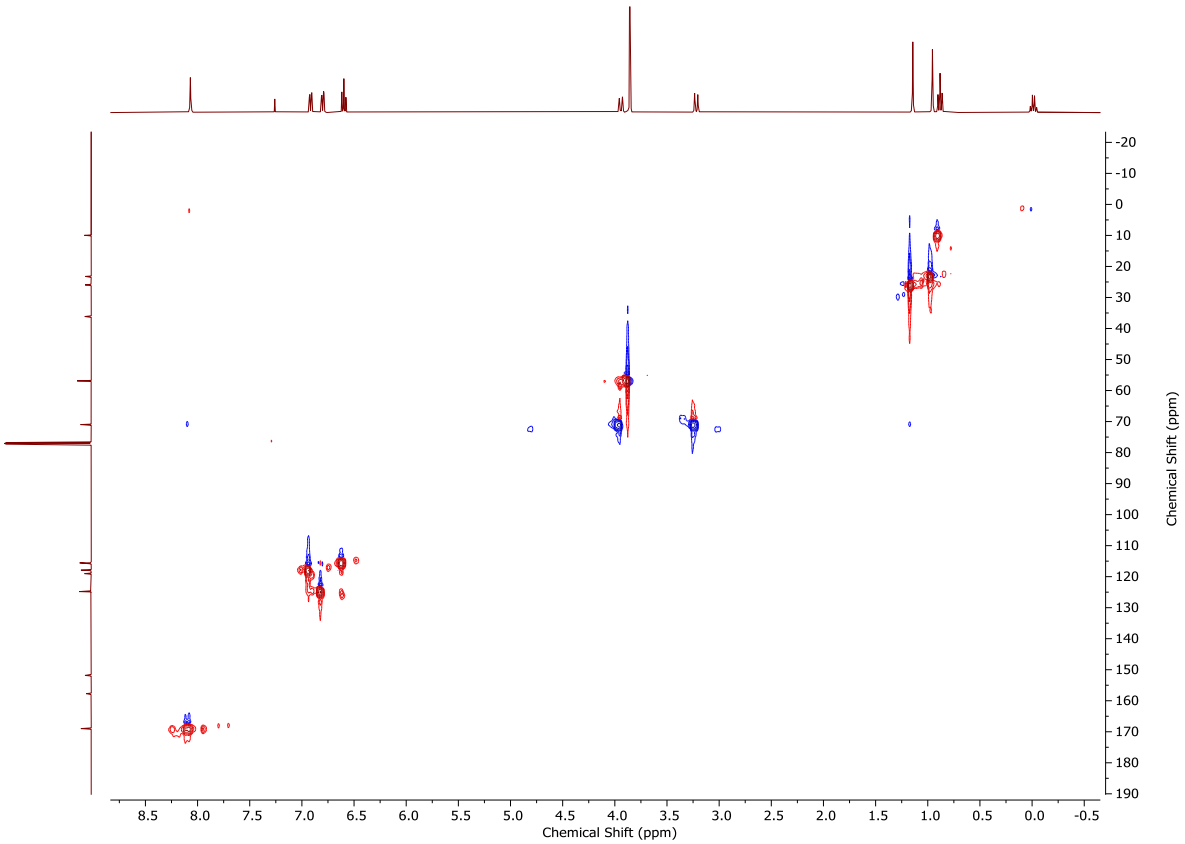


Figure S2.5. ^{1}H-^{13}C HSQC NMR Spectrum (298 K, $CDCl_3$) of complex **1**.

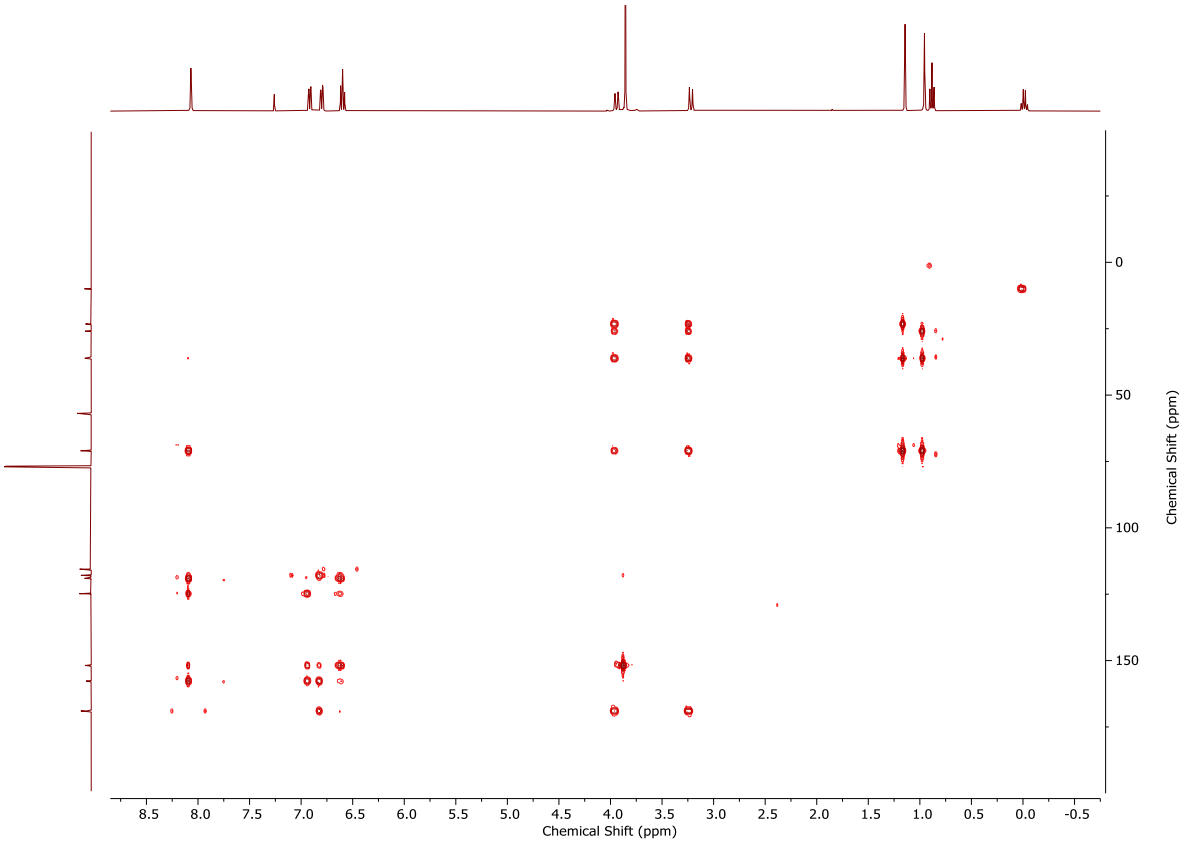


Figure S2.6. ^{1}H-^{13}C HMBC NMR Spectrum (298 K, $CDCl_3$) of complex **1**.

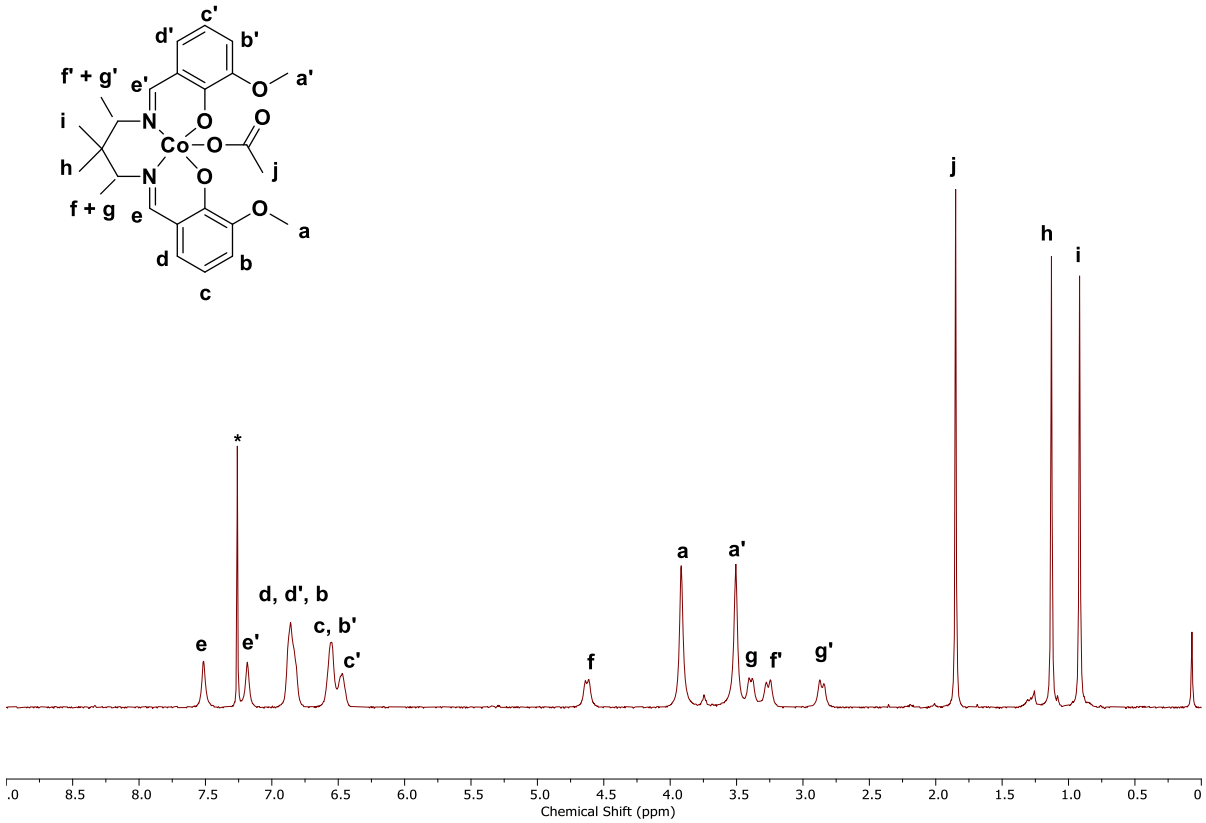


Figure S2.7. ^{1}H NMR Spectrum (400 MHz, 298 K, $CDCl_3$(*)) of complex **5**.

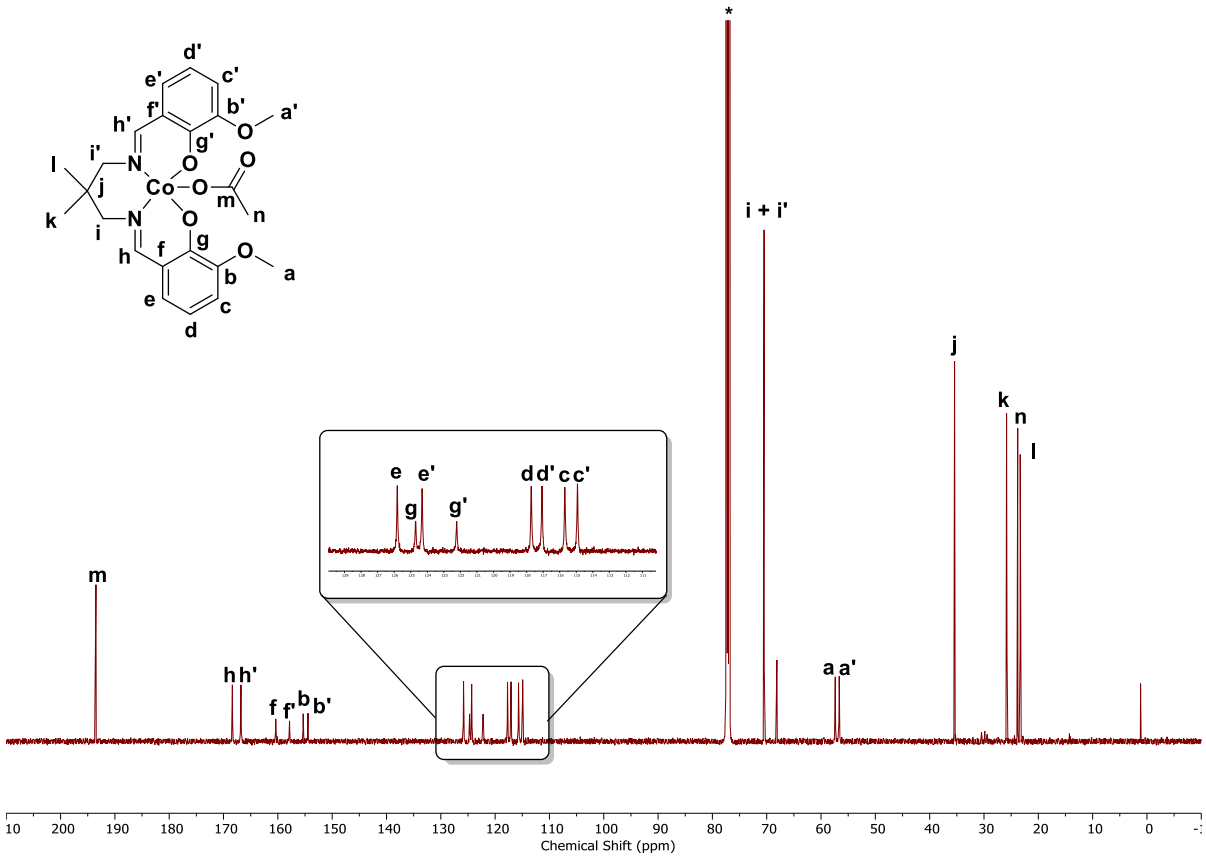


Figure S2.8. ^{13}C NMR Spectrum (126 MHz, 298 K, $CDCl_3$(*)) of complex **5**.

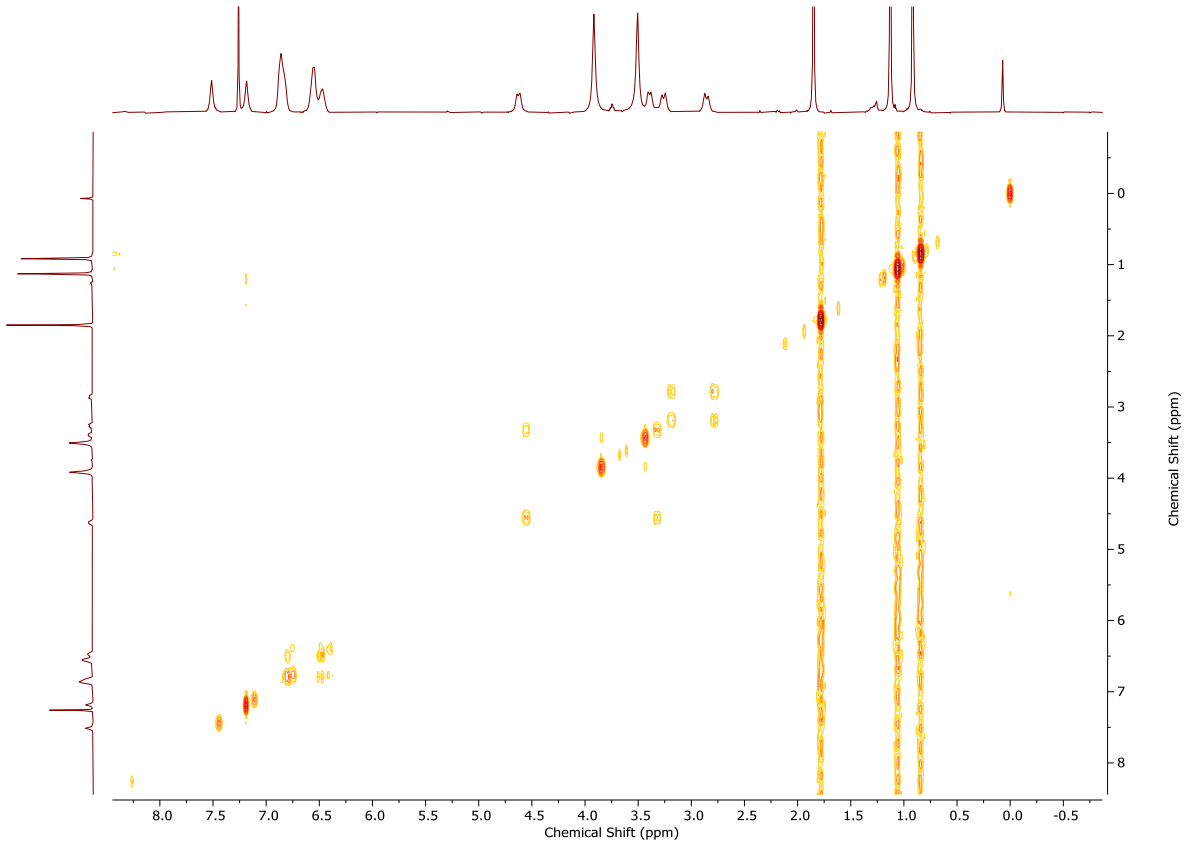


Figure S2.9. ^{1}H COSY NMR Spectrum (400 MHz, 298 K, $CDCl_3$) of complex **5**.

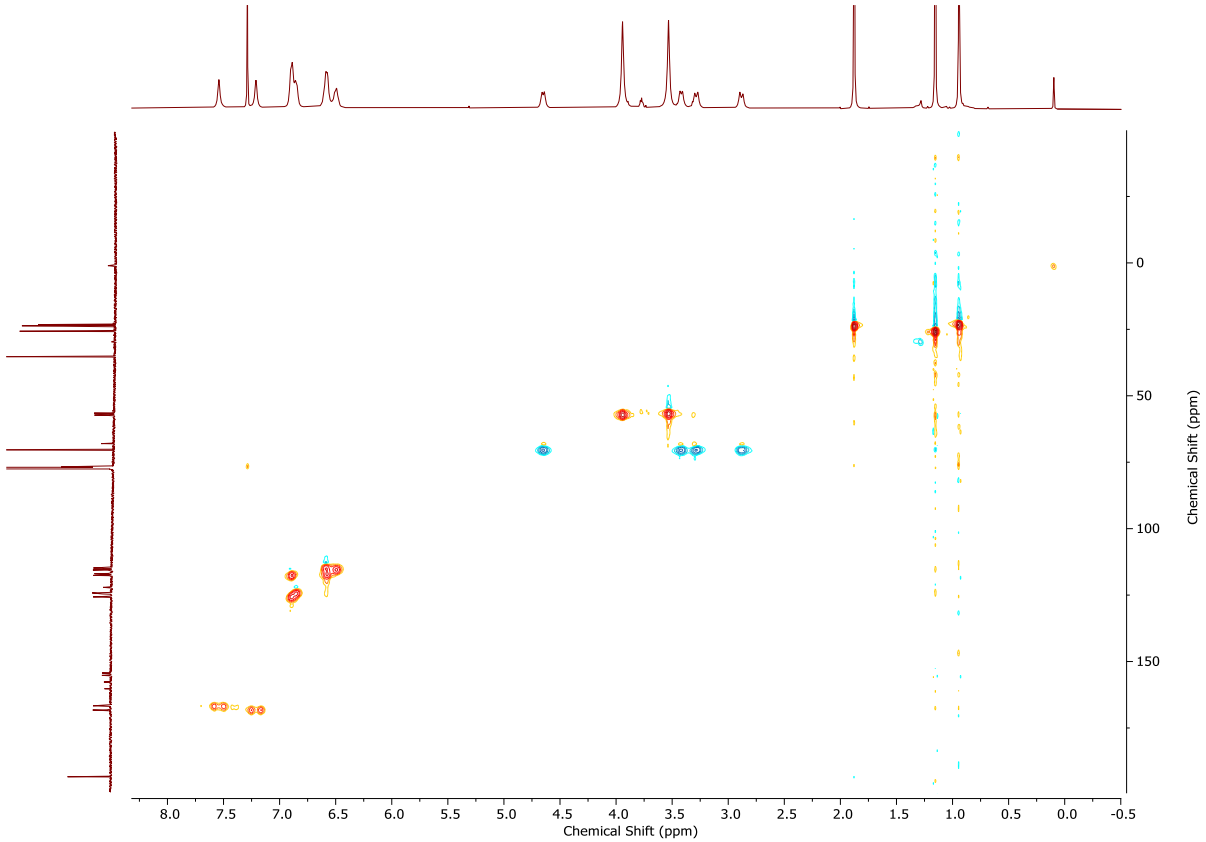


Figure S2.10. ^{1}H-^{13}C HSQC NMR Spectrum (298 K, $CDCl_3$) of complex **5**.

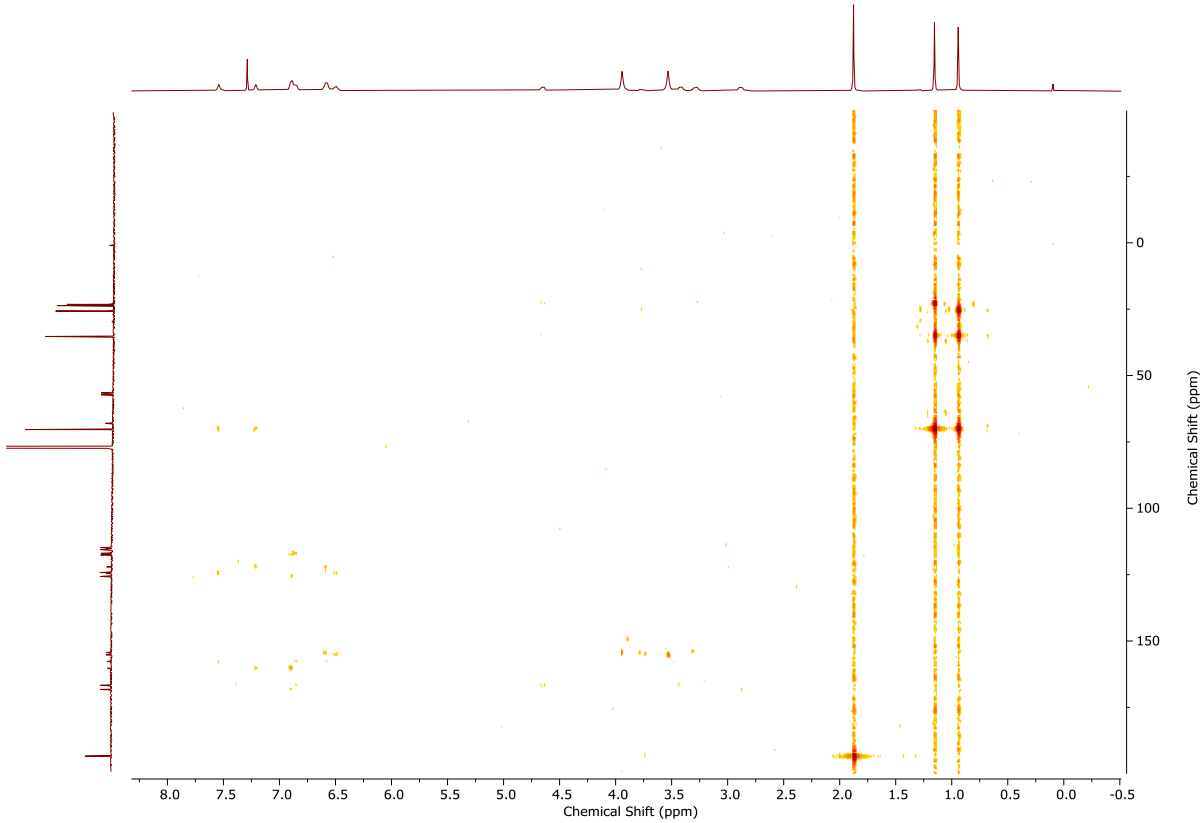


Figure S2.11. ^{1}H-^{13}C HMBC NMR Spectrum (298 K, $CDCl_3$) of complex **5**.

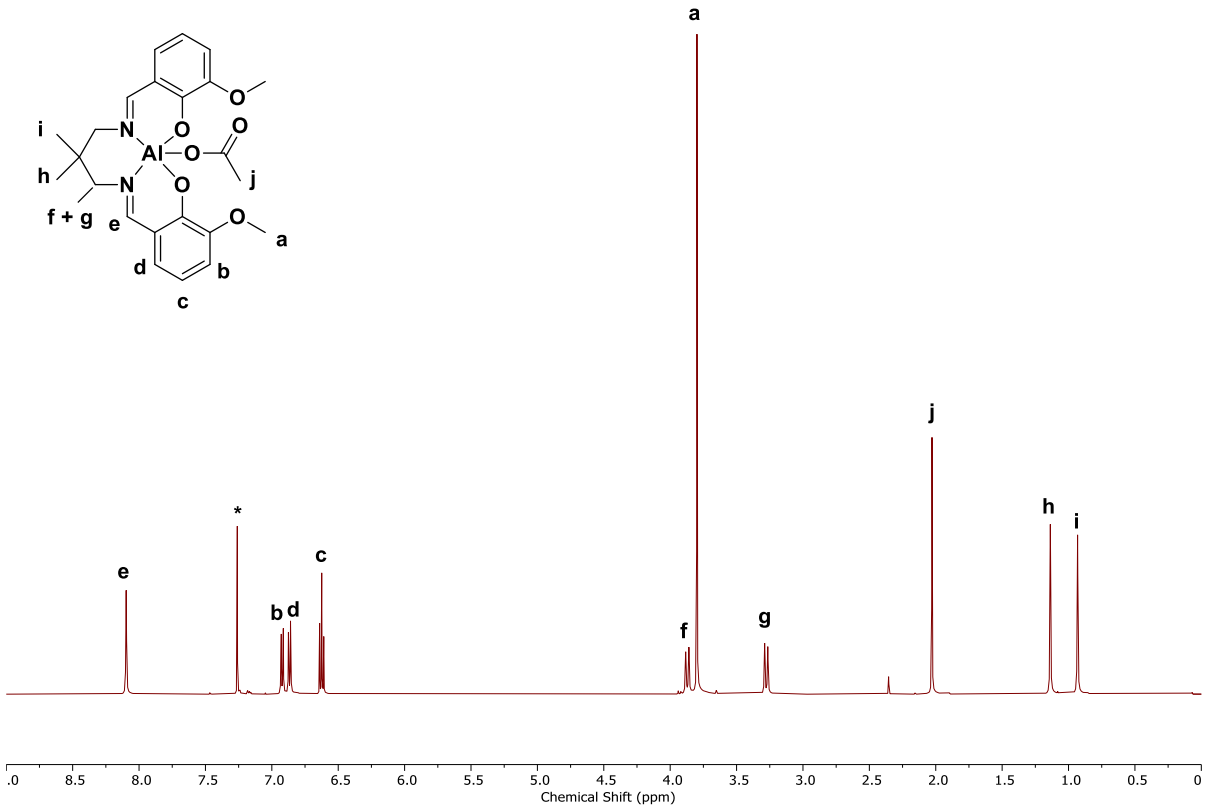


Figure S2.12. ^{1}H NMR Spectrum (400 MHz, 298 K, $CDCl_3$(*)) of complex **6**.

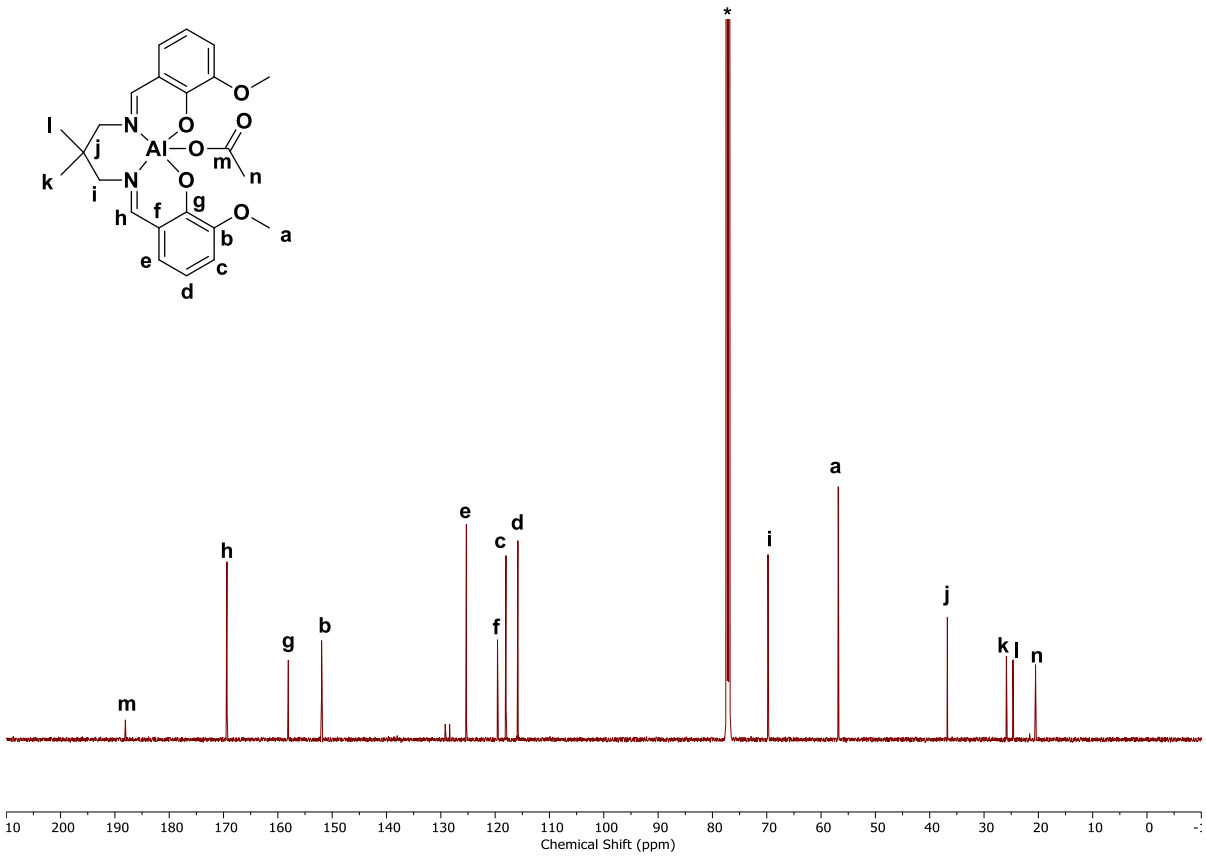


Figure S2.13. ^{13}C NMR Spectrum (126 MHz, 298 K, $CDCl_3$(*)) of complex **6**.

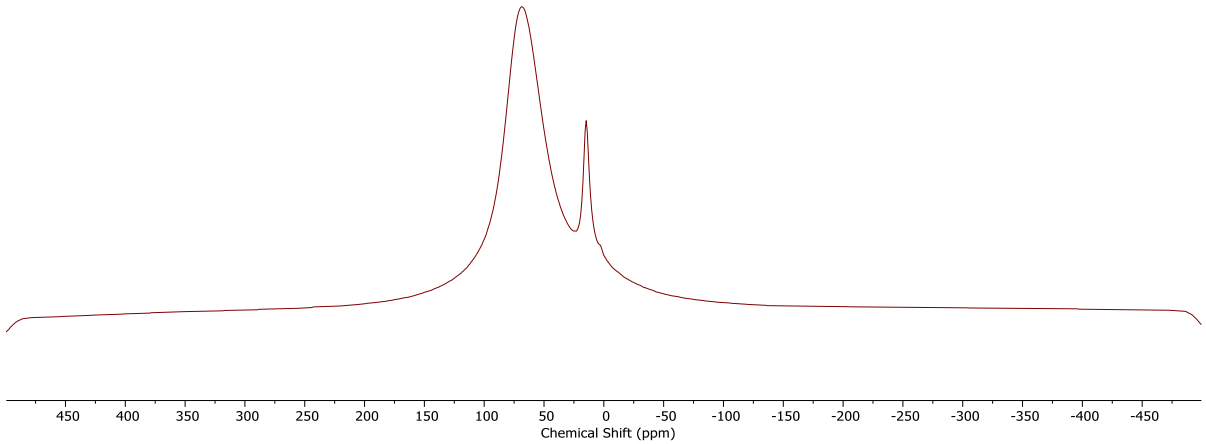


Figure S2.14. ^{27}Al NMR Spectrum (104 MHz, 298 K, CDCl3(*)) of complex **6**.

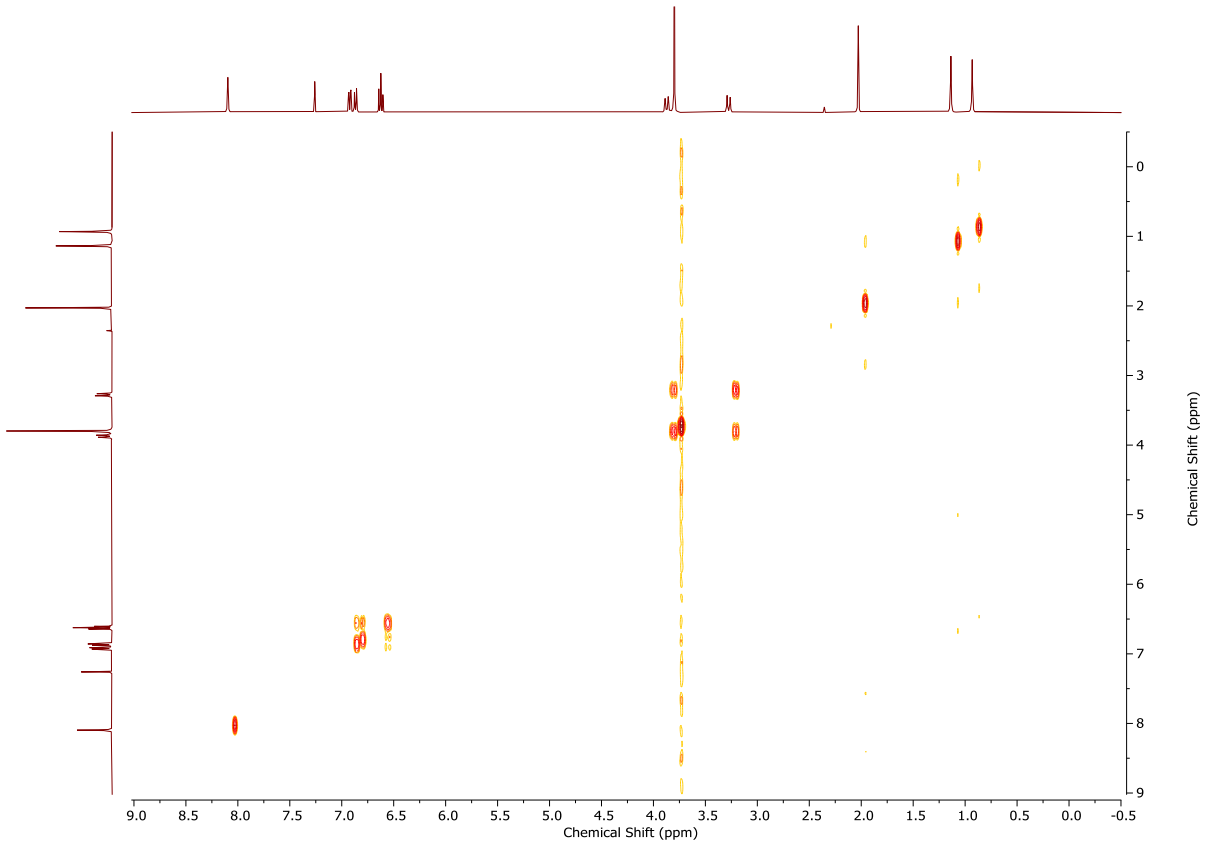


Figure S2.15. ^{1}H COSY NMR Spectrum (400 MHz, 298 K, $CDCl_3$) of complex **6**.

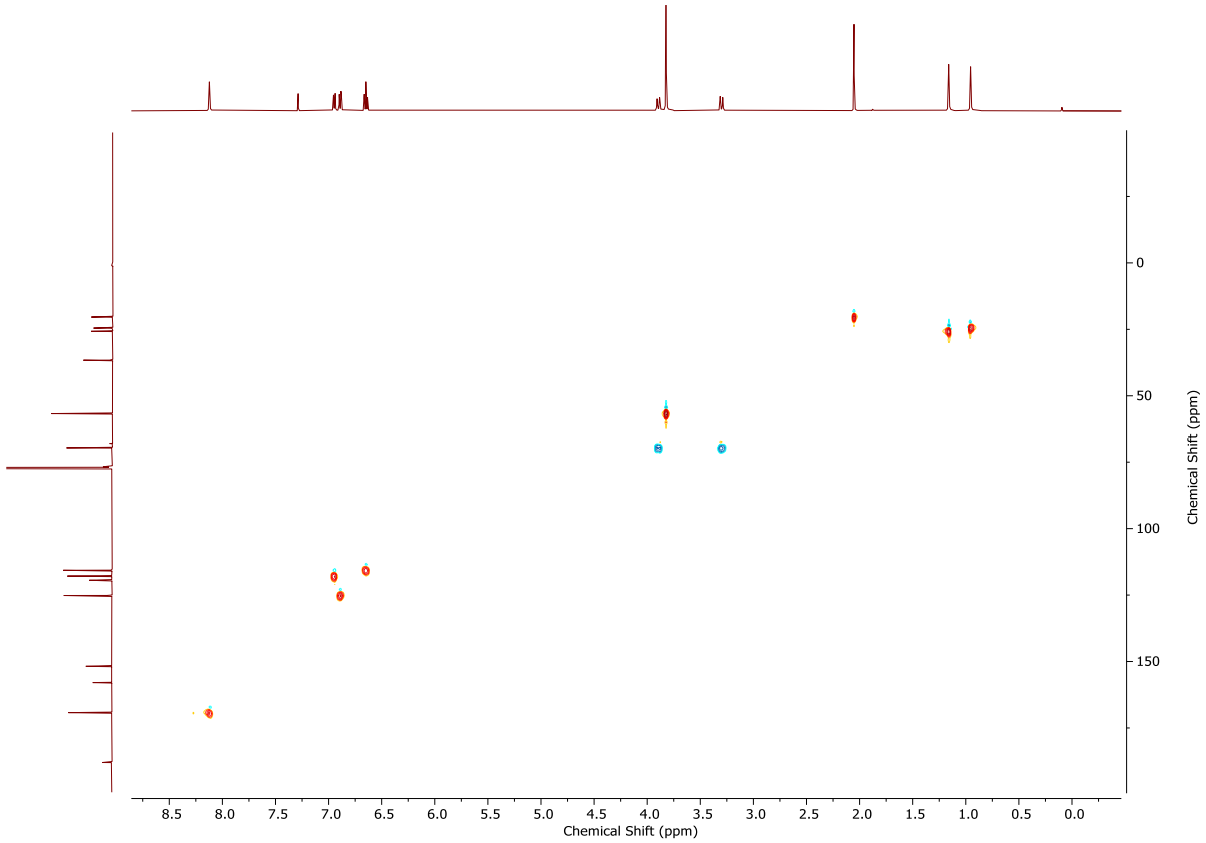


Figure S2.16. ^{1}H-^{13}C HSQC NMR Spectrum (298 K, $CDCl_3$) of complex **6**.

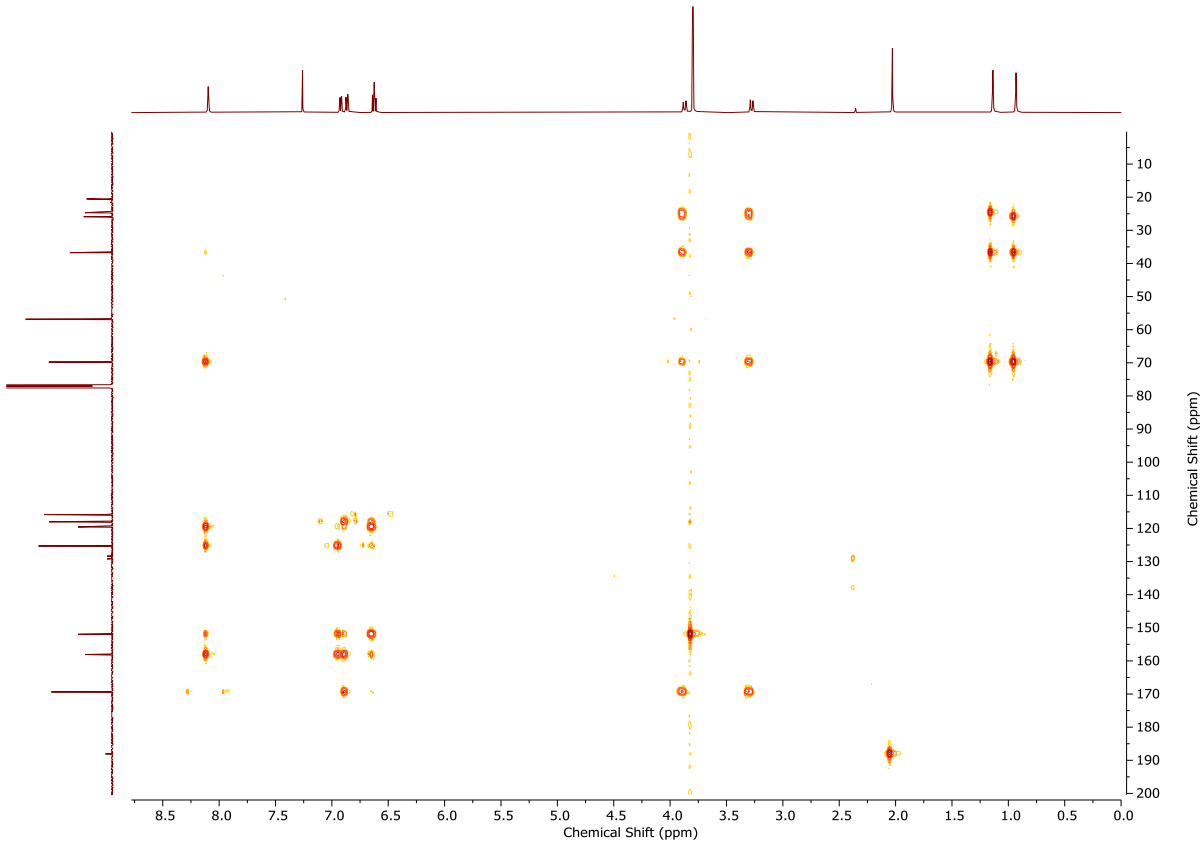


Figure S2.17. ^{1}H-^{13}C HSQC NMR Spectrum (298 K, $CDCl_3$) of complex **6**.

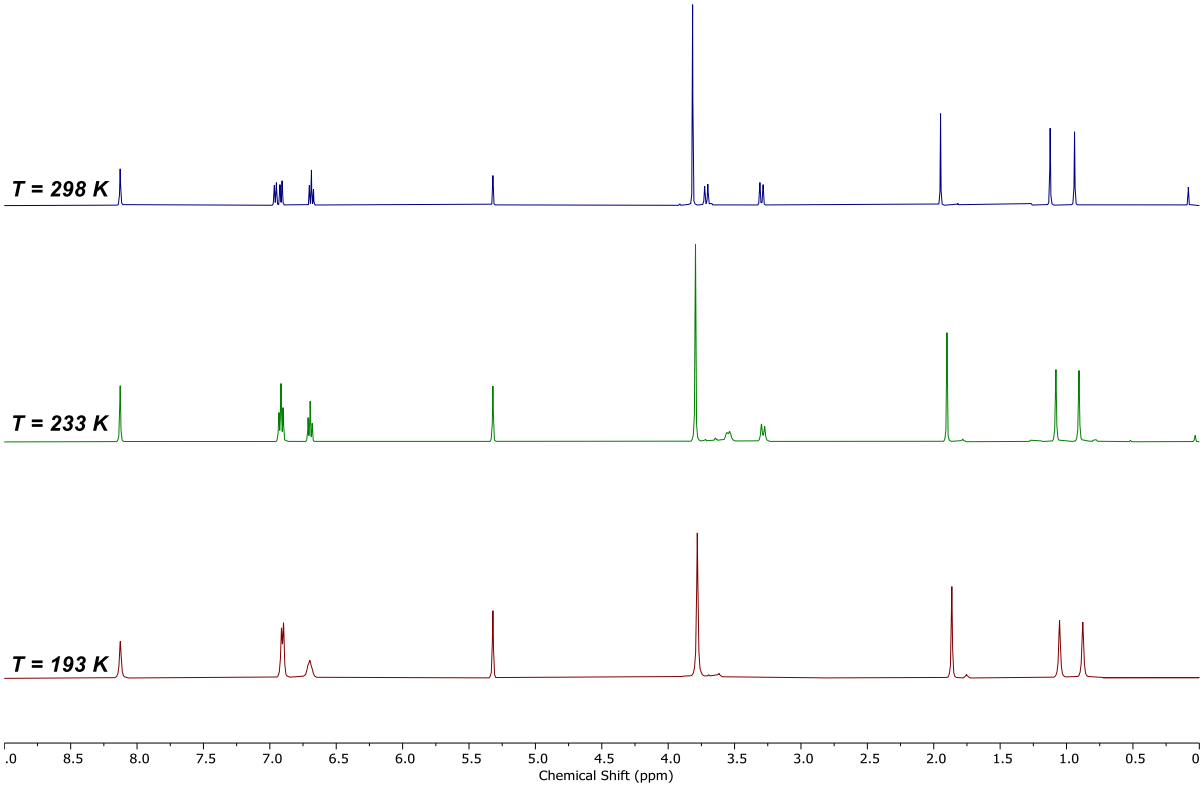


Figure S2.18. Variable temperature ^{1}H NMR spectra (400 MHz, CD_2Cl_2) of complex **6**.

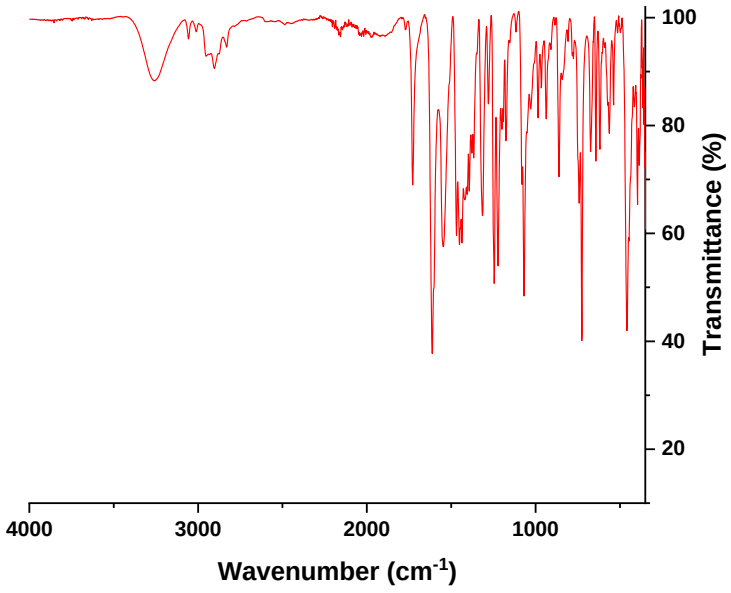


Figure S2.19. Infrared spectrum of complex **2**.

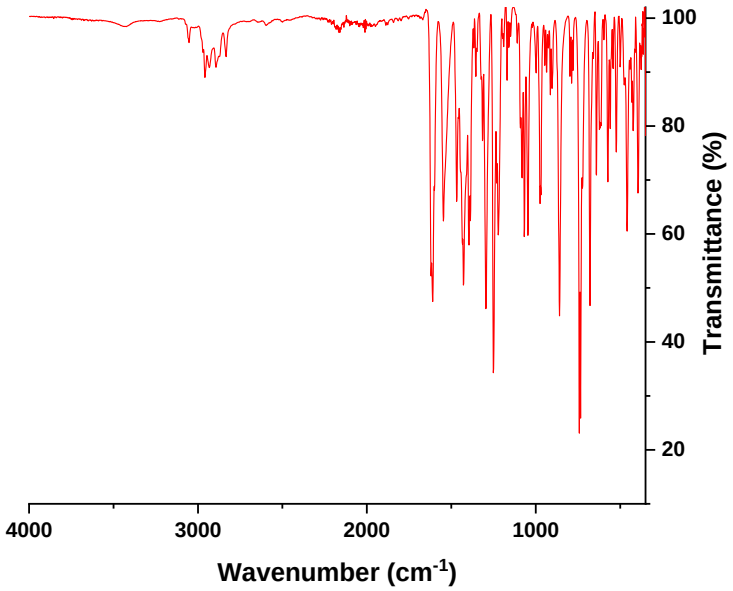


Figure S2.20. Infrared spectrum of complex **3**.

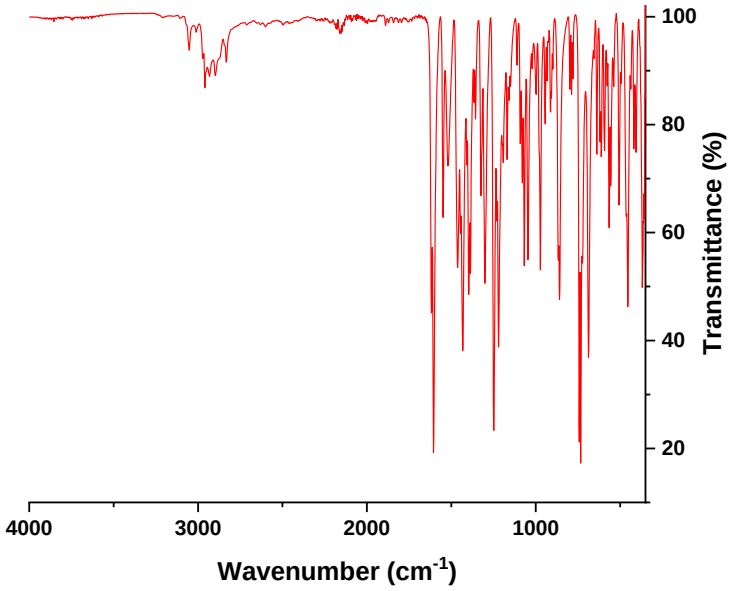


Figure S2.21. Infrared spectrum of complex **4**.

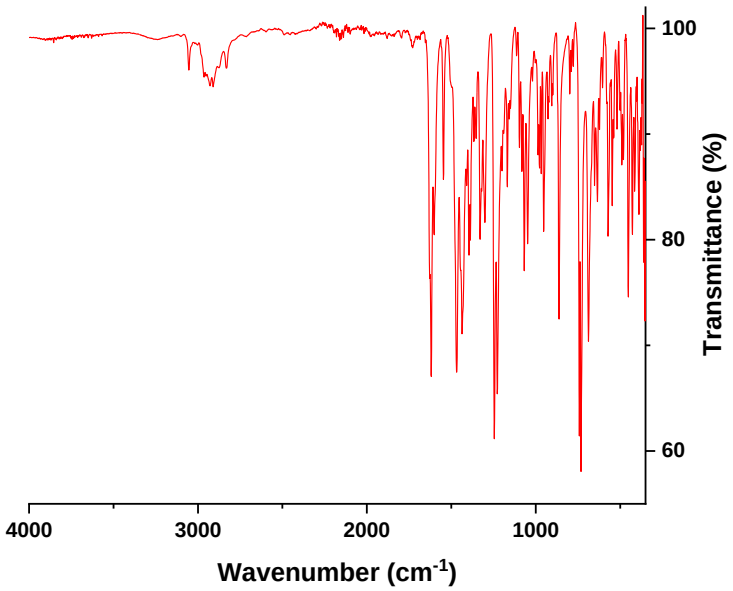


Figure S2.22. Infrared spectrum of complex **5**.

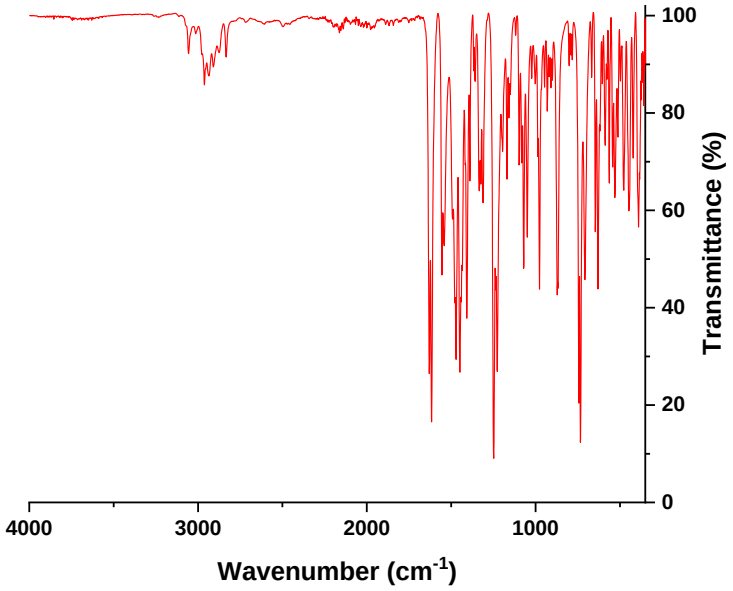


Figure S2.23. Infrared spectrum of complex **6**.

Table S2.6. Data for the ROCOP of CHO and PA at complete PA conversion for complexes **1** – **5** and [SalcyCrCl].

Entry	Catalyst[a]	Time (m)	Conv.[b] (%)	Selectivity[c] (%)	$M_{n,\ GPC}$ [Đ][e] (kg mol^{-1})	$M_{n,\ Theory}$[f] (kg mol^{-1})
1	**1** (Al)	15	100	>99	7.5 [1.16]	8.2
2	**3** (Mn)	30	100	>99	5.2 [1.29]	6.2
3	**4** (Fe)	30	100	>99	6.1 [1.52]	6.2
4	**5** (Co)	15	100	>99	6.5 [1.27]	6.2
5	[SalcyCrCl]	10	100	>99	5.1 [1.27]	6.2

[a] Catalysis conditions: [Cat]:[PPNCl]:[CHD]:[PA]:[CHO] = 1:1:2:100:500, T = 100 °C. [b] Conversion of anhydride, determined by comparison of ^{1}H NMR integrals corresponding to PCHPE (7.65 – 7.30 ppm) and PA (8.10 – 7.85 ppm). [c] Selectivity for polyester over polyether, determined by comparison of ^{1}H NMR integrals corresponding to PCHPE (5.22-5.06 ppm) and PCHO (3.60 - 3.20 ppm). [d] Determined by GPC in THF, at 30 °C, using narrow dispersity polystyrene standards. [e] Theoretical M_n values. Determined through (TON*Mn(Repeat Unit))/ (Number of equivalents of CHD + Number of equivalents of PPNCl (+ Number of equivalents of catalyst when 2 and SalcyCrCl are utilised)).

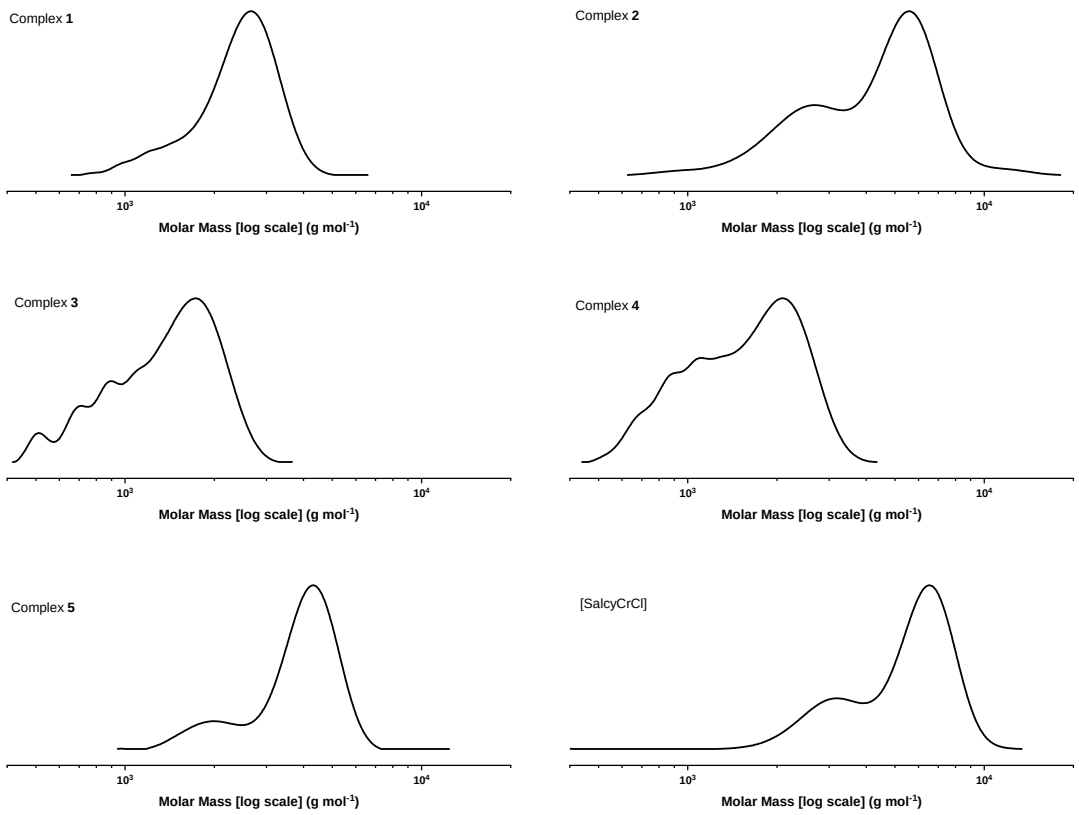


Figure S2.24. GPC trace of PCHPE obtained with complexes **1** – **5** and [SalcyCrCl], corresponding to Table 2.3, Entries 1 – 6.

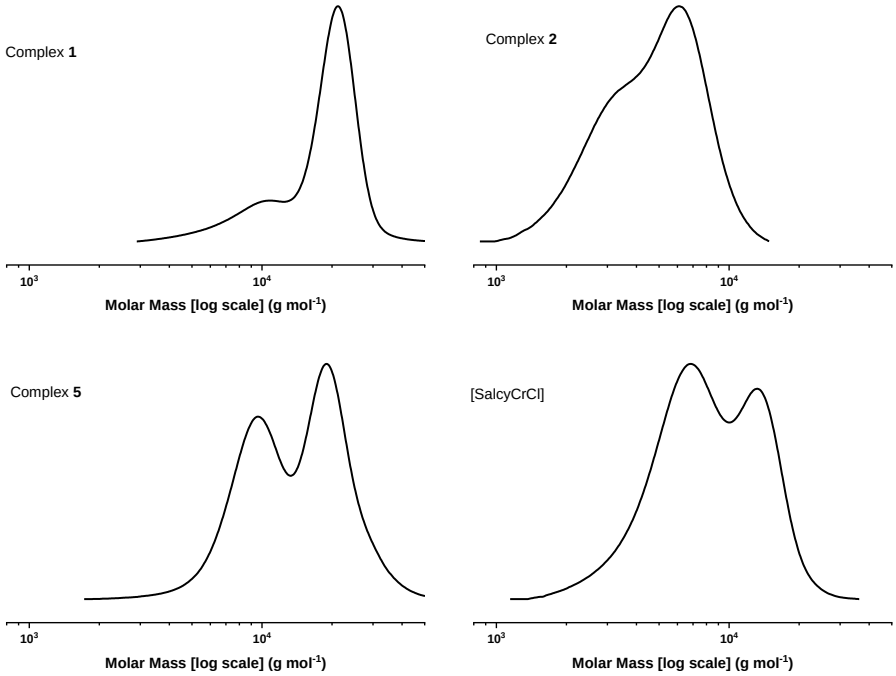


Figure S2.25. GPC trace of PDL obtained with complexes **1**, **2**, **5** and [SalcyCrCl], corresponding to Table 2.4, Entries 1 – 4.

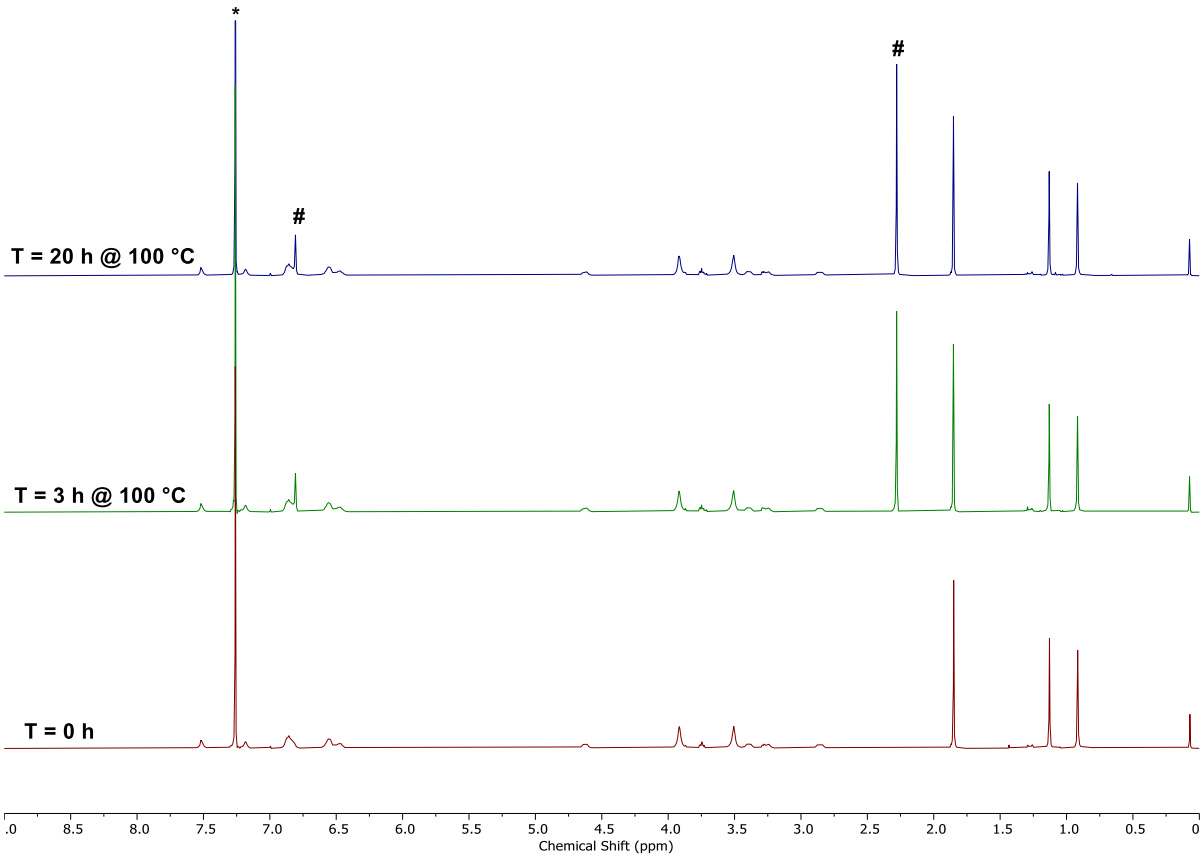


Figure S2.26. Temperature stability of complex **5**. ^{1}H NMR of complex **5** (400 MHz, 298K, $CDCl_3$) before and after heating for 20 hours at 100 °C, with an internal standard (mesitylene, #). No significant change was observed in the NMR integrals, when compared to the internal standard, before and after the heating period.

Supplementary Figures and Data for Chapter 3

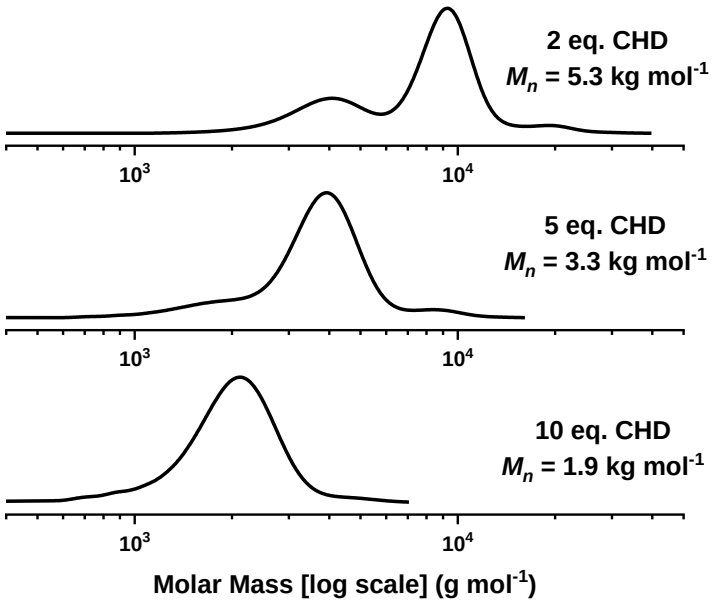


Figure S3.1. Polymer molecular mass distributions of PCHPE copolymers synthesised with complex **5**/PPNCl, at full PA conversion, measured by GPC with THF eluent, at 30 °C.

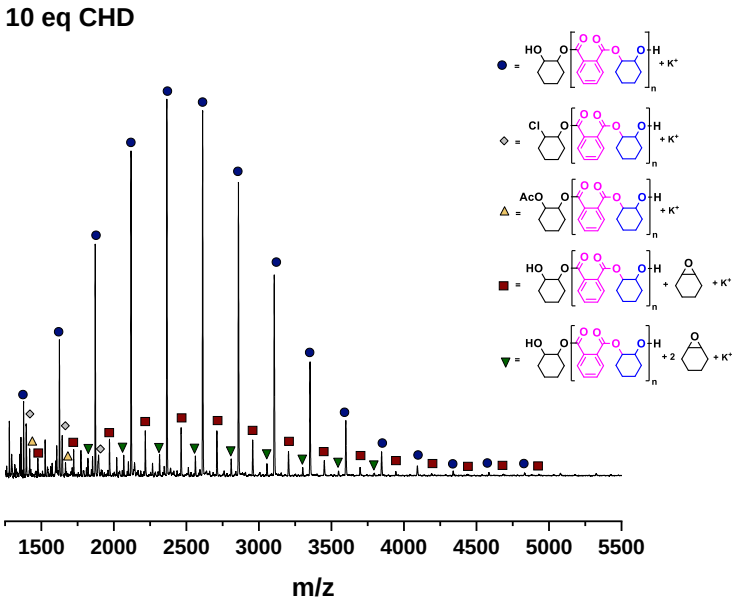


Figure S3.2 MALDI-ToF spectrum of PCHPE obtained with **5**/PPNCl and 10 equivs. of CHD.

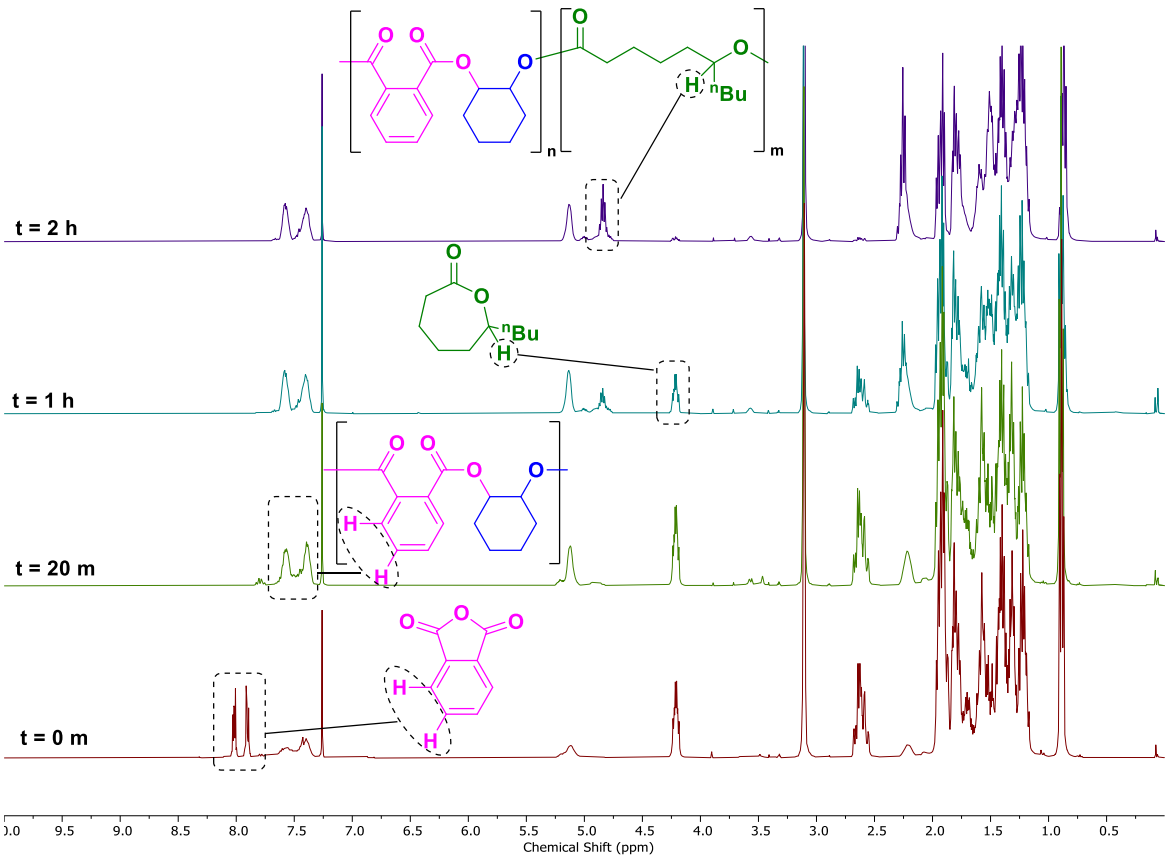


Figure S3.3. ^{1}H NMR spectra ($CDCl_3$, 400 MHz, 298 K) of aliquots taken during switchable polymerisation.

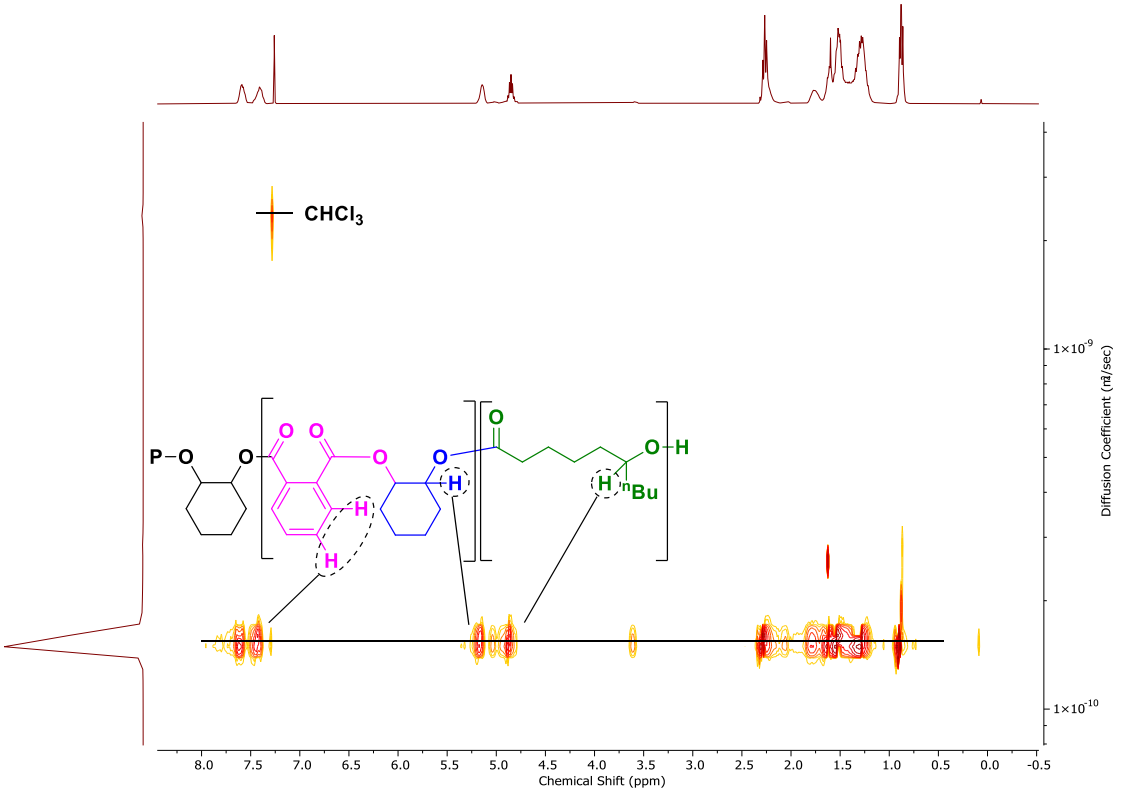


Figure S3.4. ^{1}H DOSY ($CDCl_3$, 400 MHz, 298 K) of PDL-*b*-PCHPE-*b*-PDL. A single diffusion coefficient ($D = 1.51x10^{-10}$ m^2 s^{-1}) for all ^{1}H signals is observed, including those corresponding to both PCHPE and PDL, confirming block copolymer formation.

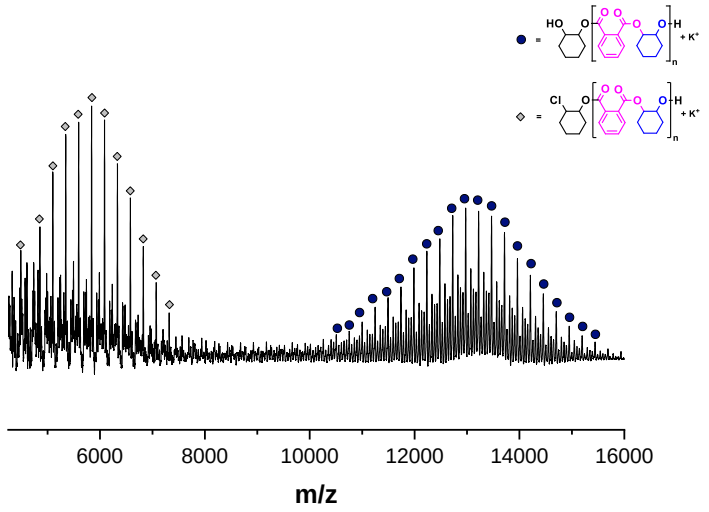


Figure S3.5. MALDI-ToF spectrum of PCHPE synthesised during switchable catalysis (Table 2.1, Entry 5) before initiation of ε-DL ROP, showing the low weight shoulder is due to initiation from chloride anions.

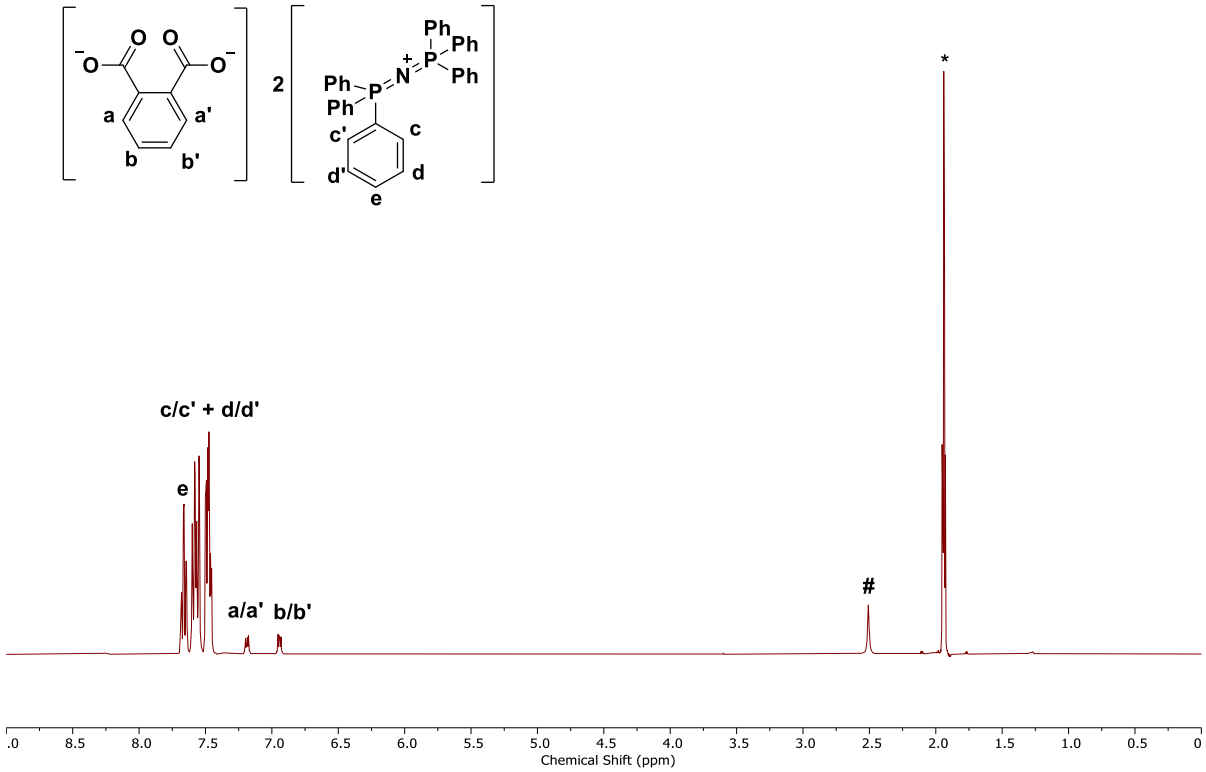


Figure S3.6. ^{1}H NMR spectrum (400 MHz, 298 K, MeCN-d_3(*)) of PPN_2PA # is water present in solvent.

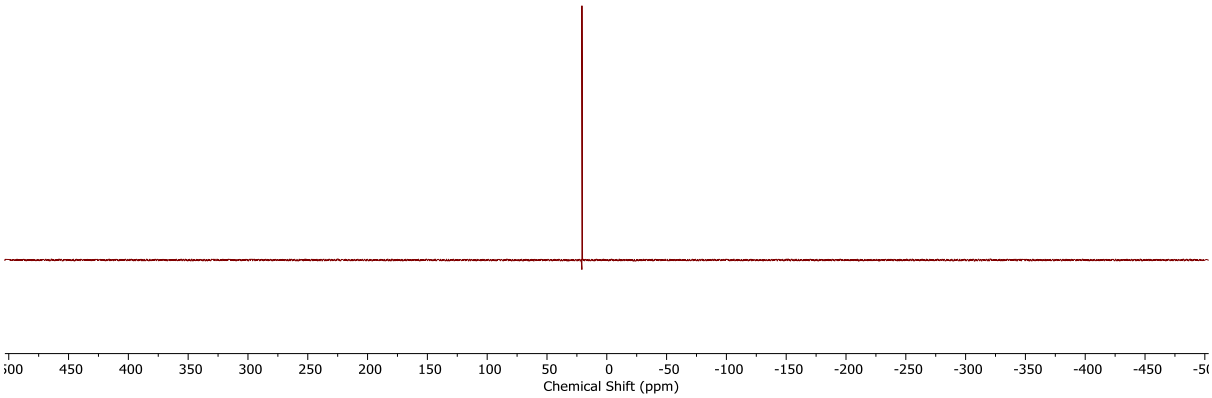


Figure S3.7. $^{31}P\{^{1}H\}$ NMR spectrum (162 MHz, 298K, MeCN-d_3) of PPN_2PA.

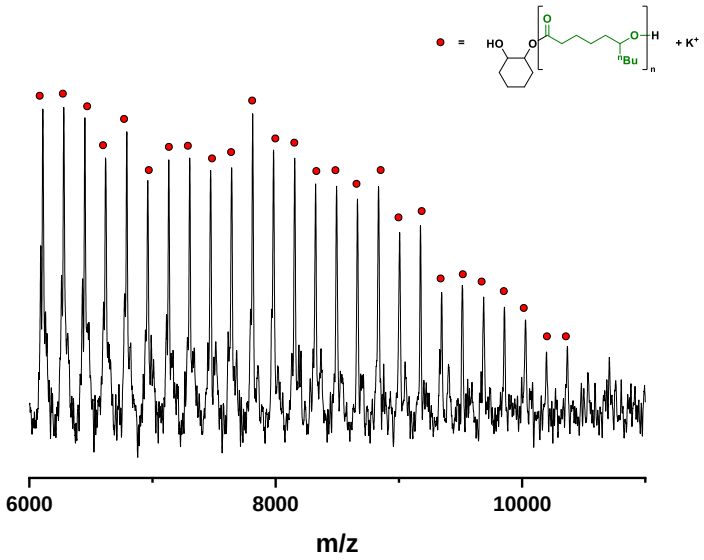


Figure S3.8. MALDI-ToF spectrum of PDL obtained with **1**/PPN_2PA and 2 equivs. of CHD. Red circle = α,ω-hydroxy end capped PCHPE.

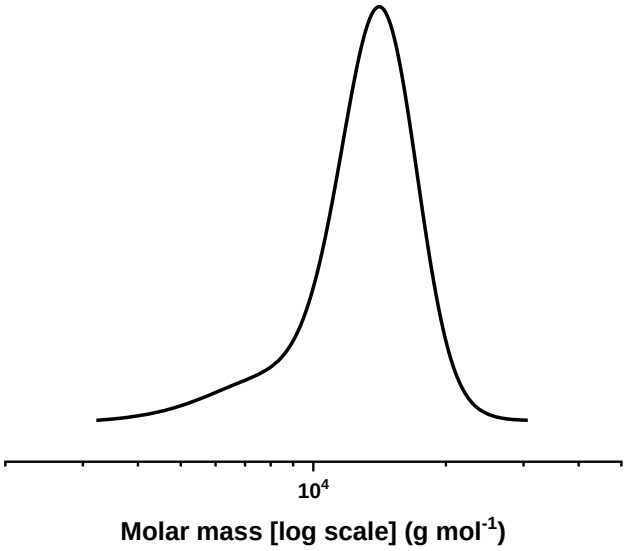


Figure S3.9. Polymer molecular mass distributions of PDL prepared with complex **1**/PPN$_2$PA.

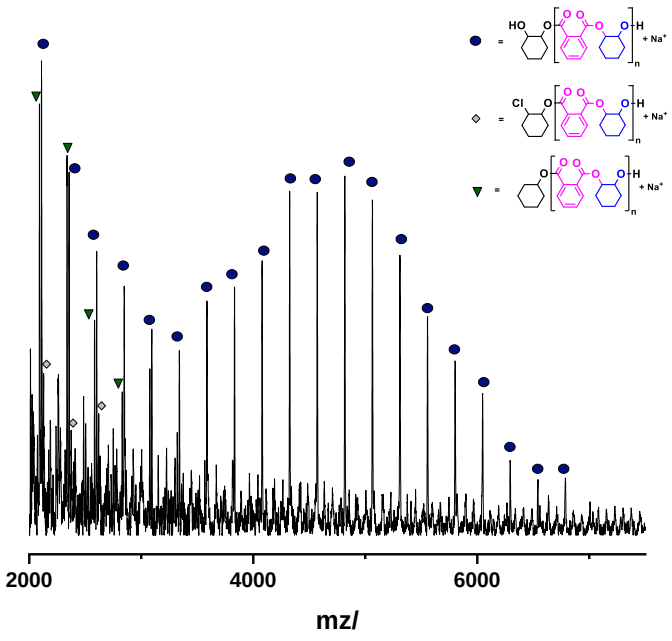


Figure S3.10. MALDI-ToF spectrum of PCHPE obtained with **1**/PPN$_2$PA and 2 equivs. of CHD. Blue circle = α,ω-hydroxy end capped PCHPE. Grey diamond = α-chloride,ω-hydroxy end capped PCHPE. Green triangle = α-cyclohexanol,ω-hydroxy end capped PCHPE.

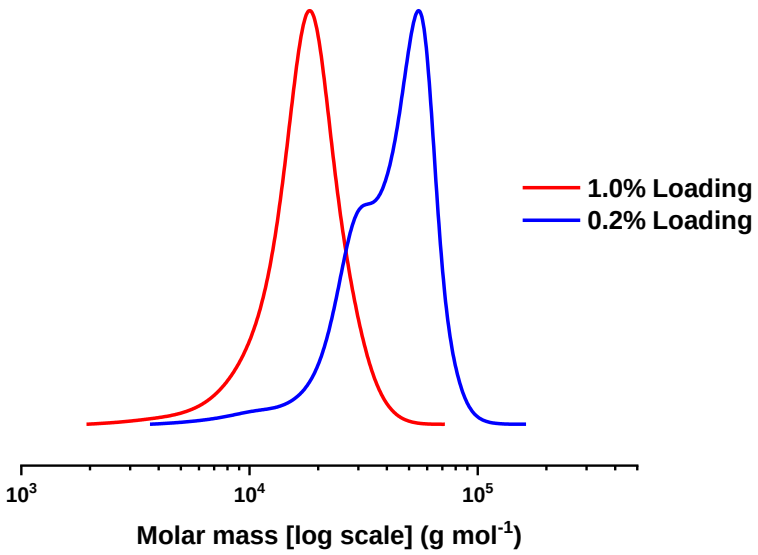


Figure S3.11. Polymer molecular mass distributions of PDL-b-PCHPE-b-PDL prepared with complex **1**/PPN$_2$PA corresponding to Table 3.3, Entries 1 and 3.

Supplementary Figures and Data for Chapter 4

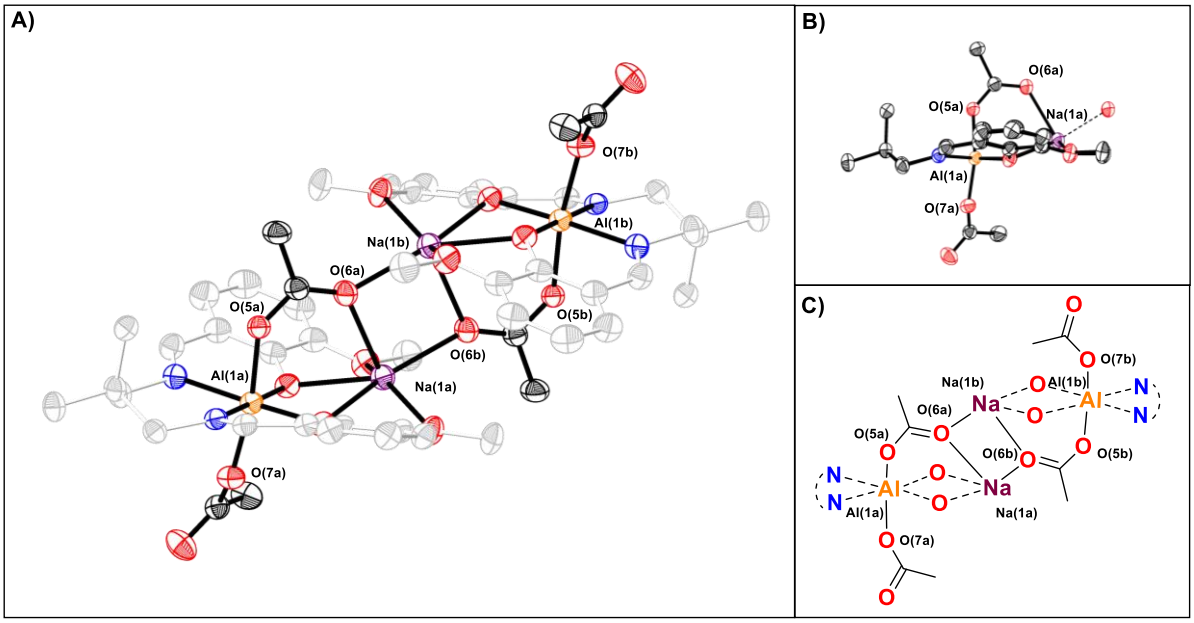


Figure S4.1. Molecular structure of complex **7**. Obtained from X-ray diffraction experiments with thermal ellipsoids presented at 50% probability and H atoms omitted for clarity (Atom colour scheme: Al (orange), Na (purple), O (red), N (blue), C (greyscale/black). A) Structure of the dimer, showing acetate co-ligands bridging between two molecules of the complex. B) Structure of one half of the dimer, showing a 'bowl' confirmation ligand, and aluminate centre. Note that the two molecules within the dimer are related by symmetry in the crystal structure. C) Schematic showing key binding of both metals and acetate groups.

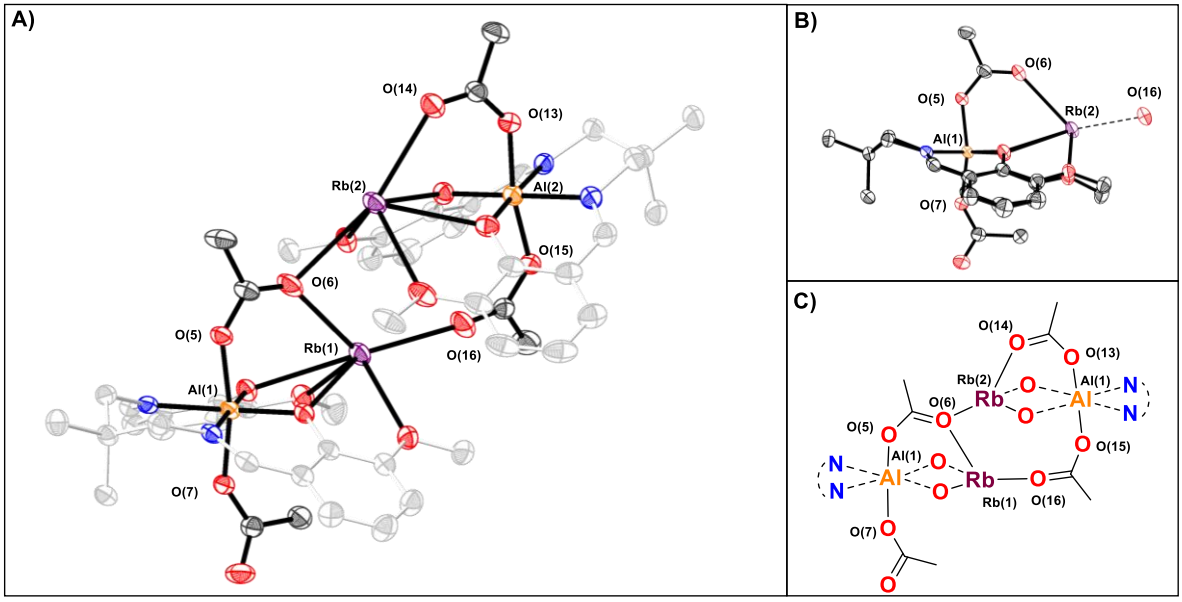


Figure S4.2. Molecular structure of complex **9**. Obtained from X-ray diffraction experiments with thermal ellipsoids presented at 50% probability and H atoms omitted for clarity (Atom colour scheme: Al (orange), Rb (purple), O (red), N (blue), C (greyscale/black). A) Structure of the dimer, showing acetate co-ligands bridging between two molecules of the complex. B) Structure of one half of the dimer, showing a 'bowl' confirmation ligand, and aluminate centre C) Schematic showing key binding of both metals and acetate groups.

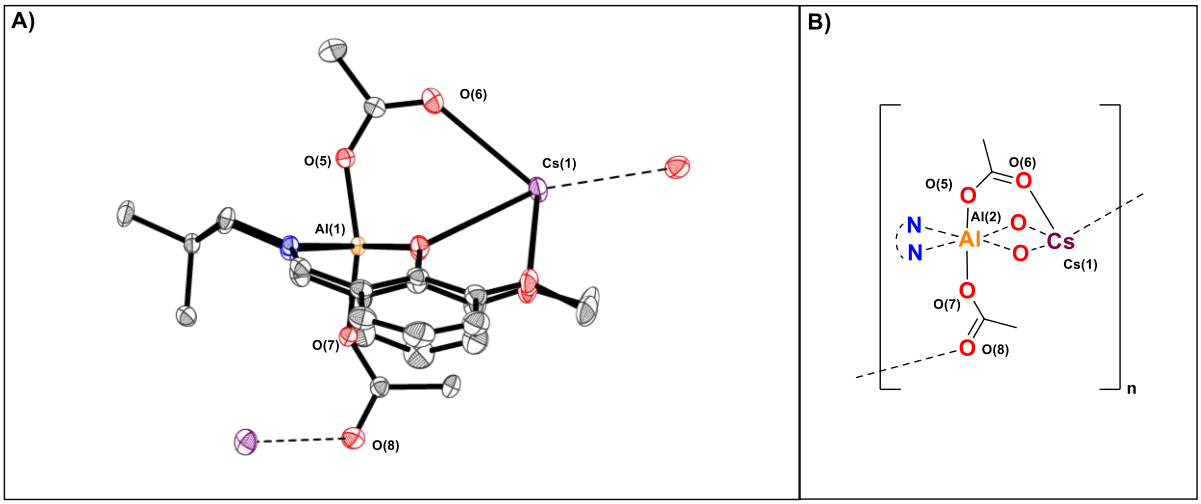


Figure S4.3. Molecular structure of complex **10**. Obtained from X-ray diffraction experiments, with thermal ellipsoids presented at 50% probability and H atoms omitted for clarity (Atom colour scheme: Al (orange), Cs (purple), O (red), N (blue), C (black). A) Structure of the monomeric unit, showing acetate co-ligands bridging between molecules in the extended polymeric crystal structure. B) Schematic showing key binding of both metals and acetate groups

Table S4.1. Selected bond lengths and angles for complex **7**.

Bond	Bond Length (Å)	Bond	Bond Angle (°)
Al(1a) – Na(1a)	3.284	O(7a) – Al(1a) – O(5a)	169.21(7)
Al(1a) – N(1a)	2.059(18)	N(1a) – Al(1a) – N(2a)	92.10(7)
Al(1a) – N(2a)	2.0350(17)	N(1a) – Al(1a) – O(2a)	90.35(7)
Al(1a) – O(2a)	1.8494(15)	N(2a) – Al (1a) – O(3a)	91.06(7)
Al(1a – O(3a)	1.8481(15)	O(2a) – Al(1a) – O(3a)	86.44(6)
Al(1a) – O(5a)	1.8967(15)	O(1a) – Na(1a) – O(2a)	64.95(5)
Al(1a) – O(7a)	1.8694(16)	O(2a) – Na(1a) – O(3a)	64.76(5)
Na(1a) – O(1a)	2.5018(17)	O(3a) – Na(1a) – O(4a)	64.69(5)
Na(1a) – O(2a)	2.3521(16)	O(6a) – Na(1a) – O(1a)	86.40(6)
Na(1a) – O(3a)	2.3756(15)	O(6a) – Na(1a) – O(2a)	145.34(7)
Na(1a) – O(4a)	2.5013(18)	O(6a) – Na(1a) – O(6b)	88.74(6)
Na(1a) – O(6a)	2.4098(17)		
Na(1a) – O(6b)	2.2934(16)		

Table S4.2. Selected bond lengths and angles for complex **8**.

Bond	Bond Length (Å)	Bond	Bond Angle (°)
Al(1) – K(1)	3.665	O(7) – Al(1) – O(5)	167.84(10)
Al(1) – N(1)	2.077(2)	N(1) – Al(1) – N(2)	90.84(10)
Al(1) – N(2)	2.038(2)	N(1) – Al(1) – O(2)	89.49(9)
Al(1) – O(2)	1.842(2)	N(2) – Al(1) – O(3)	90.13(9)
Al(1) – O(3)	1.854(2)	O(2) – Al(1) – O(3)	89.57(9)
Al(1) – O(5)	1.905(2)	O(1) – K(1) – O(2)	57.79(6)
Al(1) – O(7)	1.869(2)	O(2) – K(1) – O(3)	56.95(6)
K(1) – O(1)	2.718(2)	O(3) – K(1) – O(4)	56.31(6)
K(1) – O(2)	2.7220(19)	O(1) – K(1) – O(6)	117.58(7)
K(1) – O(3)	2.738(2)	O(2) – K(1) – O(6)	71.81(6)
K(1) – O(4)	2.853(2)	O(6) – K(1) – O(16)	119.62(7)
K(1) – O(6)	2.673(2)	O(13) – Al(2) – O(15)	169.18(10)
K(1) – O(16)	2.582(2)	N(3) – Al(2) – N(4)	89.64(10)
Al(2) – K(2)	3.519	N(3) – Al(2) – O(10)	87.84(9)
Al(2) – N(3)	2.067(2)	N(4) – Al(2) – O(11)	89.24(10)
Al(2) – N(4)	2.040(2)	O(10) – Al(2) – O(11)	93.25(9)
Al(2) – O(10)	1.853(2)	O(9) – K(2) – O(10)	57.91(6)
Al(2) – O(11)	1.843(2)	O(10) – K(2) – O(11)	60.70(6)
Al(2) – O(13)	1.871(2)	O(11) – K(2) – O(12)	57.68(6)
Al(2) – O(15)	1.907(2)	O(9) – K(2) – O(14)	120.95(7)
K(2) – O(9)	2.781(2)	O(10) – K(2) – O(14)	74.83(6)
K(2) – O(10)	2.668(2)	O(6) – K(2) – O(14)	155.60(7)
K(2) – O(11)	2.649(2)		
K(2) – O(12)	2.809(2)		
K(2) – O(14)	2.662(2)		
K(2) – O(6)	2.728(2)		

Table S4.3. Selected bond lengths and angles for complex **9**

Bond	Bond Length (Å)	Bond	Bond Angle (°)
Al(1) – Rb(1)	3.819	O(7) – Al(1) – O(5)	167.42(7)
Al(1) – N(1)	2.0445(18)	N(1) – Al(1) – N(2)	90.17(7)
Al(1) – N(2)	2.0900(17)	N(1) – Al(1) – O(2)	89.92(7)
Al(1) – O(2)	1.8632(15)	N(2) – Al(1) – O(3)	89.37(7)
Al(1) – O(3)	1.8456(15)	O(2) – Al(1) – O(3)	90.56(6)
Al(1) – O(5)	1.9103(16)	O(1) – Rb(1) – O(2)	54.45(4)
Al(1) – O(7)	1.8678(15)	O(2) – Rb(1) – O(3)	54.45(4)
Rb(1) – O(1)	2.9229(16)	O(3) – Rb(1) – O(4)	55.44(4)
Rb(1) – O(2)	2.8828(14)	O(1) – Rb(1) – O(6)	110.30(5)
Rb(1) – O(3)	2.8780(13)	O(2) – Rb(1) – O(6)	67.54(5)
Rb(1) – O(4)	2.8018(15)	O(6) – Rb(1) – O(16)	122.50(5)
Rb(1) – O(6)	2.7858(19)	O(13) – Al(2) – O(15)	167.69(7)
Rb(1) – O(16)	2.6979(17)	N(3) – Al(2) – N(4)	89.55(7)
Al(2) – Rb(2)	3.678	N(3) – Al(2) – O(10)	89.44(7)
Al(2) – N(3)	2.0450(19)	N(4) – Al(2) – O(11)	87.96(7)
Al(2) – N(4)	2.0728(18)	O(10) – Al(2) – O(11)	93.01(7)
Al(2) – O(10)	1.8418(15)	O(9) – Rb(2) – O(10)	55.55(4)
Al(2) – O(11)	1.8561(15)	O(10) – Rb(2) – O(11)	57.17(4)
Al(2) – O(13)	1.8720(16)	O(11) – Rb(2) – O(12)	55.38(4)
Al(2) – O(15)	1.8936(16)	O(9) – Rb(2) – O(14)	113.89(5)
Rb(2) – O(9)	2.8800(16)	O(10) – Rb(2) – O(14)	70.76(5)
Rb(2) – O(10)	2.7934(16)	O(6) – Rb(2) – O(14)	161.57(5)
Rb(2) – O(11)	2.8135(14)		
Rb(2) – O(12)	2.8872(16)		
Rb(2) – O(14)	2.7746(17)		
Rb(2) – O(6)	2.8786(16)		

Table S4.4. Selected bond lengths and angles for complex **10**

Bond	Bond Length (Å)	Bond	Bond Angle (°)
Al(1) – Cs(1)	3.979	O(7) – Al(1) – O(5)	165.76(7)
Al(1) – N(1)	2.065(2)	N(1) – Al(1) – N(2)	90.90(8)
Al(1) – N(2)	2.0451(19)	N(1) – Al(1) – O(2)	89.04(7)
Al(1) – O(2)	1.8417(16)	N(2) – Al(1) – O(3)	89.48(7)
Al(1) – O(3)	1.8453(16)	O(2) – Al(1) – O(3)	90.54(7)
Al(1) – O(5)	1.8719(17)	O(1) – Cs(1) – O(2)	50.82(4)
Al(1) – O(7)	1.9084(16)	O(2) – Cs(1) – O(3)	50.45(4)
Cs(1) – O(1)	3.0356(18)	O(3) – Cs(1) – O(4)	50.64(4)
Cs(1) – O(2)	3.0694(15)	O(1) – Cs(1) – O(6)	107.28(6)
Cs(1) – O(3)	3.0763(15)	O(2) – Cs(1) – O(6)	65.57(5)
Cs(1) – O(4)	3.0975(18)	O(6) – Cs(1) – O(8)	127.57(5)
Cs(1) – O(6)	2.9220(19)		
Cs(1) – O(8)	3.0478(17)		

Table S4.5. Selected bond lengths and angles for complex **12**

Bond	Bond Length (Å)	Bond	Bond Angle (°)
Al(1) – K(1)	3.5995(6)	O(7) – Al(1) – O(5)	166.72(6)
Al(1) – N(1)	2.0646(15)	N(1) – Al(1) – N(2)	90.64(6)
Al(1) – N(2)	2.0584(16)	N(1) – Al(1) – O(2)	88.45(6)
Al(1) – O(2)	1.8519(14)	N(2) – Al(1) – O(3)	90.18(6)
Al(1) – O(3)	1.8364(12)	O(2) – Al(1) – O(3)	90.85(6)
Al(1) – O(5)	1.9060(15)	O(1) – K(1) – O(2)	57.90(4)
Al(1) – O(7)	1.8784(14)	O(2) – K(1) – O(3)	58.54(4)
K(1) – O(1)	2.7808(16)	O(3) – K(1) – O(4)	57.45(4)
K(1) – O(2)	2.6588(13)	O(1) – K(1) – O(6)	111.08(5)
K(1) – O(3)	2.7137(14)	O(2) – K(1) – O(6)	67.27(4)
K(1) – O(4)	2.7698(18)	O(6) – K(1) – O(14)	122.00(5)
K(1) – O(6)	2.8365(15)	O(13) – Al(2) – O(15)	168.42(6)
K(1) – O(14)	2.6320(14)	N(3) – Al(2) – N(4)	89.11(6)
Al(2) – K(2)	3.6286(6)	N(3) – Al(2) – O(10)	89.27(6)
Al(2) – N(3)	2.0383(15)	N(4) – Al(2) – O(11)	90.03(6)
Al(2) – N(4)	2.0743(16)	O(10) – Al(2) – O(11)	91.55(6)
Al(2) – O(10)	1.8399(13)	O(9) – K(2) – O(10)	57.08(4)
Al(2) – O(11)	1.8432(12)	O(10) – K(2) – O(11)	57.78(4)
Al(2) – O(13)	1.9152(14)	O(11) – K(2) – O(12)	56.73(4)
Al(2) – O(15)	1.8982(14)	O(9) – K(2) – O(16)	104.05(5)
K(2) – O(9)	2.7923(15)	O(10) – K(2) – O(16)	65.59(4)
K(2) – O(10)	2.7330(12)	O(6) – K(2) – O(16)	156.19(5)
K(2) – O(11)	2.7296(13)	O(16) – K(2) – O(17)	79.95(5)
K(2) – O(12)	2.8129(14)		
K(2) – O(16)	2.6571(15)		
K(2) – O(6)	2.8076(14)		
K(2) – O(17)	3.146(2)		

Table S4.6.. Summary of crystallographic refinement data for complexes **7** – **10** & **12.**

Complex	**7**	**8**	**9**	**10**	**12**
Local Code	013rwfk20	063ap20	014rwfk20	016rwfk20	021rwfk21
CCDC Deposition Number	2096248	2096249	2096250	2096251	2096252
Crystal data					
Chemical formula	$C_{25}H_{30}AlN_2NaO_8 \cdot 2(CH_2Cl_2)$	$C_{50}H_{60}Al_2K_2N_4O_{16} \cdot CHCl_3$	$C_{50}H_{60}Al_2N_4O_{16}Rb_2 \cdot CHCl_3$	$C_{25}H_{30}AlCsN_2O_8 \cdot CHCl_3$	$C_{74}H_{76}Al_2K_2N_4O_{17}$
M_r	706.33	1224.54	1317.28	765.77	1425.54
Crystal system, space group	Triclinic, $P\bar{1}$	Triclinic, $P\bar{1}$	Triclinic, $P\bar{1}$	Monoclinic, $P2_1/c$	Monoclinic, $P2_1/n$
a, *b*, *c* (Å)	10.7960 (5), 11.9409 (8), 14.6196 (7)	12.4551 (6), 15.8089 (10), 16.1748 (8)	12.5460 (3), 15.7343 (4), 16.4513 (5)	14.9518 (2), 12.8871 (1), 16.7675 (2)	15.0779 (2), 30.1479 (4), 17.5249 (3)
α, β, γ (°)	66.034 (5), 84.098 (4), 69.361 (5)	65.273 (5), 82.478 (4), 76.607 (5)	64.372 (3), 82.396 (2), 76.638 (2)	90, 98.577 (1), 90	90, 114.699 (2), 90
V (Å^3)	1609.86 (17)	2812.1 (3)	2846.84 (15)	3194.72 (6)	7237.5 (2)
Z	2	2	2	4	4
Radiation type	Cu *K*α	Mo *K*α	Cu *K*α	Cu *K*α	Cu *K*α
μ (mm^{-1})	4.17	0.41	4.42	12.03	1.98
Crystal size (mm)	0.17 × 0.14 × 0.05	0.17 × 0.11 × 0.08	0.36 × 0.20 × 0.12	0.26 × 0.18 × 0.18	0.49 × 0.13 × 0.07
Data collection					
Absorption correction	Multi-scan *CrysAlis PRO* 1.171.39.46 (Rigaku Oxford Diffraction, 2018) Empirical absorption correction using spherical harmonics, implemented in SCALE3 ABSPACK scaling algorithm.				
T_{min}, T_{max}	0.893, 1.000	0.969, 1.000	0.731, 1.000	0.670, 1.000	0.778, 1.000
No. of measured, independent and observed [$I > 2\sigma(I)$] reflections	12886, 6670, 5365	21284, 13911, 8926	30073, 11825, 10423	15348, 6656, 6283	44644, 14927, 11897
R_{int}	0.031	0.040	0.032	0.028	0.051
$(\sin\theta/\lambda)_{max}$ (Å^{-1})	0.631	0.696	0.631	0.632	0.630
Refinement					
$R[F^2 > 2\sigma(F^2)]$, $wR(F^2)$, *S*	0.043, 0.121, 1.03	0.061, 0.129, 1.05	0.032, 0.088, 1.03	0.028, 0.073, 1.05	0.043, 0.114, 1.02
No. of reflections	6670	13911	11825	6656	14927
No. of parameters	404	715	715	404	900
No. of restraints	1	0	0	3	0
$\Delta\rangle_{max}$, $\Delta\rangle_{min}$ (e Å^{-3})	0.50, -0.34	0.38, -0.39	0.67, -0.50	0.70, -1.29	0.58, -0.28

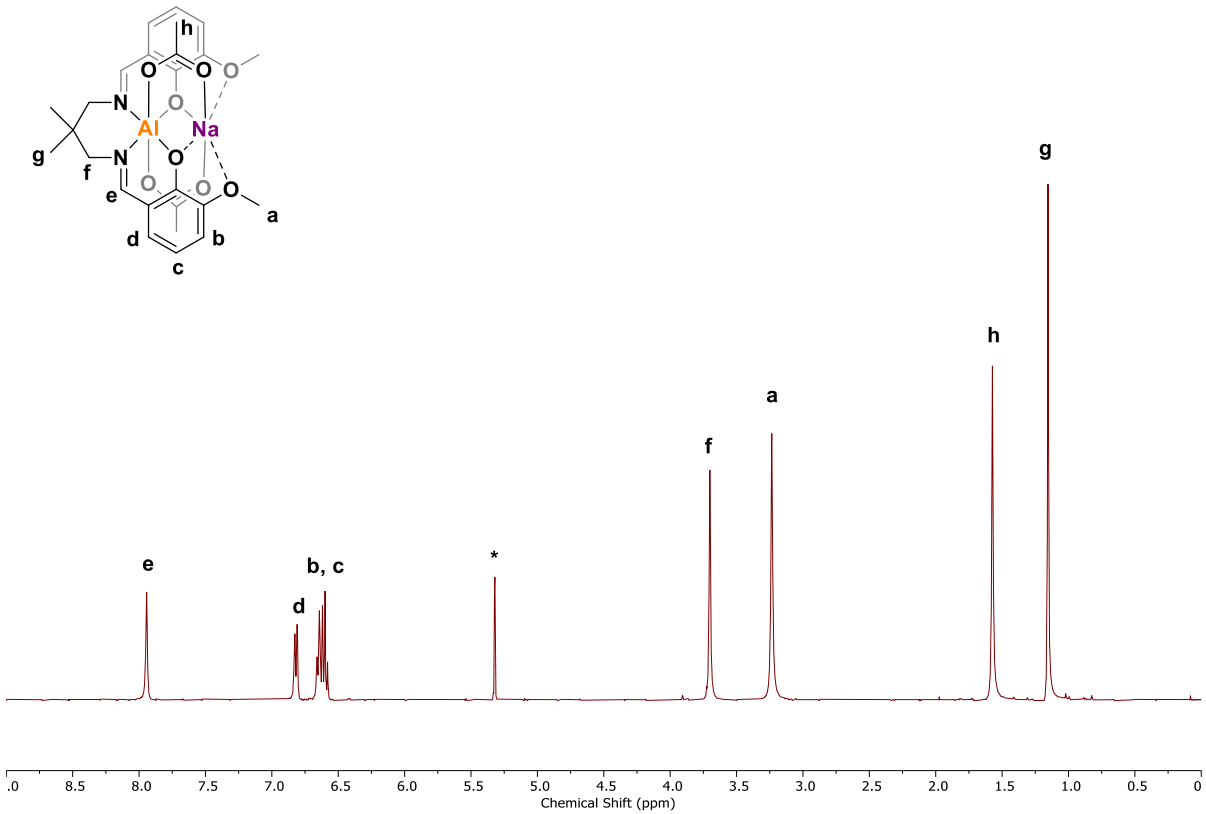


Figure S4.4. ^{1}H NMR Spectrum (400 MHz, 298 K, CD_2Cl_2(*)) of complex **7**.

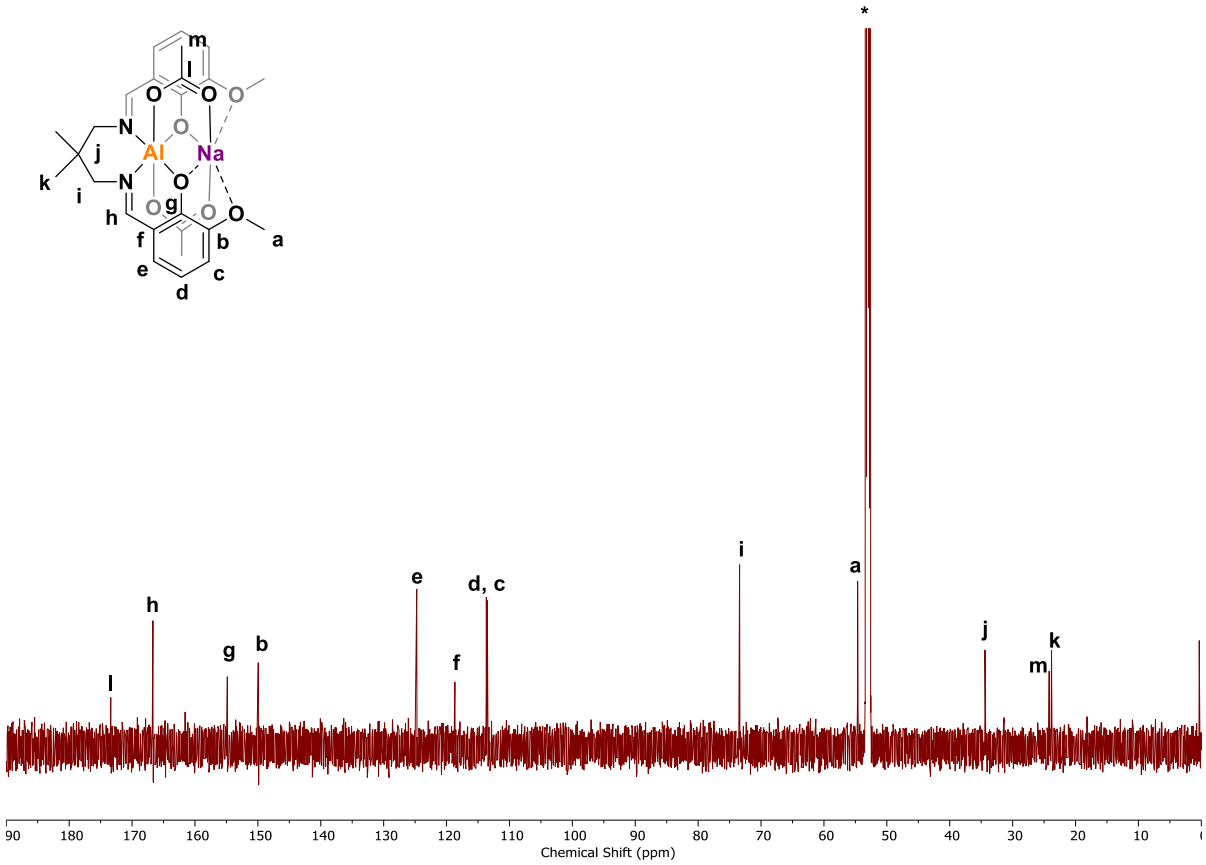


Figure S4.5. ^{13}C NMR Spectrum (176 MHz, 298 K, CD_2Cl_2(*)) of complex **7**.

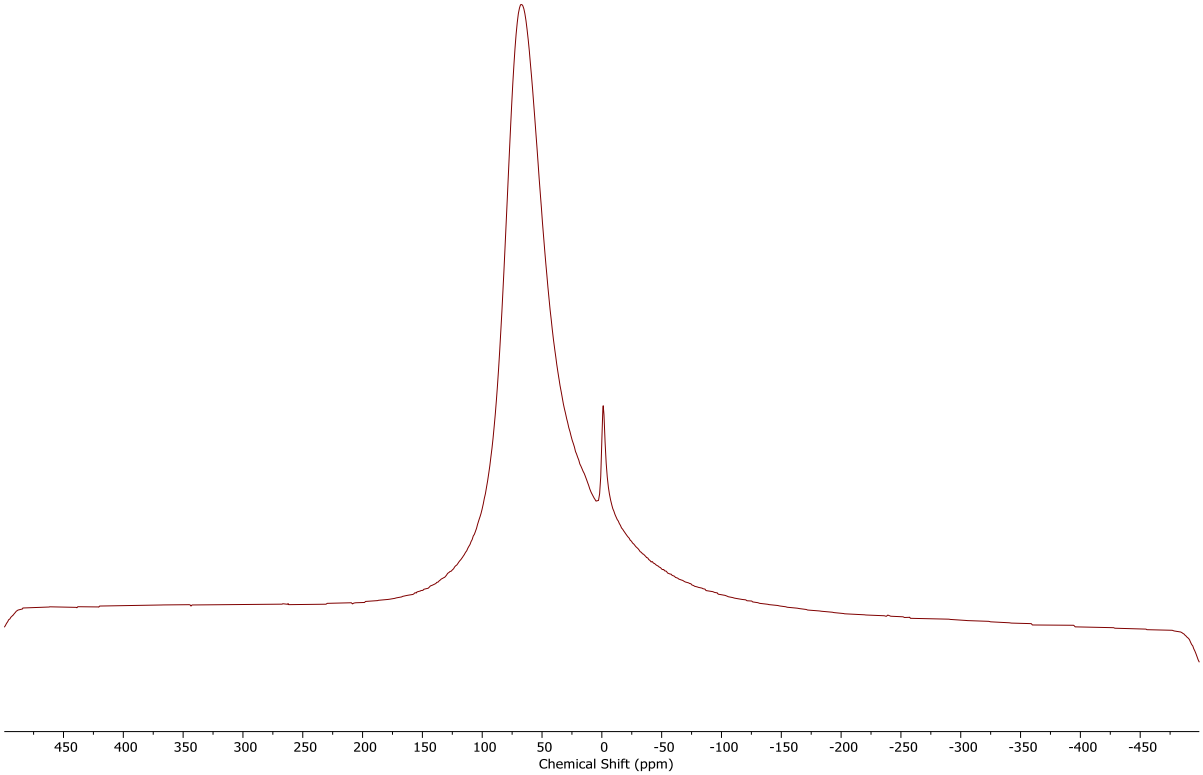


Figure S4.6. ^{27}Al NMR Spectrum (104 MHz, 298 K, CD_2Cl_2) of complex **7**.

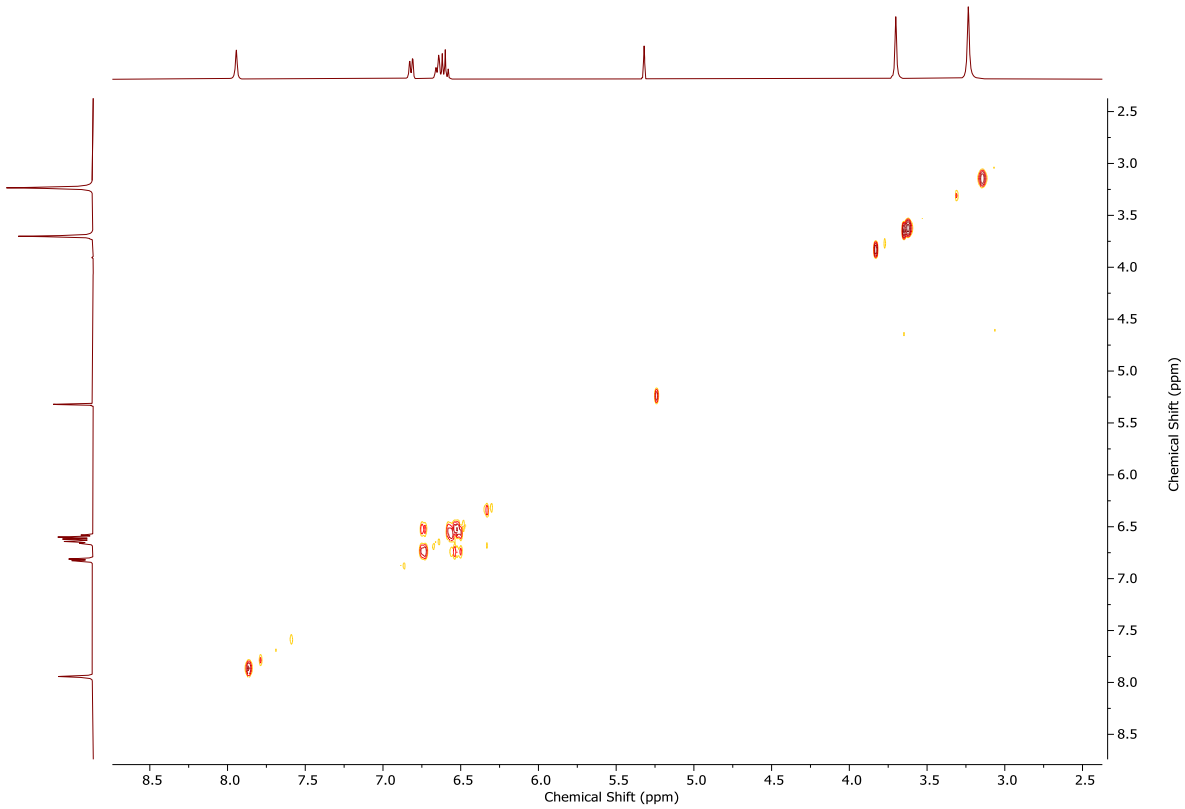


Figure S4.7. ^{1}H COSY NMR Spectrum (400 MHz, 298 K, CD_2Cl_2) of complex **7**.

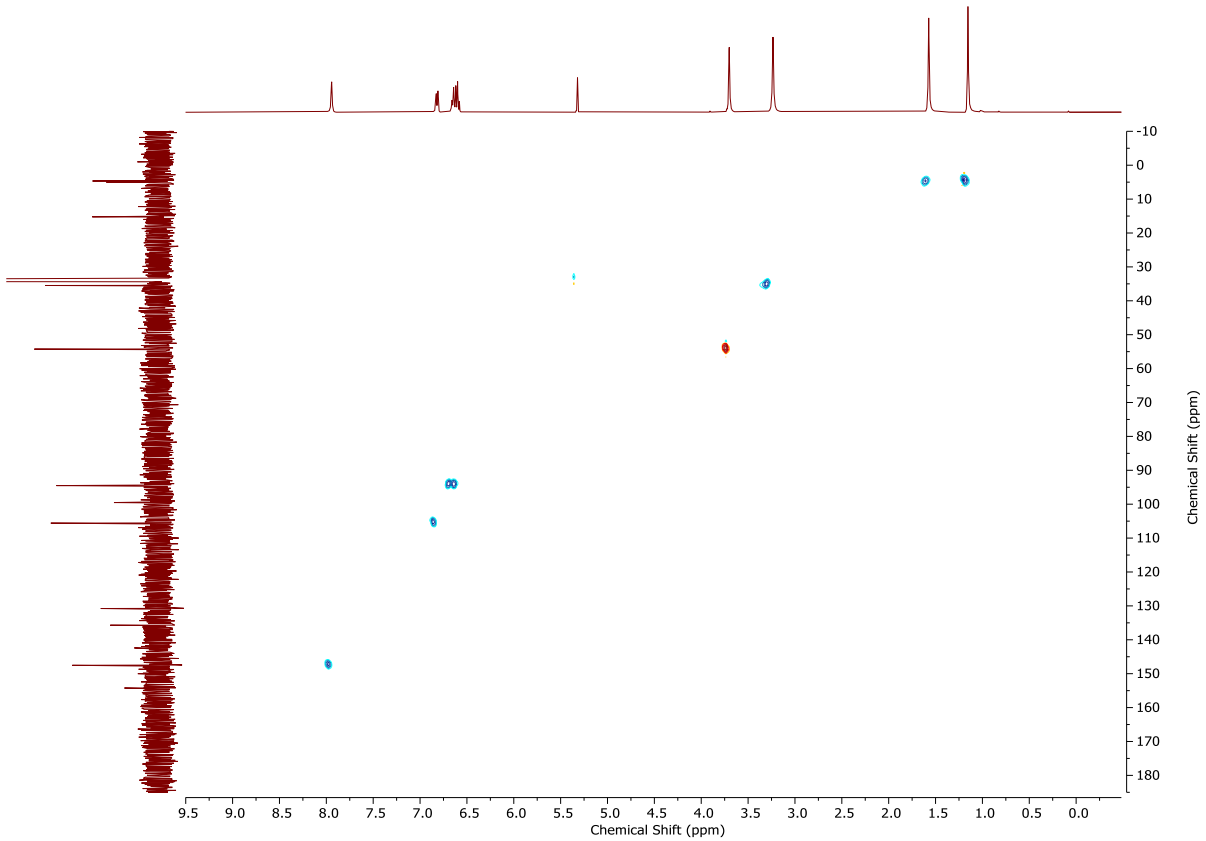


Figure S4.8. ^{1}H-^{13}C HSQC NMR Spectrum (298 K, CD_2Cl_2) of complex **7**.

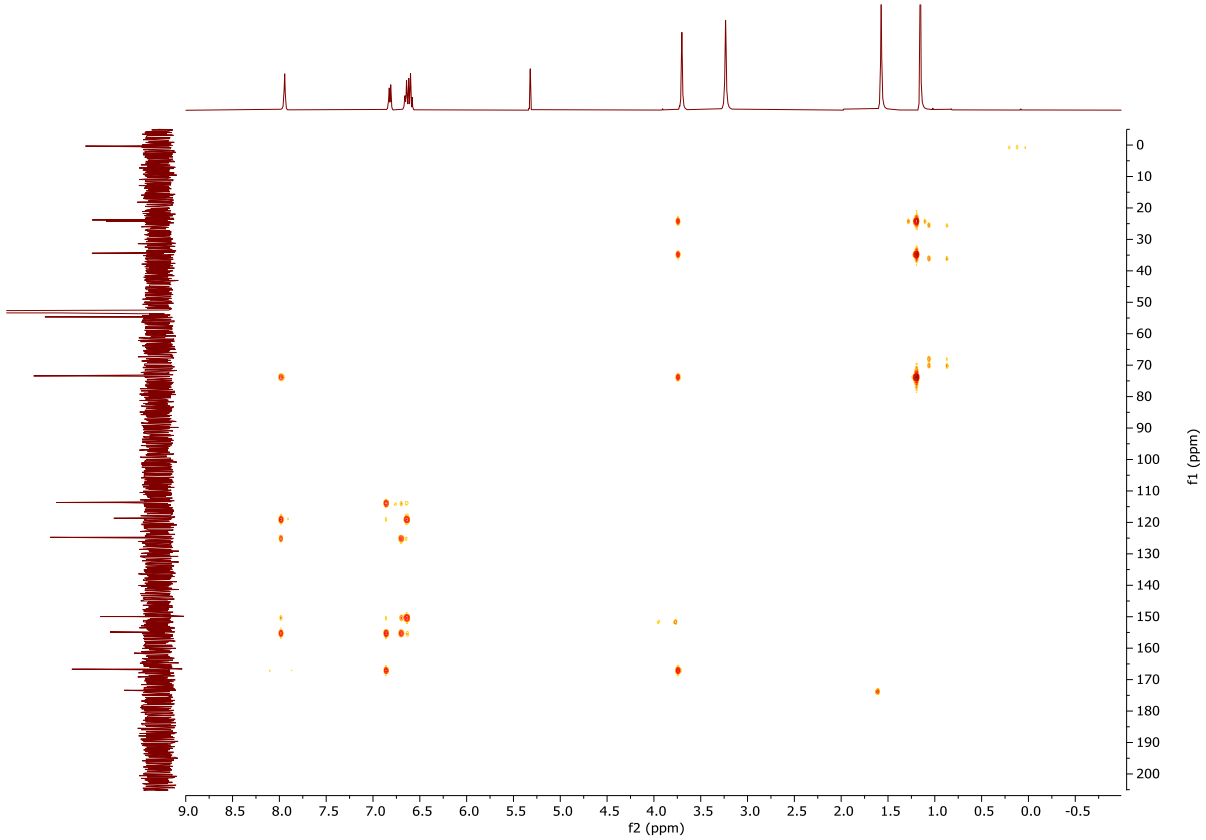


Figure S4.9. ^{1}H-^{13}C HMBC NMR Spectrum (298 K, CD_2Cl_2) of complex **7**.

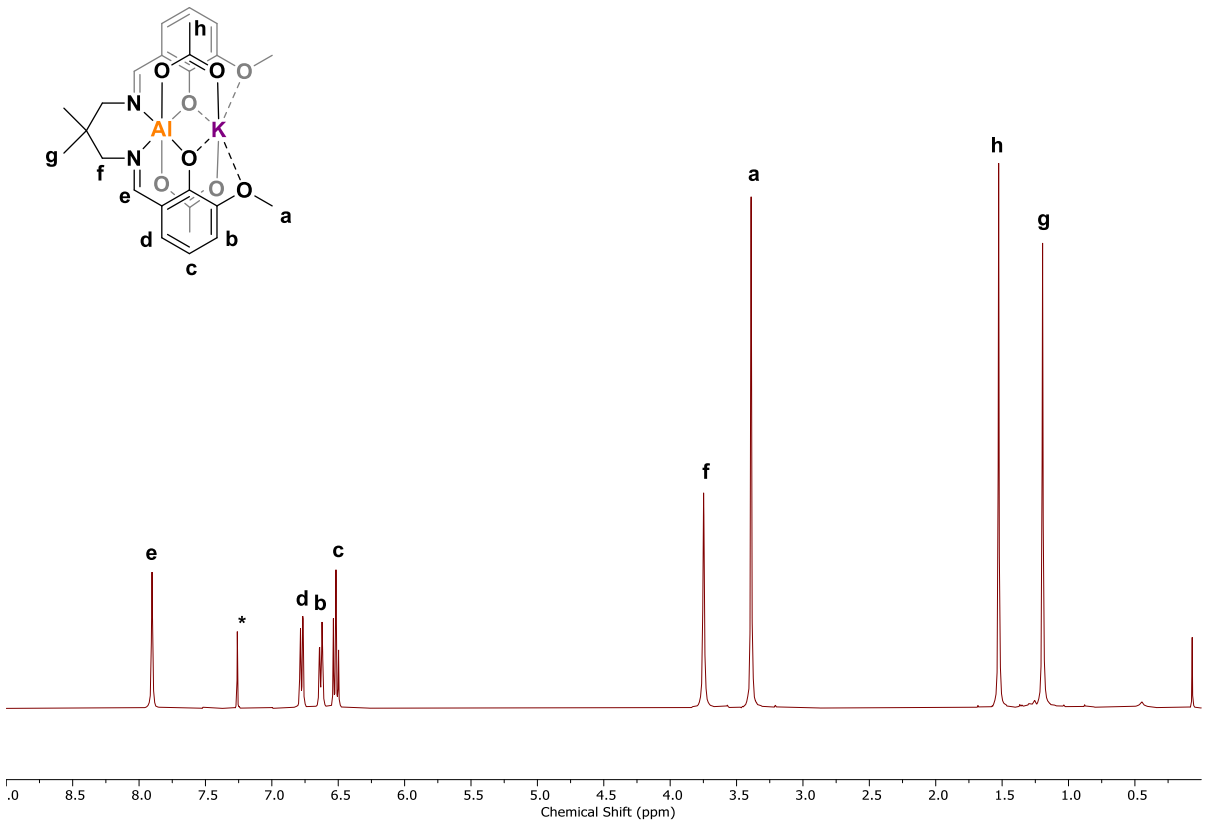


Figure S4.10. ^{1}H NMR Spectrum (400 MHz, 298 K, $CDCl_3$(*)) of complex **8**.

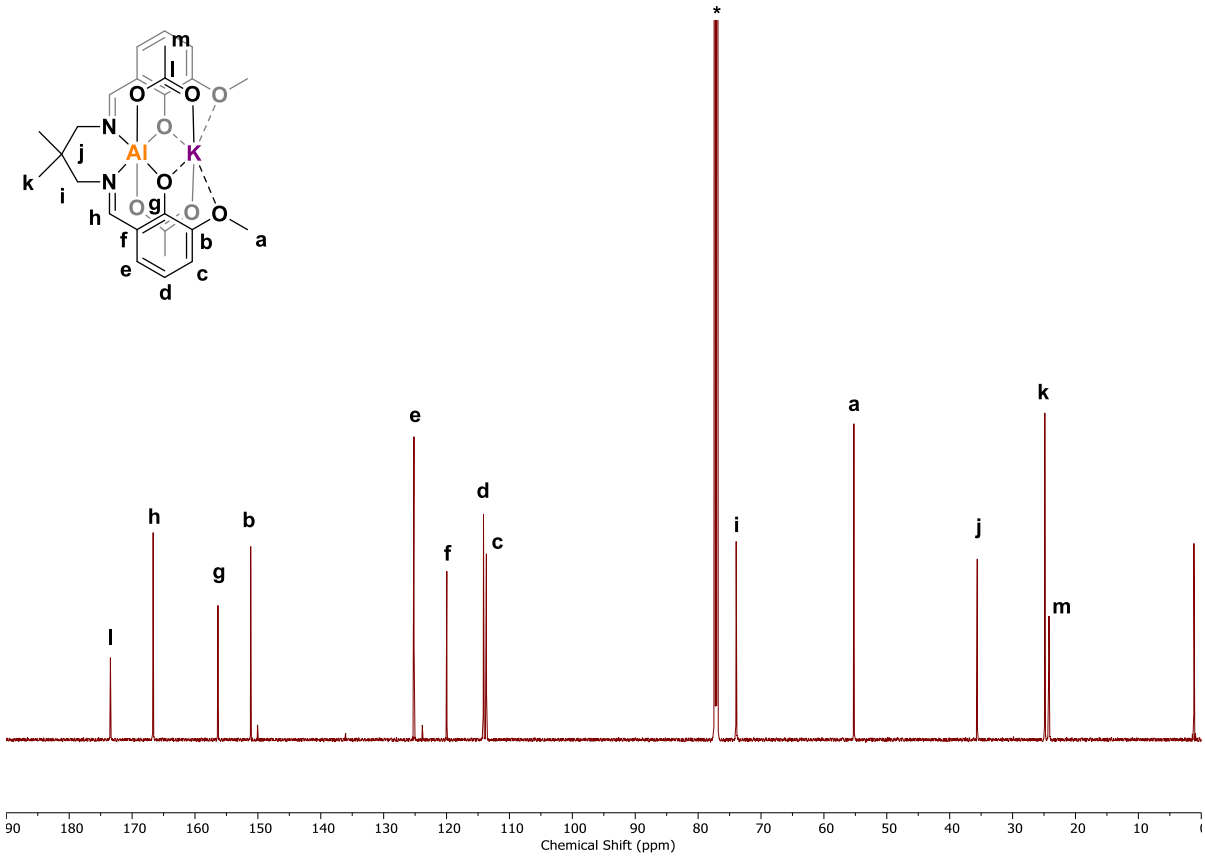


Figure S4.11. ^{13}C NMR Spectrum (151 MHz, 298 K, $CDCl_3$(*)) of complex **8**.

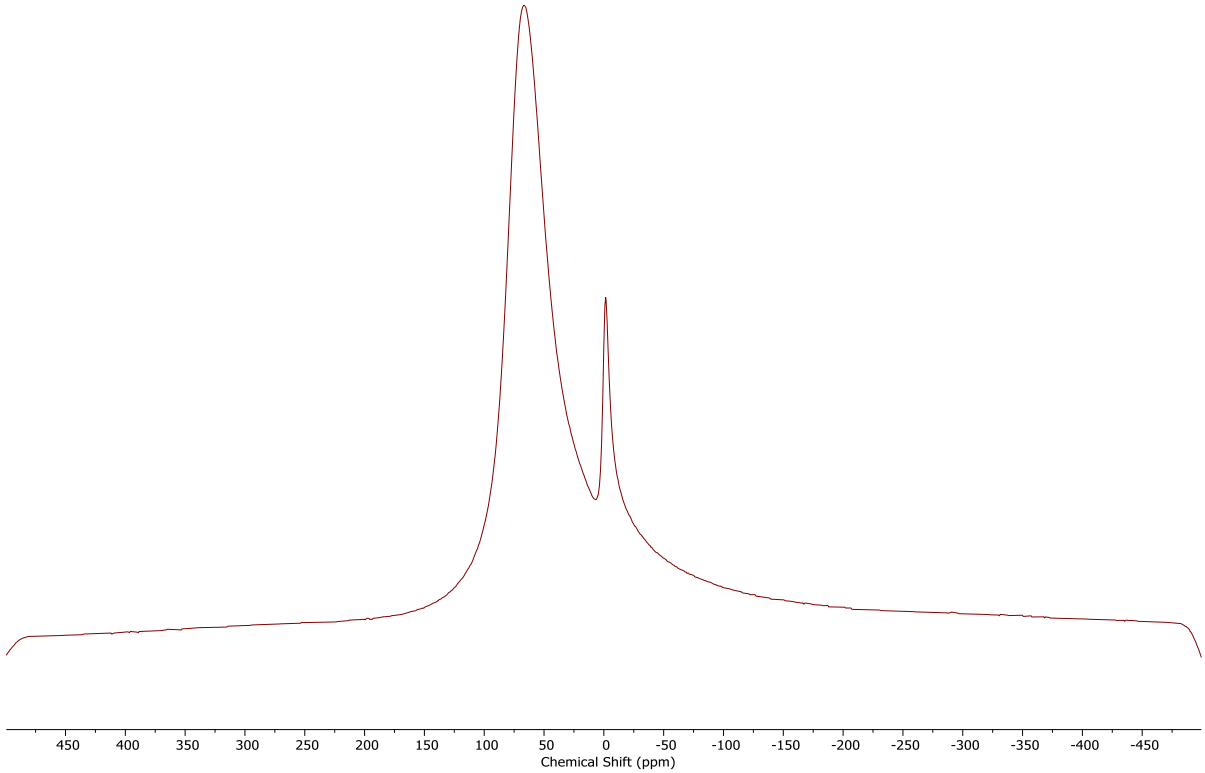


Figure S4.12. ^{27}Al NMR Spectrum (104 MHz, 298 K, $CDCl_3$) of complex **8**.

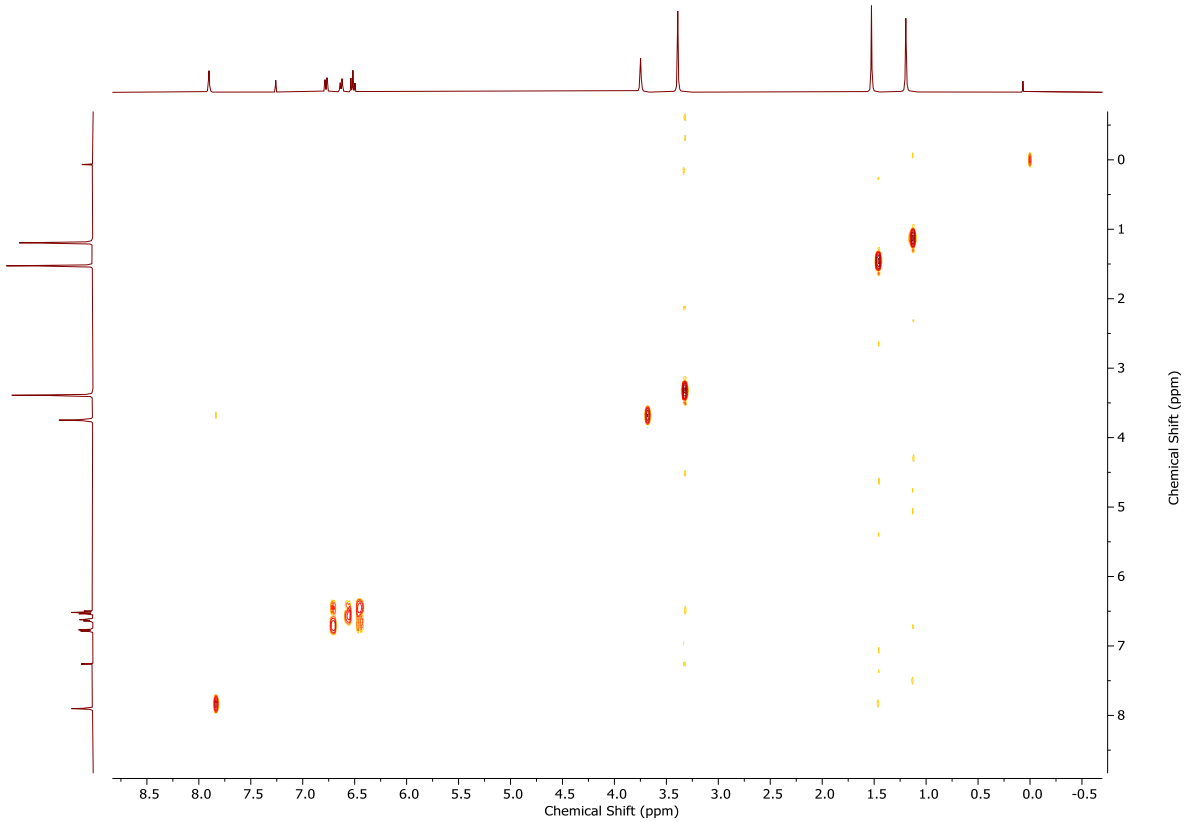


Figure S4.13. ^{1}H COSY NMR Spectrum (400 MHz, 298 K, $CDCl_3$) of complex **8**.

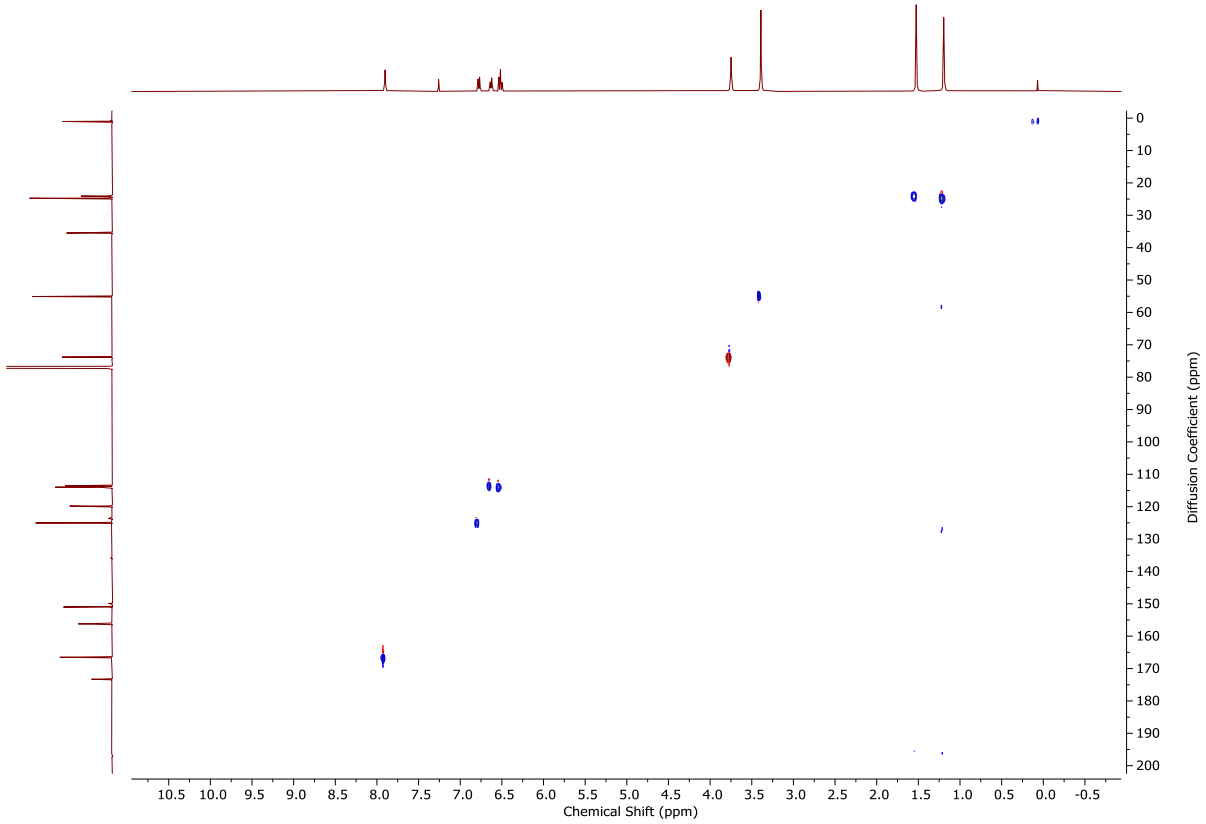


Figure S4.14. ^{1}H-^{13}C HSQC NMR Spectrum (298 K, $CDCl_3$) of complex **8**.

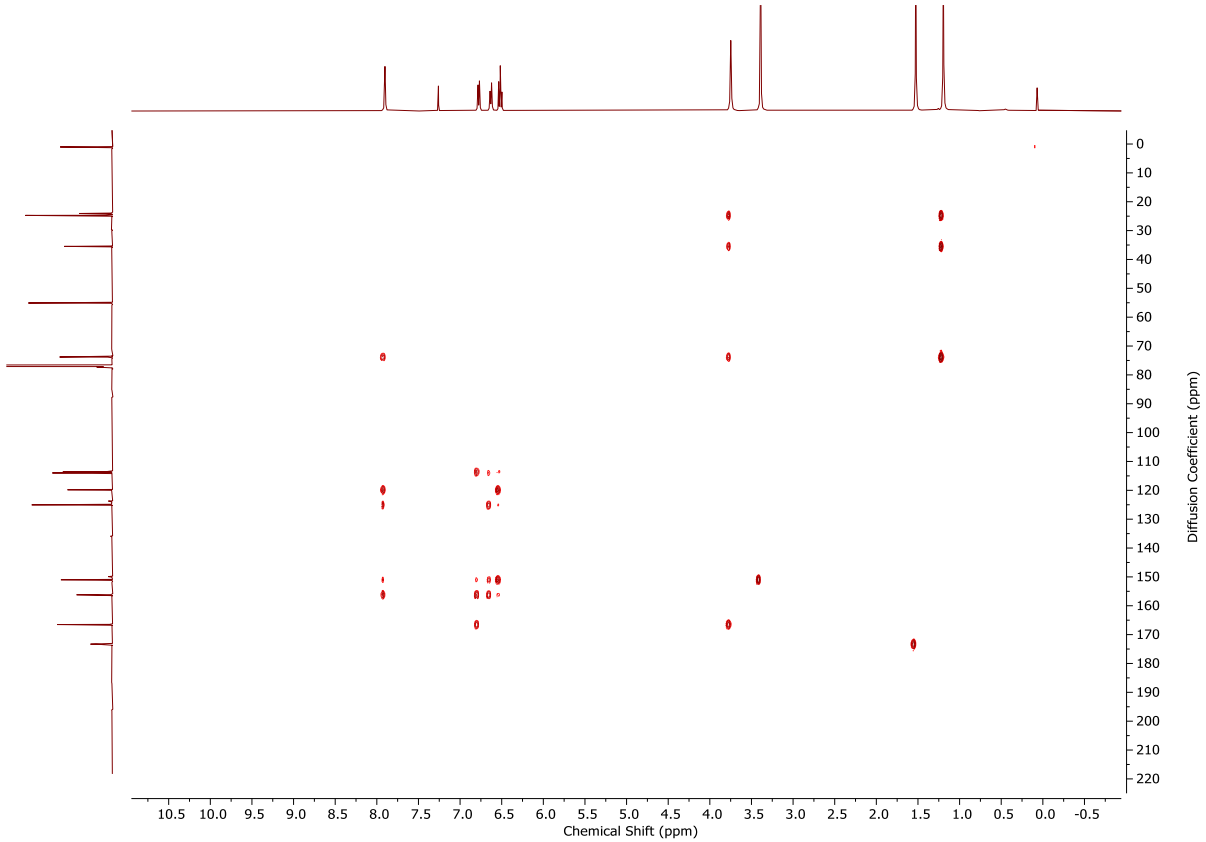


Figure S4.15. ^{1}H-^{13}C HMBC NMR Spectrum (298 K, $CDCl_3$) of complex **8**.

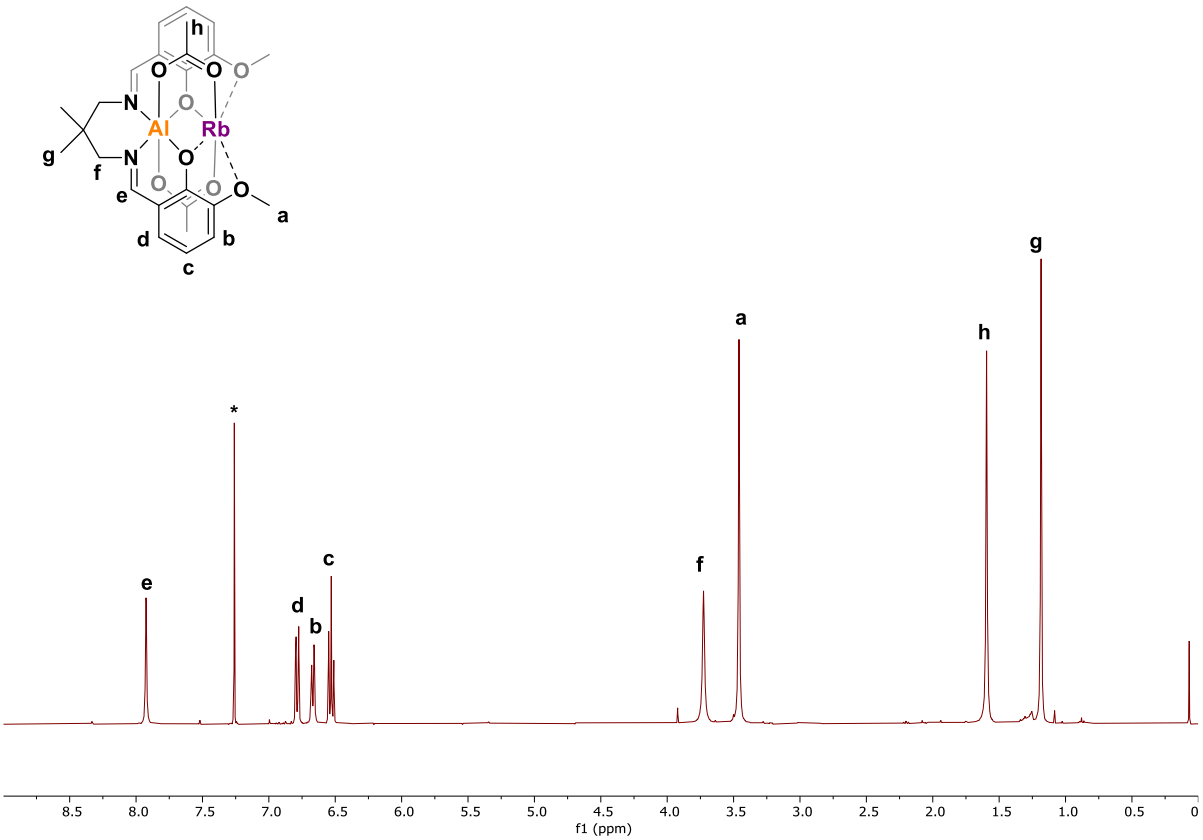


Figure S4.16. ^{1}H NMR Spectrum (400 MHz, 298 K, $CDCl_3$(*)) of complex **9**.

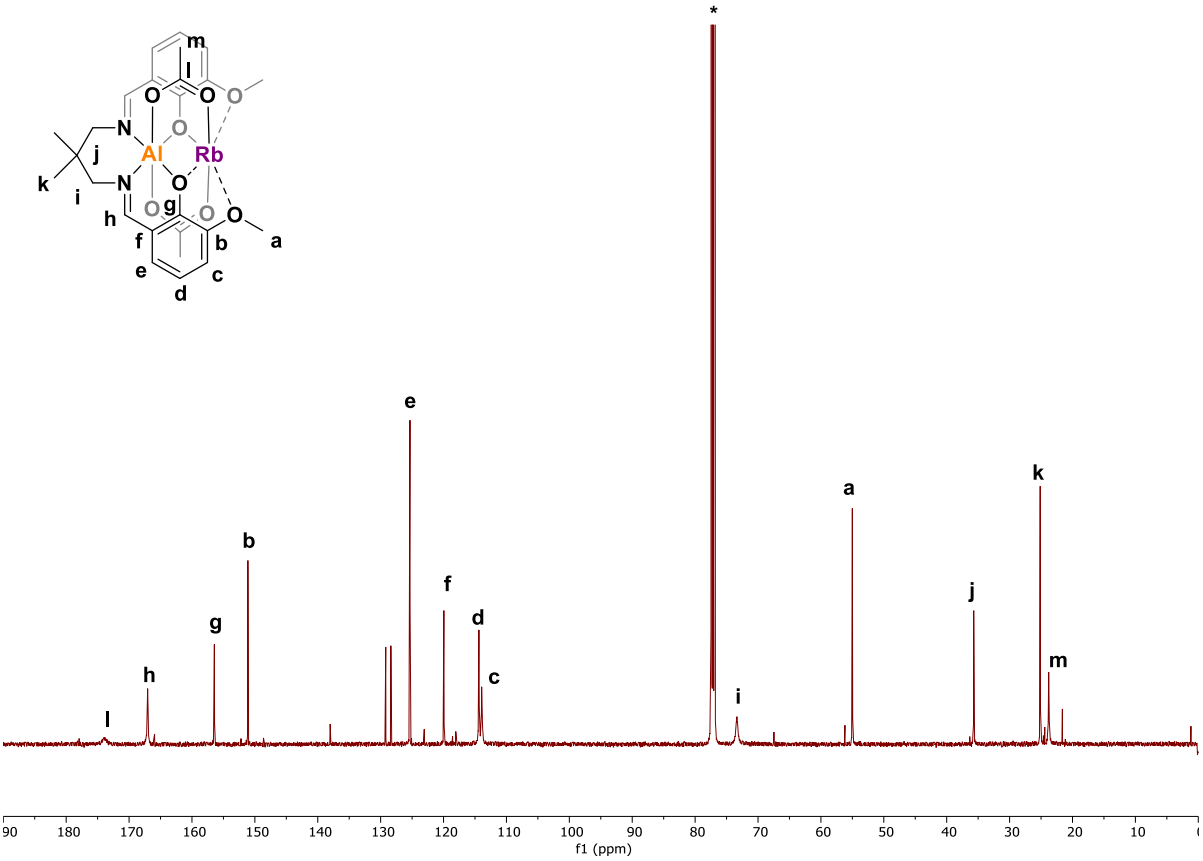


Figure S4.17. ^{13}C NMR Spectrum (400 MHz, 298 K, $CDCl_3$(*)) of complex **9**.

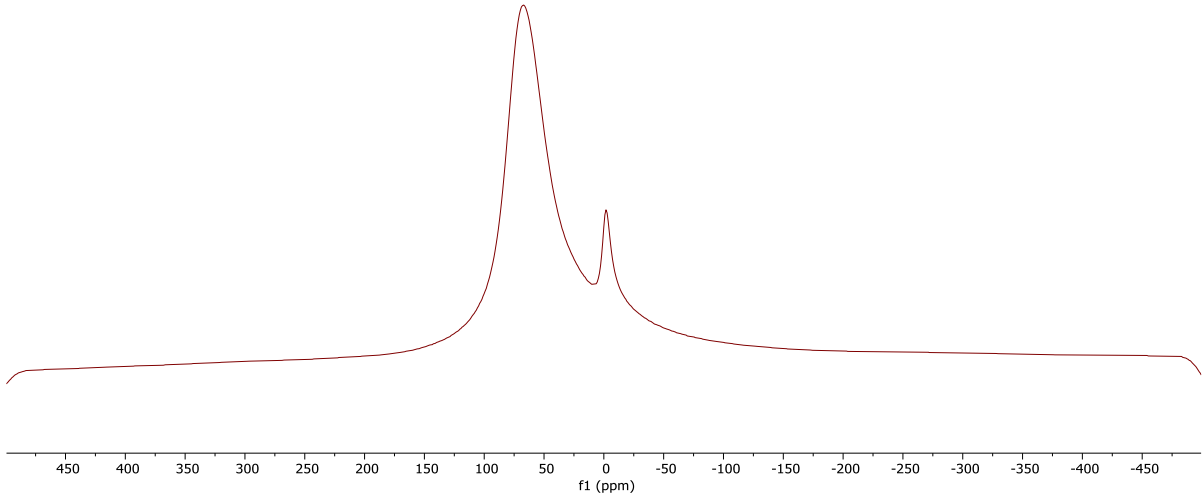


Figure S4.18. ^{27}Al NMR Spectrum (104 MHz, 298 K, $CDCl_3$) of complex **9**.

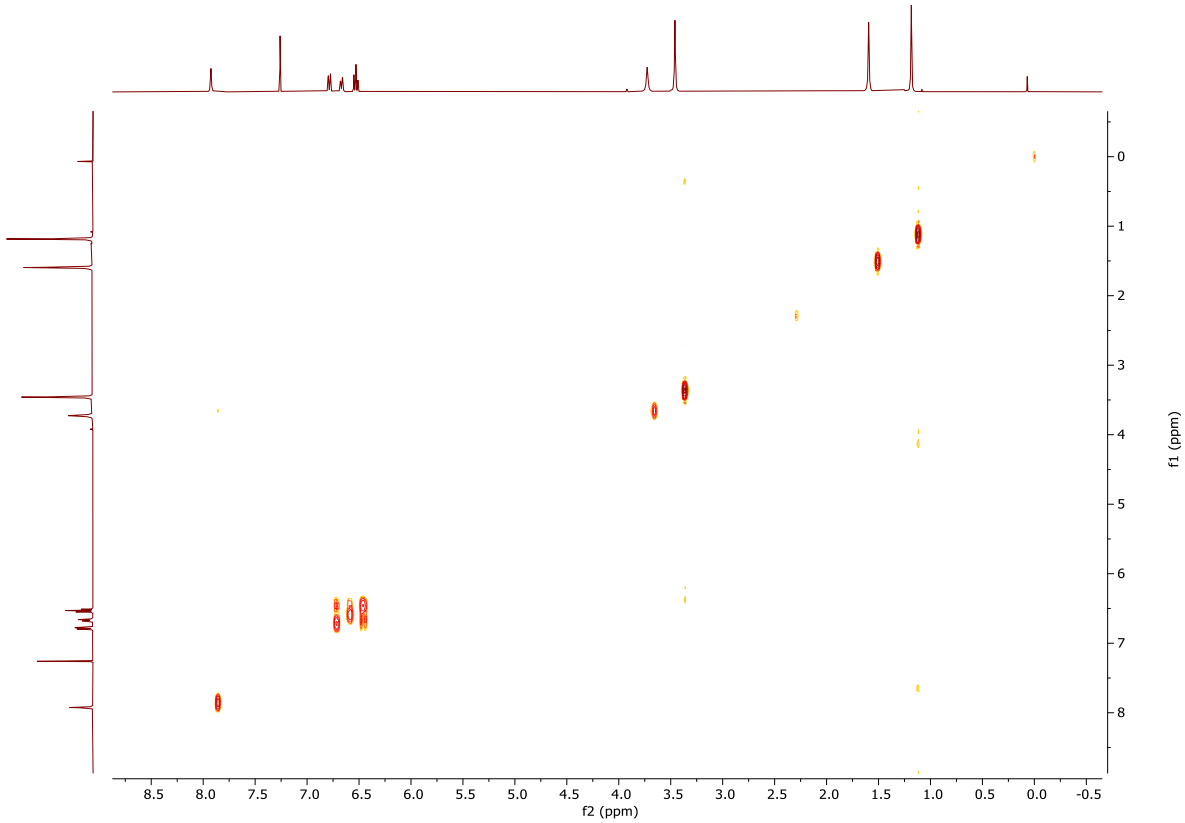


Figure S4.19. ^{1}H COSY NMR Spectrum (400 MHz, 298 K, $CDCl_3$) of complex **9**.

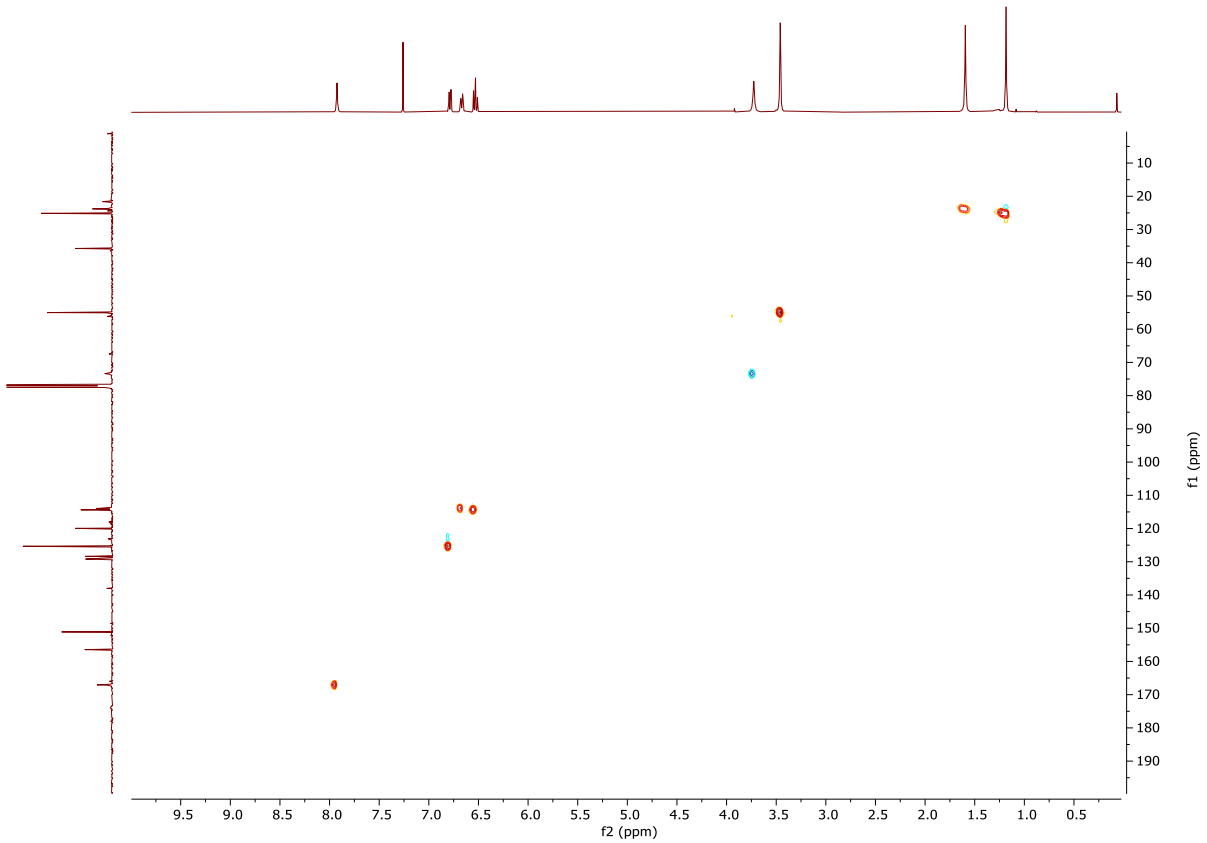


Figure S4.20. ^{1}H-^{13}C HSQC NMR Spectrum (298 K, $CDCl_3$) of complex **9**.

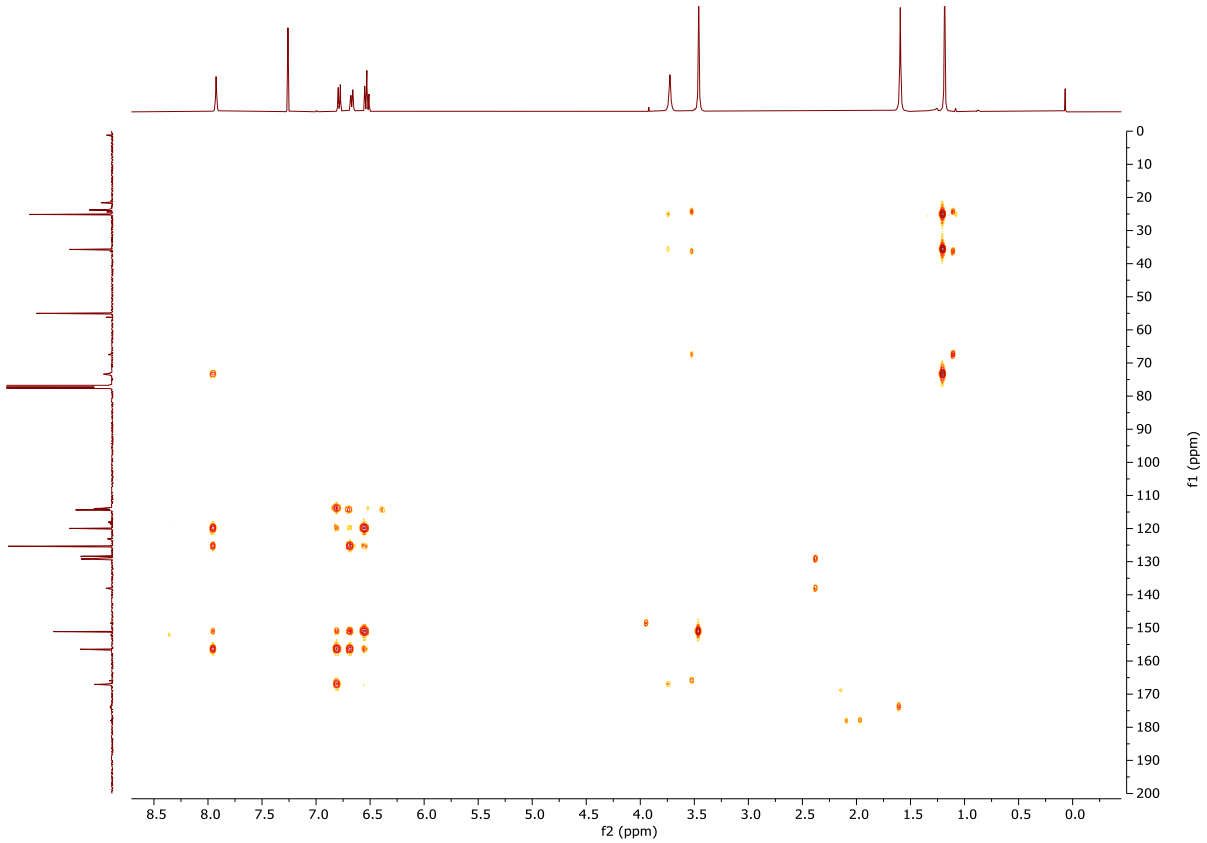


Figure S4.21. ^{1}H-^{13}C HMBC NMR Spectrum (298 K, $CDCl_3$) of complex 3.

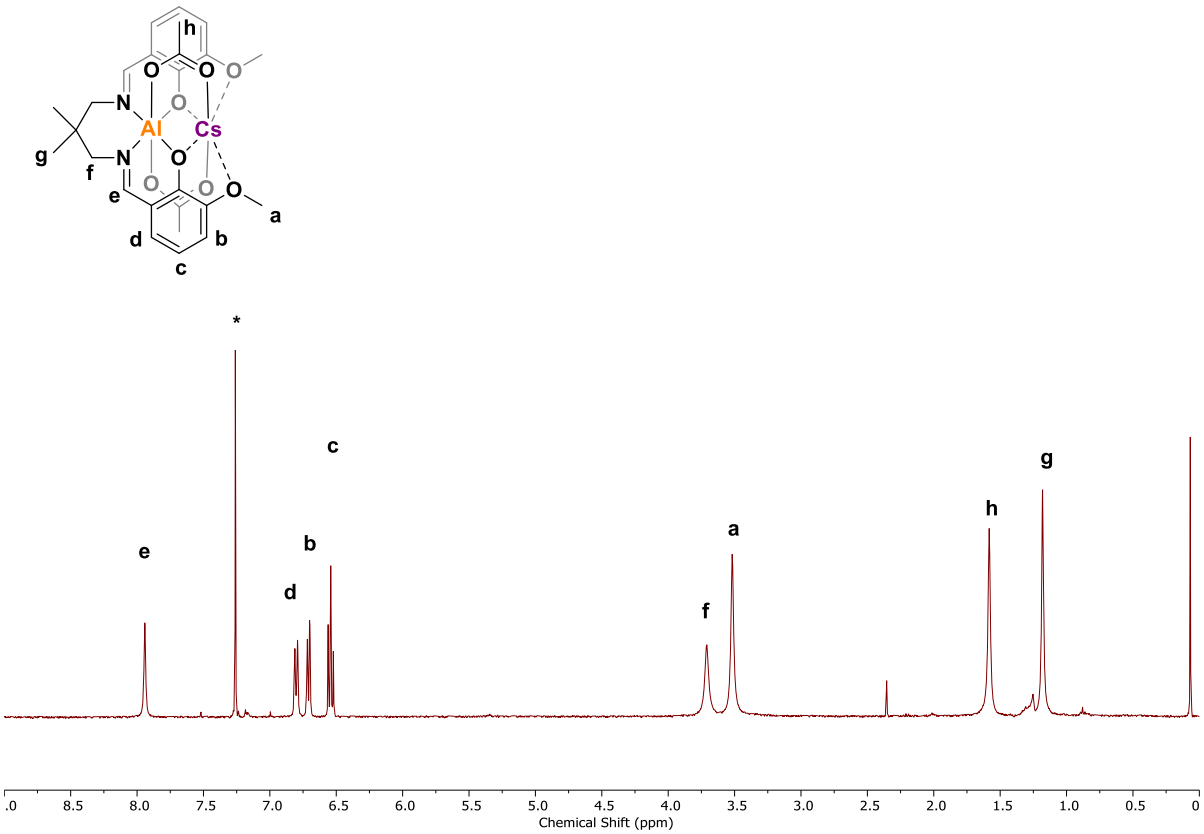


Figure S4.22. ^{1}H NMR Spectrum (400 MHz, 298 K, $CDCl_3$(*)) of complex **10**.

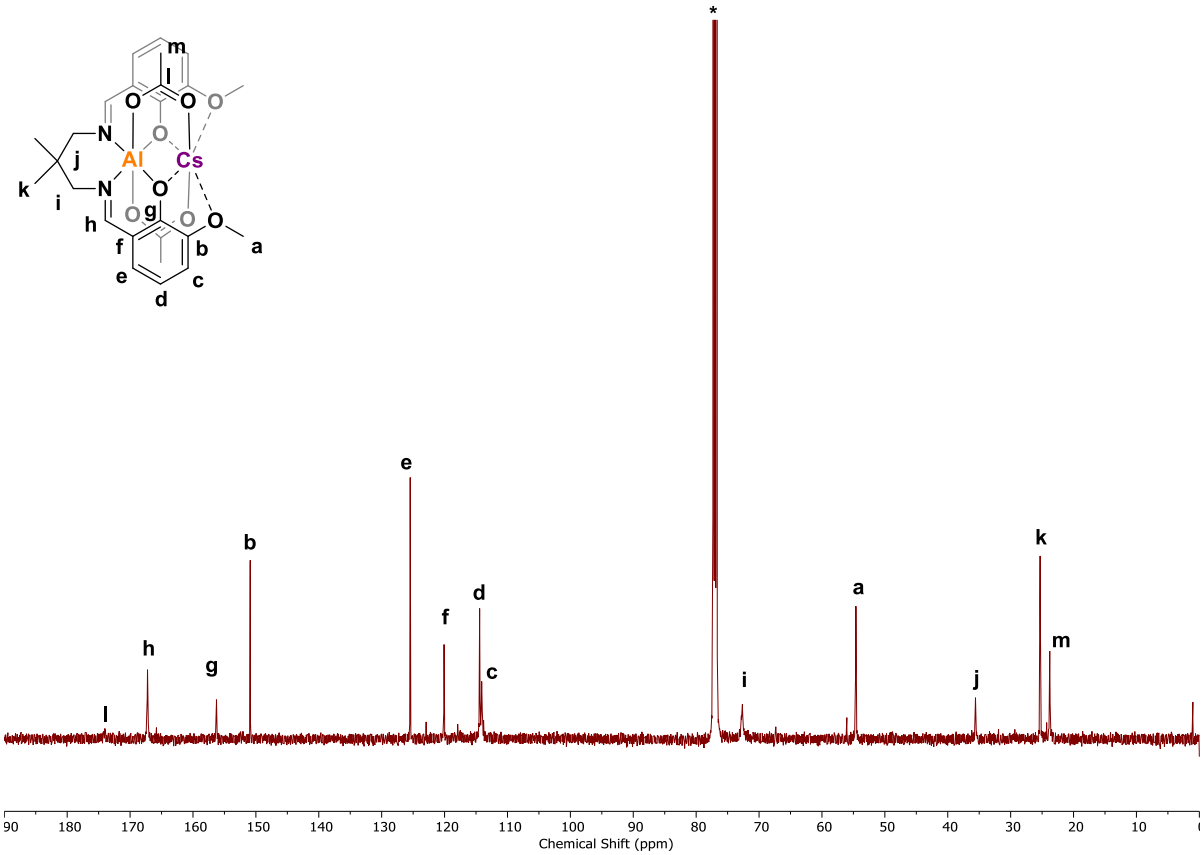


Figure S4.23. ^{13}C NMR Spectrum (126 MHz, 298 K, $CDCl_3$(*)) of complex **10**.

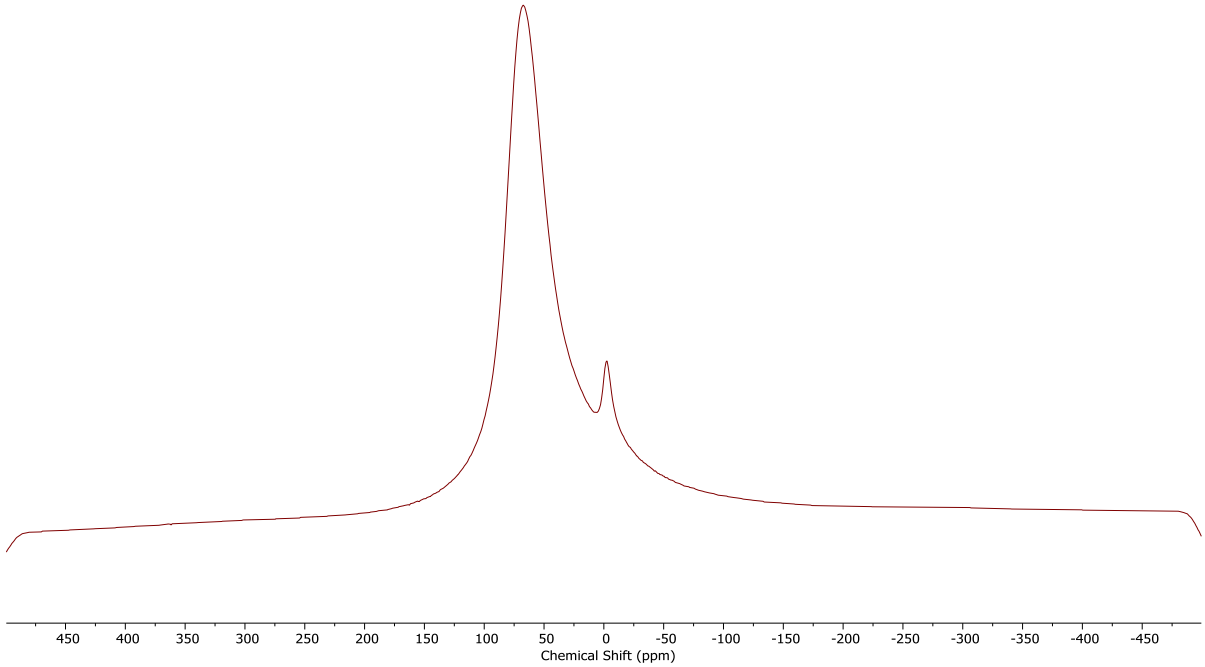


Figure S4.24. ^{27}Al NMR Spectrum (104 MHz, 298 K, $CDCl_3$) of complex **10**.

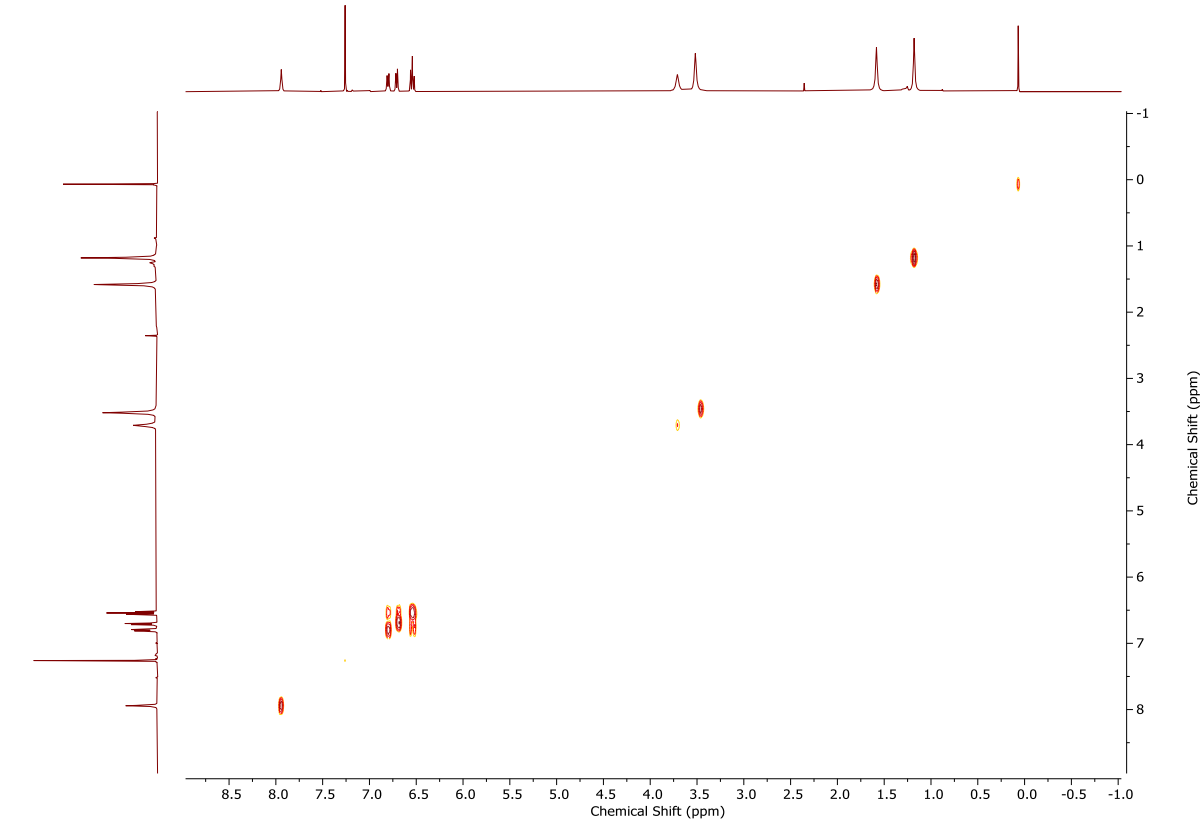


Figure S4.25. ^{1}H COSY NMR Spectrum (400 MHz, 298 K, $CDCl_3$) of complex **10**.

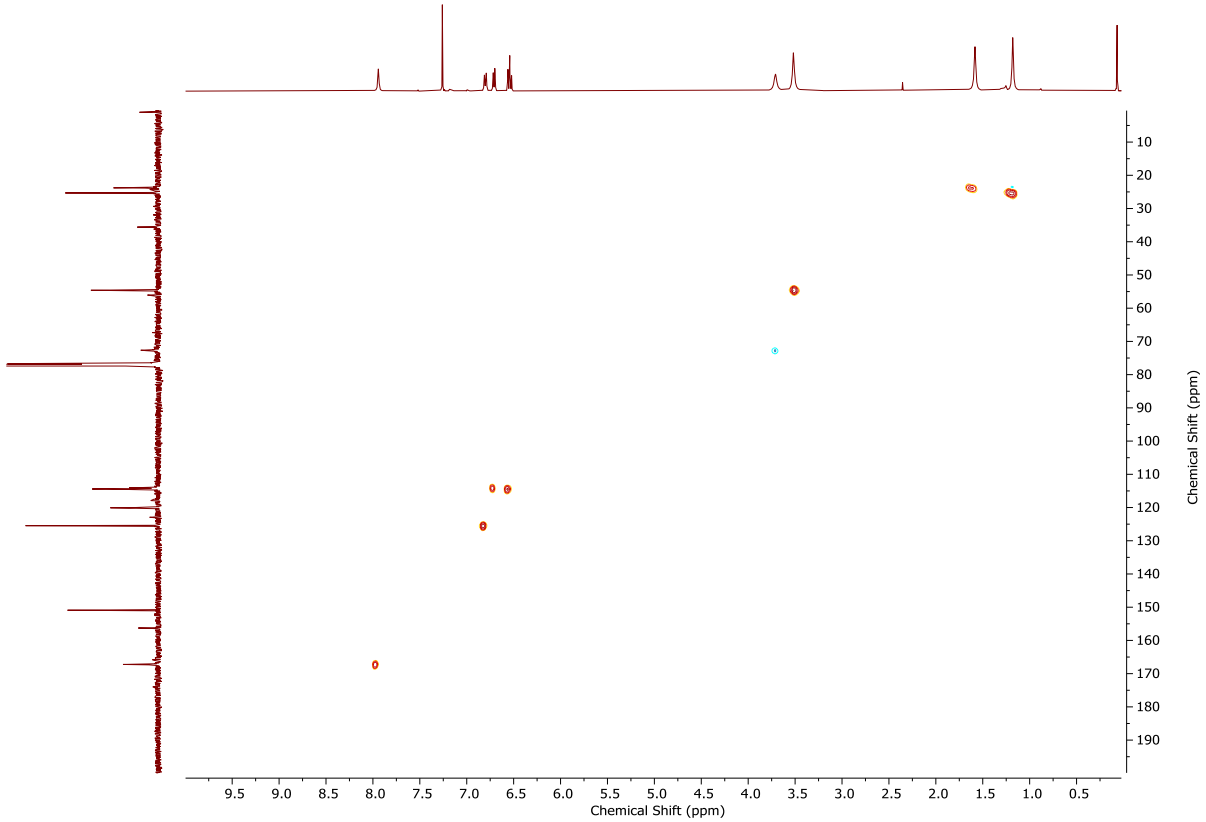


Figure S4.26. ^{1}H-^{13}C HSQC NMR Spectrum (298 K, $CDCl_3$) of complex **10**.

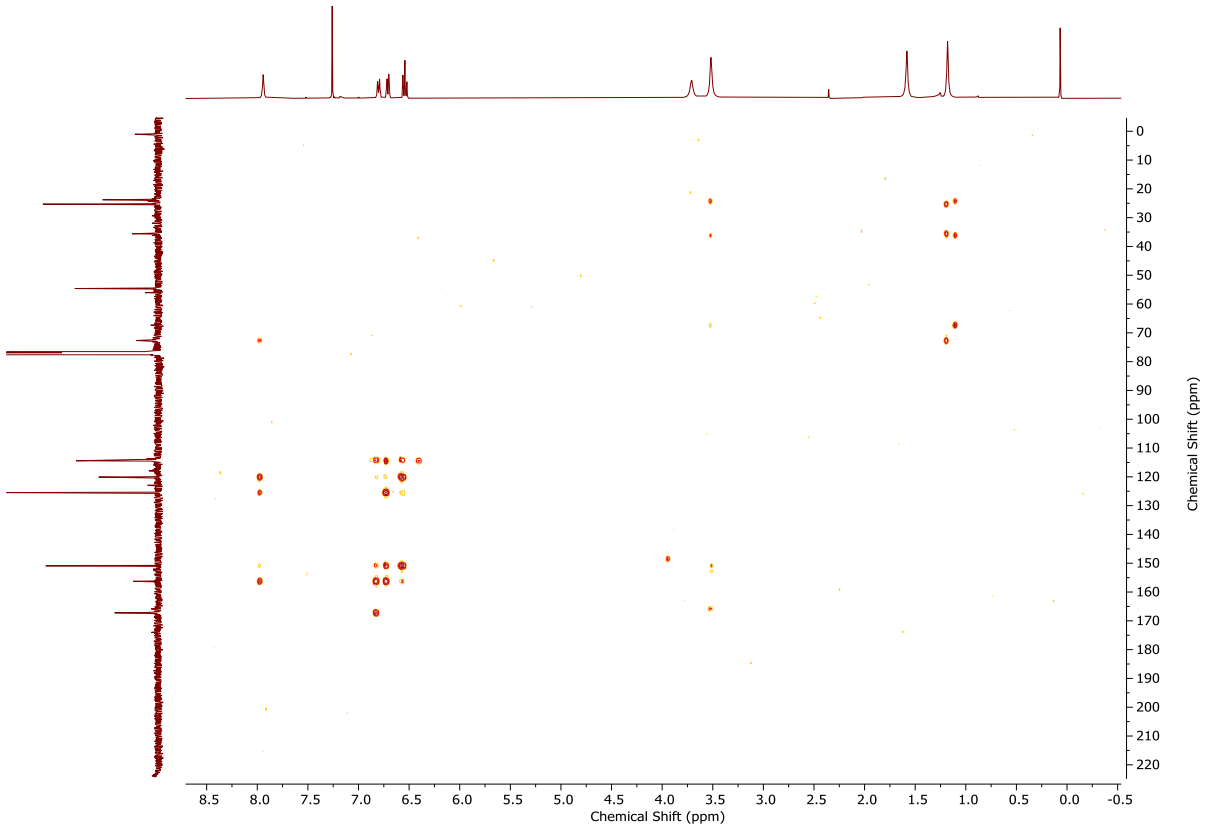


Figure S4.27. ^{1}H-^{13}C HMBC NMR Spectrum (298 K, $CDCl_3$) of complex **10**.

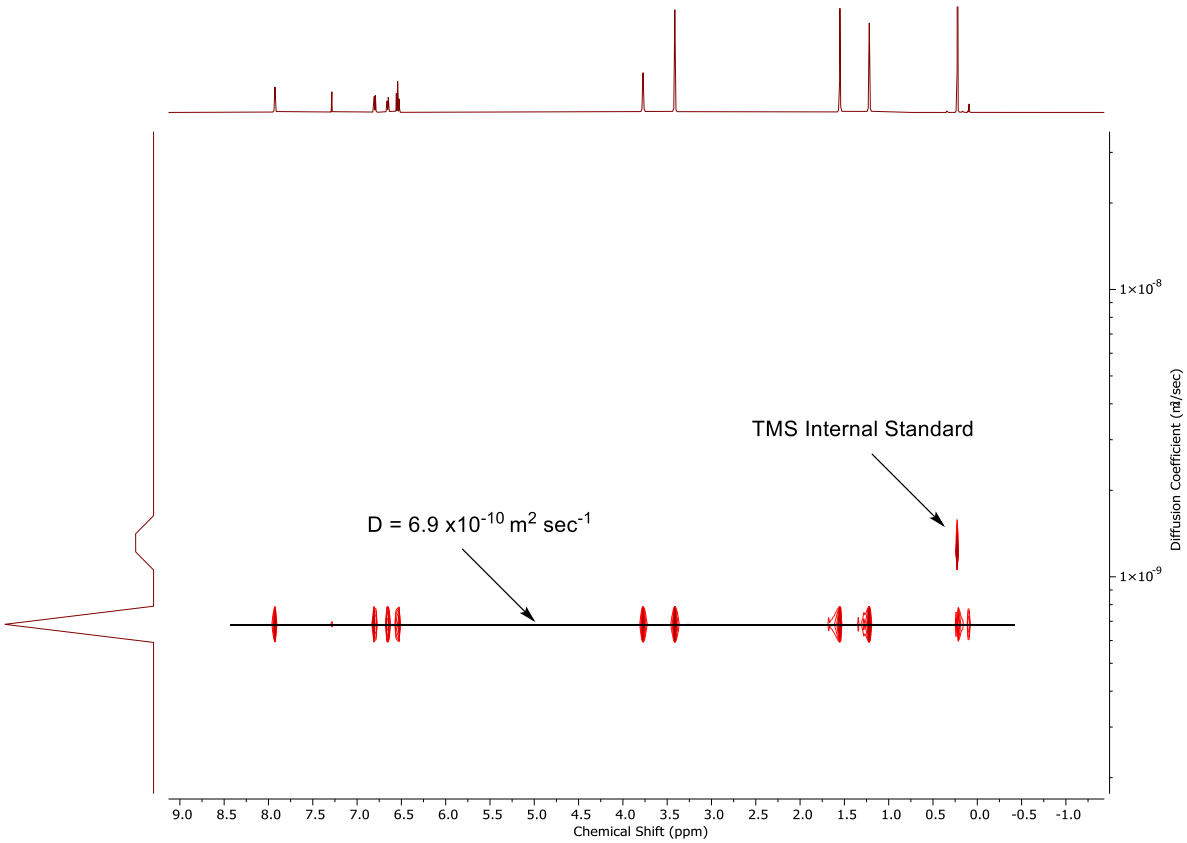


Figure S4.28. DOSY NMR spectrum (500 MHz, $CDCl_3$, 298K) of complex **8**. Use of D value obtained from this experiment in the Stokes-Einstein equation yields a solvation radius of 6.0 Å

Table S4.7. Data for the ROCOP of CHO and PA with complexes **7** – **10**.

Entry	Catalyst[a]	Time (m)	Conversion[b] (%)	TON[c]	TOF[d] (h^{-1})	Selectivity[e] (h^{-1})	k_{obs} ($x10^3$)[f] (s^{-1})	$M_{n,\,GPC}$ [Đ][g] (kg mol^{-1})
1	**7**	15	45	180	720 ± 9	>99	0.91 ± 0.02	9.3 [1.06]
2	**8**	15	67	268	1072 ± 6	>99	1.50 ± 0.03	14.3 [1.06]
3	**8**	25	>99	400	-	>99	-	20.1 [1.06]
4	**9**	15	71	284	1136 ± 6	>99	1.53 ± 0.03	14.4 [1.06]
6	**10**	15	54	216	875 ± 8	>99	1.18 ± 0.03	10.4 [1.05]

[a] Conditions: [Cat]:[PA]:[CHO] = 1:400:2000, T = 100 °C. [b] Conversion(%) of PA. Determined by ^{1}H NMR through comparison of resonances associated with PA (8.10 – 7.85 ppm) and PCHPE (7.65 – 7.30 ppm). [c] Turnover number (TON) = number of moles of anhydride consumed/number of moles of catalyst = Conversion (%) of PA*400. [d] Turnover frequency (TOF) = TON/time(hours). [e] Selectivity for polyester over polyether. Determined by ^{1}H NMR through comparison of resonances associated with PCHPE (5.22 – 5.06 ppm) and PCHO (3.60 – 3.20 ppm). [e] Observed rate constant for a linear fit of PA conversion data, without error weighting. [f] Determined by GPC, in THF, at 30 °C, using narrow dispersity polystyrene standards.

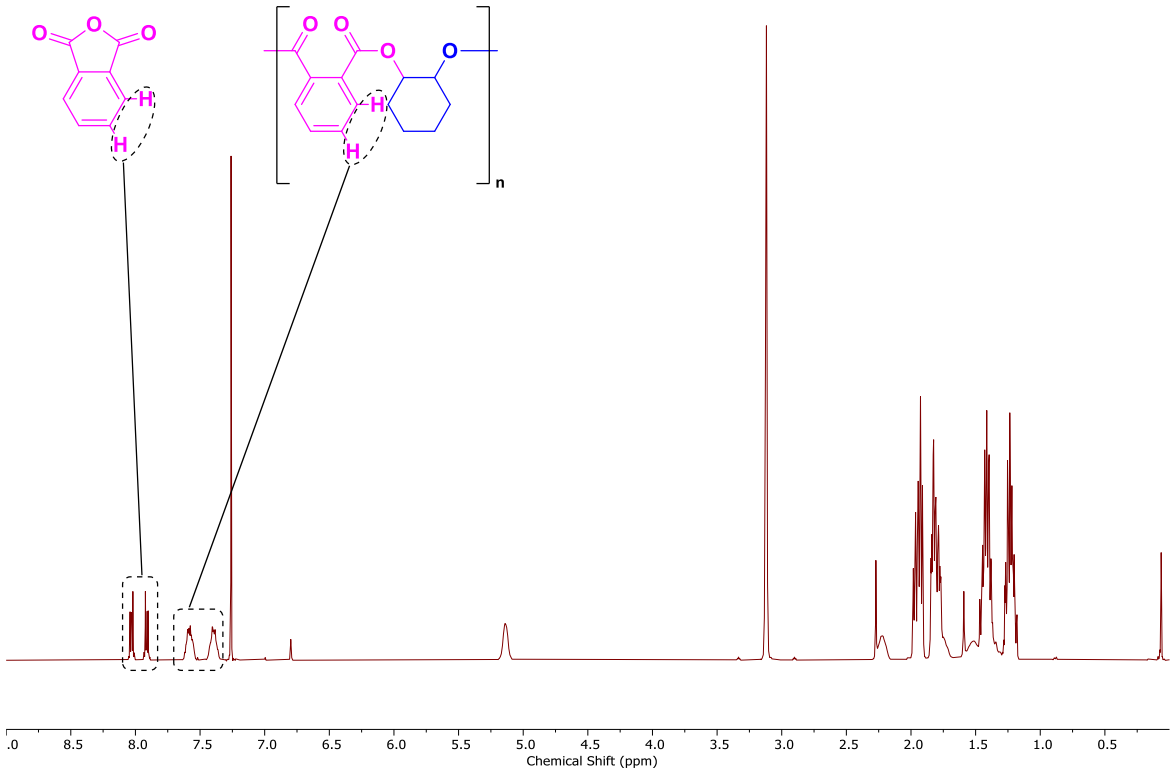


Figure S4.29. ^{1}H NMR spectrum (400 MHz, $CDCl_3$, 298 K) of reaction mixture of CHO and PA.

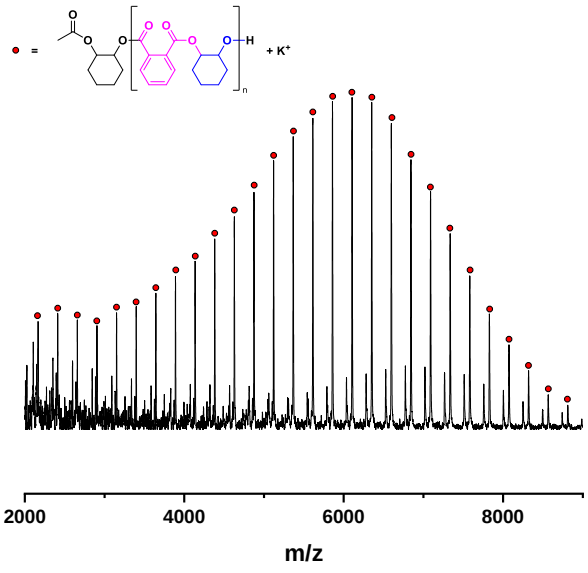


Figure S4.30. MALDI-ToF spectrum of PCHPE obtained with complex 2. Observed end group weight = 198.45 g mol-1, calculated end group weight = 197.30 g mol-1. Observed (average) distance between peaks = 246.11 g mol-1, theoretical Mn(repeat unit) = 246.26 g mol-1. Minor peaks attributed to minor cyclohexanol initiating species.[1]

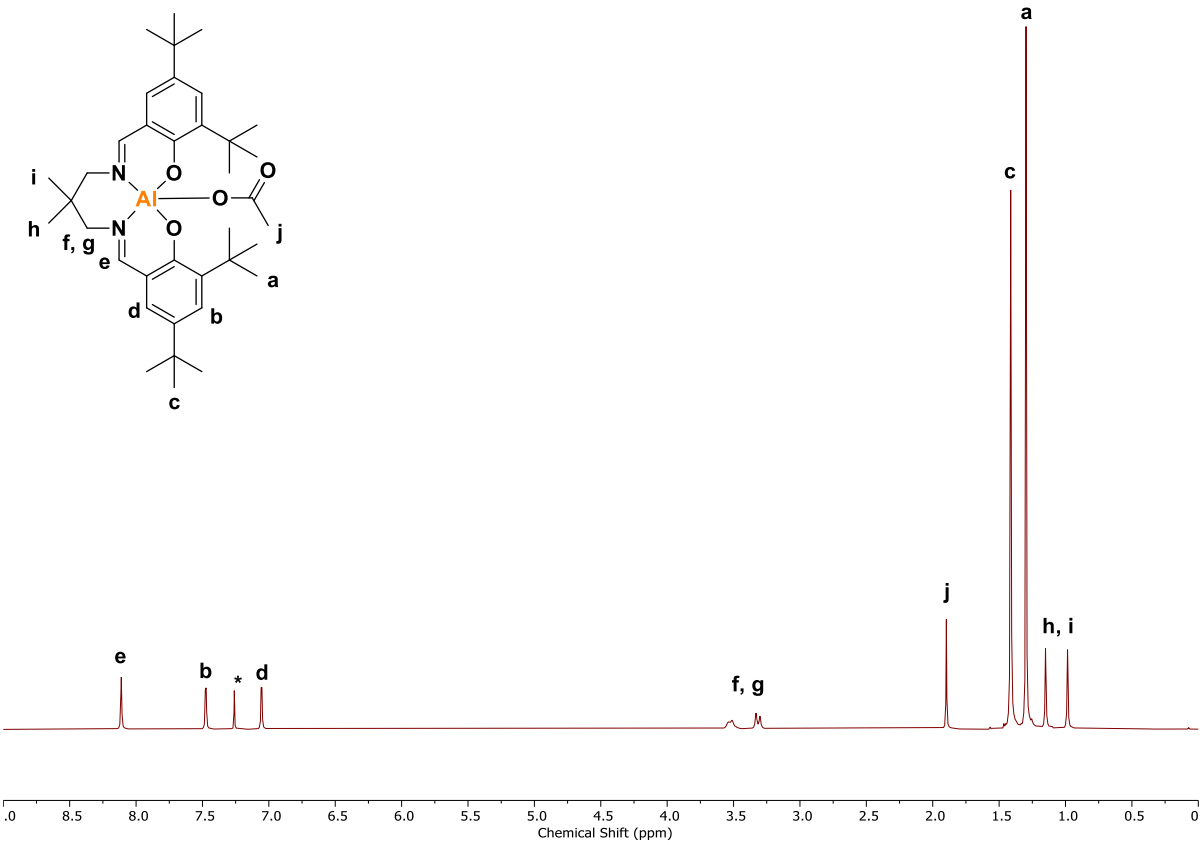


Figure S4.31. ^{1}H NMR Spectrum (400 MHz, 298 K, $CDCl_3$(*)) of complex **11**.

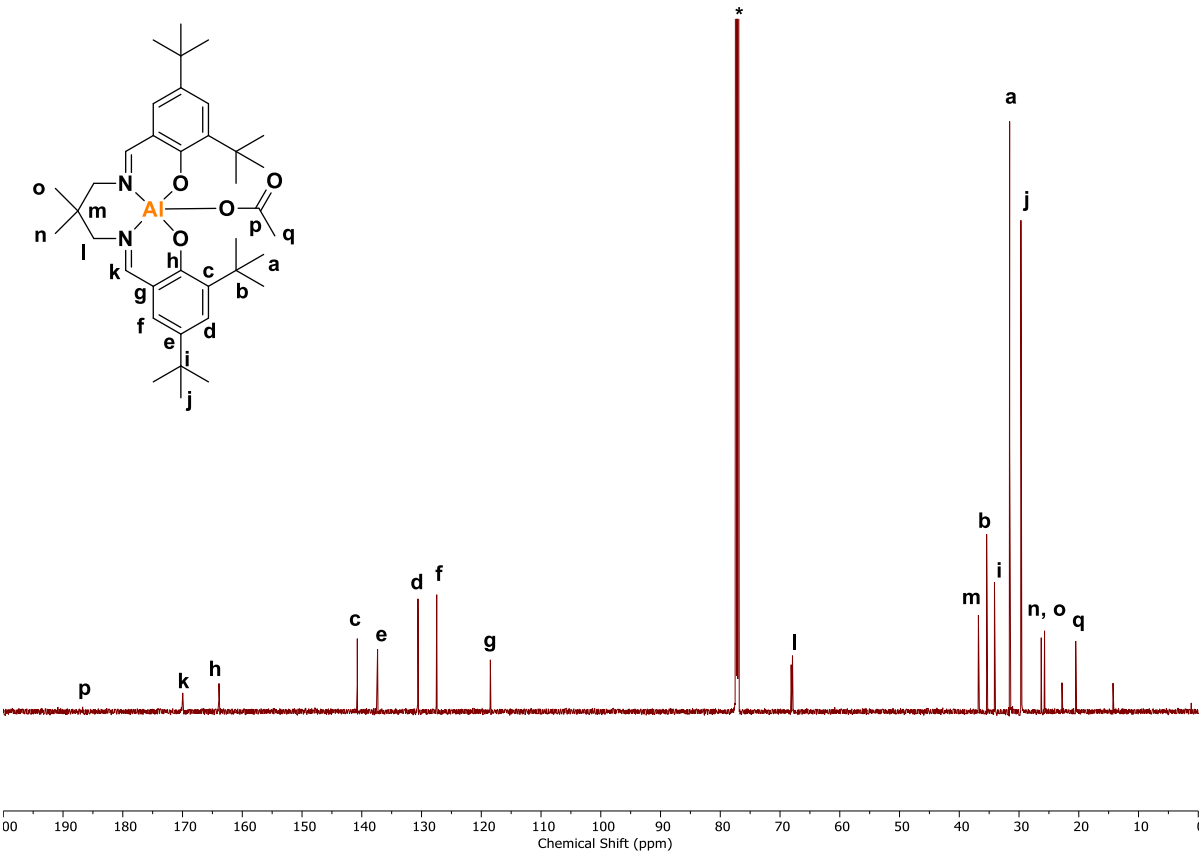


Figure S4.32. ^{13}C NMR Spectrum (176 MHz, 298 K, $CDCl_3$(*)) of complex **11**.

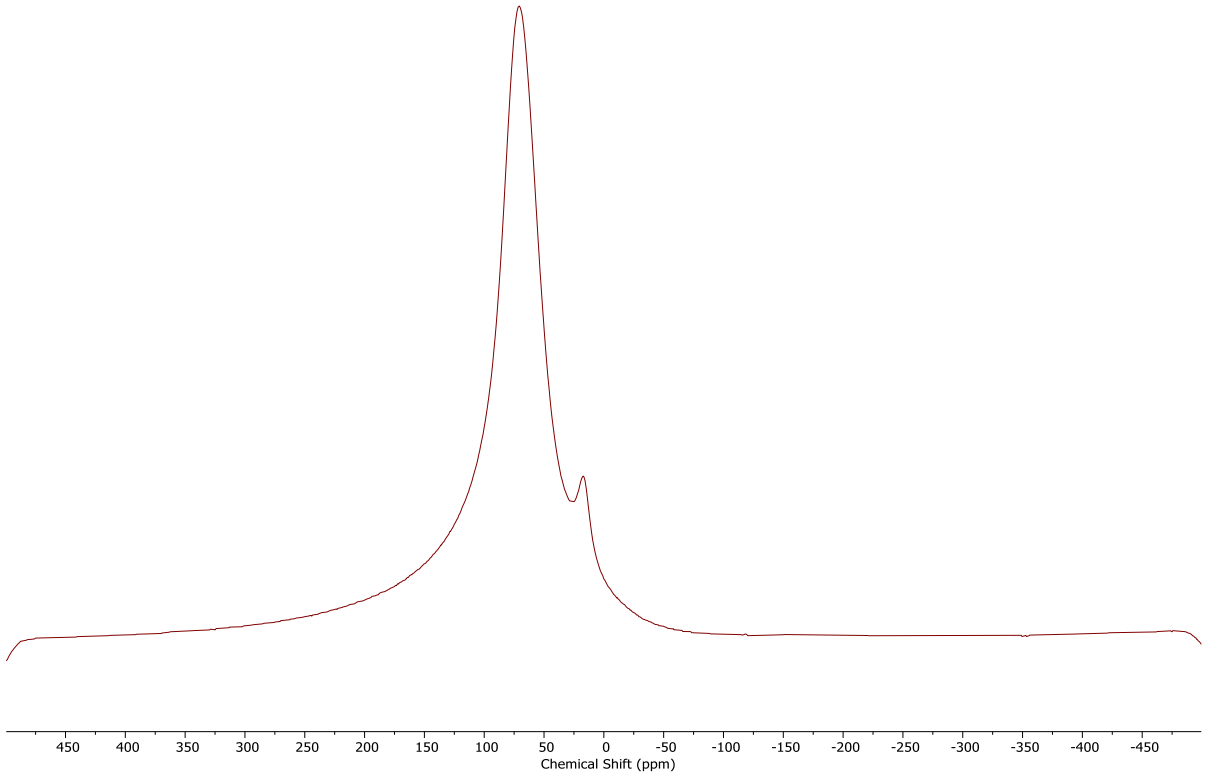


Figure 4.33. ^{27}Al NMR Spectrum (104 MHz, 298 K, $CDCl_3$) of complex **11**.

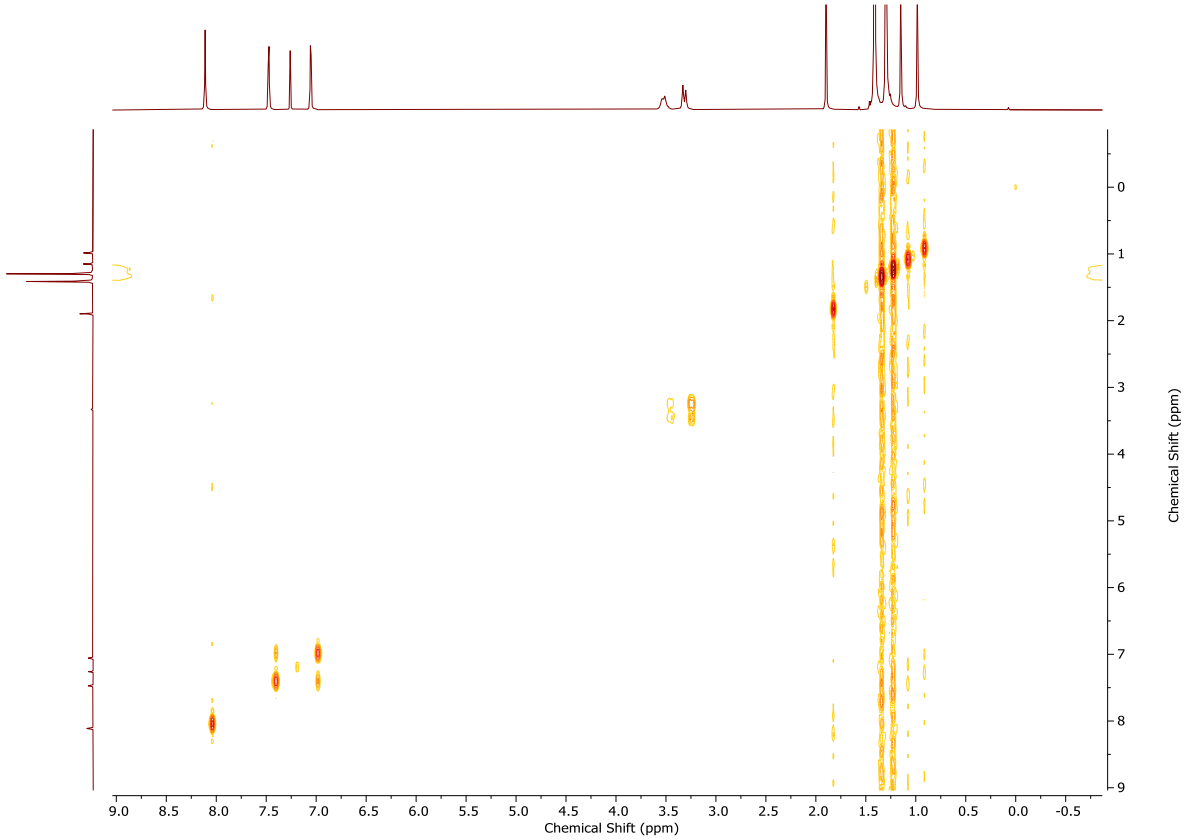


Figure S4.34. ^{1}H COSY NMR Spectrum (400 MHz, 298 K, $CDCl_3$) of complex **11**.

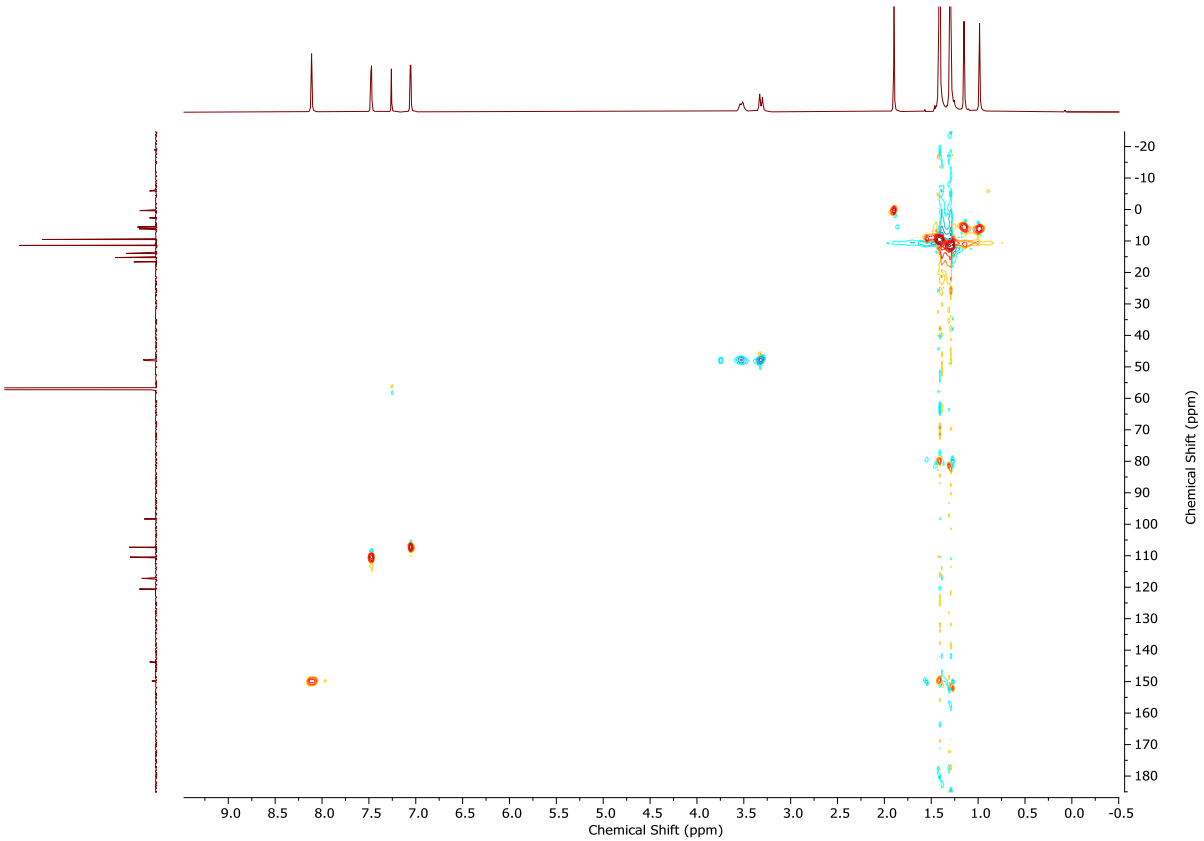


Figure S4.35. ^{1}H-^{13}C HSQC NMR Spectrum (298 K, $CDCl_3$) of complex **11**.

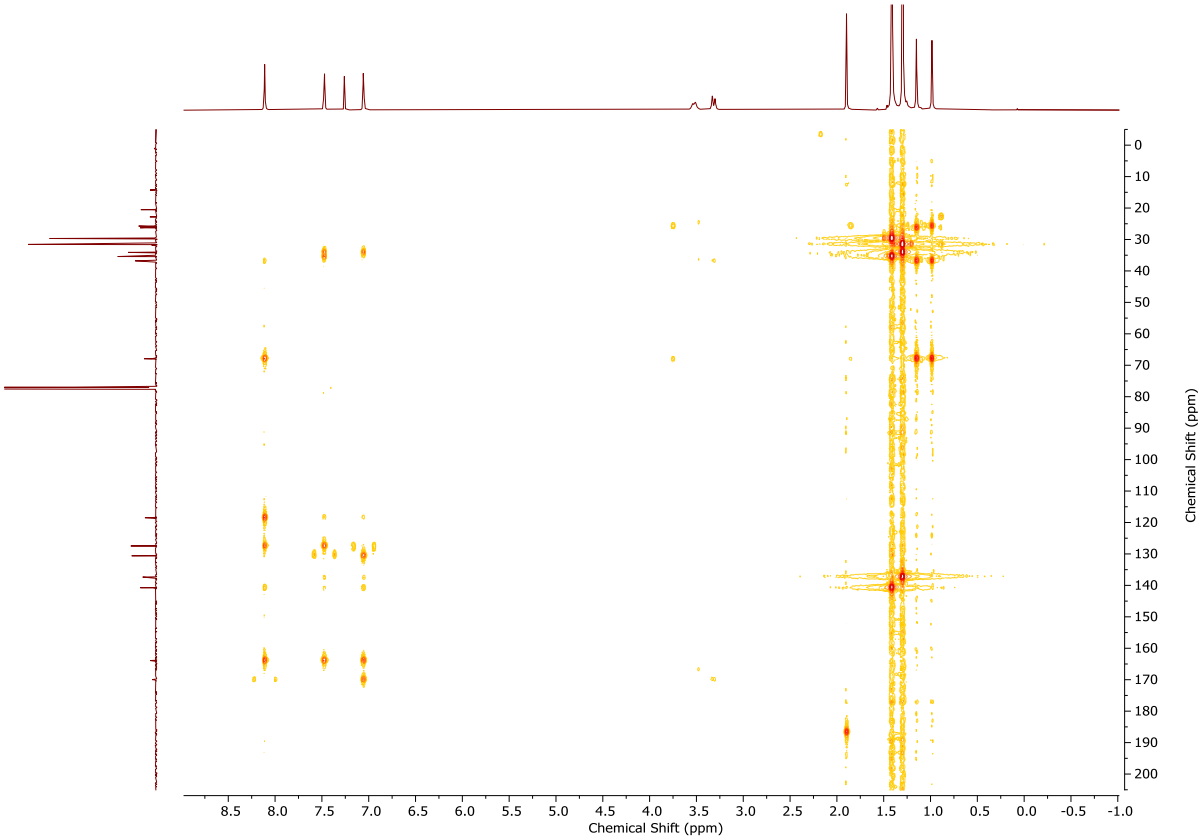


Figure S4.36. ^{1}H-^{13}C HMBC NMR Spectrum (298 K, $CDCl_3$) of complex **11**.

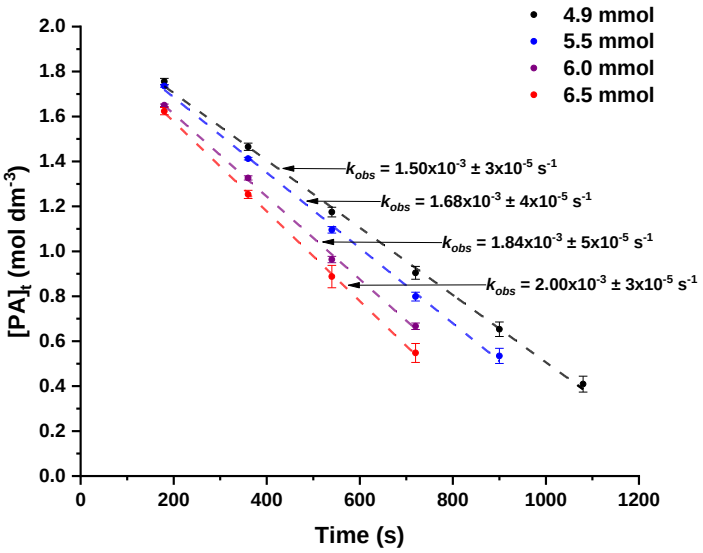


Figure S4.37. Plot of $[PA]_t$ *vs.* Time at a range of [**8**]. A linear relationship is observed in all cases. All reactions repeated in triplicate, with average values of $[PA]_t$ plotted and error $\pm\sigma/\sqrt{n}$.

Computational Details for Chapter 4

Density Functional theory (DFT) calculations were performed using Gaussian16 suite of codes (revision A.03). Geometries were fully optimised without any symmetry or geometry constraints. The nature of all the stationary points as minima or transition states (first-order saddle points) on the potential energy surface was verified by calculations of the vibrational frequency spectrum. All transition states were characterised by precisely one negative frequency corresponding to the intended reaction and were further confirmed by intrinsic reaction coordinate (IRC) calculations.

Free enthalpies were first calculated at 298.15 K and a standard-state concentration in solution of 1 M within the harmonic approximation for vibrational frequencies.

Using the GoodVibes software, free enthalpies were recomputed using Grimme quasi-harmonic approximation, with a cut off frequency of 50 cm^{-1}, and a temperature (T = 373.15 K) and concentration correction applied (at [Cat] = 4.94 mM or [CHO]0 = 9.88 M)).[2, 3]

Geometry optimisations were carried out using ωb97xD functional. The 6-31+G(d,p) basis set was used for C and H atoms, 6-311G+(d) for Al, K, O and N atoms. Solvent effects in cyclohexene oxide were computed using the cpcm continuum model, using modified parameters for THF (eps=16, epsinf=1.867).[4]

Full coordinates for all structures, together with computed energies and vibrational frequency data, are available via the corresponding Gaussian 09 output files, stored in the open-access digital repository: DOI:10.6084/m9.figshare.14955234

Table S4.8. Summary of uncorrected computed structures.

Structure	G (Hartrees)	ΔG (Kcal mol^{-1})
CHO	-309.679573	-
I	-2715.724047	-
Reference (I + CHO)	-3025.403620	0.0
I_K	-3025.402824	+0.5
Pre-$TS_{I\text{-}IIK}$	-3025.400396	+2.0
$TS_{I\text{-}IIK}$	-3025.348112	+34.8
Post-$TS_{I\text{-}IIK}$	-3025.365273	+24.1
II_K	-3025.36664	+23.2
I_{Al}	-3025.391953	+7.3
Pre-$TS_{I\text{-}IIAl}$	-3025.388626	+9.4
$TS_{I\text{-}IIAl}$	-3025.365923	+23.7
II_{Al} (/post-$TS_{I\text{-}IIAl}$)	-3025.407460	-2.4

[a] ωb97xD/C H O= 6-31+g(d,p)/K Al = 6-311+g(d)/solvent = modified THF eps=16 epsinf=1.867

Table S4.9. Correction computed structures [a]

Structure	Corrections					
	T[b]		T + [Cat][c]		T + [CHO][d]	
	G (Hartrees)	ΔG (Kcal mol^{-1})	G (Hartrees)	ΔG (Kcal mol^{-1})	G (Hartrees)	ΔG (Kcal mol^{-1})
CHO	-309.6890640	-	-309.6912960	-	-309.6823140	-
I	-2715.742497	-	-2715.744729	-	-2715.735747	-
Reference	-3025.431561	0.0	-3025.436025	0.0	-3025.418061	0.0
I_K	-3025.42225	+5.8	-3025.424482	+7.2	-3025.415500	+1.6
Pre-$TS_{I\text{-}IIK}$	-3025420565	+6.9	-3025.422797	+8.3	-3025.413815	+2.7
$TS_{I\text{-}IIK}$	-3025.367957	+39.9	-3025.370189	+41.3	-3025.361207	+35.7
Post-$TS_{I\text{-}IIK}$	-3025.384582	+29.5	-3025.386814	+30.9	-3025.377832	+25.2
II_K	-3025.38668	+28.2	-3025.388912	+29.6	-3025.379930	+23.9
I_{Al}	-3025.411441	+12.6	-3025.413673	+14.0	-3025.404691	+8.4
Pre-$TS_{I\text{-}IIAl}$	-3025.408603	+14.4	-3025.410835	+15.8	-3025.401853	+10.2
$TS_{I\text{-}IIAl}$	-3025.385207	+29.1	-3025.387438	+30.5	-3025.378457	+24.9
II_{Al}	-3025.42782	+2.3	-3025.430052	+3.7	-3025.421070	+1.9

[a] ωb97xD/C H O= 6-31+g(d,p)/K Al = 6-311+g(d)/solvent = modified THF eps=16 epsinf=1.867. [b] Temperature correction, T = 373.15 K. [c] Catalyst concentration = 4.94 mM. [d] Epoxide (CHO) concentration = 9.88 M.

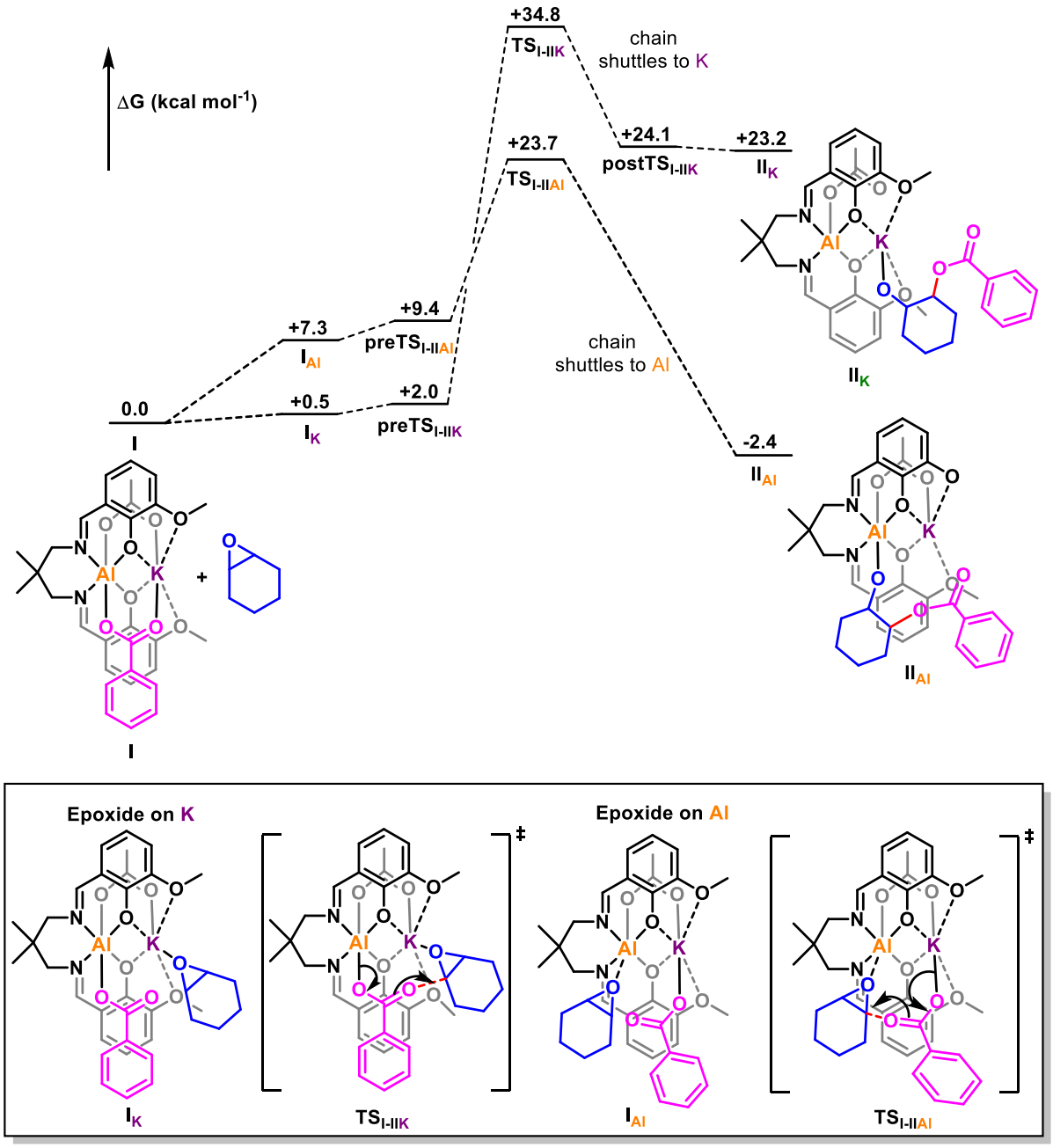


Figure S4.38. Computed Reaction Profile for epoxide ring-opening. ωb97xD/C H O= 6-31+g(d,p)/K Al = 6-311+g(d)/solvent = modified THF eps=16 epsinf=1.867 (cpcm).

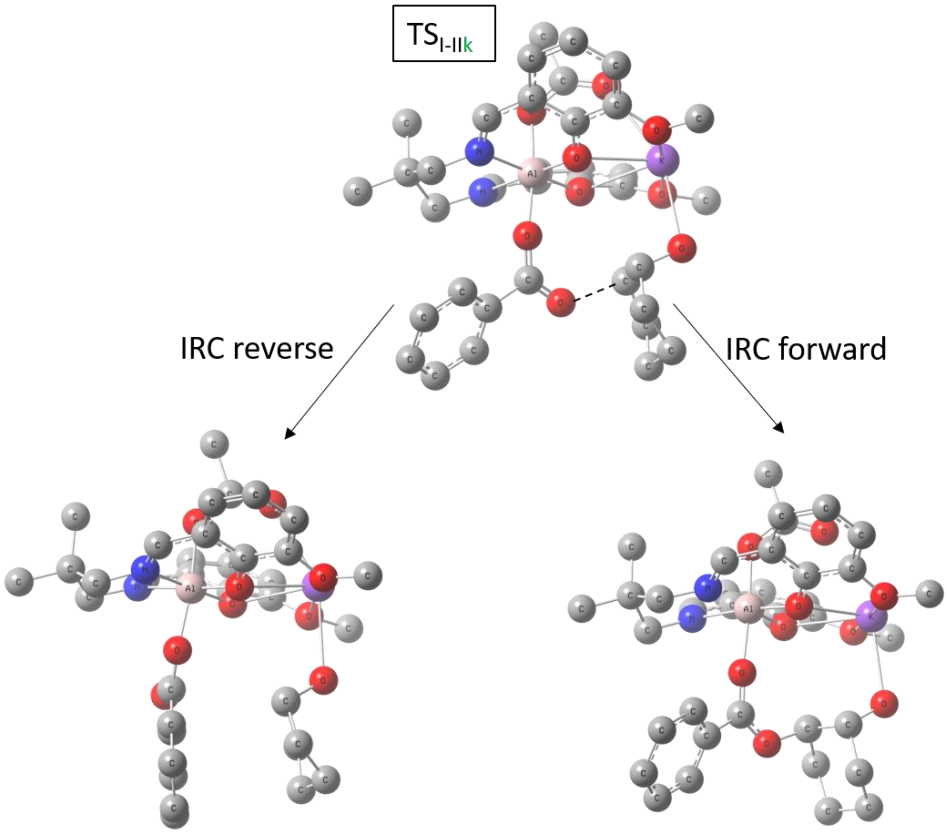


Figure S4.39. IRC for TS_{I-IIK} showing connected intermediates either side. Key bond being formed shown. Maxpoints=50, maxcycle=40, stepsize=20

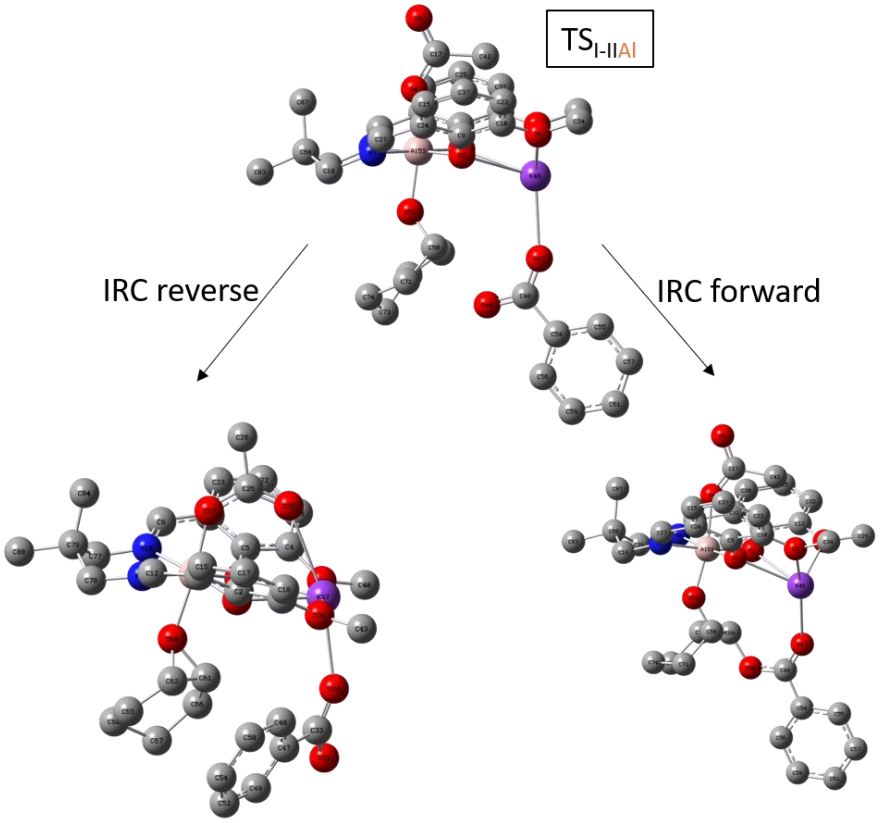


Figure S4.40. IRC for TS_{I-IIAl} showing connected intermediates either side. Maxpoints=50, maxcycle=40, stepsize=20

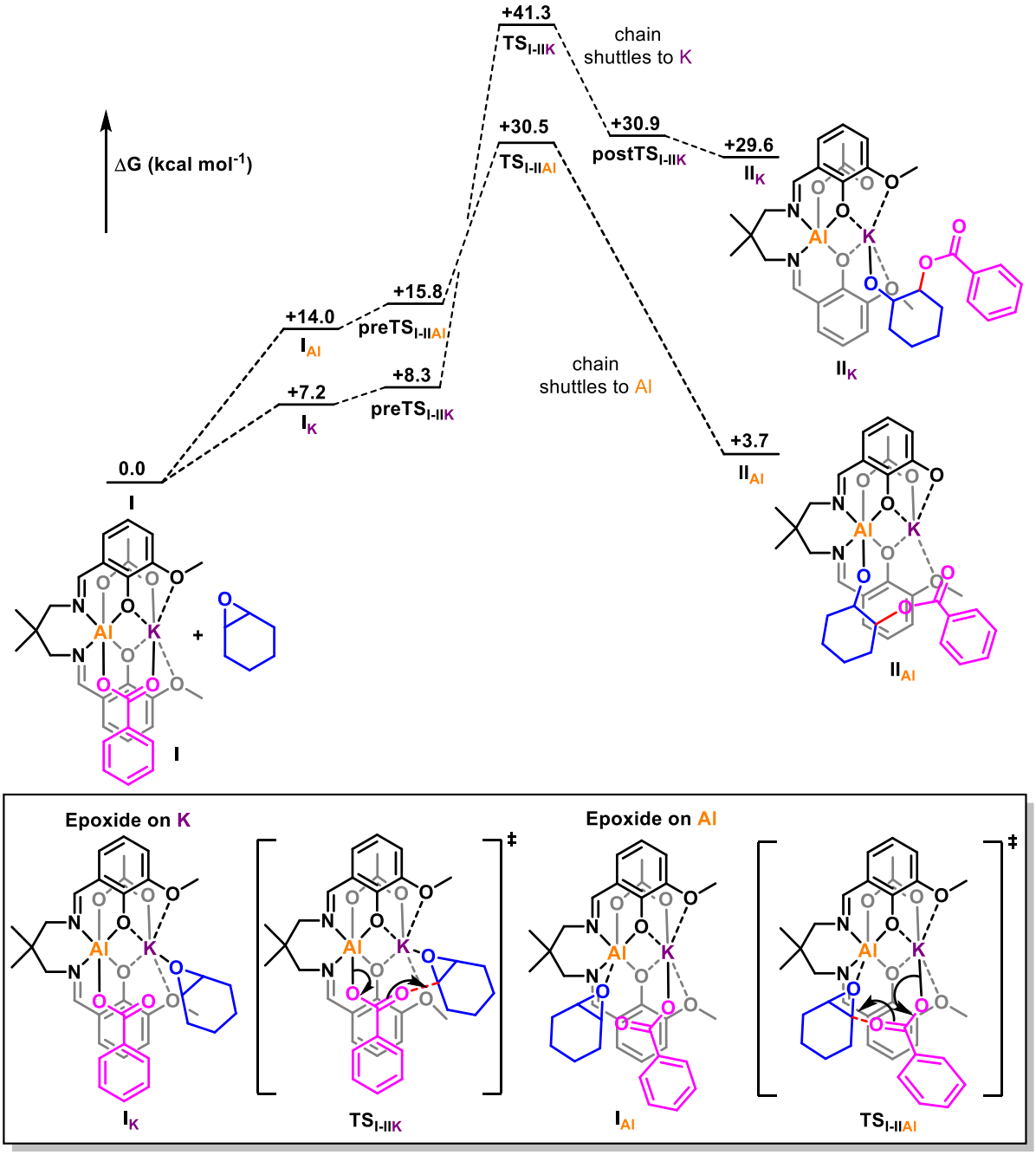


Figure S4.41. Computed Pathways for lowest free enthalpy TS. Reaction profile showing key intermediates and transitions states computed with temperature corrections and accounting for catalyst concentration.

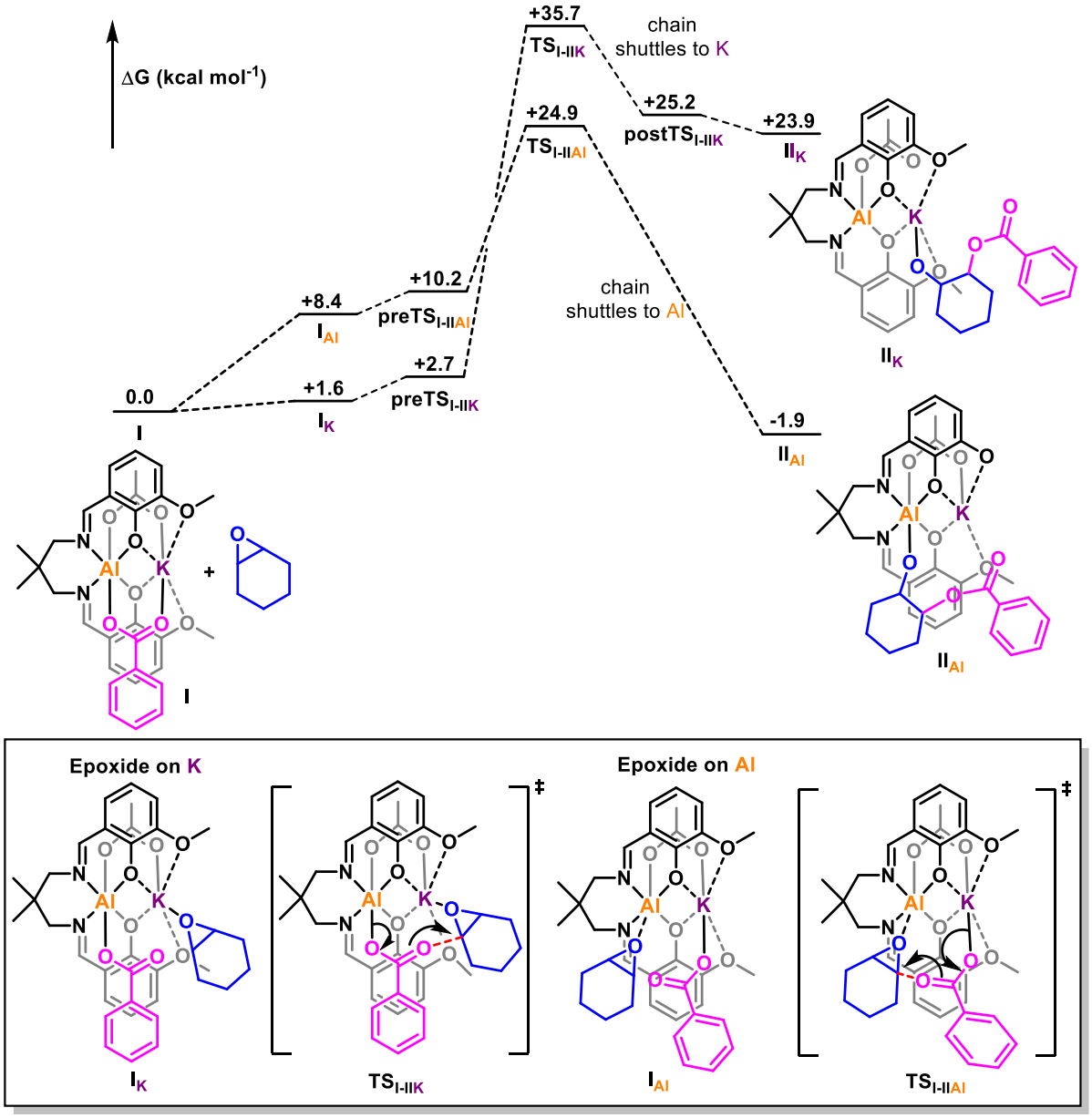


Figure S4.42. Computed Pathways for lowest free enthalpy TS. Reaction profile showing key intermediates and transitions states computed with temperature corrections and accounting for excess epoxide.

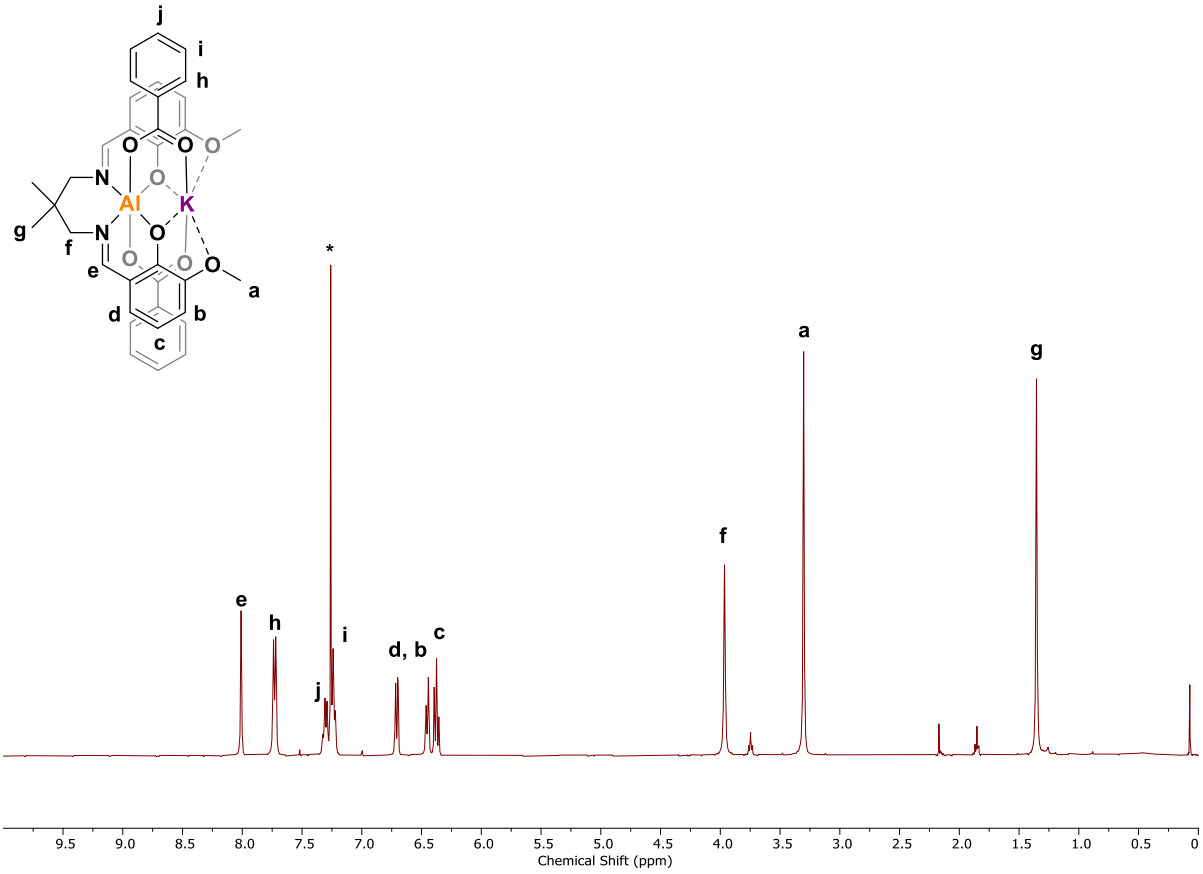


Figure S4.43. ^{1}H NMR spectrum (400 MHz, $CDCl_3$(*), 298 K) of complex **12**.

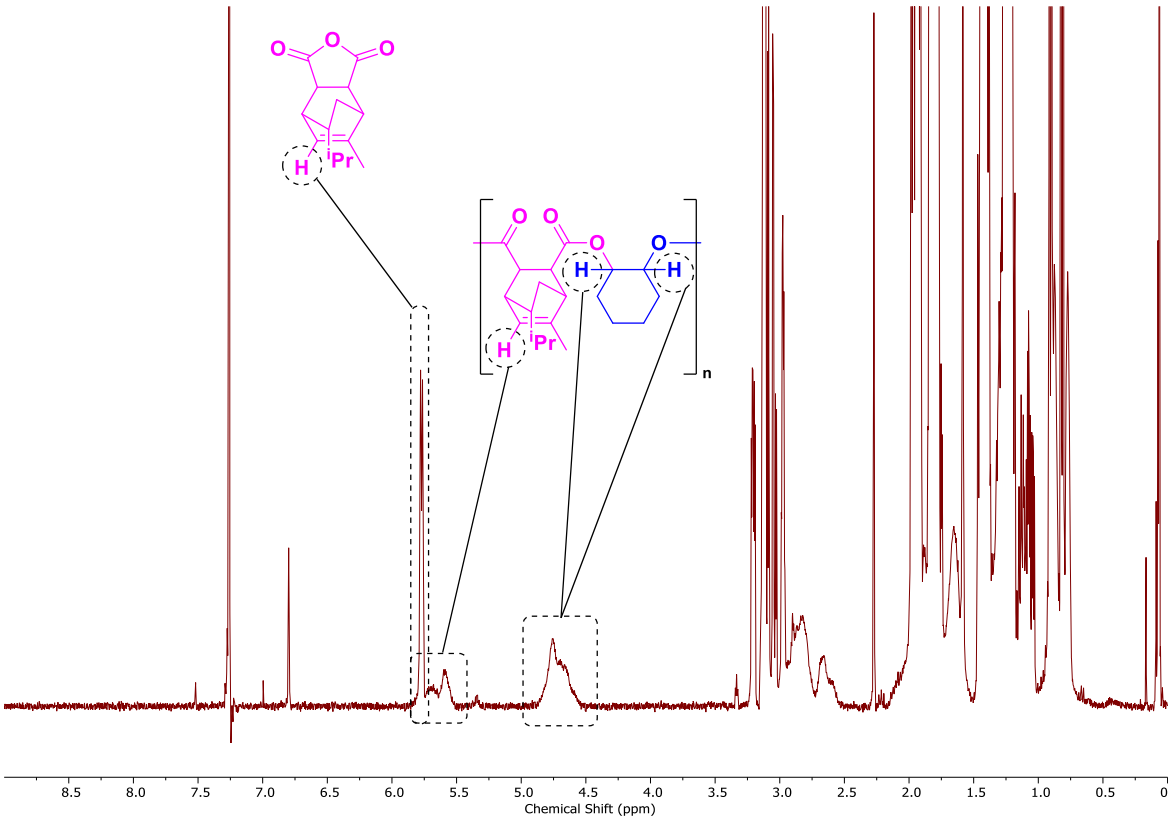


Figure S4.44. ^{1}H NMR spectrum (400 MHz, $CDCl_3$, 298 K) of reaction mixture of CHO and TCA. Conversion of TCA (%) = ((∫4.90-4.50 ppm/2)/(∫5.90-5.50 ppm))*100. $TON_{Epoxide}$ = $TON_{Anhydride}$ = Conv.(%)*400. Spectroscopic data is consistent with prior literature reports.[5]

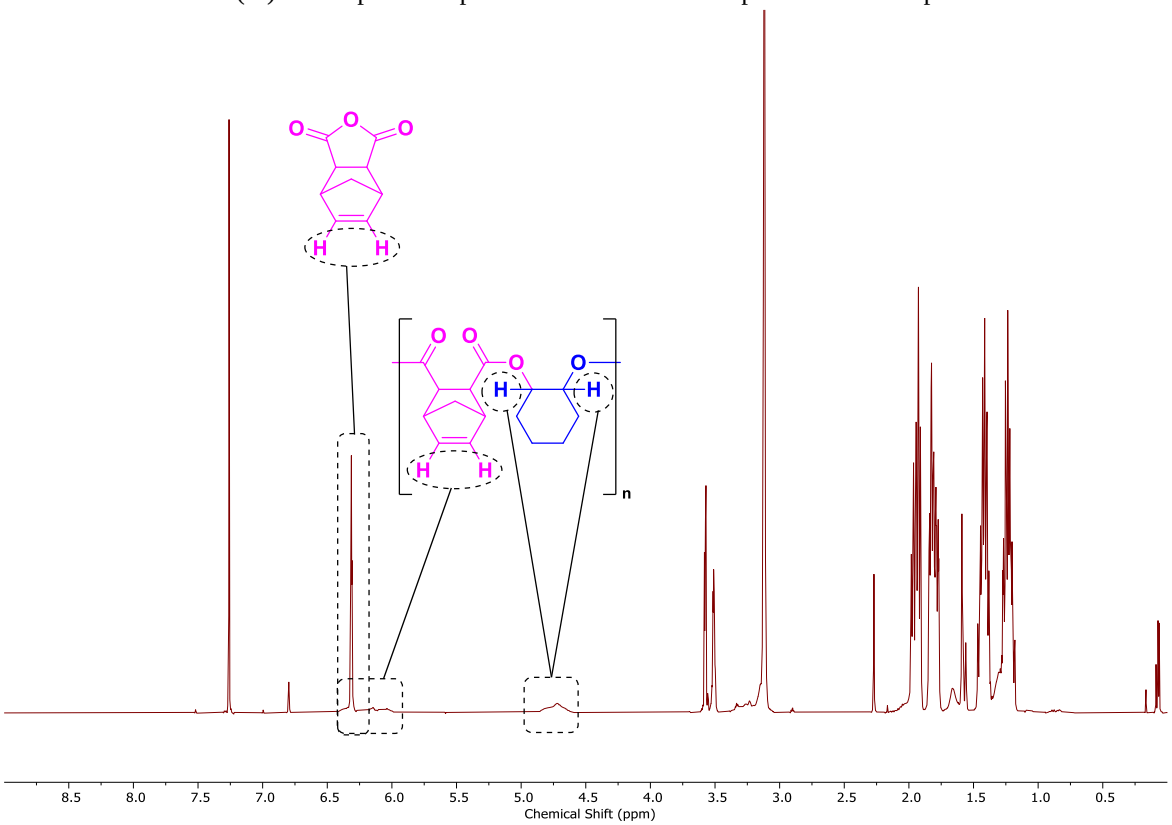


Figure S4.45. ^{1}H NMR spectrum (400 MHz, $CDCl_3$, 298 K) of reaction mixture of CHO and NBA. Conversion of NBA (%) = (∫4.90-4.50 ppm/(∫6.40-5.90 ppm))*100. $TON_{Epoxide}$ = $TON_{Anhydride}$ = Conv.(%)*400. Spectroscopic data is consistent with prior literature reports.[6]

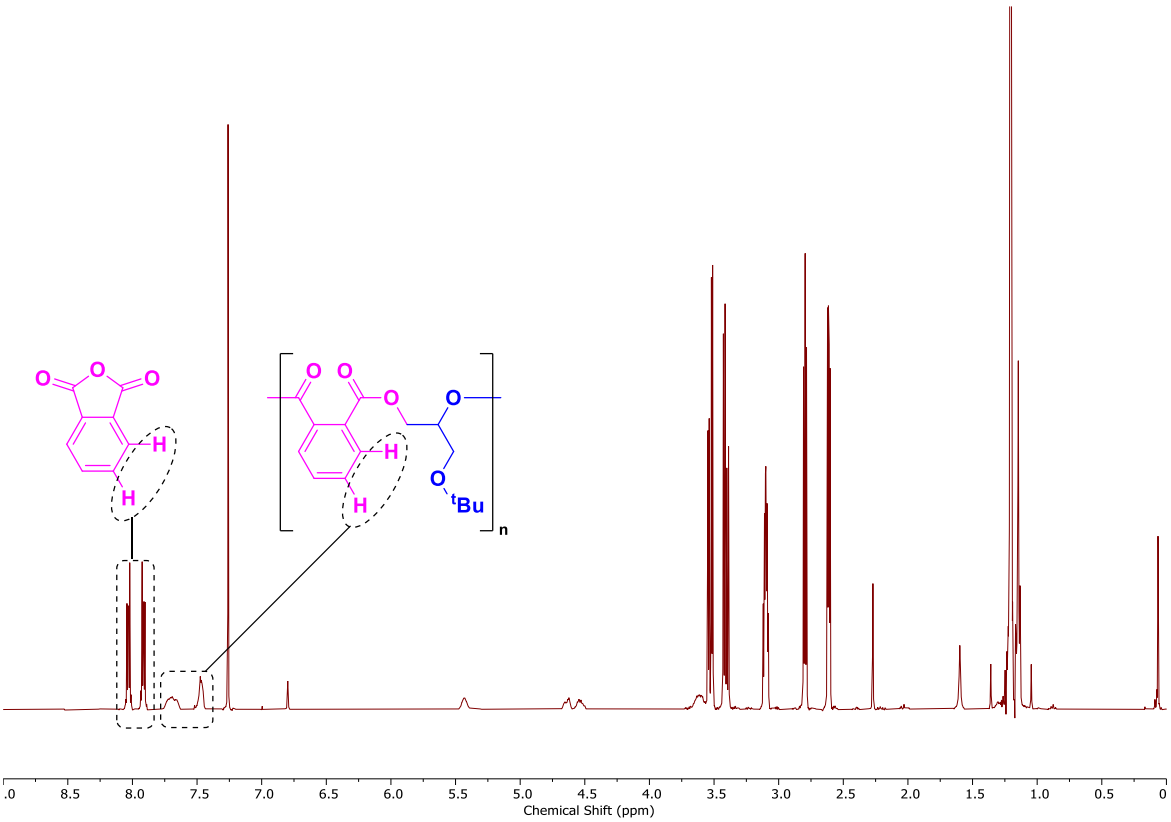


Figure S4.46. ^{1}H NMR spectrum (400 MHz, $CDCl_3$, 298 K) of reaction mixture of tBGE and PA. Conversion of PA (%) = (∫7.75-7.35 ppm/(∫8.05-7.35 ppm))*100. TONEpoxide = TONAnhydride = Conv. (%)*400. Spectroscopic data is consistent with prior literature reports.[7]

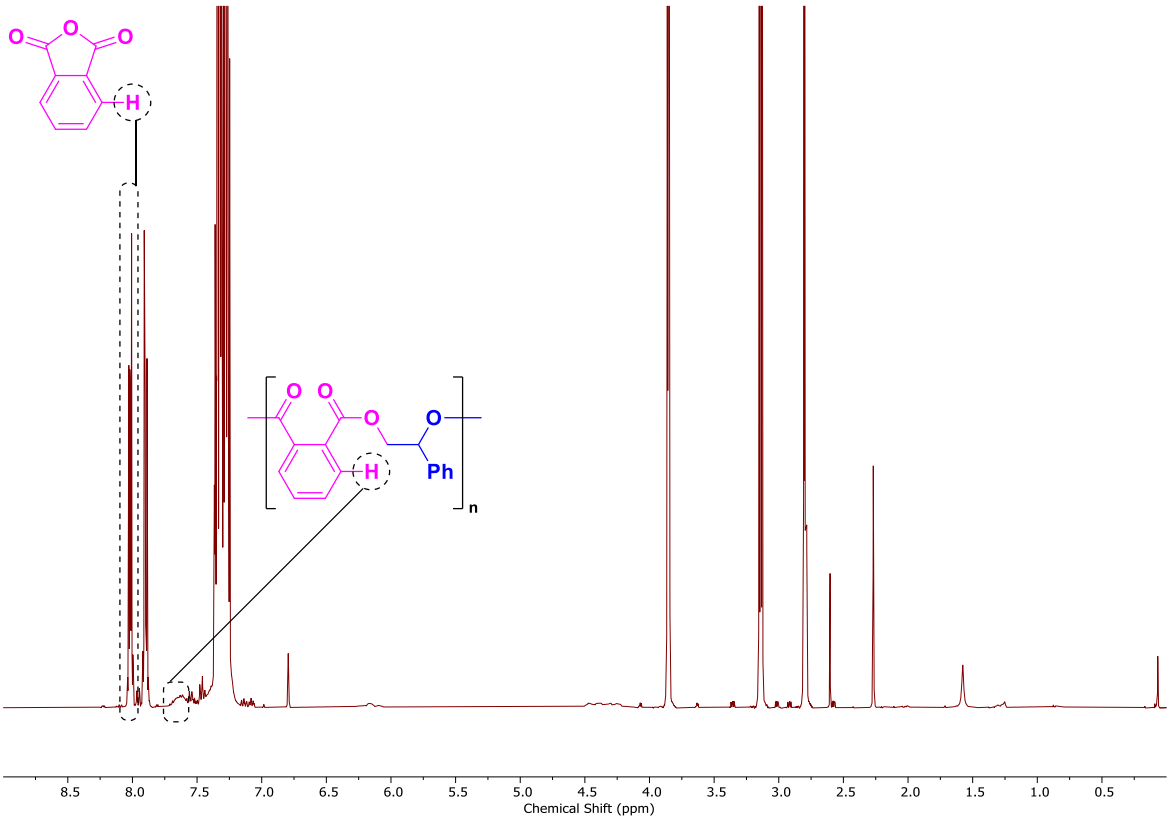


Figure S4.47. ^{1}H NMR spectrum (400 MHz, $CDCl_3$, 298 K) of reaction mixture of SO and PA. Conversion of PA (%) = (∫7.70-7.50 ppm/(∫8.00-7.90 ppm + ∫7.70-7.50 ppm))*100. $TON_{Epoxide}$ = $TON_{Anhydride}$ = Conv. (%)*400. Spectroscopic data is consistent with prior literature reports.[7]

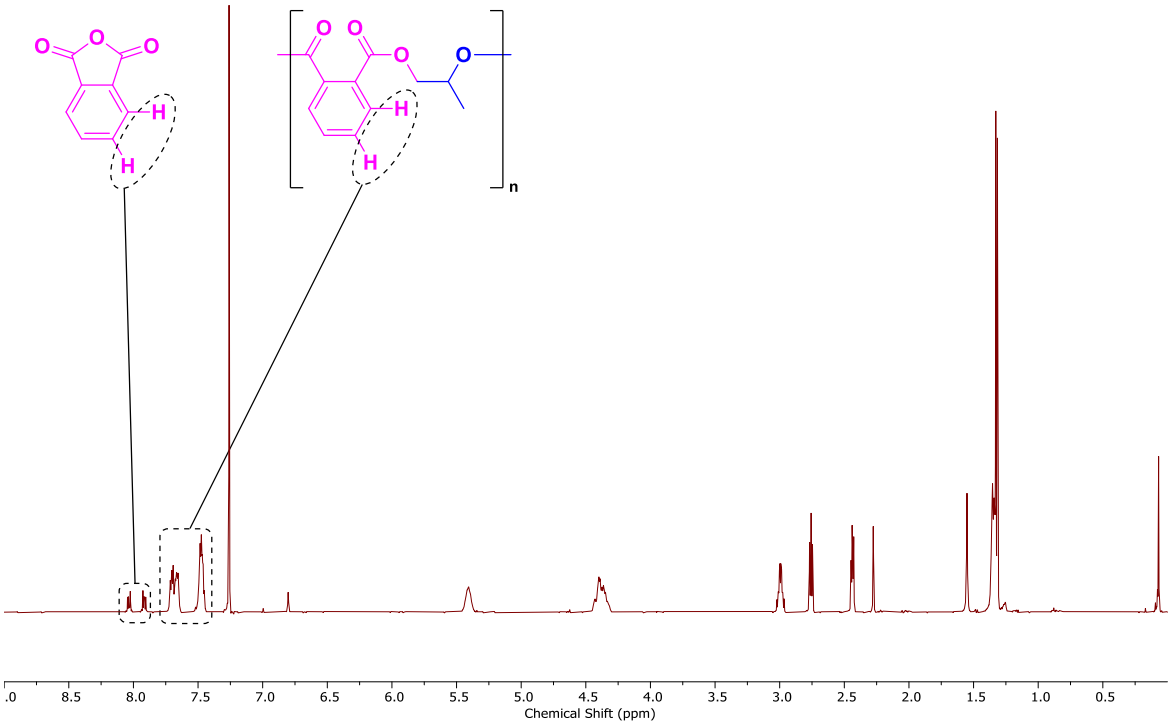


Figure S4.48. ^{1}H NMR spectrum (400 MHz, $CDCl_3$, 298 K) of reaction mixture of PO and PA. Conversion of PA (%) = (∫7.75-7.40 ppm/(∫8.10-7.40 ppm)*100. $TON_{Epoxide}$ = $TON_{Anhydride}$ = Conv. (%)*400. Spectroscopic data is consistent with prior literature reports.[7]

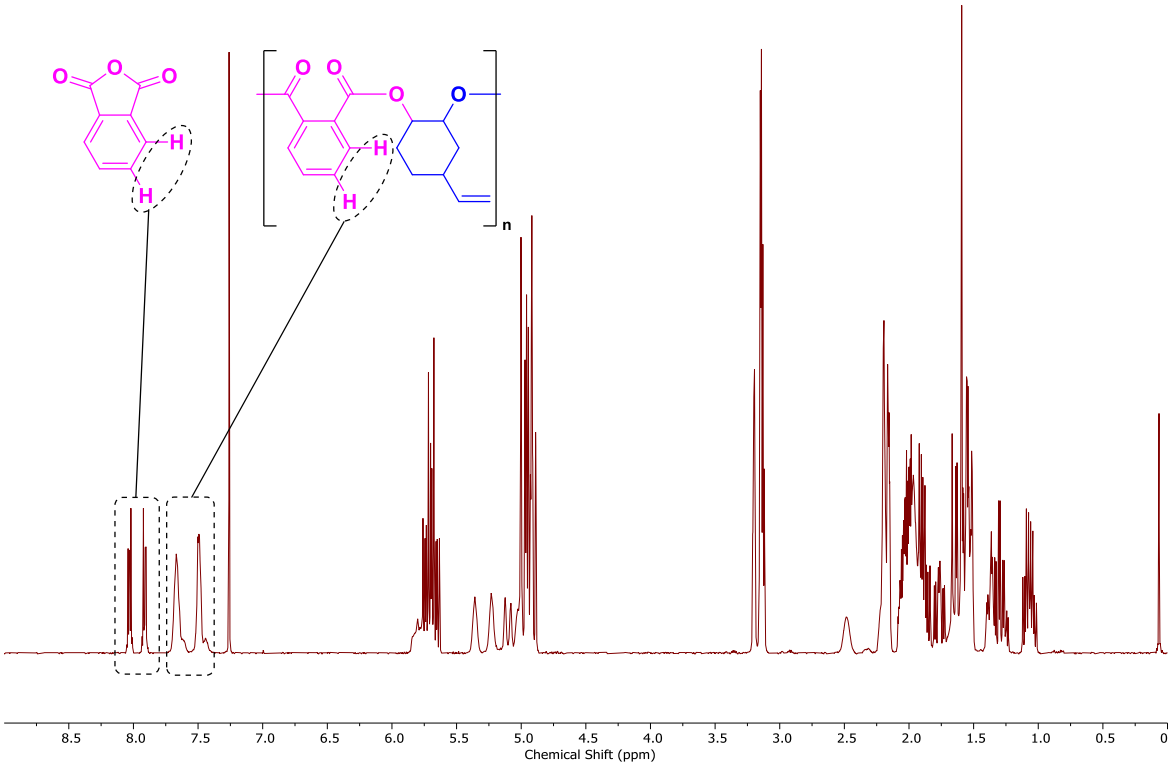


Figure S4.49. ^{1}H NMR spectrum (400 MHz, $CDCl_3$, 298 K) of reaction mixture of vCHO and PA. Conversion of PA (%) = (∫7.80-7.40 ppm/(∫8.10-7.40 ppm)*100. $TON_{Epoxide}$ = $TON_{Anhydride}$ = Conv. (%)*400. Spectroscopic data is consistent with prior literature reports.[7]

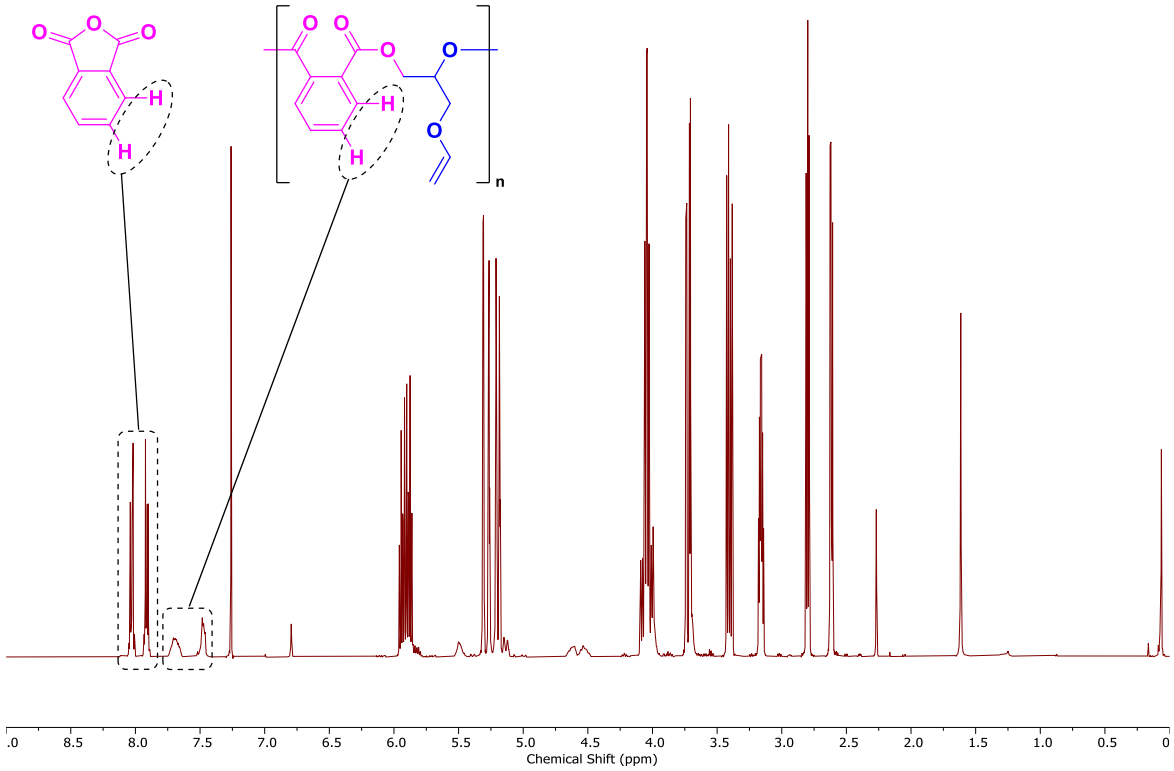


Figure S4.50. ^{1}H NMR spectrum (400 MHz, $CDCl_3$, 298 K) of reaction mixture of AGE and PA. Conversion of PA (%) = (∫7.80-7.40 ppm/(∫8.10-7.40 ppm)*100. $TON_{Epoxide} = TON_{Anhydride}$ = Conv. (%)*400. Spectroscopic data is consistent with prior literature reports.[7]

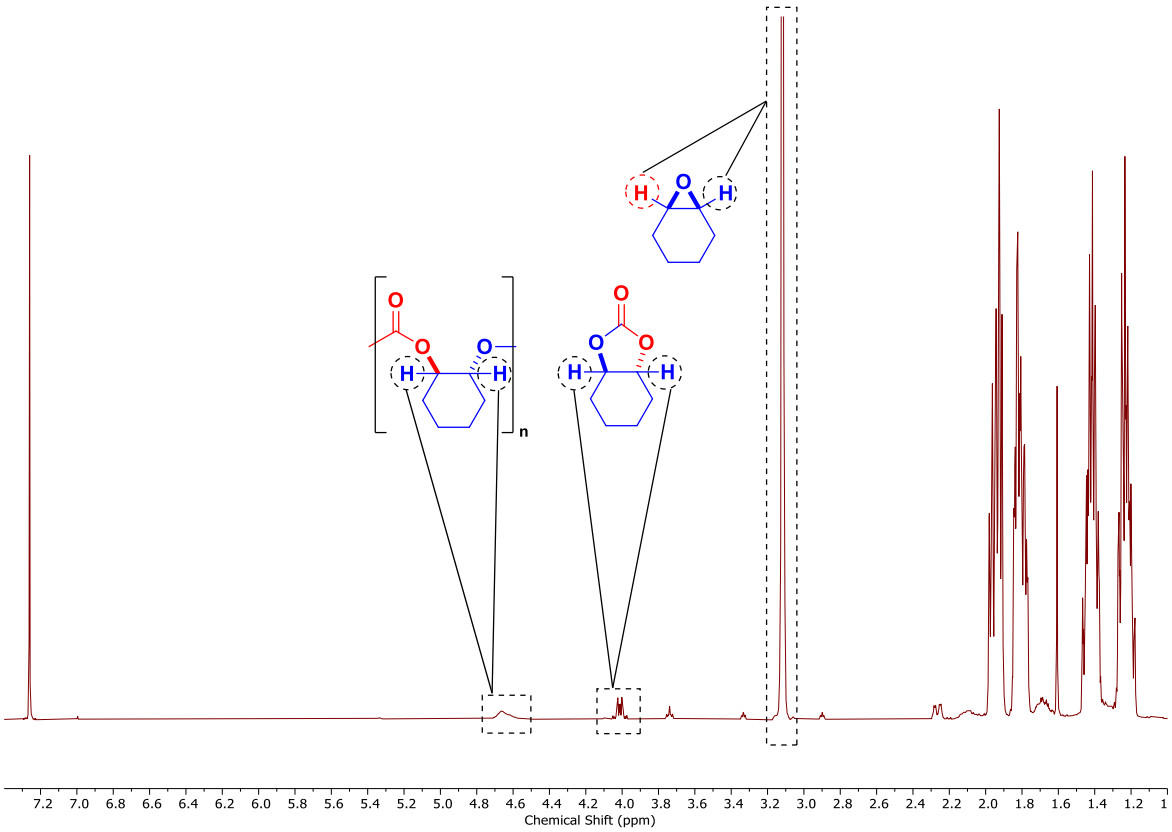


Figure S4.51. ^{1}H NMR spectrum (400 MHz, $CDCl_3$, 298 K) of reaction mixture of CHO and CO_2 (1 bar). Conversion of CHO to PCHC (%) = ((∫4.90-4.35 ppm/(∫4.90-4.35 ppm + ∫3.25-3.00 ppm)*100. TON_{PCHC} = Conv.(%)*2000. $Selectivity_{PCHC}$ (%) = (∫4.90-4.35 ppm/(∫4.90-4.35 ppm + ∫4.10-3.90 ppm))*100. Spectroscopic data is consistent with prior literature reports.[5]

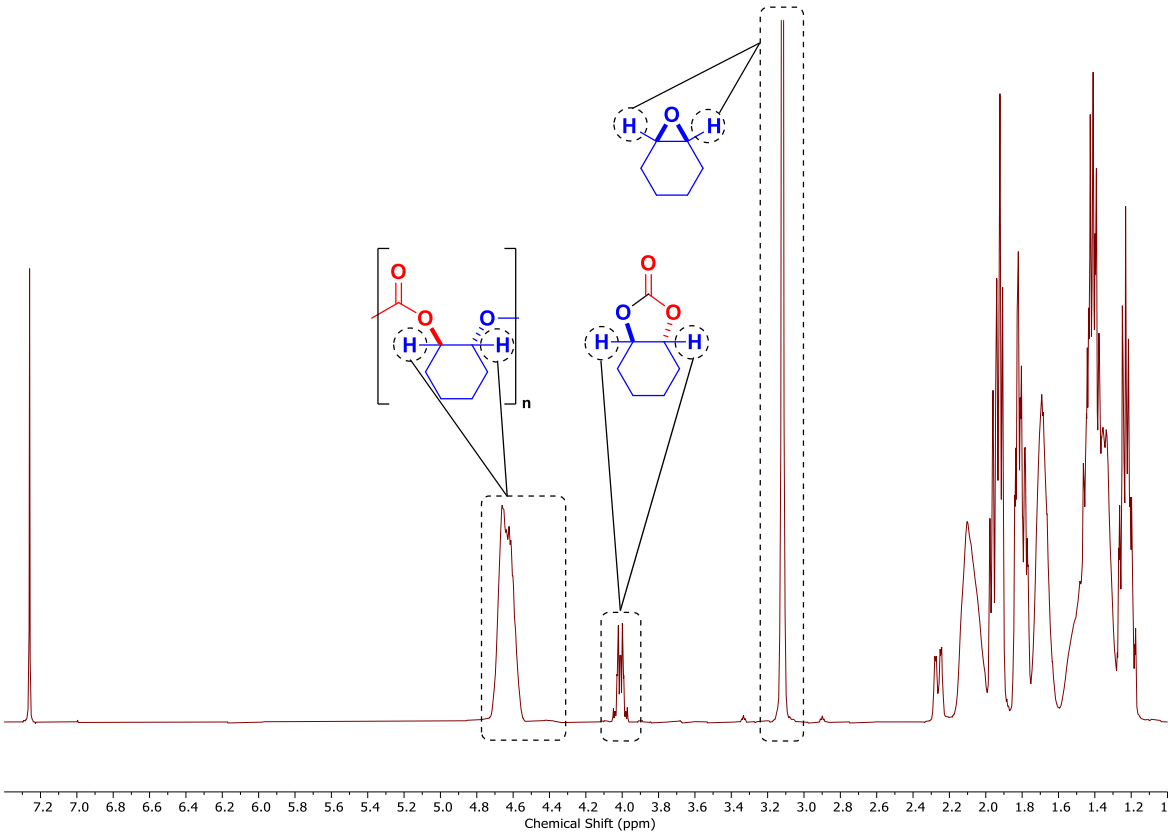


Figure S4.52. ^{1}H NMR spectrum (400 MHz, $CDCl_3$, 298 K) of reaction mixture of CHO and CO_2 (1 bar). Conversion of CHO to PCHC (%) = ((∫4.90-4.35 ppm/(∫4.90-4.35 ppm + ∫3.25-3.00 ppm)*100. TON_{PCHC} = Conv.(%)*2000. $Selectivity_{PCHC}$ (%) = (∫4.90-4.35 ppm/(∫4.90-4.35 ppm + ∫4.10-3.90 ppm))*100. Spectroscopic data is consistent with prior literature reports.[5]

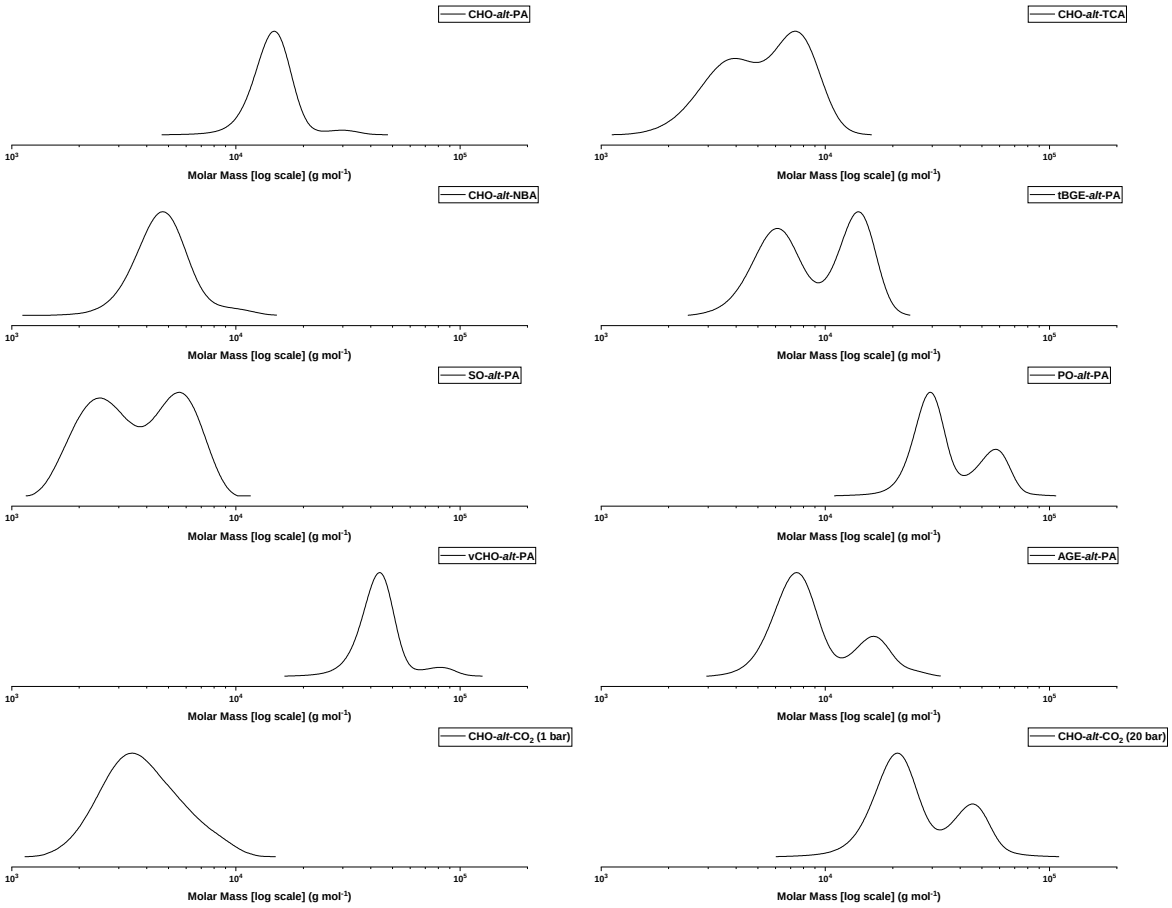


Figure S4.53. GPC traces for polymers corresponding to Table 4.3, Entries 1-10. The polymer molecular mass distributions are bimodal owing to the presence of monofunctional (acetate) and bifunctional (diol or diacid, present as a result of residual H_2O in epoxide or anhydride) initiators.

Table S4.10. Data for the ROCOP of epoxide and anhydrides with complex 2 at full anhydride conversion.[a]

Entry	Monomer	Time (m)	Conv (%)	TON[b]	$M_{n,\,GPC}$ [Đ][c] (kg mol^{-1})	$M_{n,\,Th.}$[d] (kg mol^{-1})
1	CHO / PA	26	>99	400	20.1 [1.06]	49.3
2	CHO / TCA	120	>99	400	13.4 [1.21]	66.4
3	CHO / NBA	120	>99	400	13.5 [1.13]	52.4
4	tBGE / PA[e]	90	90	360	25.5 [1.19]	55.6
5	SO / PA	165	>99	400	14.5 [1.21]	53.6
6	vCHO / PA	75	>99	400	58.3 [1.07]	55.2
7	AGE / PA[e]	85	99	398	27.4 [1.18]	49.6

[a] Conditions: [Cat]:[PA] = 1:400, 1 mL epoxide, [Cat] = 4.9 mmol, T = 100 °C. [b]Turnover number (TON) = number of moles of anhydride consumed/number of moles of catalyst. Determined by ^{1}H NMR. [c] Determined by GPC, in THF at 30 °C, using narrow dispersity polystyrene standards. [d] Theoretical M_n value. Determined through (TON x M_n(repeat unit))/(number of equivalent of catalyst x 2 (as each catalyst contains 2 acetate groups)). [e] Significant transesterification was observed after full anhydride conversion; data given before full conversion is reached.

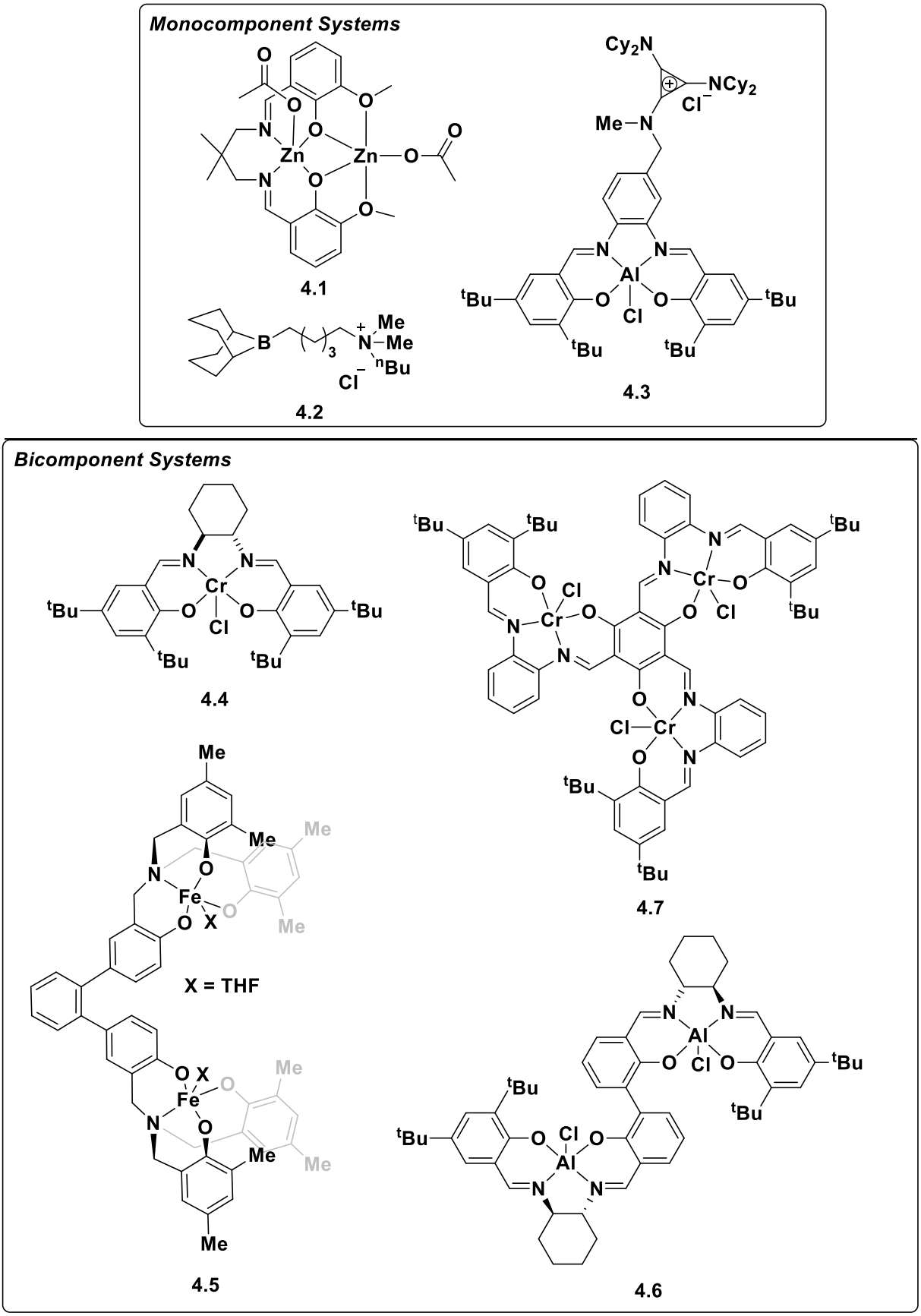


Figure S4.54. Structure of catalysts reported for epoxide/anhydride ROCOP

Supplementary Figures and Data for Chapter 5

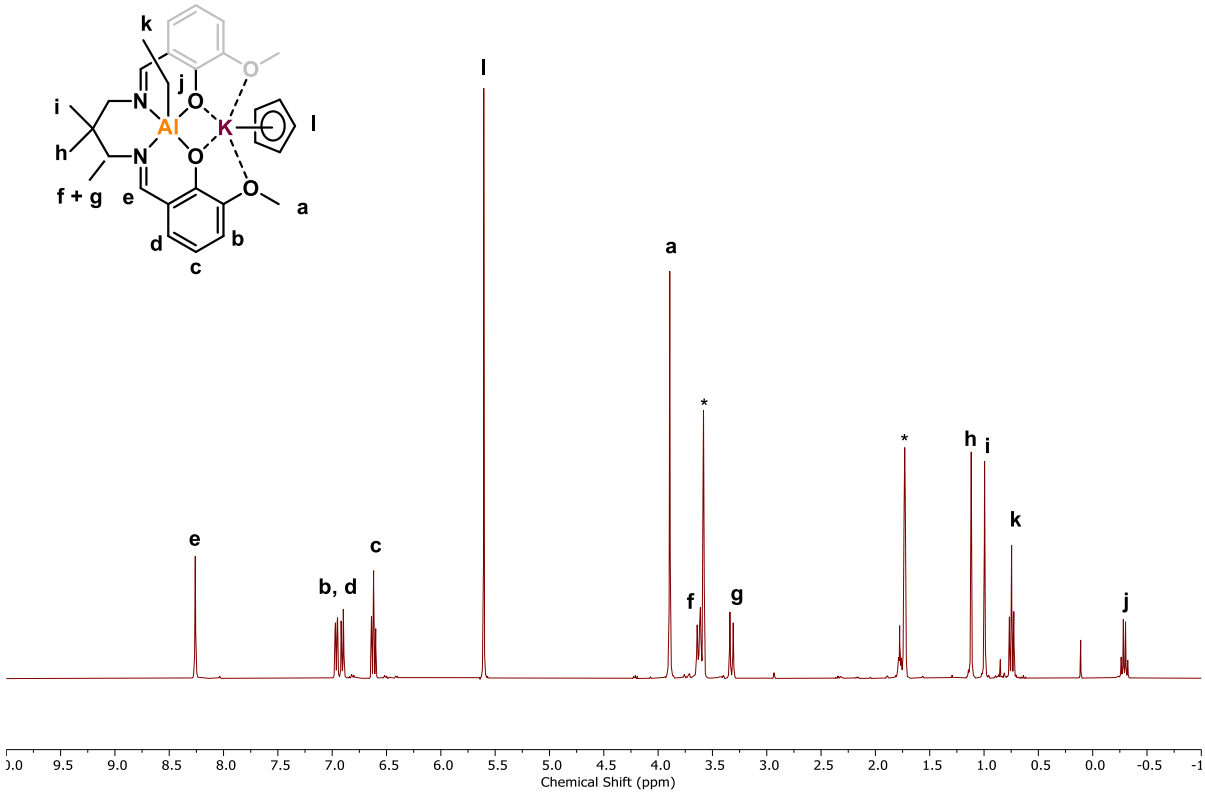


Figure S5.1. ^{1}H NMR spectrum (400 MHz, 298 K, THF-d_8) of complex **13**.

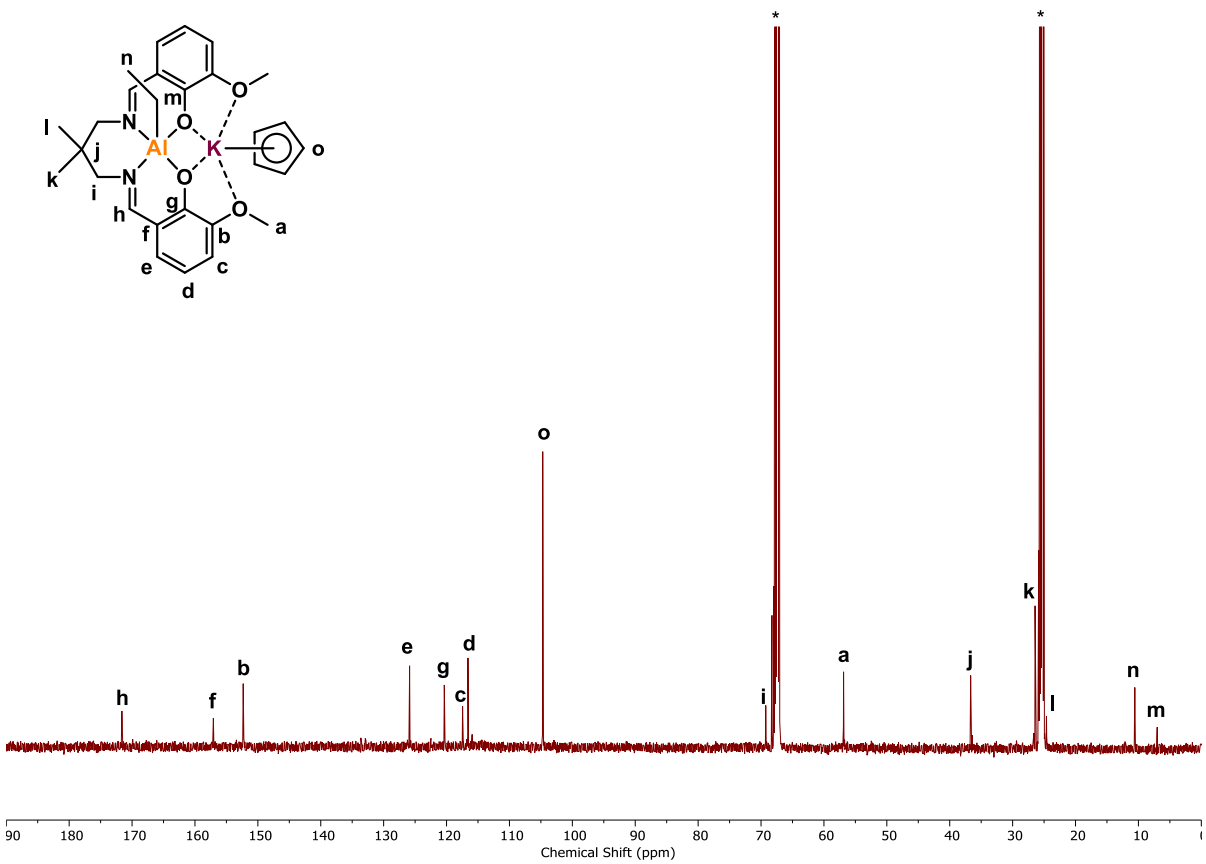


Figure S5.2. ^{13}C NMR spectrum (126 MHz, 298 K, THF-d_8) of complex **13**.

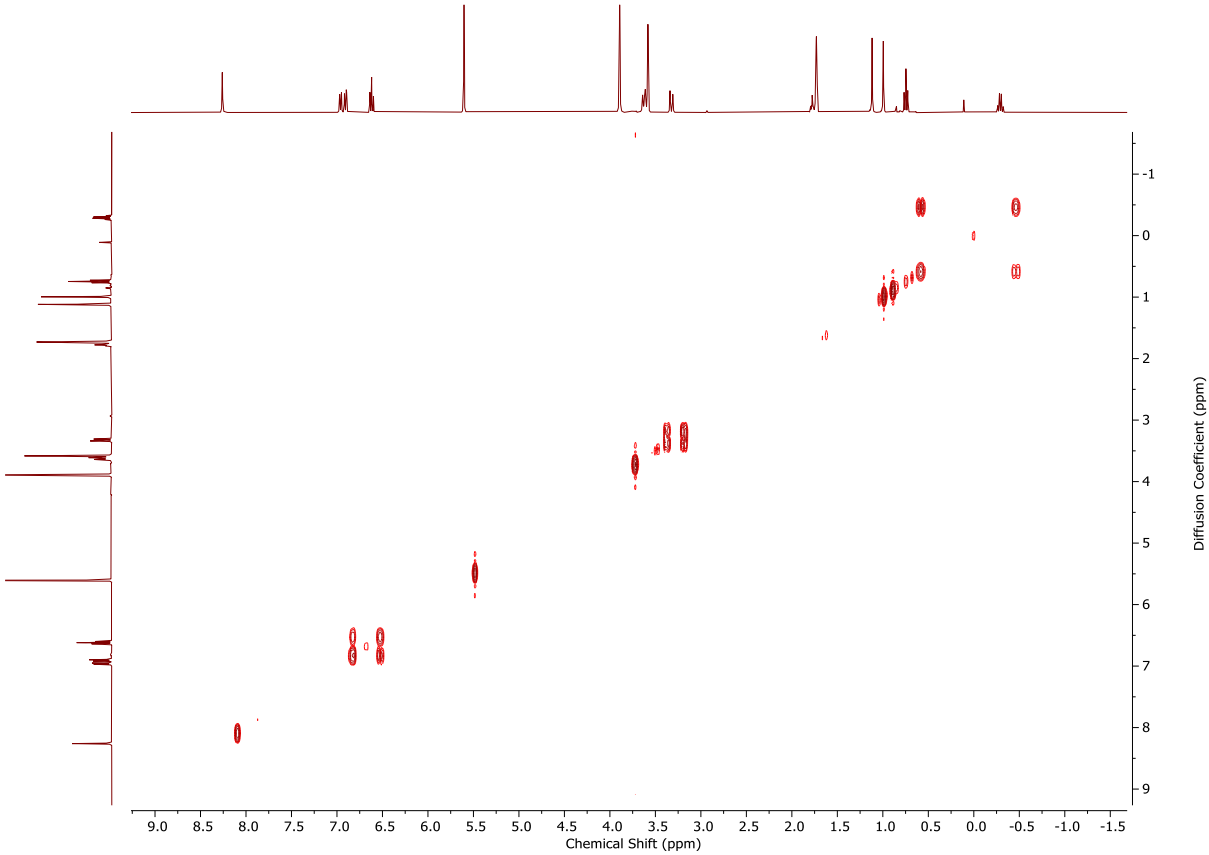


Figure S5.3. ^{1}H COSY NMR Spectrum (400 MHz, 298 K, THF-d_8) of complex **13**.

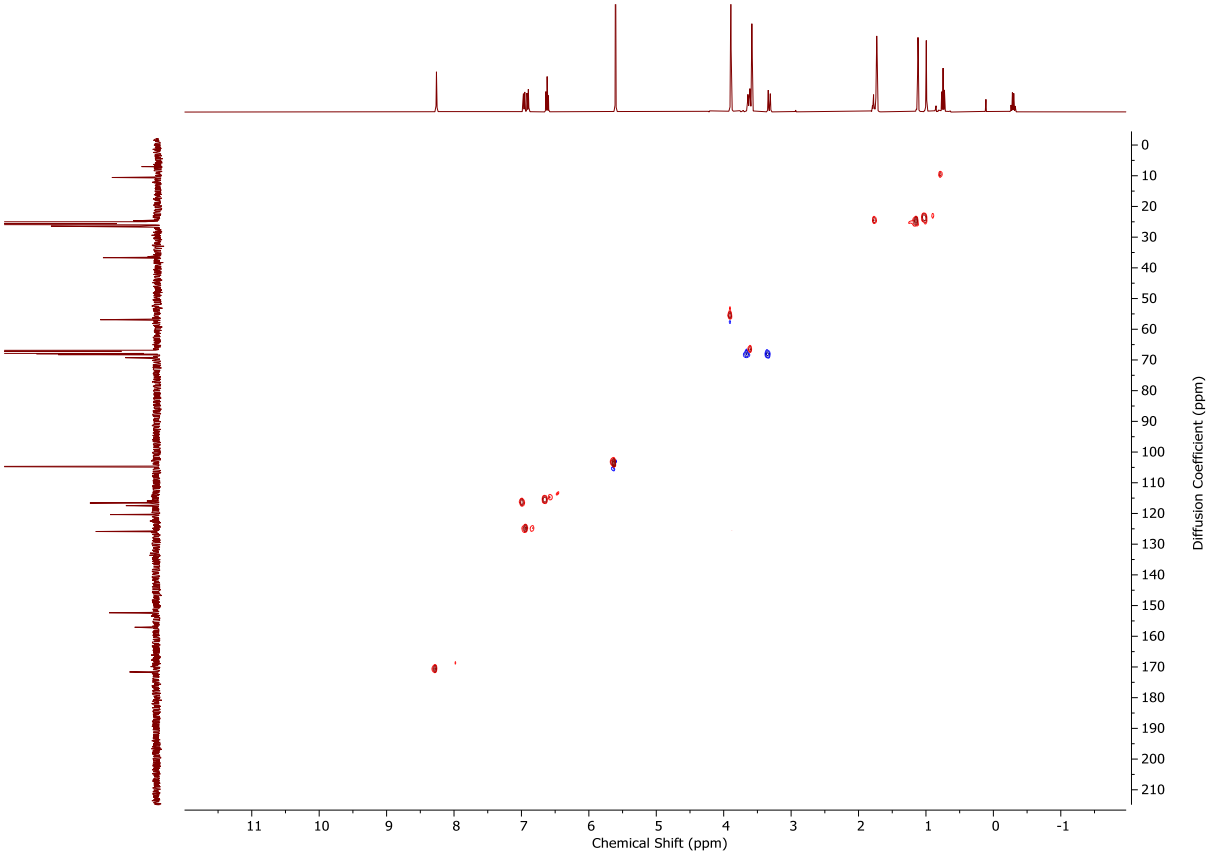


Figure S5.4. ^{1}H-^{13}C HSQC NMR Spectrum (298 K, THF-d_8) of complex **13**.

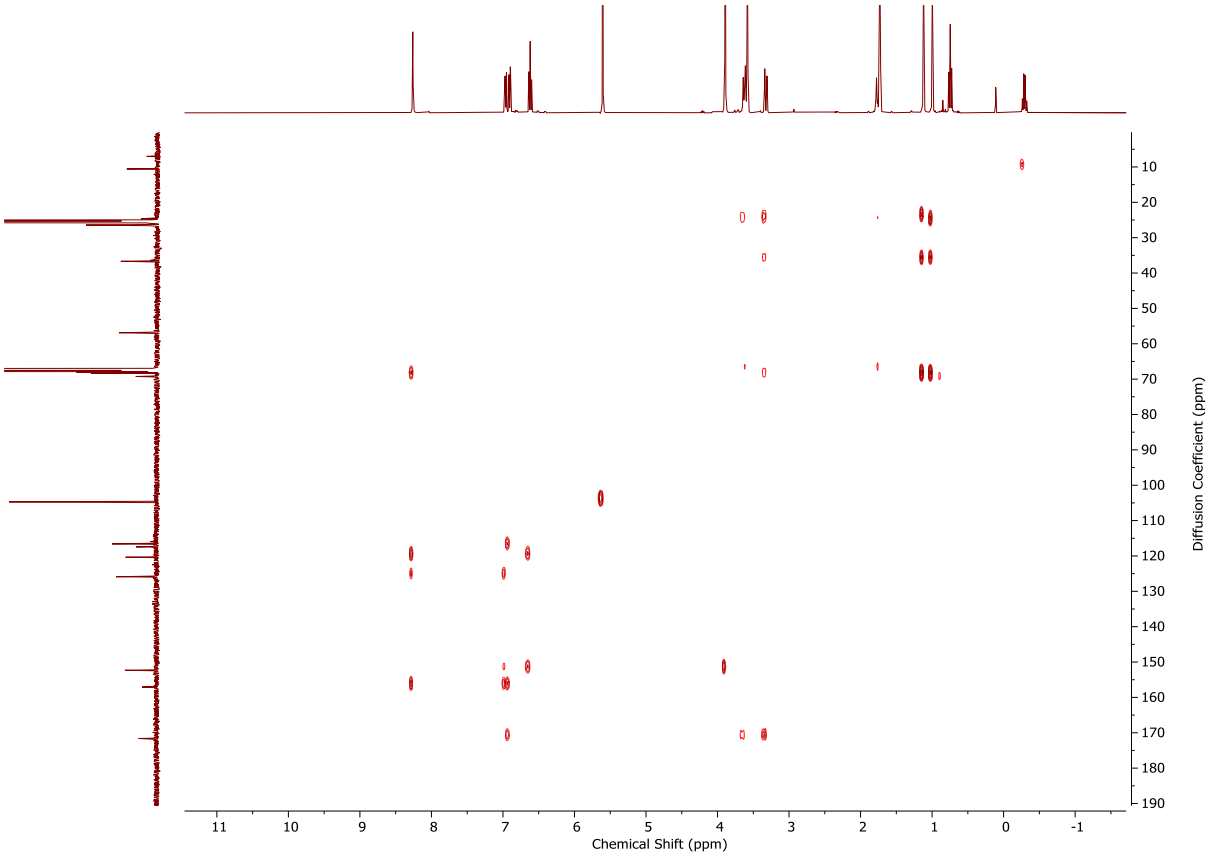


Figure S5.5. ^{1}H-^{13}C HMBC NMR Spectrum (298 K, THF-d_8) of complex **13**.

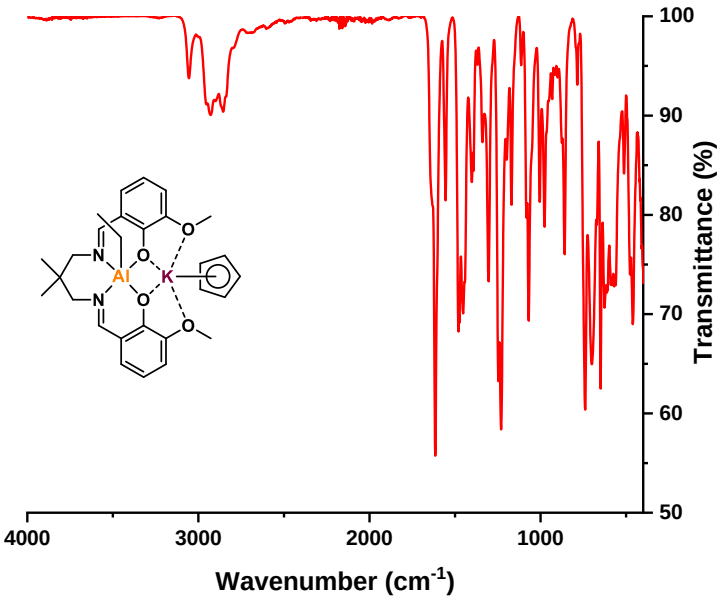


Figure S5.6. Infrared spectrum of complex **13**.

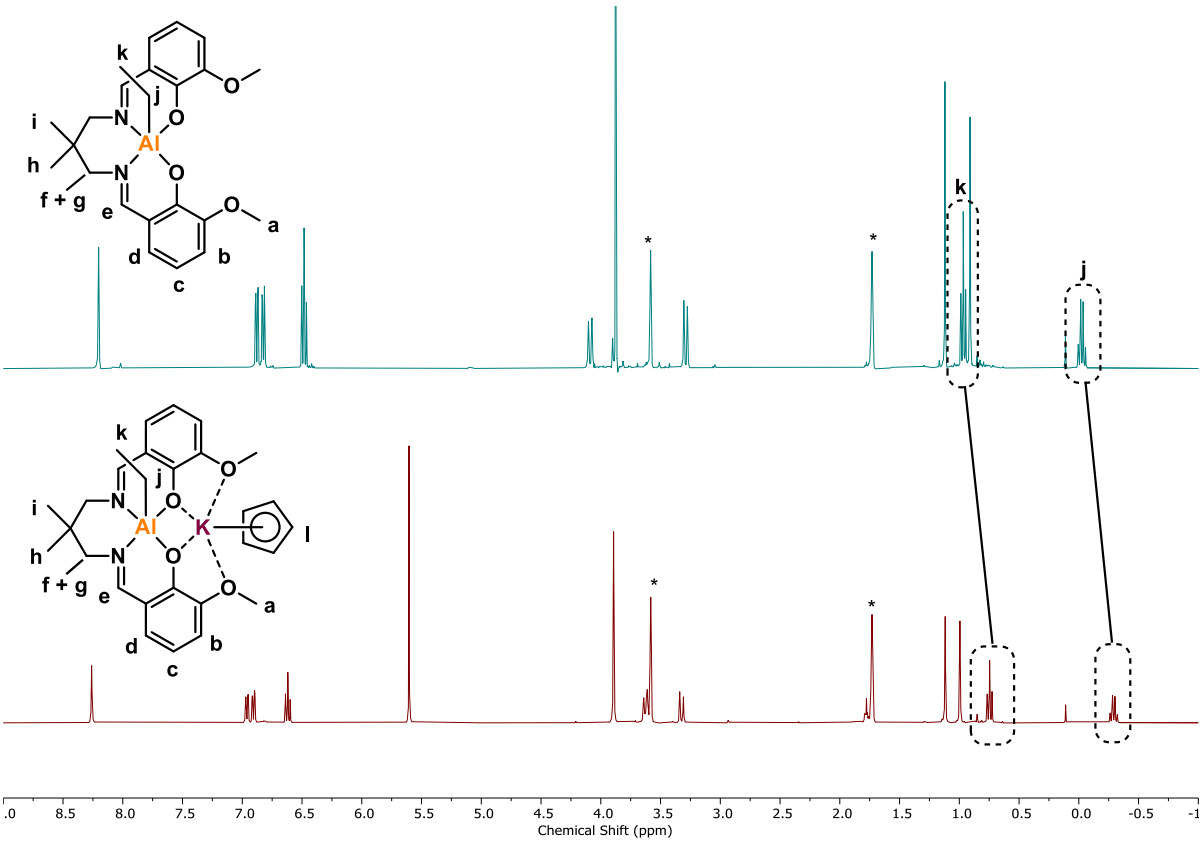


Figure S5.7. ^{1}H NMR spectra (400 MHz, 298 K, $CDCl_3$) of complexes **1** and **13**.

Taking the ratio of theoretical and experimental molecular mass:

$$\frac{M_{n,Th}}{M_{n,GPC}} = 1.25$$

Establish total amount of CTA equivs based on this ratio:

$$1.25 * [CTA]_{Added} = [CTA]_{Total} = 5$$

Back-calculate residual CTA equivalents:

$$[CTA]_{Total} = [CTA]_{Residual} + [CTA]_{Added}$$

$$[CTA]_{Residual}: [PA]: [vCHO] = 1: 800: 4000$$

Figure S5.8. Calculation of residual CTA equivalents.

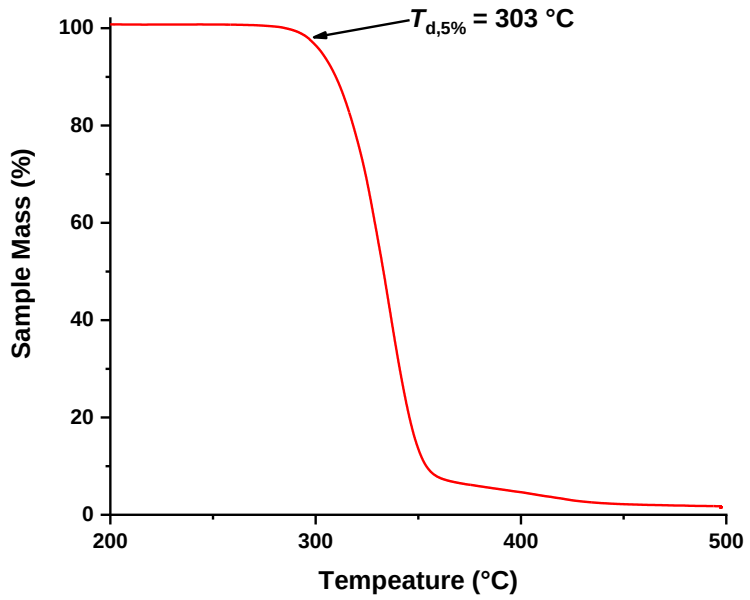


Figure S5.9. TGA trace for PvCHPE-24

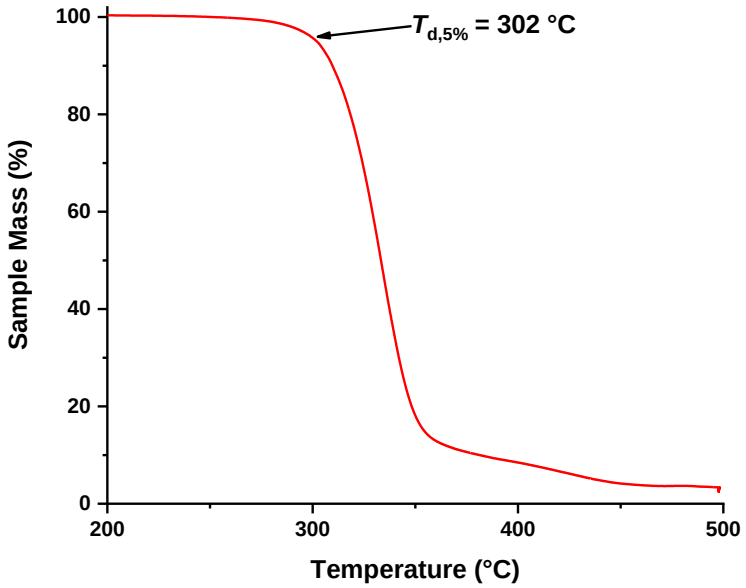


Figure S5.10. TGA trace for PvCHPE-44.

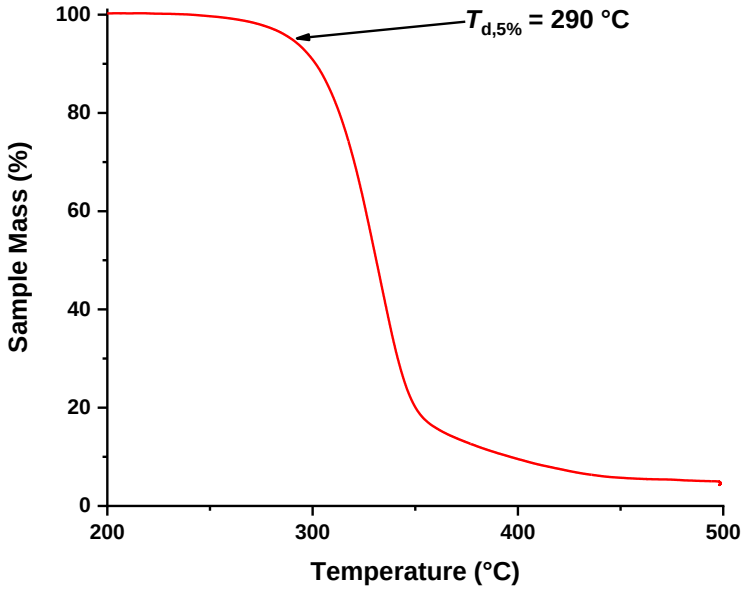


Figure S5.11. TGA trace for PvCHPE-70.

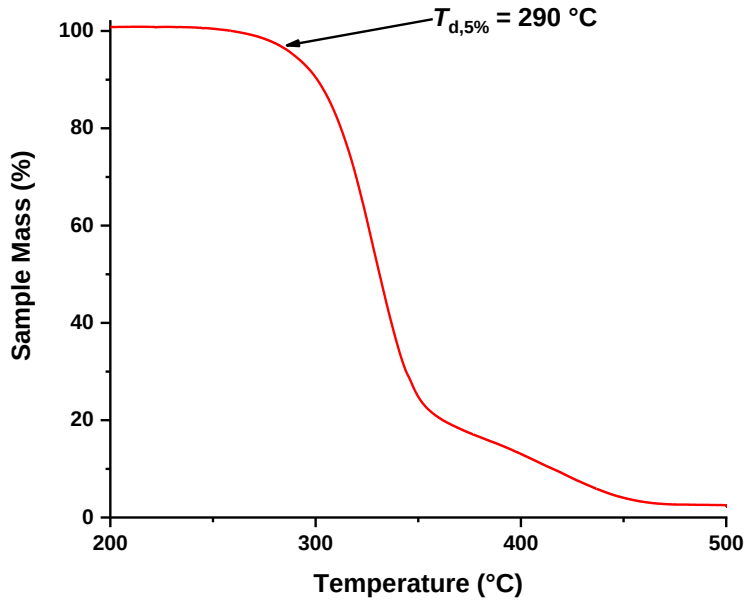


Figure S5.12. TGA trace for PvCHPE-91.

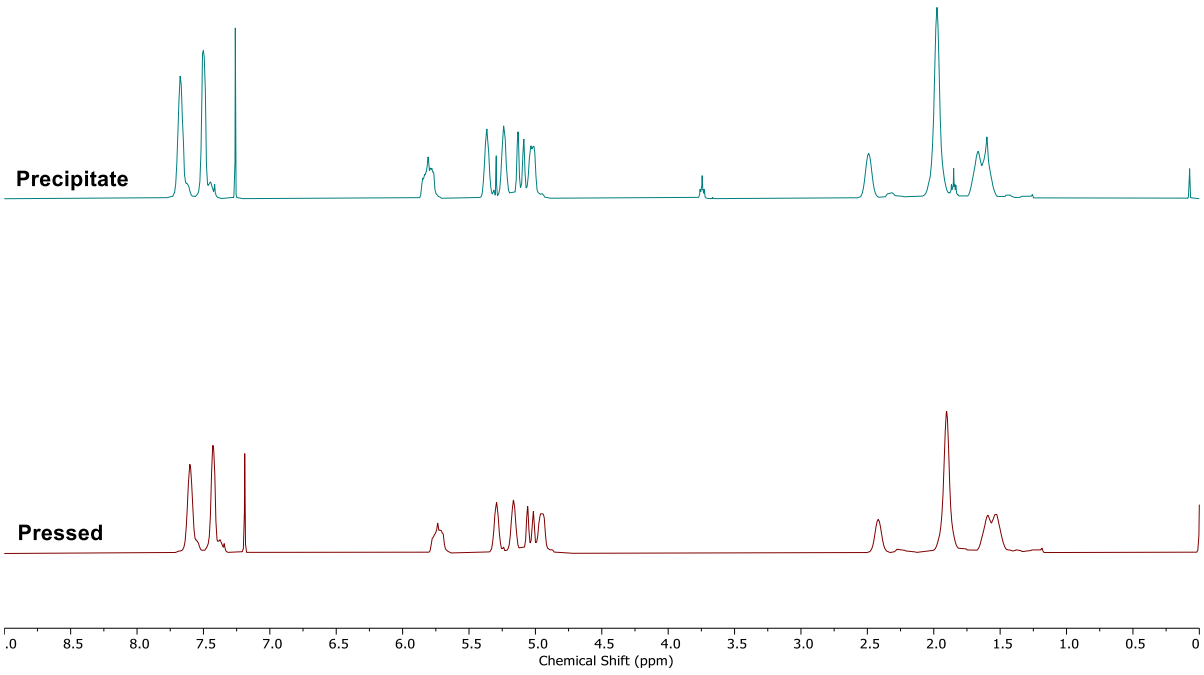


Figure S5.13. ^{1}H NMR spectrum (400 MHz, 298 K,$CDCl_3$) of PvCHPE-24 before and after hot pressing.

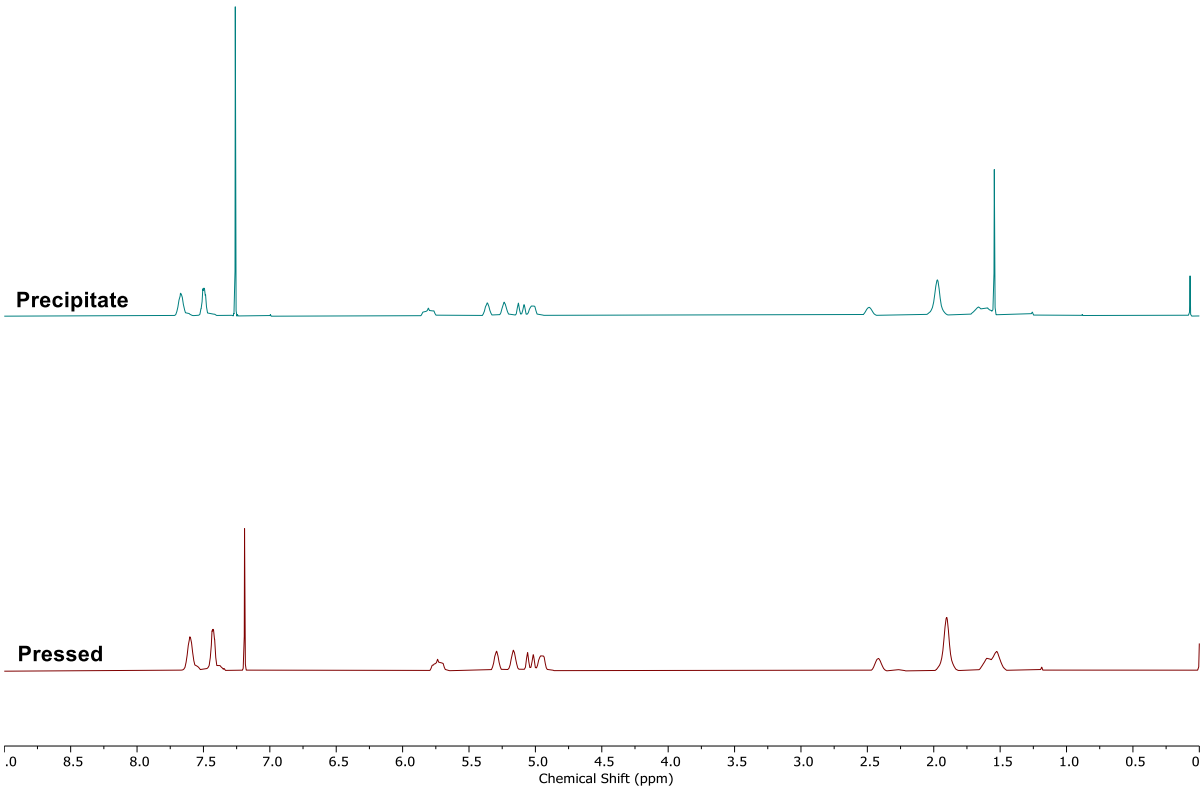


Figure S5.14. ^{1}H NMR spectrum (400 MHz, 298 K,$CDCl_3$) of PvCHPE-44 before and after hot pressing.

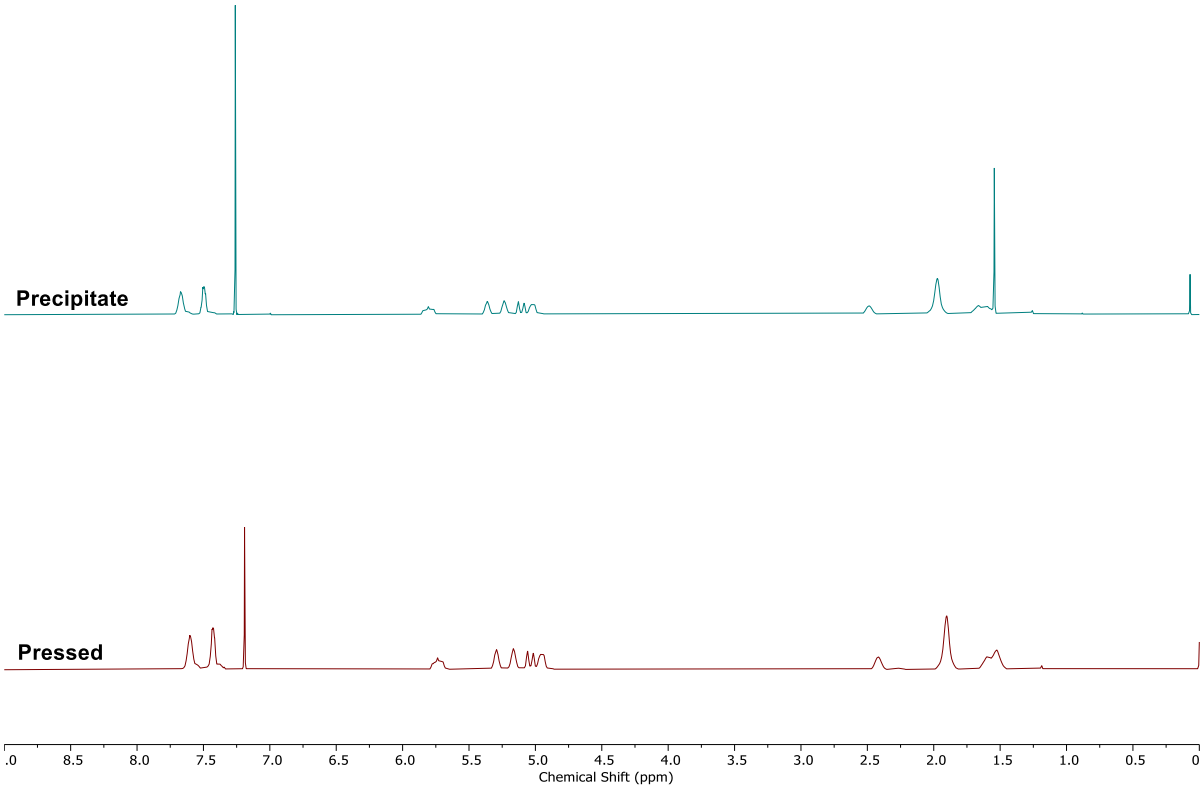


Figure S5.15. ^{1}H NMR spectrum (400 MHz, 298 K,$CDCl_3$) of PvCHPE-70 before and after hot pressing.

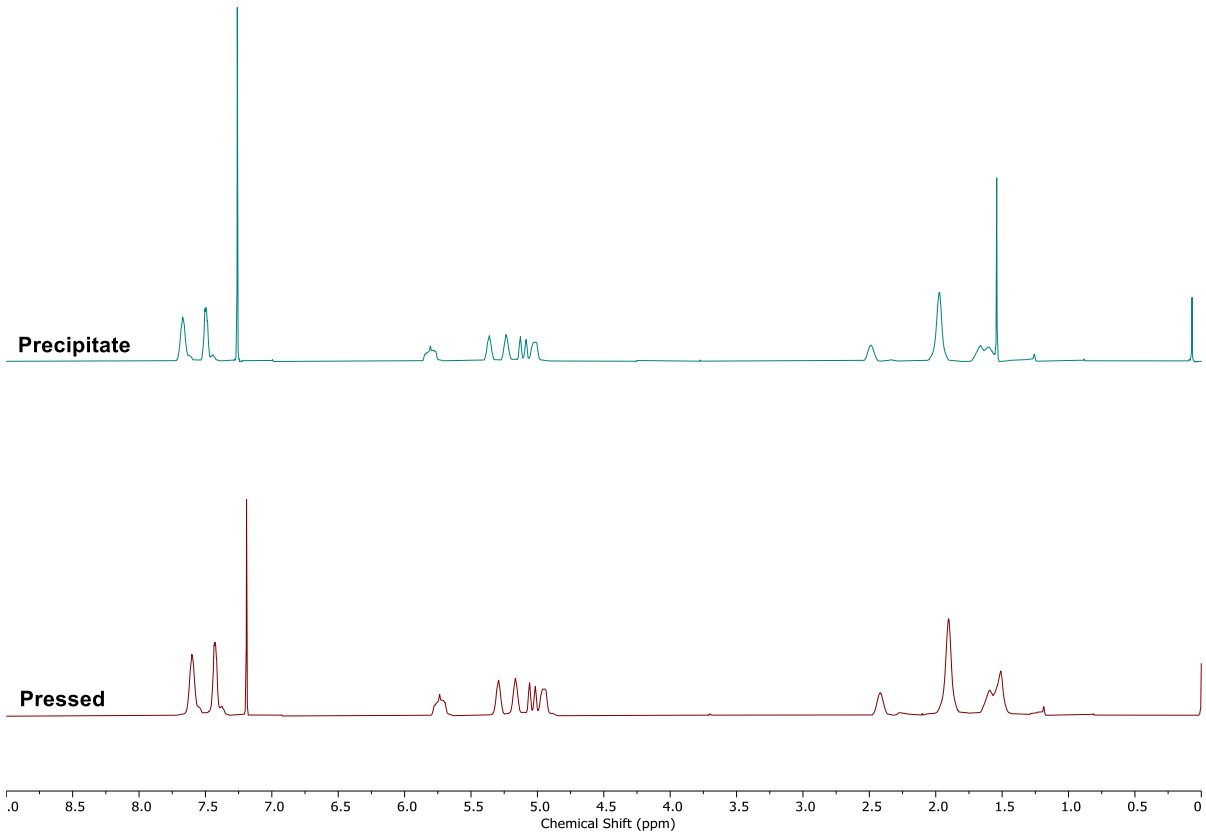


Figure S5.16. ^{1}H NMR spectrum (400 MHz, 298 K,$CDCl_3$) of PvCHPE-91 before and after hot pressing.

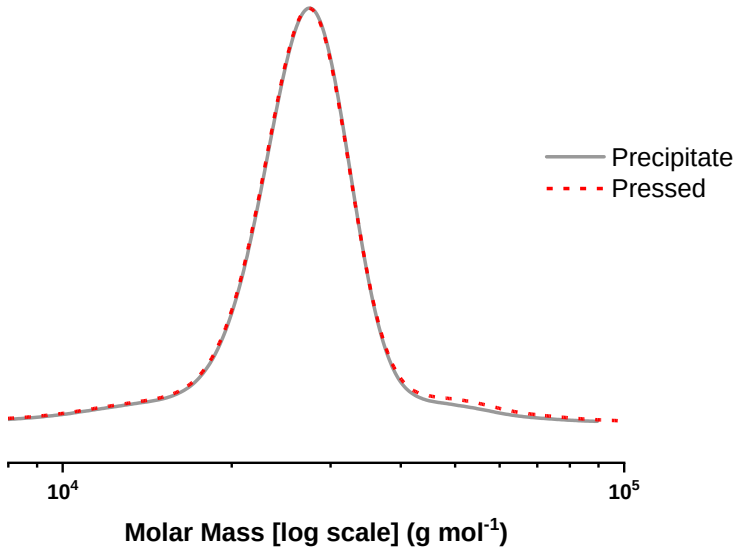


Figure S5.17. GPC Trace of PvCHPE-24 before and after processing *via* hot press.

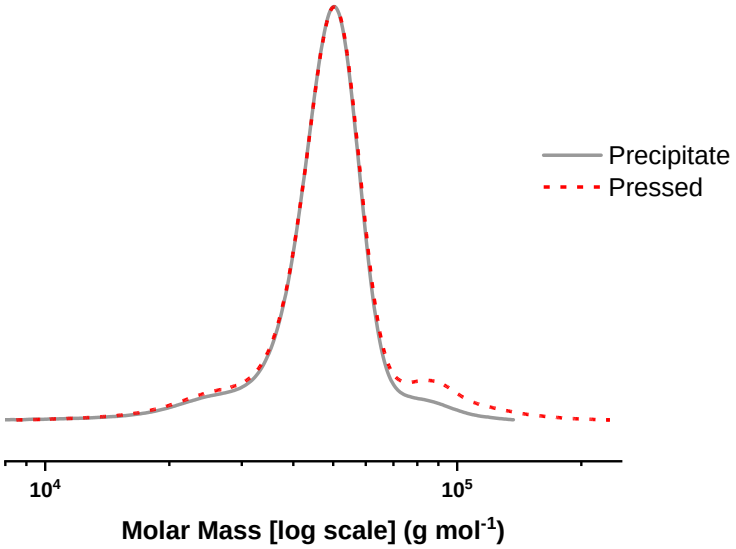


Figure S5.18. GPC Trace of PvCHPE-44 before and after processing *via* hot press.

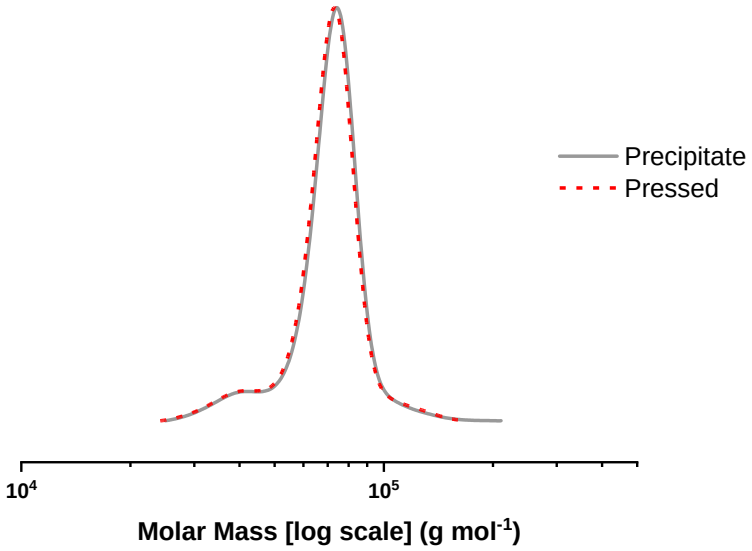


Figure S5.19. GPC Trace of PvCHPE-70 before and after processing *via* hot press.

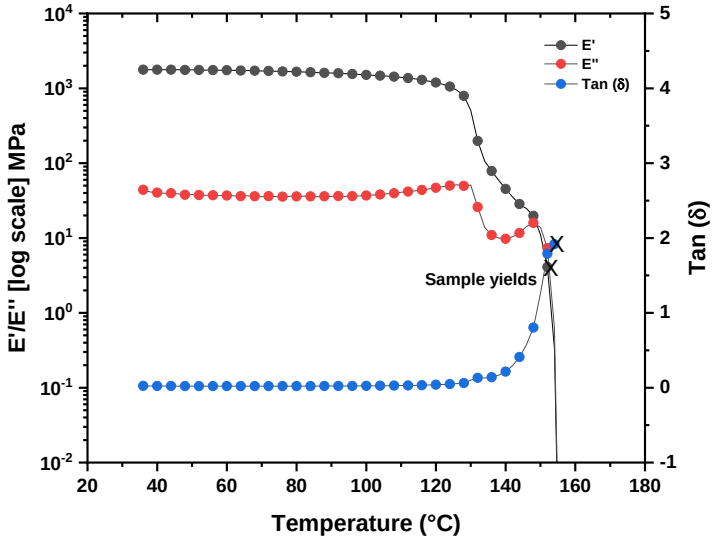


Figure S5.20. Results from DMTA of PvCHPE-44 between 30 – 200 °C

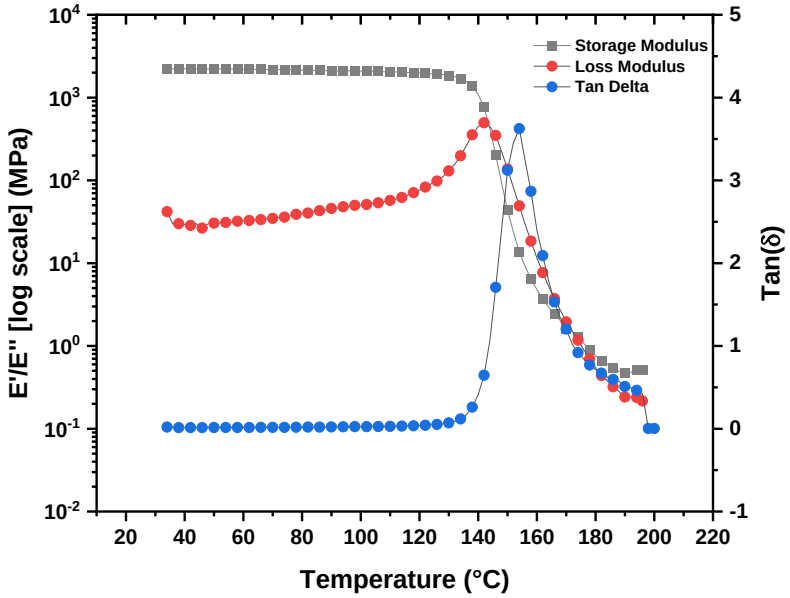


Figure S5.21. Results from DMTA of PvCHPE-70 between 30 – 200 °C.

References for Appendix

1. J. Deng, M. Ratanasak, Y. Sako, H. Tokuda, C. Maeda, J. Y. Hasegawa, K. Nozaki and T. Ema, *Chem. Sci.*, 2020, **11**, 5669-5675.
2. G. Luchini, J. V. Alegre-Requena, I. Funes-Ardoiz and R. S. Paton, *F1000Research*, 2020, **9**.
3. S. Grimme, *Chem. Eur. J.*, 2012, **18**, 9955-9964.
4. G. Scalmani and M. J. Frisch, *J. Chem. Phys.*, 2010, **132**, 114110.
5. G. Rosetto, A. C. Deacy and C. K. Williams, *Chemical Science*, 2021, DOI: 10.1039/d1sc03856g, 10.1039/d1031sc03856g.
6. B. A. Abel, C. A. L. Lidston and G. W. Coates, *J. Am. Chem. Soc.*, 2019, **141**, 12760-12769.
7. H. Li, H. T. Luo, J. P. Zhao and G. Z. Zhang, *Macromolecules*, 2018, **51**, 2247-2257.